CRANFIELD UNIVERSITY

NOFRIZAL

CORROSION OF HIGH STRENGTH PIPELINE STEEL WELDMENT USING SUBMERGED JET IMPINGEMENT

SCHOOL OF AEROSPACE, TRANSPORT AND MANUFACTURING

PhD

Academic Years: 2015 - 2019

Supervisor: Dr. Susan A. Impey
Associate Supervisor: Dr. Konstantinos Georgarakis
March 2019

CRANFIELD UNIVERSITY

SCHOOL OF AEROSPACE, TRANSPORT AND MANUFACTURING

PhD

Academic Years: 2015 - 2019

NOFRIZAL

CORROSION OF HIGH STRENGTH PIPELINE STEEL WELDMENT USING SUBMERGED JET IMPINGEMENT

Supervisor: Dr. Susan A. Impey
Associate Supervisor: Dr. Konstantinos Georgarakis
March 2019

This thesis is submitted in partial fulfilment of the requirements for the degree of PhD

ABSTRACT

The aim of this research is to evaluate submerged jet impingement (SJI) as a tool for assessing the effect of flow and the associated corrosion behaviour across an X65 high strength pipeline weldment. The focus is corrosion caused by turbulent artificial sea water at different velocities impinging onto the weldment. An SJI target consisting of 3 rings (centre, inner and outer) based on a previous design [13], was constructed from an X65 pipeline steel weldment. Parent material (PM), heat affected zone (HAZ) and weld metal (WM) are analysed together in a high shear stress environment and changes in the weldment in a range of hydrodynamic conditions evaluated.

Electrochemical measurements were performed with X65 pipeline steel with stagnant and flowing artificial seawater saturated with carbon dioxide at 1 bar at 0 -10 m/s at 25 ^{o}C and pH 4. The behaviour with and without an inhibitor was also examined. Galvanic current characteristics between coupled weldment regions were recorded using a zero-resistance ammeter (ZRA), and self-corrosion analysed using linear polarisation resistance (LPR) measurements.

Computational fluid dynamic (CFD) analysis was undertaken to understand the hydrodynamic effects and velocity changes across the SJI target in flowing conditions. The velocity distribution across the target varied in each weld region where the centre, outer and inner electrodes are 25, 33 and 50% of the impinging jet velocity respectively. The inner electrodes of the SJI target experience 30% of the expected wall shear stress calculated from the impinging jet velocity.

Alternative SJI target configurations are proposed to represent a wide range of shear stress and fluid velocities across the target with good precision and accuracy. For low turbulence, the target centre electrode is minimised or placed at the target edge. To achieve maximum turbulence, an electrode 4 mm from the target centre is proposed. To achieve 10 m/s on the suggested target, a jet velocity of just over 15 m/s is required.

Keywords: Submerged jet impingement, preferential weld corrosion, X65 carbon steel, inhibitor, carbon dioxide

ACKNOWLEDGEMENTS

I would like to express my sincere appreciation and gratitude to my supervisors Dr. Susan Impey, Dr. Konstantinos Georgarakis for the guidance, inspiration, support, and patience throughout this study. I would like to acknowledge Dr. Michael J. Robinson as my previous supervisor and thank him for his assistance in designing and constructing a new submerged jet impingement target.

I would like to thank the technical staff of the School of Manufacturing, Cranfield University, in particular, , Mr. Steve Pope, Ms Christine Kimpton and Drs Xianwei Liu,Tracey Roberts, Christine Chalk, Andy Pidcock for their help throughout this study. Huge thanks to Dr. Michail Papanikalaou to help me to run and interpret the CFD simulation to make this thesis more comprehensive.

I would like to acknowledge the Ministry of Energy and Mineral Resources Republic of Indonesia which covers my tuition fees and supported my living expenses during the term of this study and Cranfield University for supporting this study with good facilities.

My sincere thanks to all my friends, and colleagues who never fail to help and encourage me during my study.

Last but not least, my sincere appreciations to my wife, Meyliana Wulandari who constantly supports me, my lovely children Alya Rahima Khairunnisa and Alifa Azzahra Khairunnisa and also my parents for always being there for me.

TABLE OF CONTENTS

LIST OF FIGURES

LIST OF TABLES

LIST OF EQUATIONS

LIST OF ABBREVIATIONS

DC	Direct Current
EDM	Electrical Discharge Machining
EDX	Energy Disperse-ray
EIS	Electrochemical Impedance Spectroscopy
EOR	Enhanced Oil Recovery
FAC	Focused Ion Beam
GMAW	Gas Metal Arc Welding
GTAW	Gas Tungsten Arc Welding
HAZ	Heat Affected Zone
LPR	Linear Polarisation Resistance
MSDS	Material Safety Data Sheet
OCP	Open Circuit Potential
OFN	Oxygen Free Nitrogen
PM	Parent Metal
PWC	Preferential Weld Corrosion
RCE	Rotating Cylinder Electrode
SAW	Submerged Arc Welding
SCE	Standard Calomel electrode
SEM	Scanning Electron Microscopy
SJI	Submerged Jet Impingement
WM	Weld Metal
XRD	X-ray Diffraction
ZRA	Zero Resistance Ammeter

1 INTRODUCTION

This chapter describes drivers and scope of this study using a submerged jet impingement (SJI) technique to evaluate the effect of flow and the associated corrosion behaviour, including galvanic interactions, across a weldment surface in sea water.

The weldment examined is an X65 high strength steel pipeline weldment. The significance of weld corrosion in oil and gas pipelines provides the research context and the research aim, objectives and scope of this study are presented.

1.1 Background

Corrosion is a crucial problem that strongly affects natural and industrial environments around the world. Steel, commonly used to design infrastructures or process facilities in many industries can experience different types of corrosion, and one such is galvanic attack.

The study of a specific type of aqueous corrosion behaviour, known as galvanic corrosion of dissimilar metals is challenging. Typically, corrosion rates can vary considerably when different materials are combined in static or dynamic aqueous environments. It is more challenging when three or more materials are linked and immersed in a fluid with variable flow rates.

Many examples of dissimilar materials in aqueous environments are found in freshwater, the marine environment and industries that rely on pipelines conveying fluids which experience turbulent flow [1,2].

Some critical areas within the petroleum industry, include welded pipelines which are vulnerable to galvanic attack where a range of fluids are conveyed in very diverse and hostile environments. Pipeline steels carry water, oil, gases (CO_2 and H_2S) and other fluids for both downstream and upstream facilities. At such facilities, carbon steel pipelines are crucial to the transport of oil and gas during the exploration and production periods. Oil and gas transportation over long

distances require extended pipelines and galvanic corrosion and the impact of the degradation is critical due to the numerous welds within the pipeline system.

A weldment comprises three different areas, namely parent metal (PM), weld metal (WM) and heat affected zone (HAZ). These areas have small differences in composition and microstructure, but these small differences can be enough to cause galvanic corrosion, particularly in a flowing environment. The effect of weld corrosion in oil and gas, especially in offshore production, is particularly detrimental, with the associated marine environment and wide fluctuations in exposure to salt water and temperatures. Carbon dioxide (CO_2) dissolved in petroleum product is a reactive agent particularly in the water phase. CO_2 will attack the pipeline material and the welded joints and can create serious corrosion issues which can damage the process equipment with high rates of weldment corrosion as Figure 1-1 [3–8].

In general, the effects of corrosion attacks on various industries directly affect the economic, technological, safety and environmental sectors around the world. In the UK, the latest study found that the overall financial loss per year due to corrosion of metal reached about 4.5% of the gross national product (GDP) [3]. In the United States, the Federal Highway Administration (FHWA) released a report on corrosion cost in 2000, stating that, in several sectors , the loss incurred as a result of corrosion is approximately $ 257 billion / year, which is about 3.5% of their GDP [4–6].

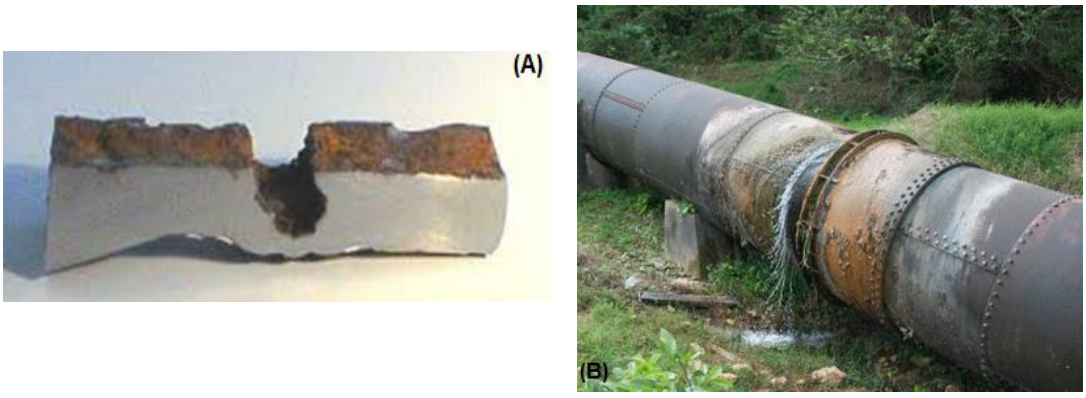

Figure 1-1 Weld corrosion in a (A) a pipeline steel [7] and (B) an oilfield [8]

In the oil and gas industry, carbon dioxide and hydrogen sulphide can create serious corrosion problems which can destroy process equipment, cause human endangerment, and high financial losses [9]. Particular attention is required for CO_2 corrosion, which can lead to localised corrosion in welded steel, associated with oil and gas production which attack the integrity of a carbon steel pipeline.

It has been reported that the percentage financial loss due to welding failure in the oil pipeline is 60 % of the total corrosion problem [10,11]. Examples are:

- In Alaska, during 2006, due to a small corroded hole in a pipeline wall, operated by British Petroleum (BP), a significant volume of crude oil spilled into the sea. It is estimated that at least a $100 million loss was incurred. The sea's ecosystem was also severely effected as a result of the spill.
- In November 2006, a natural gas pipeline in East Java Indonesia at a pressure of 440 psi failed and caused a major explosion. Eleven fatalities and 25 industrial gas customers were affected by the incident [10].
- Weld corrosion was identified as responsible for a severe disaster occurring in 2006 in Prudhoe Bay field North America. A small hole initiated by a weld failure was responsible for 5000 barrels of crude oil contaminating 1.9 acres of sea. British Petroleum incurred losses of up to $320 million including fines for endangering the safety of the environment and the public [12].

One of the recommended ways to protect pipelines and welded joints from CO_2 corrosion attack is by applying a corrosion inhibitor. The chemical inhibitor will adsorb onto the metal surface to build a protective film layer. For weldments, the inhibitor needs to be equally effective on the pipe welds as on the parent pipeline steel. Ideally, the weld metal should be more cathodic than the base material so that it is protected from preferential corrosion attack. However, in some cases, the weld metal becomes anodic and suffers severe localised corrosion due to a current reversal, the results of which are shown in Figure 1-1(a) [13]. It is thought that this reversal is due to the inhibitor detaching preferentially from the weld

metal at high flow rates, while the parent material is still covered and protected by the active film layers [13,14].

It is generally agreed that the location and morphology of weldment attack can be influenced by many parameters, which includes the environment, flow patterns, the composition of the weld metal relative to the parent metal and the welding method, among others [15,16]. However, from the information available and experience, the mechanisms of this corrosion phenomenon are still unclear. The most accepted explanation of selective or preferential corrosion is the difference in composition and microstructure across the weldment. In addition, it is still difficult to predict the weld corrosion rate that may be experienced, the exact location of attack (such as, weld metal and heat affected zone), or the effectiveness of corrosion inhibitors. Care is also needed in applying curative measures for other applications because of the complexity of interacting factors that may lead to additional problems. To this end, good predictions supported by relevant experimental testing are essential for applications where selective weld corrosion is possible or anticipated.

Many numerical models offer advantages because they are cost-effective and adjusted quickly. However, it is still necessary to compare the simulation results with experimental data. Fluid conveyed in a pipeline system will experience dynamic turbulent flow which should ideally be replicated in controlled conditions experimentally. In this case, any experimental method should allow not only turbulent flow but for a range of fluid velocities across a surface to be monitored for corrosion.

Several techniques have been developed to evaluate the effect of flow on corrosion, including for the carbon dioxide corrosion on the carbon steel. Many methods with a variety of approaches are applied in hydrodynamic conditions in turbulent flow environments. The rotating cylinder electrode (RCE), recirculating flow loop, rotating cage and the submerged jet impingement (SJI) are systems that have been applied widely in corrosion studies in the flowing environment.

However, the choice of appropriate evaluation method is important due to each method of having disadvantages and limited application [17–20].

SJI has been used successfully to investigate the behaviour of weldment in high strength steel pipelines to assess the behaviour of a weldment (three materials; PM, HAZ, WM) and their interactions in a dynamic flowing environment at the same time [16,21–25].

1.2 Submerged jet impingement for evaluating weld corrosion

Submerged jet impingement (SJI) is an experimental approach to link materials behaviour (i.e. corrosion or erosion) with the hydrodynamic characteristics of flowing media (e.g. fluid or particles). The response of pipelines to a range of hydrodynamics is very important since the fluid velocity, changing pressures, water composition and the rate of water condensation significantly affects the corrosion inhibitor performance on the solid surface of the steel. Particular concerns are the development of slug flows. Slug flow is a temporary disturbance, in that every time a slug passes a point the flow is severely disturbed, but then normalized after the slug passes [26]. The slug is a multiphase flow pattern that develops in a pipeline system, linking the wells at the sea bed to production platforms at the surface in oil and gas production.

Efird *et al.* [23,24,27] reviewed the available methods commonly applied for monitoring weld corrosion in flowing conditions in Table 1-1, which includes the rotating cylinder, flow loop, rotating cage and submerged jet impingement.

Table 1.1 shows the primary parameters used for method selectio for monitoring weld corrosion in a flowing environment. Accessibility to the electrochemical test is important and application of the recirculating flow loop, rotating cylinder and jet impingement in many applications is suitable. The rotating cylinder (RCE) and recirculating method are not applicable with single-phase fluid, and it is difficult to reach some high shear stresses achieved by moving parts. Submerged jet impingement is a method that can be applied to complex fluids with few limitations. The advantage of the SJI method is that it can operate in high wall

shear stress conditions that commonly occu in oil and gas industries, an is one of the reasons for the use of submerged jet impingement in this study.

Table 1-1 Method used for monitoring the weldment corrosion [23]

Parameter	Flow Test Method				
	Recirculating Flow Loops		Rotating Cylinder	Jet Impingement	Rotating Cage
	Small Diameter	Large Diameter			
Fluid Requirements	High	Very High	Low	Medium	Low
Construction Cost	High	Very High	Low	Medium	Low
Operating Cost	High	Very High	Low	Medium	Low
Test Work Effort	Medium	High	Low	Medium	Low
High pressure operation	Yes	Yes	No	Yes	Yes
Determine k and/or τ	Yes	Yes	Yes	Yes	No
Operation at high τ (> 1000 Pa)	No	Yes	No	Yes	Yes
Multiphase Testing	Yes	Yes	No	Yes	Yes
Scale up – liquid	Yes	Yes	No	Yes	No
Scale up - gas	No	Yes	No	Possible	No
Coupons	Yes	Yes	Yes	Possible	Yes
Electrical resistance Probes	Yes	Yes	Yes	Yes	No
Electrochemical Test Methods	Yes	Yes	Yes	Yes	No

Adegbite *et al.* [13] describe the use of a submerged jet-impingement flow loop to investigate preferential weld corrosion of an X65 steel weldment. A novel jet-impingement target from samples cut from the weldment was constructed. The target was positioned beneath a nozzle in the flow loop with inhibited and uninhibited flowing brine at 5 and 10 m/s. The results showed that at a low flow rate, the weld metal and heat affected zone remain cathodic and partially protected by the sacrificial corrosion of the parent material. However, in certain conditions, including a high flow rate, a current reversal leads to accelerated corrosion of the weld region. The results are explained in terms of the selective removal of the inhibitor film from different regions of the weldment at high flow rates, particularly in the presence of oxygen.

With this context in mind, the present study builds upon the work of Adegbite. In the SJI target, samples of the weldment are assembled into three concentric ring electrodes which give the potential for a range of hydrodynamic conditions

ranging from stagnation to high turbulence. The SJI target is thus adapted to accommodate the three weldment materials across three different regions, nominally high, low turbulence and stagnant conditions simultaneously. The target comprises electrodes positioned in different hydrodynamic areas beneath a jet to allow electrochemical corrosion measurements to be made simultaneously in different flow conditions. In this present study the focus is the SJI technique and the hydrodynamics across the target, which are qualitatively and quantitatively assessed. Uninhibited and inhibited conditions are examined at jet velocities up to 10 m/s. A CFD model is used to validate and discuss the findings. A new target is constructed and comparison is made between the two weldments. The corrosion products and surface morphology are studied in detail using optical and electron microscopy and surface analytical techniques.

This study is to demonstrate the potential of the SJI method to evaluate weldment corrosion and particularly galvanic corrosion, applicable to petroleum fields. It focuses on corrosion caused by a turbulent fluid at different velocities impinging onto an X65 pipeline steel weldment surface.

An overview of the influence of flow at wall shear stresses around 72 Pa or 5 m/s on the total corrosion rate of each weldment segment is shown in Figure 1-2. At this simulated wall shear stress, an X65 steel weldment showed high risk of premature service failure arising from preferential weld metal corrosion. At typical oilfield production flow rates, corresponding to wall shear stresses of 120 Pa [28], it could be anticipated that deleterious oilfield incidents, traceable to PWC, may occur and could be mitigated with knowledge of managing PWC. Such oilfield preferential weld corrosion incidents have been reported by Mahajanam and Joosten [29], Winning et al [30] and, Abduh [10], among others.

There is a desire to be able to avoid or mitigate against preferential weld corrosion of valuable and critical assets such as pipelines in oil and gas production. Research focusing on gathering accurate and reliable data for evaluating corrosion in a range of complex environments requires an understanding of the effects of corrosion of different materials (and their behaviour when coupled

together) in a range of flow rates typical within pipelines. The novel target used in Adegbite's and this study is justified as an important improvement, capable of being used as predictive tool for PWC and related studies.

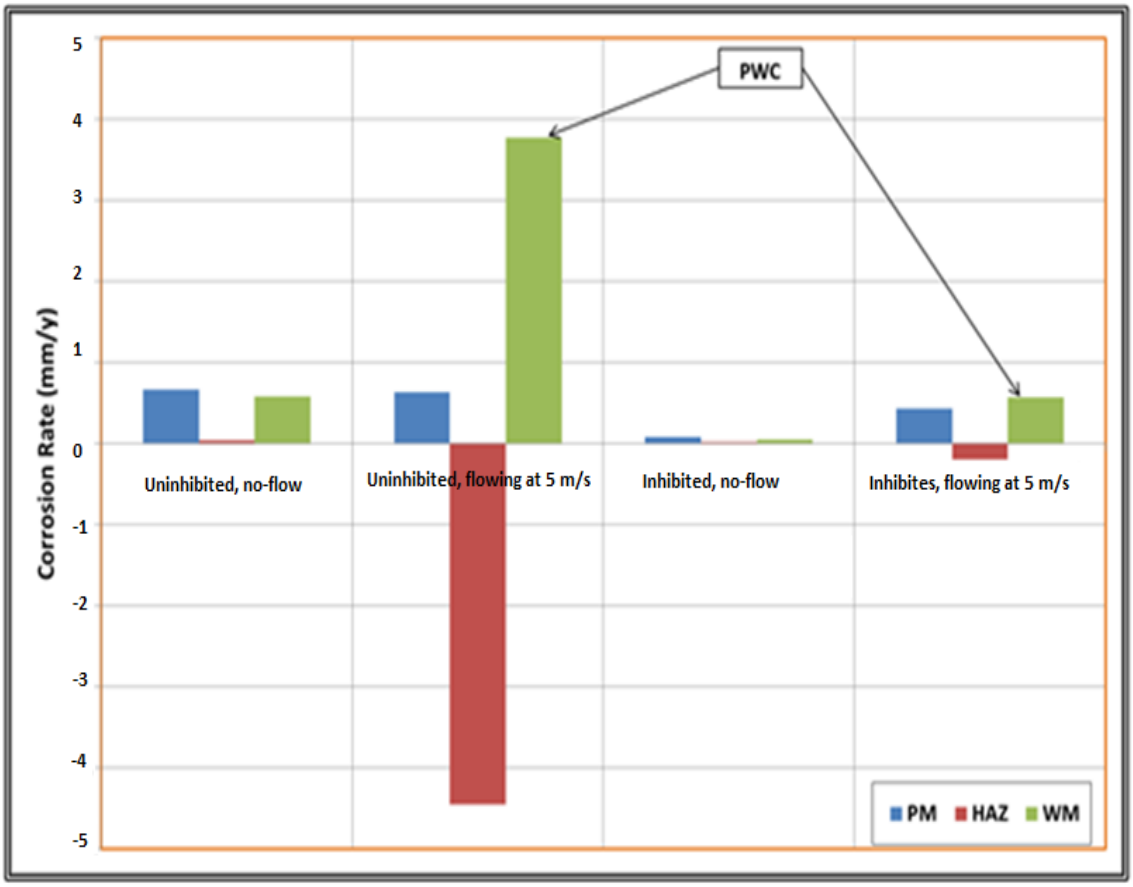

Figure 1-2 The effect of flow and inhibition in CO_2 saturated brine solution [13]

1.3 Research aim and objectives

The aim of this research is to evaluate submerged jet impingement as a tool for assessing the effect of flow and the associated corrosion behaviour across a X65 high strength pipeline weldment surface with a range of jet velocities of sea water. It focuses on corrosion caused by a turbulent fluid at different velocities impinging onto an X65 pipeline steel weldment surface. The fluid does not contain solid particles.

To achieve this aim, the following objectives are proposed.

- Assess the corrosion behaviour of X65 pipeline steel weldment in typical oilfield conditions.
- Describe the hydrodynamics across a SJI target and assess the associated corrosion behaviour of X65 weldment.
- Critically assess submerged jet impingement as a tool for assessing the effect of flow and the associated corrosion behaviour across a X65 high strength pipeline weldment surface with a range of jet velocities of sea water.

A list of tasks is given as illustrated in Figure 1-3, a schematic of the methodology selected to achieve the objectives.

1. A literature review
2. Create a weld and construct a jet impingement target from the weld
3. Construct a flow loop for CO_2 saturated brine with the jet impingement target.
4. Measure the uncoupled (self-corrosion) and coupled (galvanic behaviour) of each weld region across the target. In this way, study the effects of different hydrodynamic conditions on total corrosion (galvanic and self-corrosion).
5. Use optical and electron microscopy and surface analytical techniques to investigate the surfaces in different flow conditions and relate them to the corrosion behaviour.
6. Examine the effectiveness of a typical oilfield corrosion inhibitor in controlling weld corrosion by incorporating a corrosion inhibitor into the system.
7. Compare results with previous work to validate the methodology and findings.
8. Use CFD simulation of velocity distributions across the target to validate data and findings.

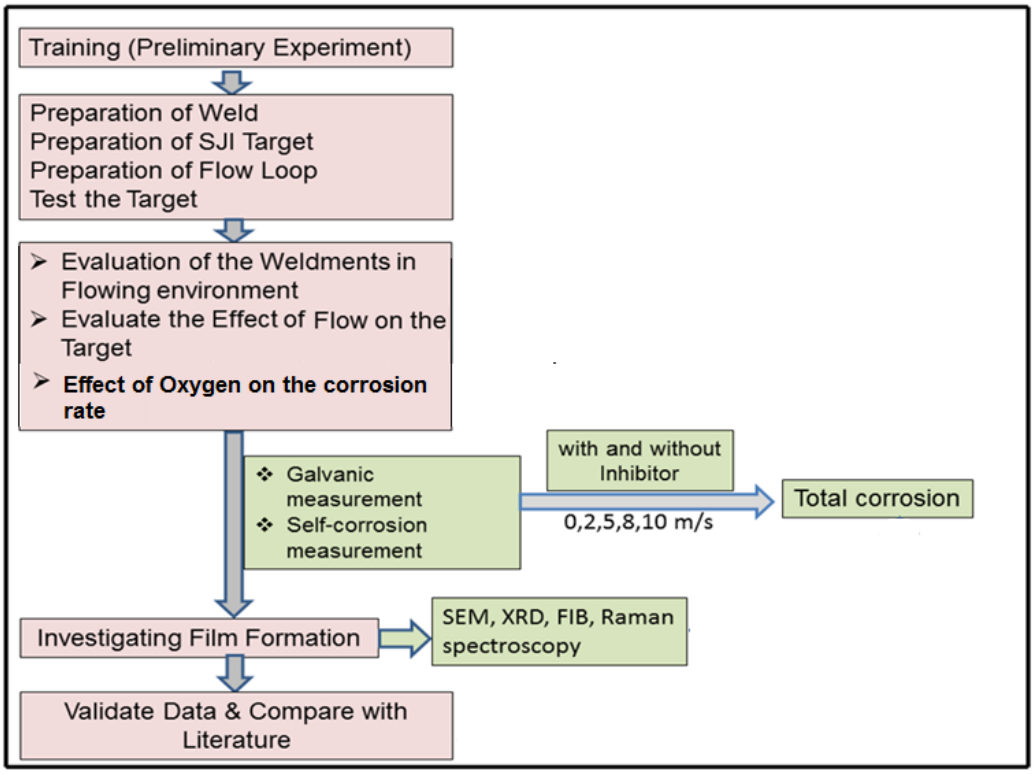

Figure 1-3 A schematic of the research methodology and objectives

1.4 Thesis structure

This thesis consists of 10 chapters, structured as follows:

1. Chapter 1 is the research background, the aim and objectives.
2. Chapter 2 is a literature review consists of X65 low alloy carbon steel, fundamental principles of corrosion and weldment corrosion. It also identifies CO_2 corrosion products and the techniques used to evaluate weld corrosion in flowing conditions with CO_2 saturated brine and application of inhibitors to minimise weld corrosion.
3. Chapter 3 is the methodology. In this chapter, the preparation and construction of the submerged jet impingement target and flow loop to study the effectiveness of typical oilfield corrosion inhibitor are explained.
4. Chapter 4-9 are results and discussion sections of corrosion behaviour with and without flowing brine solution, the effect of an inhibitor and of dissolved oxygen, and an assessment of the SJI target and discussion.
5. Conclusions and research recommendations are given in Chapter 10.

2 LITERATURE REVIEW

This chapter will discuss high strength low alloy steels that are used as pipelines, valves, and joining systems in the oil and gas industry. The microstructural characteristics due to the welding of high strength pipeline materials are reviewed. Corrosion in CO_2 containing environments or 'sweet corrosion' and influencing factors are reviewed as well as techniques to monitor corrosion rates.

2.1 High-Strength Low Alloy Steels (HSLA)

HSLA steels are low carbon steels that contain up to 5-10 % of alloying additions. The alloying elements permit HSLA steels to be quenched and tempered to obtain high levels of strength and impact toughness. The chemical composition of high strength low alloy steels consists of a low carbon content of between 0.05% – 0.25% for sufficient formability and weldability, and manganese content up to 2.0%. Small variations of the quantities of manganese, chromium, nickel, molybdenum, copper, nitrogen, vanadium, niobium, titanium, and zirconium are used in various combinations [31].

High strength low alloy carbon steels are commonly used for constructional applications in several industrial sectors including automotive, construction, aerospace, petrochemical, and oil & gas [8]. High strength low alloy carbon steels are fabricated by quenching to form martensite that is subsequently tempered at an intermediate temperature. Tempering of martensite enables the carbon atoms to diffuse out and form precipitates like cementite (Fe_3C) between fine martensite grains. The steel has to be converted entirely into martensite to enhance the strength. This ability to form martensite by quenching is referred to as hardenability, and the effectiveness of this process will rely on the configuration of the component and the composition of steel [32]. This is because the cooling flow rate is equal to the cross-section of the metal sample [33]. Austenitisation of HSLA steels at low temperatures (typically 870 °C) forms good austenite grain sizes before quenching (Q), and tempering (T) [33,34].

Recently, in the oil and gas industries, the use of X65 steel as a pipe material has increased significantly due to its low cost, good strength, increased hardness, flexibility, and increased gauge thickness. A weld produced from such steel is commonly used in heavy industrial applications such as petroleum and petrochemical transportation, land transportation, infrastructure, paper industry, chemical process industries, power installations, and many others. However, this steel is commonly used in corrosive environments such as in oil and gas facilities. Thus, many metals, especially carbon steels, and their alloys; are very vulnerable to pitting corrosion accelerated due to chloride ions and salts.

Corrosion of carbon steel in high-pressured atmospheric conditions is due to absorption of air and water molecules on the metal surface, while at very low concentration, are adequate enough for corrosion to progress. In oil and gas industry, some impurities such as water content, CO_2 and H_2S concentrations and, sometimes, the influence of temperatures, pressure, and pH; have led to severe localised corrosion in carbon steel pipes [35–38].

2.2 The Weld Microstructure and Composition

Welding is a process to join two or more materials (such as pipeline steel) by heating and/ or pressure to produce a longer pipe. The weld consists of a complex structure that may have differences in composition and microstructure compared to the parent material of the pipework. During welding, several different structural regions form. The regions are classified as follows: the weld metal (WM), fusion zone, heat affected zone (HAZ) and parent material (PM). Figure 2-1 illustrates five unique areas within the structure of a weldment. Figure 2-2 is a set of micrographs in which the microstructural distinction between the regions is seen when a penetration weld has been performed.

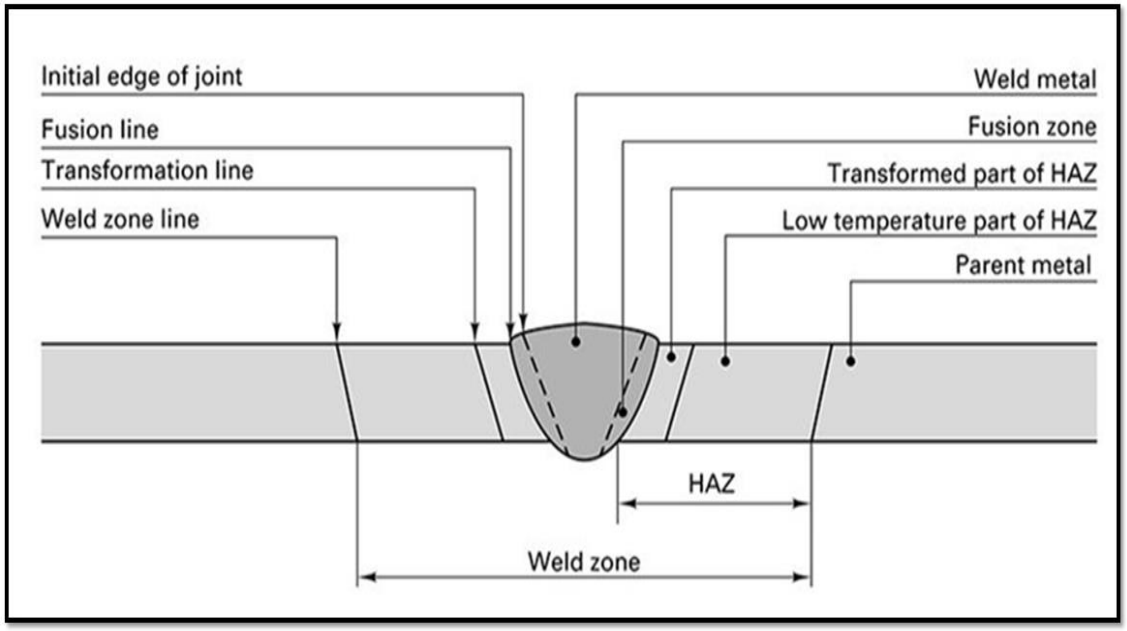

Figure 2-1 Characteristic regions at a welded structure [39]

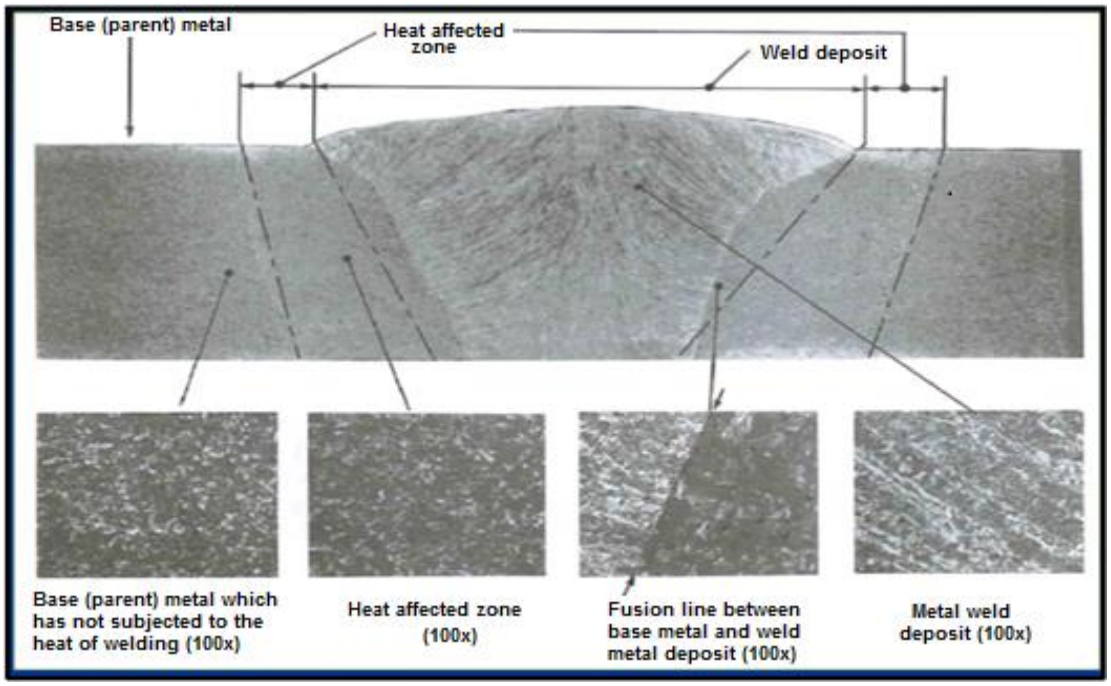

Figure 2-2 Microstructural illustration of weld structural regions with full penetration weld [40]

2.2.1 Weld metal and fusion zone

Weld metal (WM) is the material that has melted and re-solidified as a result of the welding operation. When filler metal used during the welding, the composition of the weld metal is different compared to the parent material. However, in cases where no filler material is added (resistance, electron beam, laser, and some autogenous arc welding), the weld metal has a similar composition to the parent material.

Fusion zone is the area of the weldment in which the filler and the parent material have been melted during the welding operation. The fusion zone has the tendency to display the most notable compositional difference when compared to the PM. Microstructural separation happens during the process of cooling, the melted material begins to solidify at different of rates depending on the surface area to volume exposed. A small area, between the base metal and the fusion zone called the un-mixed area, is established. In this step, the un-mixed base metal is melted and cooled rapidly in order to create a stable composition that is almost the same as the PM [9].

2.2.2 The Heat Affected Zone (HAZ)

The heat affected zone (HAZ) is a region of the PM that does not melt, but its microstructure and chemical properties change due to the heating process. During selection of the carbon steel, the characteristics of HAZ are essential because the metallurgical and mechanical properties are directly linked to the selected steel [41]. For example, during welding of carbon steel, outer part of the HAZ was exposed the heat of 700 ˚C, while the inner part closest to the fusion zone reaches 1400 ˚C (Figure 2-3). This very high temperature causes a microstructure change, but this temperature is not sufficient to cause melting. The HAZ can also be changed to the next section which is determined by the thermal gradient situated in the fusion zone towards PM.

A partial melt zone exists in a HAZ consisting of several grains and grain boundaries. The HAZ areas will have a different grain structure. In the inner-most portion of the HAZ, a high number of grains develop with maximum temperature input and a slow cooling rate. At the outer-most section of the HAZ, tiny grain sizes appear, because of very low heat input to the material and a high cooling rate [42,43].

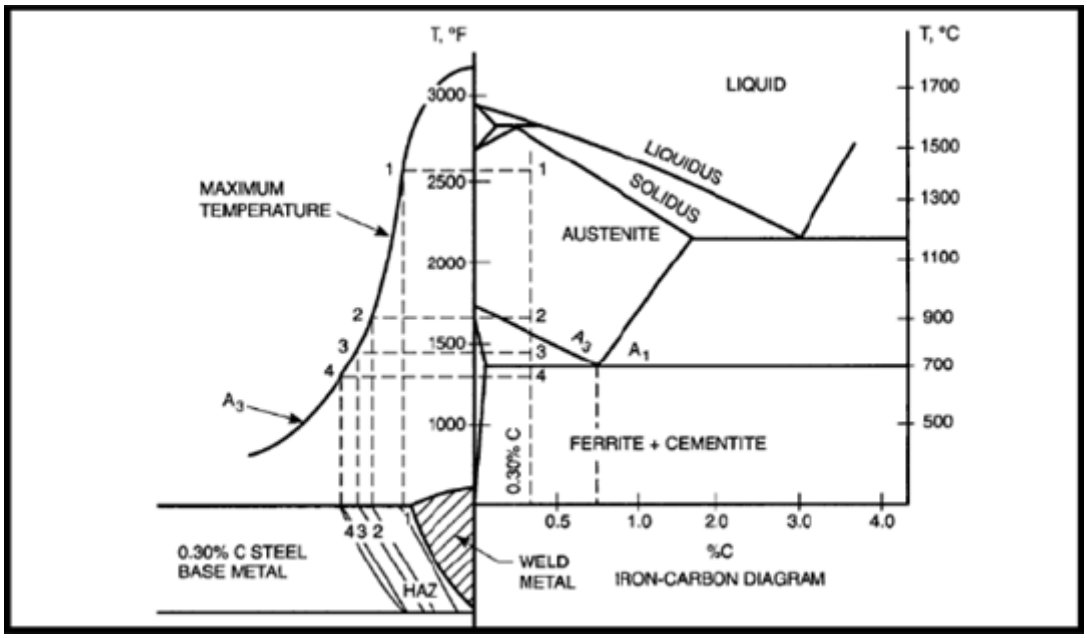

Figure 2-3 Typical Changes in Carbon Steel with Temperatures [42]

2.2.3 Base (Parent) Material

The PM is an area that does not change metallurgically during the welding process (Figure 2-4). However, the PM and overall welding areas are in a state of stress due to transverse and longitudinal expansions as a result of heating and cooling. The variation of chemical composition and/or microstructure between base metal, weld metal, and HAZ are critical to the failure of the welded constituent in service. The microstructures of the weld metal (WM) and the HAZ changes considerably due to the welding process. The WM structure can be ferritic or a mixture of ferritic and austenite, while the HAZ can be ferritic, pearlitic, bainitic or martensitic [39]. Indeed Figure 2-4 shows the heat affected zone as a series of transformation zones between the weld metal and unaffected base

material (PM). This complex microstructure may give rise to gaps in knowledge with regards to understanding the microstructural dependence of corrosion behaviour of the WM and HAZ [11,44,45]

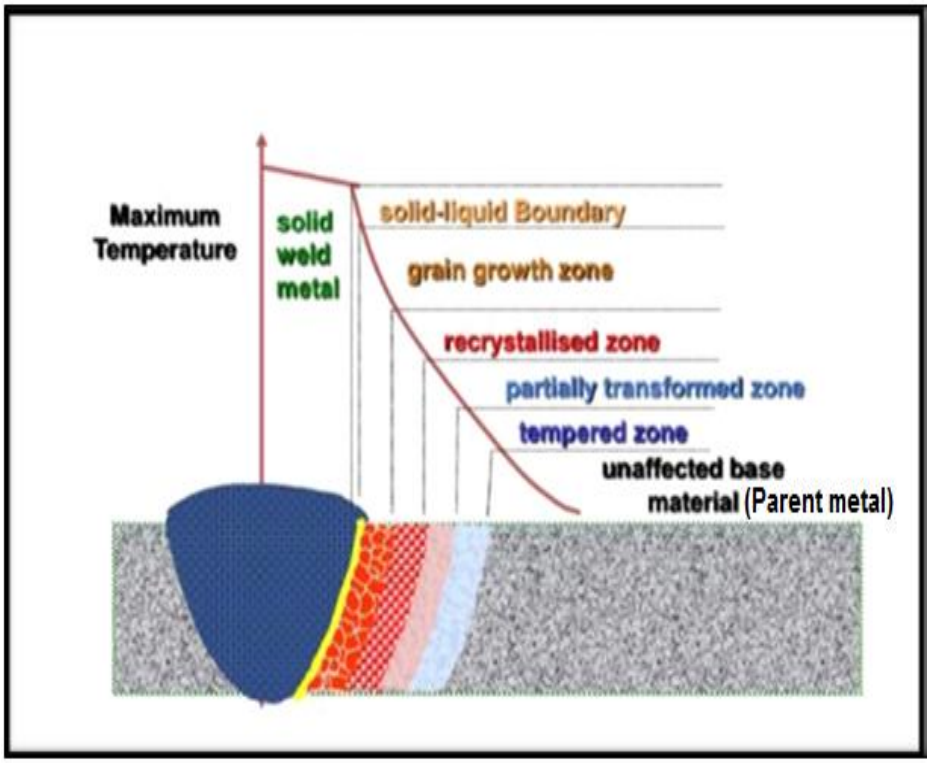

Figure 2-4 An schematic of a weldment showing the heat affected zone is a series of zones between the weld metal and unaffected base material (PM) [45]

2.3 Introduction to Corrosion

The term corrosion is described as the chemical or electrochemical interactions of a material with its environment [5]. The oxidation reactions produce metal ions and electrons, where the electrons are directly consumed during the reduction reaction phase of the process (Figure 2-5).

When steel is in a corrosive environment, the iron on the anodic side of the surface goes towards the solution as a ferrous ion (anodic reaction). When the iron (Fe) atoms undergo oxidation, Fe ions release electrons from which the negative charges will accumulate in the metal and prevent subsequent anodic (corrosion) reactions on the cathodic side, the electrons react with the reduced electrolyte component [4,46].

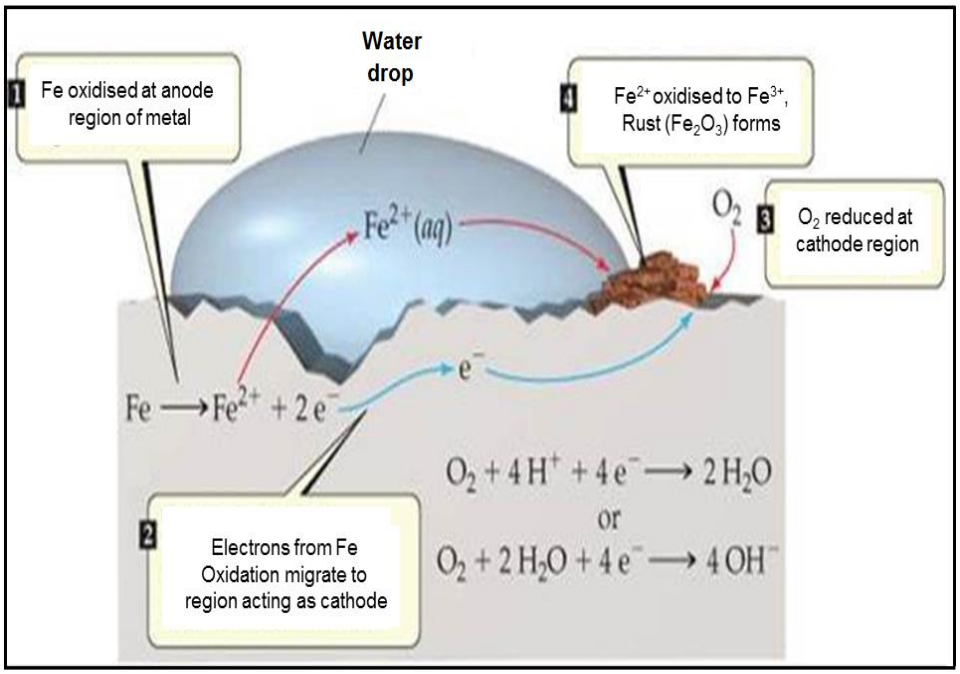

Figure 2-5 Corrosion reaction of steel [46]

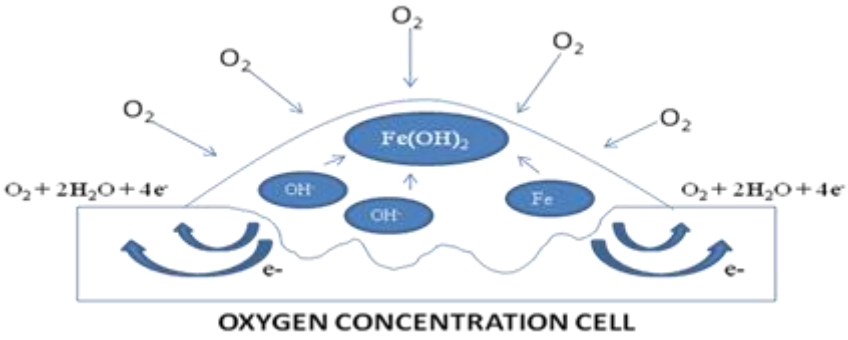

Figure 2-6 Mechanism and reaction of iron corrosion [5]

The total reaction, summarising the result of these chemical equations mentioned in Figure 2-6 above, are:

$$Fe^{2+}_{(aq)} + 2OH^{-}_{(aq)} \rightarrow Fe(OH)_2 \quad \textbf{(2-1)}$$

$$2Fe_{(s)} + 2H_2O_{(aq)} + O_{2(g)} \rightarrow 2Fe(OH)_{2(aq)}\ (cell) \quad \textbf{(2-2)}$$

The $Fe(OH)_2$ further reacts with available oxygen and water

$$4Fe(OH)_{2(aq)} + O_2(g) + H_2O_{(l)} \rightarrow 4Fe(OH)_{3(s)} \quad \textbf{(2-3)}$$

The final product that precipitates from the solution written in an hydrated form as $FeOOH.nH_2O$. Several forms of hydrated iron oxides and iron oxide-hydroxide can develop depending on the environment. Iron(III) oxide is ferric oxide (Fe_2O_3) and red, while black iron oxide is iron(II) iron(III) oxide (Fe_3O_4) or ($FeO.Fe_2O_3$). The red oxides are collectively known as rust and black iron oxide is often indicative of deaerated conditions. Both the red and black iron oxides form layers on a steel surface [47].

2.4 Corrosive Environments

The corrosion reaction is a natural process of degredation that cannot be stopped but can be controlled. One of the most important factors in the corrosion reaction is the influence of environmental conditions that support corrosion mechanism. By knowing the various conditions that can trigger a corrosion reaction, attacks can be minimised. All environments are corrosive to some extent. Some of these environments are listed below [5].

1. Air and humidity.
2. Natural, urban, marine, industrial environments.
3. Chlorine (Cl_2) from steam and gases.
4. Hydrogen sulphide (H_2S).
5. Carbon dioxide (CO_2).
6. Fuel gases (hydrocarbon gas).
7. Acids (hydrochloric acid and sulphuric acid).
8. Fresh, purified, salt and seawater.

In this research, the interest is in exploring the typical effects of corrosion on welded steel in an offshore environment in oil & gas productions. In oil and gas production, the oil and natural gas that consists hydrocarbon compounds are produced together with other impurities such as water, salts, and gases such as carbon dioxide (CO_2), hydrogen sulphide (H_2S), oxygen (O_2), nitrogen (N_2), etc. The main factors affecting corrosion reaction are carbon dioxide (CO_2), hydrogen sulphide (H_2S) and oxygen (O_2) concentration. CO_2 corrosion is the most

predominant in oil and gas production because it can react with water producing carbonic acid [35,48,49].

2.5 Galvanic Corrosion

Galvanic corrosion takes place when two dissimilar metals are in contact in a corrosive environment. A galvanic couple is formed between the two metals (with different corrosion potential), where one metal becomes the anode, and the other one forms the cathode. The anode (sacrificial metal) corrodes and deteriorates quickly, while the cathode deteriorates slower.

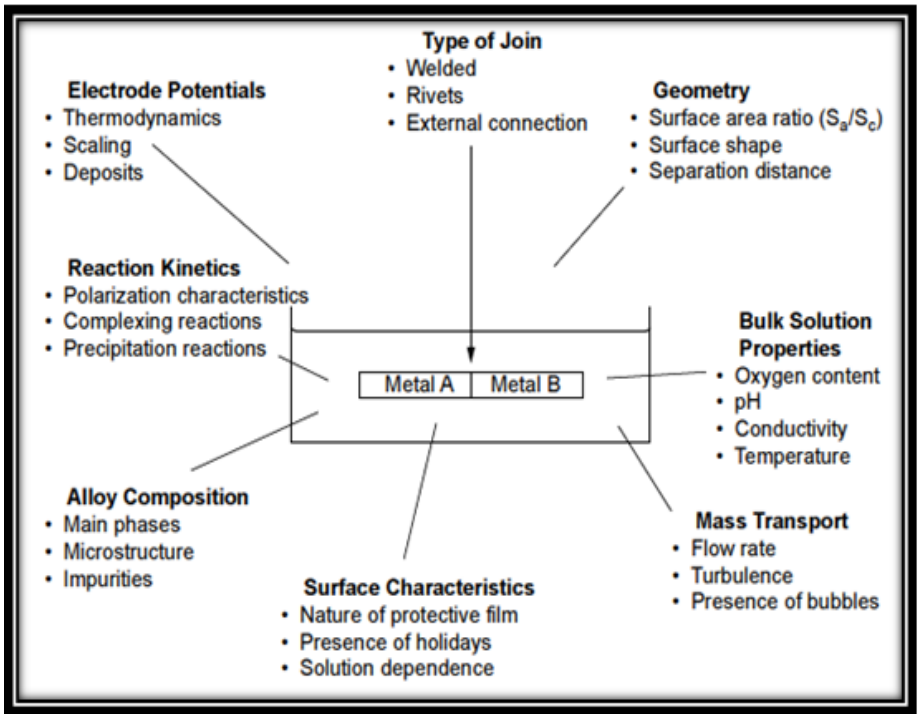

Figure 2-7 The factors that contribute the coupled (galvanic) corrosion phenomenon [50]

There are three essential environments needed for galvanic corrosion [50,51]:

- The metals must have different corrosion potentials
- There is electrical contact between at least two metals, and
- The metals should be exposed to a corrosive environment

The potential difference between the two coupled metals will initiate the corrosion reaction, and the more active metal (less noble) will be preferentially attacked

compared to nobler metal. The rate of corrosion of a coupled metal depends on the surface reaction. Large cathode/anode area ratios will frequently result in a large galvanic attack, and this problem commonly occurs in oil and gas pipelines. In a real condition, the potential value from each metal that creates the galvanic interaction slightly changes depending on the effect of synergism of the coupled and condition parameter as summarised in Figure 2-7.

In the oil and gas industry, the effect of mass transport is a very crucial factor particularly in high flow rates inside the pipeline. Hara et al [52] observed that passive film was destroyed due to high flow rates leaving the substrate without any protection. Then the galvanic corrosion attacked the metal synergistically.

In general, the electrochemical reaction that occurs during the galvanic process is similar to general corrosion in the aqueous phase for uncoupled material. However, in the galvanic reaction, a significant contribution to determining the reaction rate is the size of the potential difference between two coupled metals. An increase in galvanic corrosion occurs with an increase in potential difference.

Figure 2-8 shows the galvanic series of some commercial metals and alloys in a seawater environment. The corrosion potential values change from the most active to the noblest material, graphite, to the most reactive material, magnesium. For those materials that are close in potential or have a very small potential difference, the galvanic interaction is not affected significantly. When alloy steel, which has potential of -0.64 V, is coupled with stainless steel (-0.3 V), the steel will corrode faster due to being less noble compared to stainless steel.

Table 2.1 shows the potential galvanic risk when metals or alloys are coupled together. Information from Table 2-1 helps in the selection of compatible metals to be combined and thus, minimize the risk of a galvanic attack. Green areas are safe regions for combining, but red areas should be avoided because they will potentially cause the galvanic corrosion.

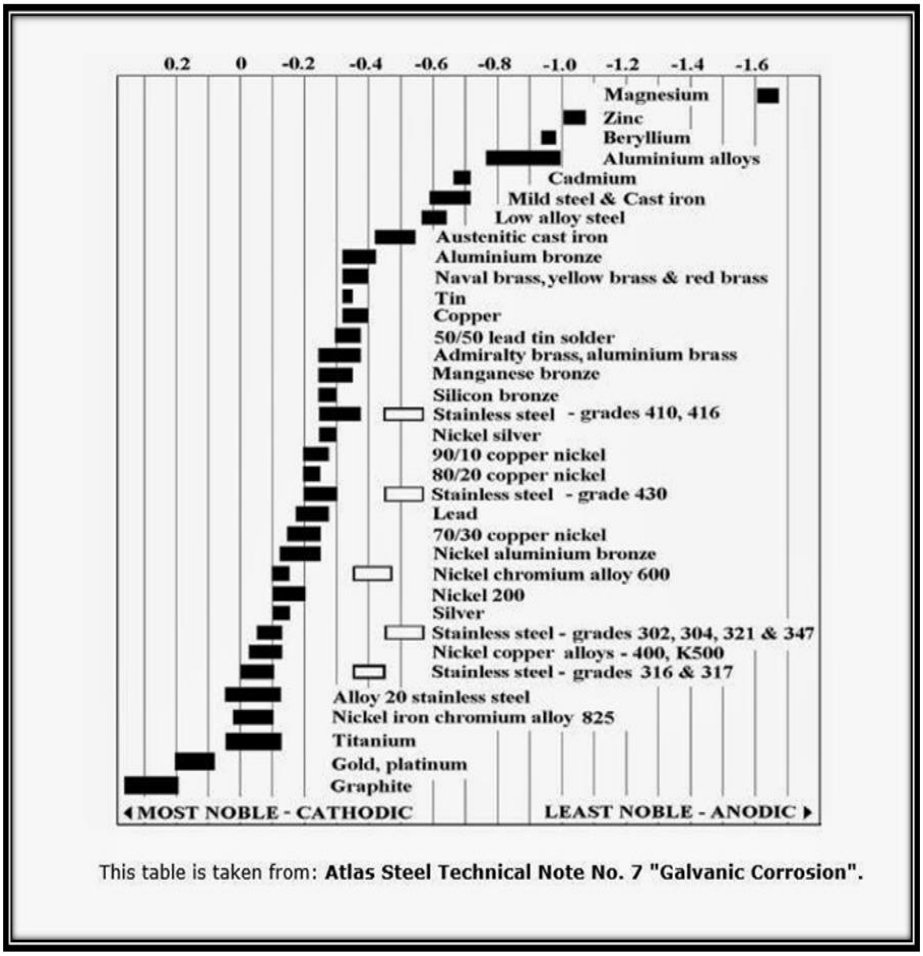

Figure 2-8 Potential values of some metals and alloys commonly used in for industrial sectors [53]

However, the potential difference is not always a sufficient parameter used to predict the risk of coupled corrosion. Metals which have a potential difference of only about 0.05 V have been found with galvanic corrosion problems, while some metals are successfully coupled together with no corrosion observed despite th potential difference of 0.8V [53]. In some cases, the potential differences between the metals provide less information on the kinetics of galvanic corrosion which also depend upon the current interaction between both metals. There are several factors which affect the severity of galvanic corrosion such as area ratio, temperature, flow rate and corrosion environment (media) [53].

Table 2-1 The potential galvanic risk when metals or alloys coupled together [53]

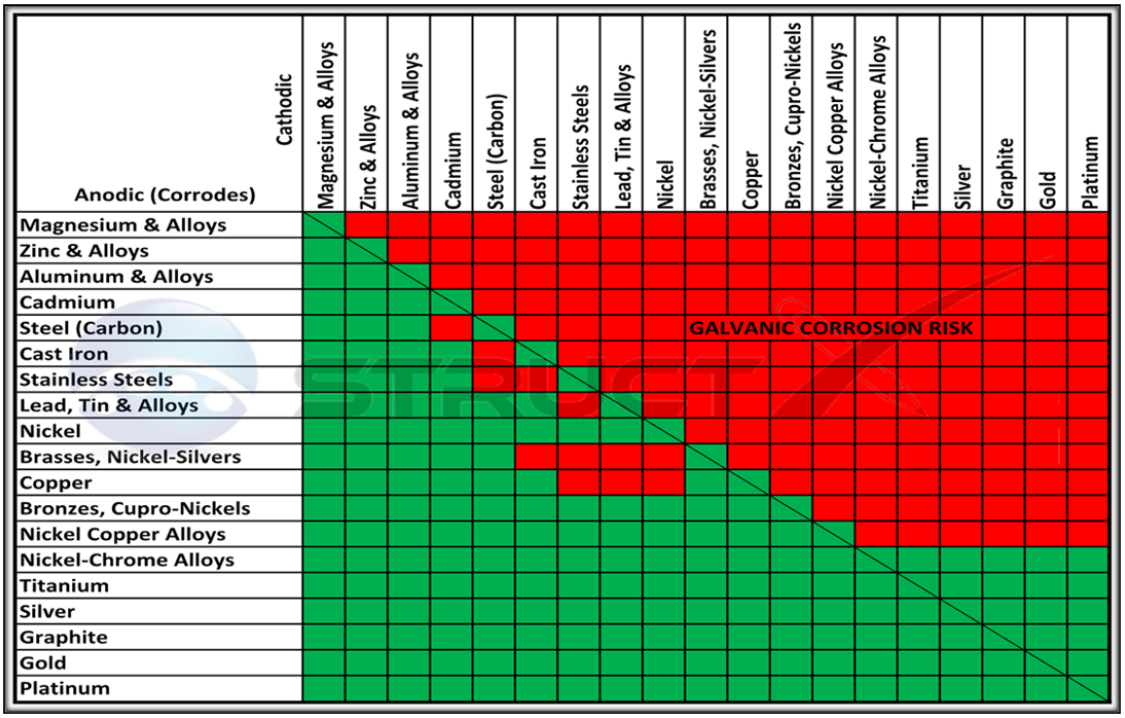

In oil and gas industries and in corrosion environments with a high concentrations of chloride (brine solution), a weldment may be subject to galvanic corrosion due to the different microstructure and composition of the PM, WM and HAZ [54].

Welded joints, including autogenous connections (created without filler metal), are vulnerable to galvanic corrosion due to electrochemical interactions between local anodes and cathodes in the weld area. The area of the WM and HAZ is very small compared to the PM area. Therefore, it would be preferred that the PM should be anodic to the WM and the HAZ in order to avoid significant loss of the WM and the HAZ (though a preferential weld galvanic corrosion effect). Corrosion of the WM and the HAZ results in preferential PWC, which can cause premature attack; and after a certain period, may damage production process facilities, harm humans, and negatively affect the ecosystem [42,55].

2.6 Preferential weld corrosion (PWC)

Preferential weld corrosion is one of the common types of corrosions that normally attacks the weld area of a structure. It was reported that the case of PWC on steel weldment from high strength low alloy (HSLA) steel in the CO_2 environment has been increasing in recent years. Many PWC cases have been found in the UK, including central, northern and southern sectors of the North Sea, and on-shore gas station facilities, while a similar accident occurred in the Gulf of Mexico several years ago [56]. Some significant PWC problems due to galvanic corrosion have also been found in off-shore gas production in the Natuna Sea in Indonesia [57].

In petroleum industries, pipelines made of high carbon alloy steel that generally used in upstream and downstream facilities can be very sensitive to PWC attacks. The issues of PWC in the oil & gas production have been observed for many years, and various researches have been conducted to reduce the negative impact of PWC on economic losses, environmental waste, and human fatalities [3,13,58].

In many cases, the galvanic effect initiates the PWC problem. It takes place when dissimilar metals are coupled in a corrosive aqueous environment. The effect of coupling dissimilar metals increases the corrosion rate of materials that have a higher electronegative potential (anodic), and minimises the corrosion rate of the materials that have a lesser electropositive potential (cathodic) [59]. Previous studies have shown that the composition of weld metal microstructure (parent and weld metal), the type of welding process, inhibitor efficiency, and environment conditions including the fluid flow have influenced the PWC significantly [60].

A weldment that consists of PM, WM, and HAZ can be considered as different metals due to different chemical compositions and could be subject to PWC attack. A study by Lee and Woollin [60] found that additions nickel and silicon, up to 0.7 wt %, into the weld metal composition can protect the weld metal from PWC attack. Another study conducted by Kermani *et al.* [61] pointed out that 1.5 wt.%

chromium in the weld metal was sufficient to minimize PWC based problems. Mahajanam and Joosten [29] suggested that adding 1 % nickel into the filler metal provides excellent overall resistance to PWC. However, the above results are not in good agreement with those obtained from a study of the inhibitory effect on weld metal that contains 1 % nickel in sweet corrosion (CO_2) conditions. In another study, Turgoose *et al.* [62] found a significant corrosion potential difference between the weld and parent metal due to the inability of inhibitor molecules to penetrate a nickel-rich corrosion product on the weldment. This can induce fast localised attack of the weld metal. The welding procedure and weld consumable are important factors to take into account for PWC of pipelines. Submerged arc welding (SAW) operates with high heat inputs to create a ferritic-pearlitic microstructure compared to gas metal arc welding (GMAW) applied with low heat input. Low heat input welds on susceptible steels cause HAZ PWC attack [4,9,63].

Adding a corrosion inhibitor to fluid conveyed within a pipe is one of the best procedures to minimise PWC attacks. The corrosion inhibitor works physically attaching itself to metal surface in order to create an active protective film [7,8]. Ideally, the effectiveness of the inhibitor should be the same on the weld as on the parent metal. However, the high flow rate of oil and gas inside a pipeline may cause a weak attachment of inhibitor molecules on the weld metal, while a large area of PM remains protected by the inhibitor film [4, 9–13].

The effect of flow is one of the crucial factors that exacerbates PWC attack. Higher flow rates means high turbulence which accelerates the corrosion reaction on the steel surface. The result of this is an increase in corrosion rate when no active corrosion layer develops on the surface of the steel. Ideally, if the surface of weld metal is covered by an inhibitor, the PWC attack will decrease due to the weld metal being more cathodic compared to PM or HAZ. However, when the current reversals occur, the flow affects the film on each region of the weld, and as a consequence, the weld metal is unprotected by inhibitor and will suffer PWC attacks [14–16].

Some experimental methods have been reported to simulate similar hydrodynamic circumstances at the steel surface for pipeline flow [17–20]. However, the results from these studies still do not address the mechanism of PWC attack specifically.

2.7 Carbon Dioxide Corrosion

In oil and gas facilities, “sweet corrosion” due to dissolved carbon dioxide is a significant factor linked to damaged production and process facilities [45][38]. The existence of carbon dioxide in oil & gas production is due to the CO_2 gas production from the gas reservoir during exploration or due to CO_2 injection into reservoirs purposely for Enhanced Oil Recovery (EOR) [46]. Carbon dioxide is a dry gas and a non-corrosive agent in petroleum production facilities. However, when dissolved in the aqueous phase, it will make a spontaneous reaction, producing a carbonic ion (weak acid) that can initiate a corrosion reaction between steel surface and corrosive brine solution [47].

CO_2 corrosion is a complicated process that consists of several step reaction mechanisms that involve mass transport activities between the surface of the steel and the corrosive media. Every step reaction can be very sensitive and mostly dependent upon temperature, pressure, flow, and the chemical composition of corrosive media [48].

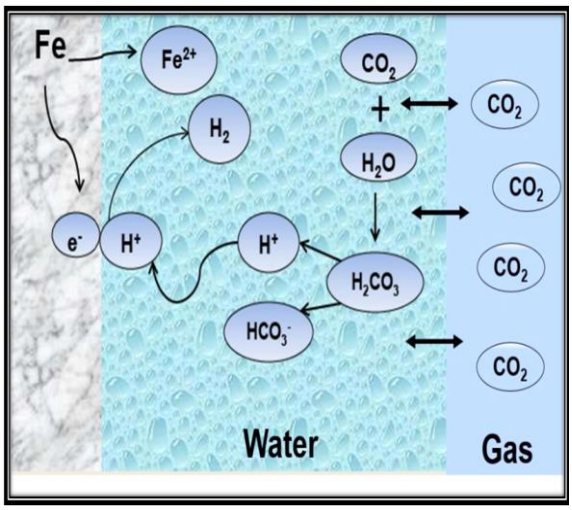

Figure 2-9 The chemistry of CO_2 steel corrosion in a wet environment [41]

Figure 2.9 describes the water chemistry of steel corrosion in a dissolved CO_2 aqueous solution environment. The process started when the CO_2 reacts with water to form carbonic acid (H_2CO_3) and partially dissociates with two-step reaction creating bicarbonates (HCO_3^-) and carbonate (CO_3^{2-}) ions. The phases of the reaction are listed below [82]:

(i) The first reaction stage shows a dissociation reaction to form bicarbonate and carbonate ions [82]:

$$CO_2(g) \leftrightarrow CO_2(aq) \quad \textbf{(2-4)}$$

$$CO_2(g) + H_2O(l) \leftrightarrow H_2CO_3(aq) \quad \textbf{(2-5)}$$

$$H_2CO_3 \leftrightarrow H^+ + HCO_3^- \quad \textbf{(2-6)}$$

$$HCO_3^- \leftrightarrow H^+ + CO_3^{2-} \quad \textbf{(2-7)}$$

(ii) Second stage reaction is a cathodic reaction by reduction of hydrogen ions, or the reduction of carbonic acid or bicarbonate ions:

$$2H^+ + 2e- \leftrightarrow H_2 \quad \textbf{(2-8)}$$

$$2H_2CO_3 + 2e- \rightarrow H_2 + 2HCO_3^- \quad \textbf{(2-9)}$$

$$2HCO_3^- + 2e- \rightarrow H_2 + 2CO_3^{2-} \quad \textbf{(2-10)}$$

(iii) The last stage is the anodic dissolution reaction of iron:

$$Fe \rightarrow Fe^{2+} + 2e- \quad \textbf{(2-11)}$$

Sometimes this reaction is followed by the precipitation of $FeCO_3$ with a direct reaction with carbonates anions, or through a multi-reaction with bicarbonates ion:

$$Fe^{2+} + CO_3^{2-} \rightarrow FeCO_3 \quad \textbf{(2-12)}$$

$$Fe^{2+} + 2HCO_3^- \rightarrow Fe(HCO_3)_2 \quad \textbf{(2-13)}$$

$$Fe(HCO_3)_2 \rightarrow FeCO_3 + CO_2 + H_2O \quad \textbf{(2-14)}$$

In oil and gas production, the hydrocarbon compounds mix with complex impurities with CO_2, water, H_2S within the pipeline. The presence of water is a serious concern because it contains high quantities of dissolved oxygen and can create an additional reaction in the cathodic site (oxygen reduction) as shown in Equation 2-15:

$$O_2 + 2H_2O + 4e^- \rightarrow 4OH^- \quad \textbf{(2-15)}$$

The significant contribution of oxygen to corrosion has been studied by several researchers. Song et al [64] created a model to predict the effect of oxygen on the steel corrosion rate in oil and gas production and transportation systems (Figure 2.10). The corrosion activity increases when the vapour pressure of O_2 increases. When vapor pressure increases from 0 to 0.04 atm, the corrosion rate increases from 0 to 0.2 mm/y, then 0.4 mm/y with a vapour pressure of 0.12 atm.

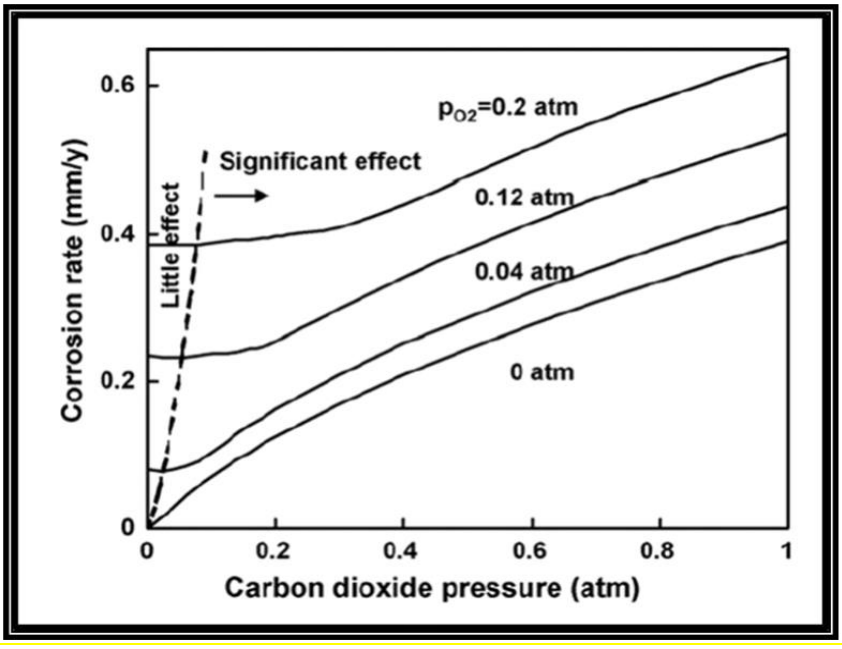

Figure 2-10: Effect of oxygen on corrosion attack [64]

Jung *et al.* [65] studied the effect of dissolved oxygen on different pipe material. They found that corrosion in carbon steel increased more than ten times when oxygen rose from 2 to 9 mg/L. Rosli et al. [66] found that the presence of oxygen dissolved in pure water at 65^{o}C was six times more corrosive than 1 M equivalent concentration of CO_2.

2.8 Sweet CO_2 Corrosion of Carbon Steel

In gaseous form, the CO_2 is harmless but becomes reactive to carbon steel once it dissolves in water, forming carbonic acid. This acid has been recognised as one of the most common corrosive compounds in service facilities and transport production systems [43]. A corrosion attack initiated by CO_2 will produce various types of corrosion depending on the environmental conditions and chemical composition of the material [67,68].

This type of attack can be either homogeneous, localised, pitting or mesa corrosion as shown in Figure 2-11, and Table 2-2 describes the type of sweet CO_2, and the influencing factors.

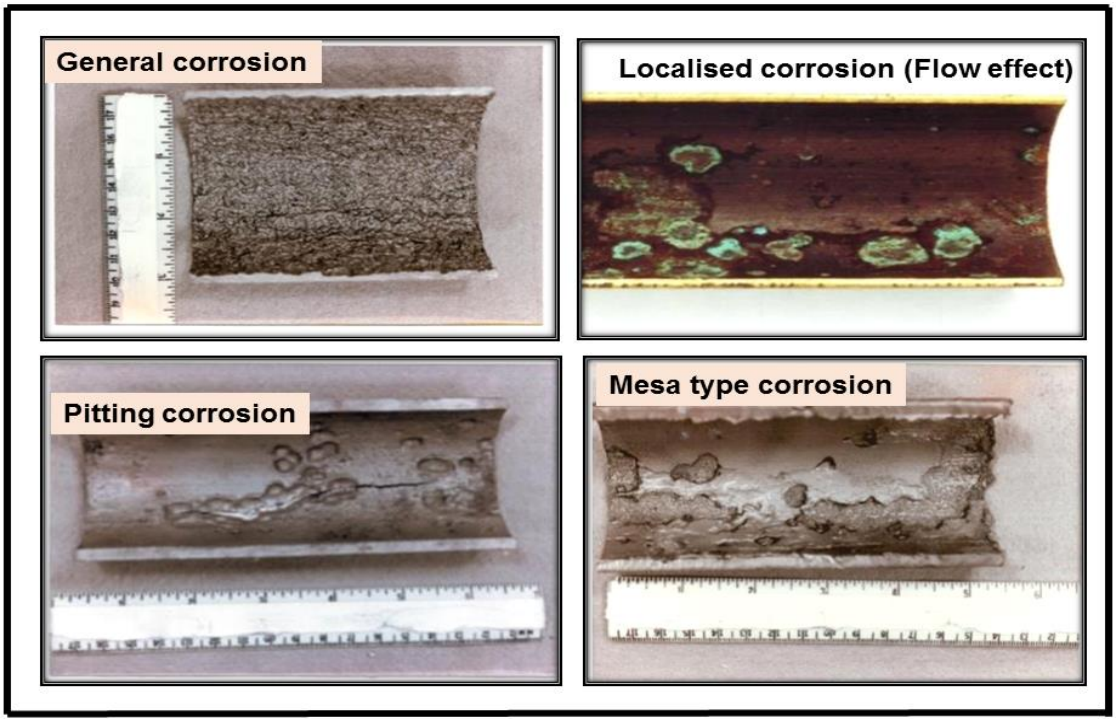

Figure 2-11 Types of corrosion seen in sweet CO_2 corrosion environments [68]

Table 2-2 Characteristics of CO_2 corrosion [67]

No	Type of Corrosion	Triggers
1	Homogeneous corrosion	When the material was degraded uniformly, forming a carbonate film as a protective layer
2	Localised corrosion	Mainly caused by lower flow rate in the system and stresses that can arise from the growth of the corrosion deposits. In certain faster flowing conditions the iron carbonate can be removed and it is difficult to reform
3	Pitting corrosion	It cause deep craters on the surface of the material at temperatures near dew point and where low flow conditions are present.
4	Mesa corrosion	It develop in low to a medium environment where unstable of the iron carbonate layer leaves surfaces exposed and more susceptible to attack.

2.9 CO_2 Corrosion Products

The effect of corrosion products on the performance of steel, when exposed to CO_2 environments is crucial. A protective carbonate film that often forms on the surface of the steel is beneficial to protect the pipelines from internal corrosion [69–71]. Farelas & Nesic [72] stated that the iron carbonate film could retard the corrosion reaction by creating an active diffusion barrier for protecting the metal surface and minimise the activity of corrosion activity on the metal surface.

Dugstad [73] found the corrosion film naturally grows during the flowing condition after several days without protection, and more corrosion product will develop in the stagnant-electrolyte condition. Even though not all films act as a protection barrier, for certain films the stability, protectiveness, and adherence to steel substrates have a positive correlation to reduce the rate of corrosion attack.

There are several types of corrosion products formed due to electrochemical interaction of steel in brine saturated with CO_2. The most common corrosion products are either iron carbonate ($FeCO_3$) and iron carbide (F_3C), or, a mixture of iron carbide (Fe_3C) and iron carbonate ($FeCO_3$) [70,74,75]. Table 2.3 shows characteristics for each corrosion product with different temperature ranges [76].

Table 2-3 Characteristics of CO_2 corrosion films [76]

Type of corrosion product	Temperature range	Characteristic/nature	Major component
Iron carbide	No range	Less than 100µm thick, metallic, conductive and non-adherent	Spongi and brittle, consisting of Fe, C and O
Iron carbonate	50-70 ° C	Adherent, protective and non-conductive	Cubic morphology, consisting of Fe, C and O

2.9.1 Iron carbide (Fe_3C)

Iron carbide/cementite (Fe_3C) is well known as a corrosion product found in CO_2 corrosion of low-alloy steels with a percentage of carbon composition up to 0.15% [74]. Iron carbide is part of the basic steel microstructure in the non-oxidised part that accumulates on the weld surface after the preferential dissolution of ferrite (α-Fe) into ferrous cation (Fe^{2+}) [77]. Dugstad [78] noted that the ferrite-pearlite microstructures could result in the evolution of a porous Fe_3C layer, which remains un-corroded when exposed to brine saturated with CO_2. The fragile,

porous, and dense Fe_3C residue is non-protective and therefore not likely to protect the material from corrosion in flow conditions.

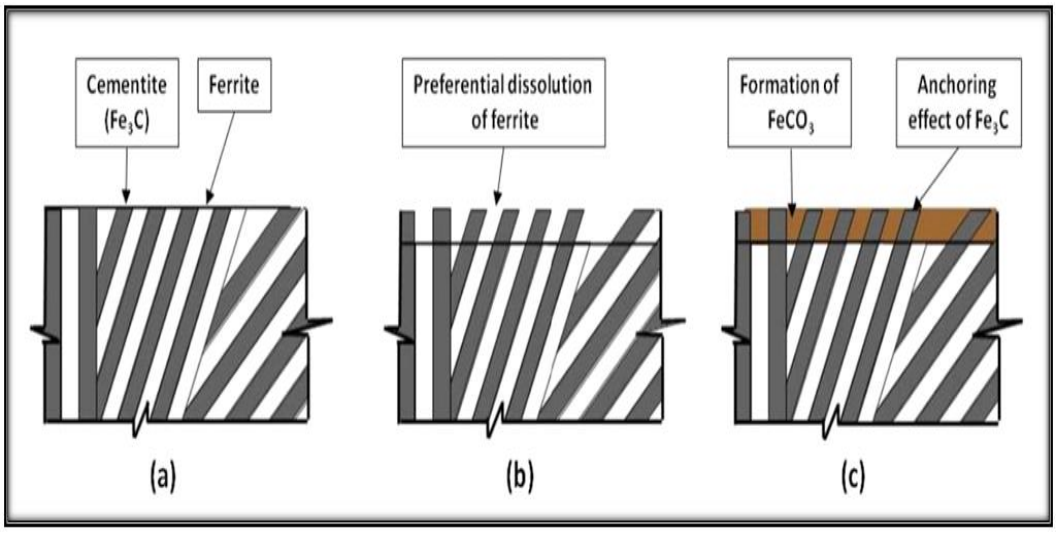

Figure 2-12 The sequence of the process of CO_2 corrosion product, (a) the microstructures, (b) preferential dissolution of ferrite only and (c) formation of $FeCO_3$ initiated by Fe_3C (carbide) [79]

The presence of Fe_3C is not always detrimental. Under some environmental conditions (pH, temperature, pCO_2, ferrous ion concentration and flow rate), it has been observed that the Fe_3C layer may help to form an anchor which protects the steel surface from corrosion [79] as illustrated in Figure 2.12. The formation of $FeCO_3$ layer can protect the steel by preventing the diffusion of ferrous cations from the steel surface to enhance its properties and protectiveness is shown in Figure 2-12 [79,80].

2.9.2 Iron carbonate-Siderite ($FeCO_3$)

A $FeCO_3$ film is the most common corrosion product found on steel surfaces in brine saturated with CO_2. $FeCO_3$ is a trigonal crystal system with a rhombohedral shape and a density of 4 g/cm^3. Figure 2-13B shows the planar stereochemistry of $FeCO_3$ structure with iron atoms occupies octahedral positions [53].

When the amount of ferrous cations (Fe^{2+}) and carbonate ion (CO_3^{2-}) surpasses the solubility limit, the precipitation of siderite ($FeCO_3$) on the steel surface will occur (Equation 2-16). The precipitation rate of the corrosion product will

determine the thickness of protective films. The $FeCO_3$ film acts as a diffusion barrier for the corrosive constituents that react with the metal surface by blocking-off areas on the metal so as to minimise electrochemical reactions on the surface of steel [46].

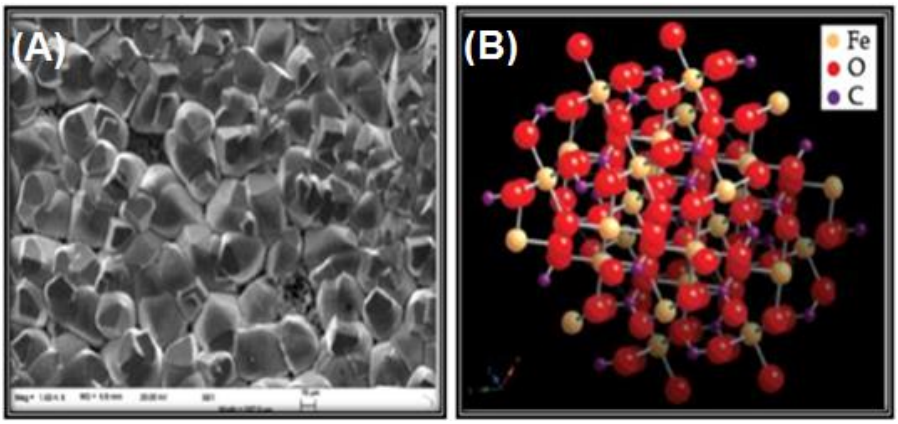

Figure 2-13 The morphology and structure of $FeCO_3$ [53]

The ability of $FeCO_3$ film to protect the steel surface is shown by several researchers [81,82]. A further demonstration by Nesic *et al.* [82] shows that the tendency to form the $FeCO_3$ active layer can be calculated from the saturation factor (SS) which is the multiplication of the cation Fe^{2+} concentration with the carbonate ion concentration (CO_3^{2-}) and then divided with the solubility product constant (Ksp) as given in equation below:

$$SS = \frac{[Fe^{2+}][CO_3^{2-}]}{Ksp} \quad \textbf{(2-16)}$$

The supersaturation of $FeCO_3$ is a fundamental factor affecting the deposition process. The nucleation of Fe-carbonate commences along the steel surface when reaching the solubility limit of $SS(FeCO_3) > 1$. These conditions promote the dense and uniform $FeCO_3$ film that will grow on the metal surface acting as a diffusion barrier for the corrosive agents that react with the metal surface by

blocking off the cathodic reaction on the system and minimise the corrosion attack on the metal surface [83].

However, when SS($FeCO_3$) < 1, the formation of the dense $FeCO_3$ protecting film is not favourable. There is the possibility that the nuclei formation will also form a porous film on the steel surface. However, the film protection is not permanent (partially protective). The film surface formed on a particular area may be damaged or destroyed and will subsequently create a localised corrosion attack. Figure 2-14 shows the development of $FeCO_3$ based on SS values [56,83].

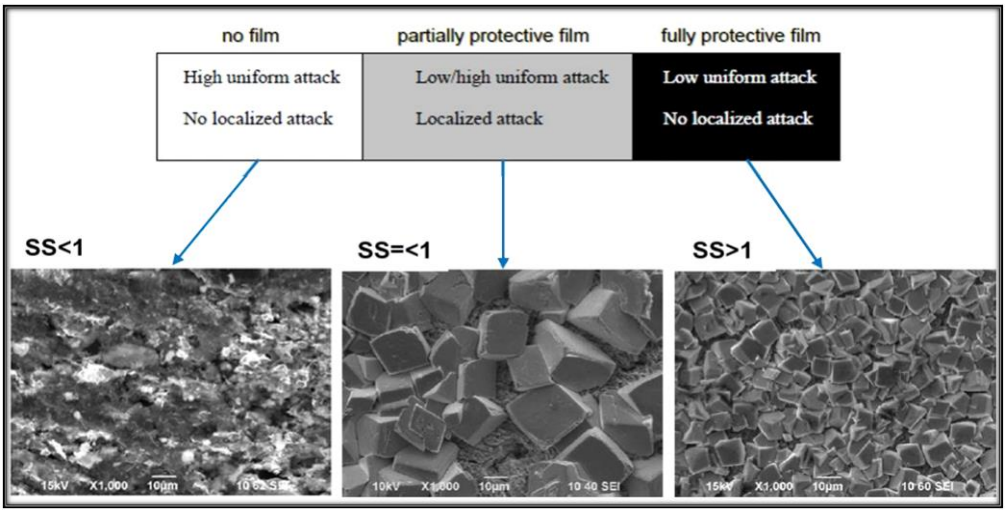

Figure 2-14 Growth of protective $FeCO_3$ based on solubility limit values [56]

2.10 Factors Affecting the Formation of CO_2 corrosion products

Several environmental parameters influence the rate of CO_2 corrosion and the formation of corrosion product on the metal surface. The factors include: partial pressure of CO_2, pH, temperature, and the hydrodynamic conditions [84,85]. Particularly in oil and gas production, hydrodynamic characteristics of the pipelines are highly important, since the characteristic of flow, pressure drop, water hold-up, and water condensation rate, play a very important role in the accessibility of the chemical inhibitor that is present on the surface of the metal that is under protection [86,87].

2.10.1 Effect of Partial Pressure

The CO_2 partial pressure (P_{CO2}) plays a significant role in CO_2 corrosion for both no-film and film-forming environments. Previous studies based on conditions for no-film formation, found a positive correlation between CO_2 partial pressure and the steel corrosion rate [88]. DeWaard and Milliams [88], found the corrosion rate increases by more than 100 % when PCO_2 increases from 3 to 10 bar (Figure 2-15). When PCO_2 increases, the H_2CO_3 concentration increases accelerating the cathodic reaction. Wang et al (2004) [89] claim the anodic reaction is essentially unaffected when the CO_2 partial pressure increases from 3 to 20 bar and the cathodic limiting current density increases due to a huge reservoir of H_2CO_3.

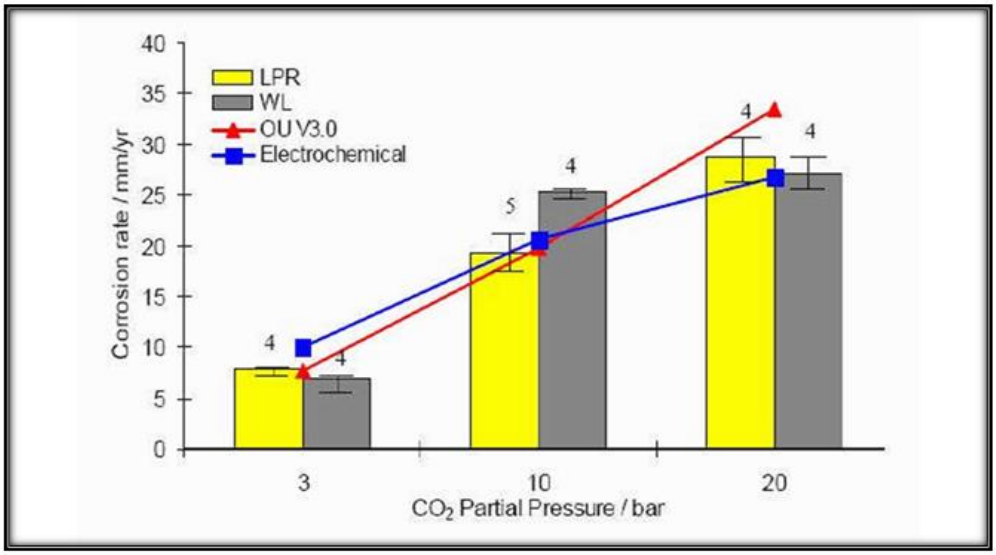

Figure 2-15 The effect of CO_2 partial pressure on corrosion rate [89]

On the other hand, the effect of partial pressure under film formation conditions was investigated by several authors [87,90]. J. Han et al. [90] studied the effect of pressure on the solubility of CO_2 film that directly impacted localised corrosion propagation. He found that, at higher CO_2 partial pressures CO_2 dissolution will increase. This means that the solubility of Fe-carbonate decreases and may easily create a protective film. A study from Gao et al. [91] found good agreement with Han. He noted that with increasing CO_2 partial pressure, the layer becomes more compact and layer thickness improves with a reduction in grain size of carbonate films.

2.10.2 Effect of Temperature

Temperature has a critical effect on the formation rate of the corrosion product layer [38,92]. At low temperature (25-40 ^{o}C), the precipitation rate of $FeCO_3$ is much slower, and very thick and protective iron carbonate films can be formed. Hunnik et al. [92] report that the formation of protective films of iron carbonate can significantly increase at high temperatures (>40 ^{o}C) due to its lower solubility. This will automatically decrease the corrosion rate.

Yin et al. [93] describe an experiment was performed to study the influence of the temperature and the thickness of corrosion product layer using P110 carbon steel (Figure 2-16). Results show that precipitation of $FeCO_3$ is fast at temperatures of 50 to 70 ^{o}C. The average corrosion rate at 50 ^{o}C is much higher than those at increased temperatures, as shown in Figure 2-16. In this tests, the average corrosion rate is lowest at 100 ^{o}C, which then increases slightly with increasing temperature [93].

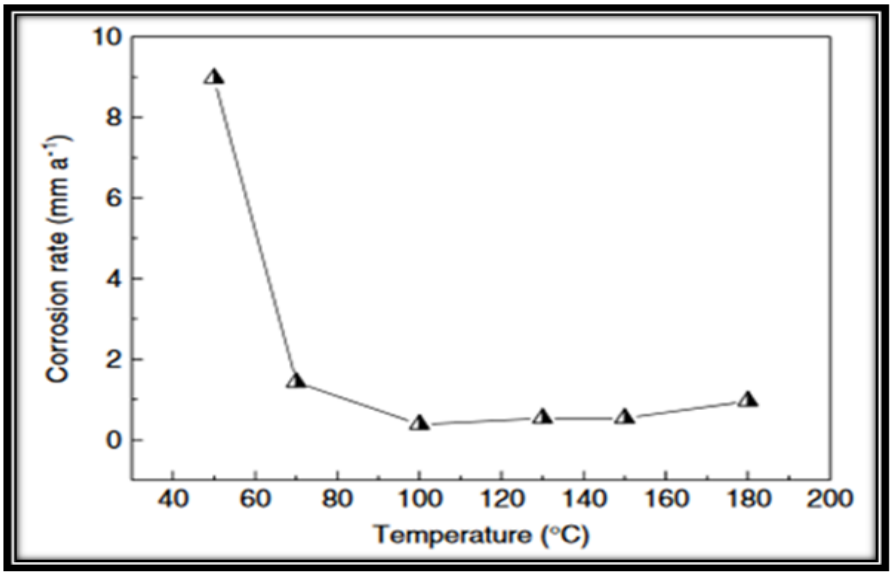

Figure 2-16 The influence of temperature to corrosion rate [93]

However, not all carbonate films formed can act as protective films. Under certain conditions at higher temperatures the formation of a protective film is unlikely to occur due to the high solubility of the $FeCO_3$ layer. When a thin layer of carbonate starts to form, it will dissolve quickly. Under these conditions, the corrosion product formed is porous and cannot be used as a protection against corrosion.

A study from Munoz *et al.* [70] found that; a temperatures below 40 ^{o}C iron carbide (Fe_3C) develops on the ferritic-pearlite steel surface.

To predict the rate of CO_2 corrosion rates, De Waard and Williams [88] proposed a calculation tool that consists of four parameters: temperature (from 0-140 ^{o}C), corrosion rate (from 0.02-20 mm/y), CO_2 pressure (from 0.01-10 bar) and a scale factor from 0.1-1 as shown in Figure 2-17. The scale rate was determined by comparison of measured corrosion rate at different temperatures above 60° C and this value is considered as the synergistic effect of the protective film. For example, a rough estimate of corrosion of carbon steel in the brine saturated with CO_2 at a pressure of 0.2 bar and temperature of 120^{o} C is 10 mm/y.

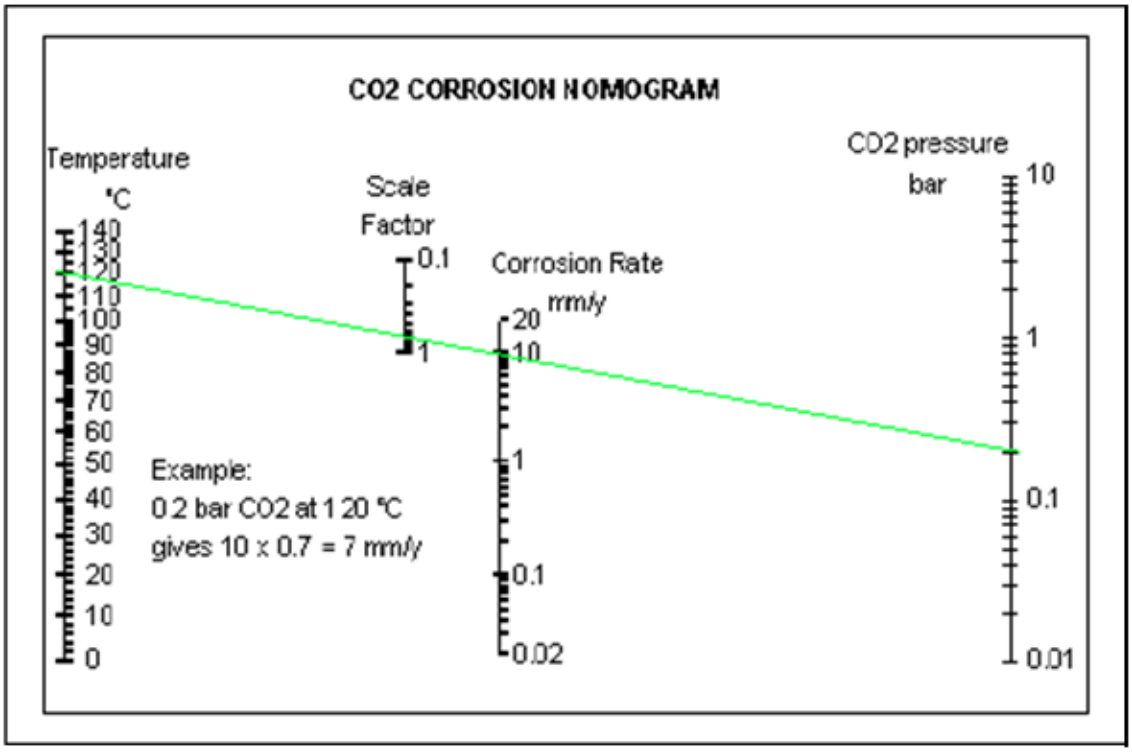

Figure 2-17 De Waar & Millliam Nomogram for predicting CO_2 corrosion of carbon steel [88]

2.10.3 Effect of pH in Brine Solution

The pH has a significant effect on the corrosion rate, at lower pH more hydrogen ions are present in the solution so that interactions with the anions from the brine solution will increase. The presence of CO_2 in a brine solution will also affect the

pH, making it lower. A lower pH will increase the solubility of the carbonate film so that protective film formation on the metal surface will be reduced. Conversely, at higher pH, corrosion is reduced withless H^+ in solution, causing an increase in $FeCO_3$ formation on metal surfaces. This can reduce the corrosion rate [67,94,95].

Another experiment was conducted to study the effect of pH of mild steel at elevated temperatures. Electrochemical impedance spectroscopy (EIS) and linear polarisation resistance (LPR) measurement methods were used to study the corrosion rate at temperatures of 80, 120, 150 and 200ºC along with pH values of 4.0 and 6.0 [67] (Figure 2-18).

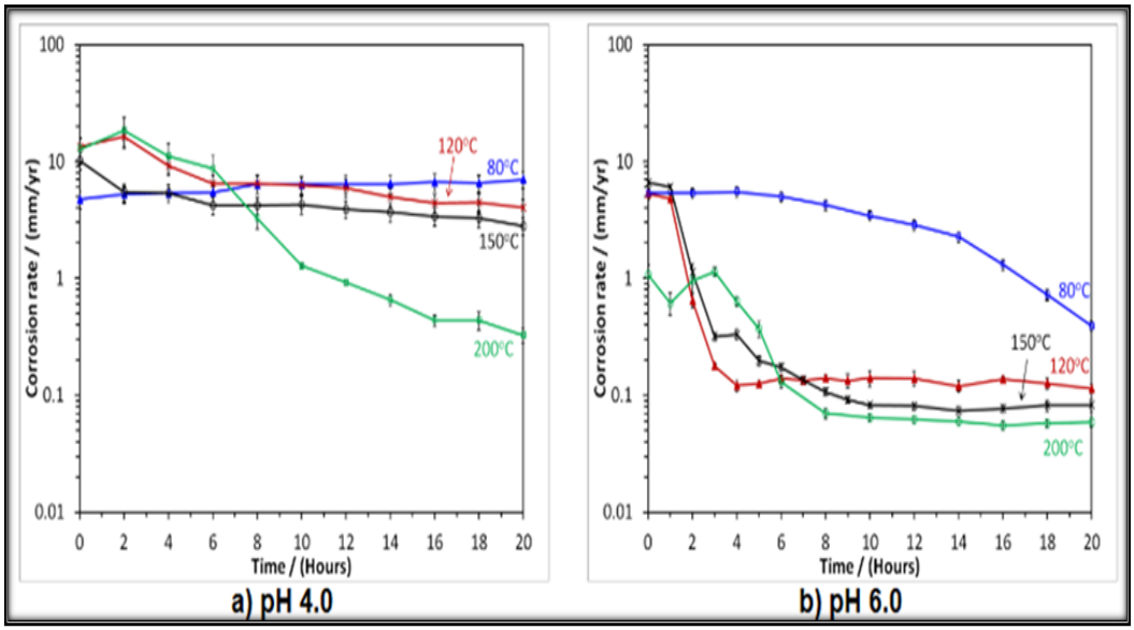

Figure 2-18 Corrosion rate and temperature at pH values (a) 4.0 and (b) 6.0 [67]

From Figure 2-18, it can be concluded that at higher temperatures and a pH value of 6.0 has a lower corrosion rate than the pH value of 4.0. This is because of formation of $FeCO_3$ is favourable at lower pH when the temperature increases. Therefore, the corrosion rate is lower because $FeCO_3$ forms on the steel surface and has the function of a diffusion barrier.

Tanupabrungsun *et al.* (2013) [94] studied the effect of acidity at temperatures up to 100ºC. It was clear that the carbonate film layer at pH (4-8) at similar temperature results in more protection for the steel. The formation of the

protective layer was found to be more obvious with crystal characteristics being small and compact (Figure 2-19). On the other hand, Pessu *et al.* [96] found that at low pH values (3), pitting corrosion occurs faster compared to a higher pH values (7.5) due to the high concentration of H^+ in solution.

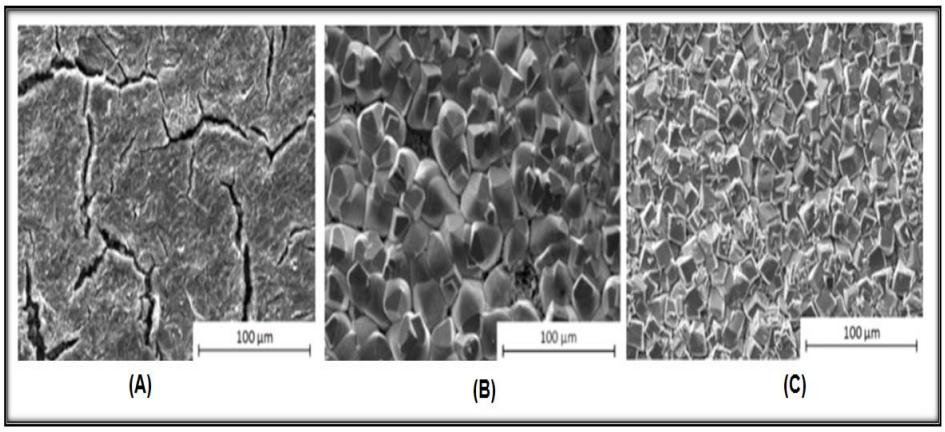

Figure 2-19 SEM of X6 surfaces after immersion in a 3.5 wt.% NaCl solution saturated with CO_2 a 50°C for 168 hours and pH (a) 3.8 (b) 6.6 and (c) 7.5 [96]

2.10.4 Effect of Hydrodynamics (Fluid Velocity)

Fluid flow (velocity) plays an important role to the stability of the protective film in a CO_2 environment, investigated by many researchers [13–16,58,97–99]. A high flow rate leads to an enhanced mass transfer process. Ferrous cations Fe^{2+} are more easily released from the steel surface, while H^+ ions are transported to the steel surface (decreasing the pH will increase the corrosion rate) [73]. Figure 2-20 is a schematic of mass transfer between species in a flowing condition [56].

There are two types of CO_2 corrosion mechanisms which can be distinguished based on the formation of a protective film under flowing conditions. When no carbonate film is formed on the steel surface (at pH <4 and SS<1), the rate of corrosion becomes faster due to turbulent flow (high shear stress). This raises the rate of species transportation from and towards the steel surface [75, 76]. This fast movement of species increases the rate at which hydrogen ions are replenished and generated, ferrous ions are released from the surface, which in turn increases the corrosion rate.

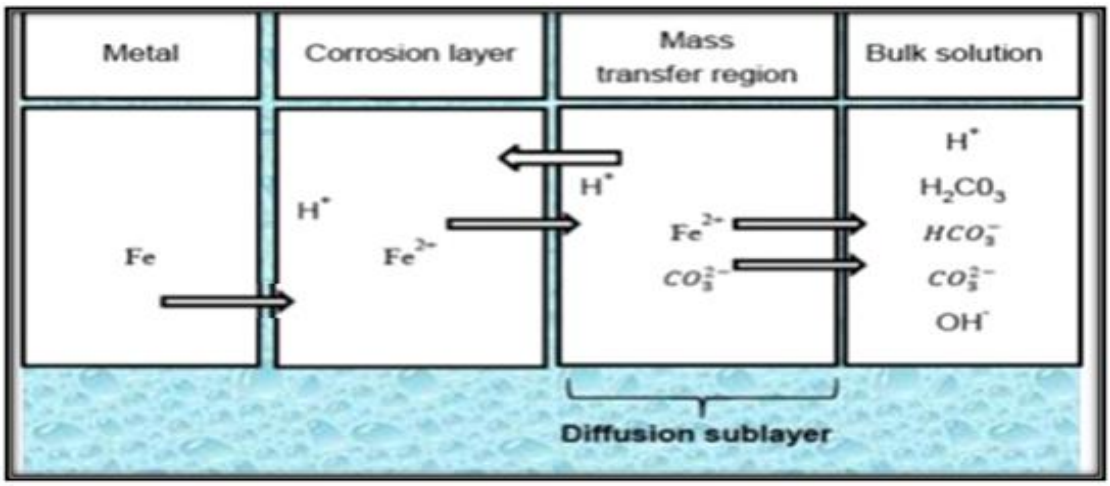

Figure 2-20 The schematic mass transfer between the species in flowing condition [56]

Conversely, when $FeCO_3$ is formed on the steel surface (at higher pH (>4) where SS>1) or when inhibitor layer exist on the surface of the steel, the influence of flow, in this case, becomes unimportant. However, a high wall shear stress can destroy the $FeCO_3$ corrosion product layers leaving the surface of steel without any protection, directly exposed to the aggressive corrosive environment [77,78]. This local breakdown of the $FeCO_3$ layer can also contribute to localised corrosion, which has the potential to be more serious than uniform corrosion [79].

The effect of wall shear stress on mass transfer was described by previous researchers [80, 81]. It was found from experiments that the magnitude of the wall shear stress is too low for scale destruction by hydrodynamics. On the other hand, above a critical wall shear stress magnitude, flow-induced localised corrosion is initiated [80]. In this study, submerged jet impingement was used to create higher shear stresses, as explained in the next chapter.

2.10.5 Characteristics of Turbulent Flow

In oil and gas production, the effect of turbulent flow is the primary consideration because of its tendency to accelerate the rate of corrosion [100]. Turbulent flow is identified by disorderly and rapid fluctuations of swirling regions through-out the flow. The pipe roughness and fluid viscosity will play a significant role in turbulent flow. When a fluid flows through a rough pipeline, the pipe wall will create local currents (Eddy currents) which have a significant effect on the

resistance due to friction. Viscous fluids will generally flow at a slower rate in the pipeline and thus they will not create any significant currents, and therefore, the roughness present within the pipe will not have an effect on the frictional resistance, following laminar flow. However, when a fluid with low viscosity flows inside a small pipe which has high internal roughness, it will generate a higher local current and produce a high friction factor (turbulent flow) (Figure 2-21).

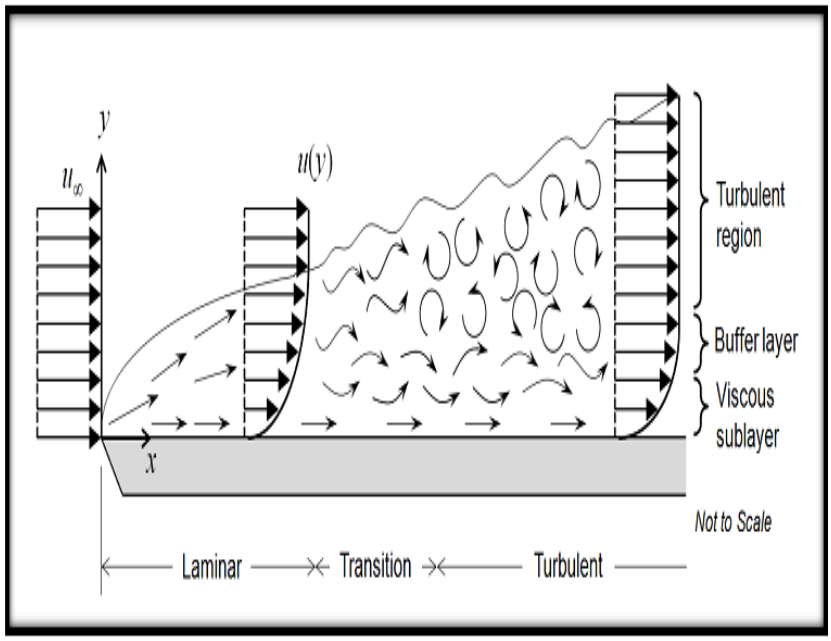

Figure 2-21 The change of flow characteristics from laminar to turbulence [101]

In turbulent flow, fluctuations fluid create an additional mechanism for momentum and energy transfer. The transfer activities that involve mass, momentum, and energy transfer to another region, flow much more rapidly than molecular diffusion momentum. As a result, turbulent flow is associated with much higher values of friction, heat and mass transfer (between the surface and electrolyte).

Efird [102], assumed that fully developed turbulent flow is a turbulent core where the mean velocity is essentially constant with the boundary layer near the solid/fluid interface. The majority of the changes in fluid stress, turbulence, mass transfer and fluid interaction with the wall occur within this boundary. His description of the turbulent boundary layer is shown in Figure 2-22 showing the energy, momentum and mass transfer that happen within the boundary.

The turbulent boundary layer is a specific area where the corrosion process is controlled by film formation. Praturi and Brodkey [103] found that the mobility of the anions and cations towards the wall and of the products of corrosion from the wall, and all electrochemical mechanisms with the wall, must happen in this place (boundary layer). They also suggested that any uncertainty in the turbulent boundary layer, especially in the close proximity with the viscous area, must be a factor influencing the overall rate of corrosion.

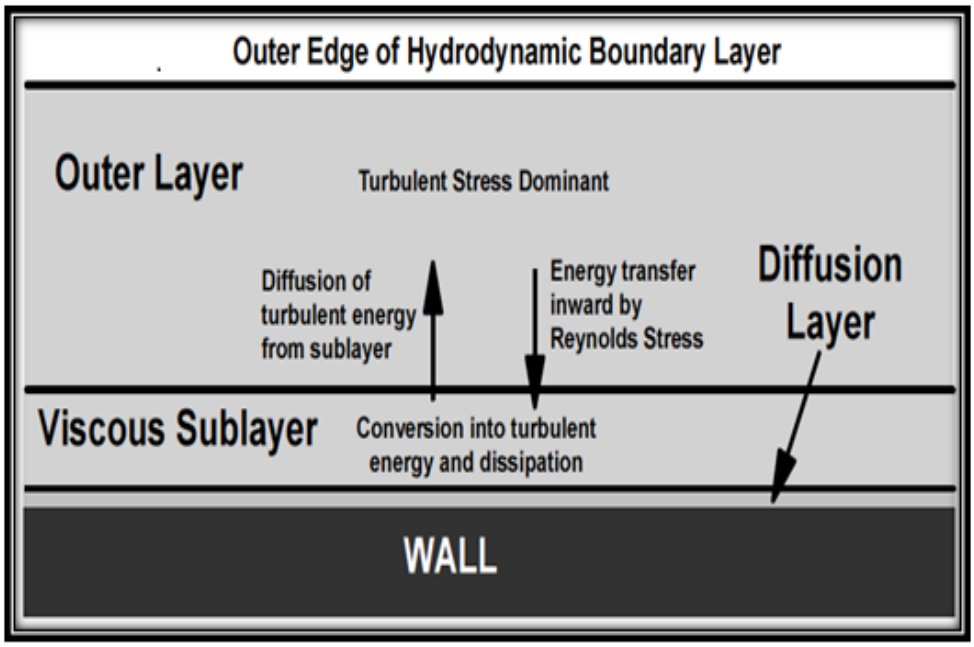

Figure 2-22 Hydrodynamic boundary layer structure under turbulent flow [102]

The film formation process, which acts as a corrosion control mechanism, occurs in the region between the hydrodynamic boundary layer and the corrosion boundary layer. All electrochemical reactivity between the corrosion species and the resulting corrosion product occurs these areas as well [25,101,102,104].

The relationship of the metal surface and the unstable nature of the turbulent flow, in the viscous area and diffusion boundary layer, is the primary argument that mass transfer and wall shear stress are crucial hydrodynamic parameters affecting the rate of corrosion with flowing electrolyte rather than a still condition.

2.10.6 Determination of Wall Shear Stress

The wall shear stress is the isothermal loss in pressure in a mobile fluid along an increasing length as a result of fluid flow friction from contact with a static wall. It is a force in the fluid at the wall rather than a force exerted by the wall on to the fluid. The total shear stress in a fluid moving past a static wall is found by a summation of the viscous and Reynolds stresses as Equation 2-17 [102].

$$\tau_w = \upsilon \left(\frac{\partial U}{\partial y}\right) - U_x U_y \quad \textbf{(2-17)}$$

Where U = fluid velocity (m/s) and υ= fluid kinematic viscosity (m/s). At the wall, $U_x = U_y = 0$, it means the Reynolds number ($U_x U_y$) goes to zero at the wall, leaving the viscous stress in the fluid only. τ_ω is defined as viscous shear stress at y=0 and expressed as equation 2-18:

$$\tau_w = \upsilon \left(\frac{\partial U}{\partial y}\right) \qquad \text{at } y = 0 \quad \textbf{(2-18)}$$

2.10.7 Mass Transfer Coefficient

Mass transfer coefficient (K_d) is defined as a diffusion rate constant in the relationship between the mass transfer rate, mass transfer area, and concentration change as the driving force [27]:

$$K_d = \frac{D_j}{\delta_d} \quad \textbf{(2-19)}$$

Where D_j : diffusion coefficient for species J in the bulk solution (m^2/s)

δ_d : diffusion boundary layer thickness (m)

Wall shear stress and mass transfer of turbulent flow patterns are related very closely to each other. Based on the Chilton-Colburn analogy [105], both equations are inseparable experimentally and mathematically. More than that, these equations are strongly related such that the change in one parameter will affect the other [106,107]. The relationship between the parameters may differ

from one flow geometry to another. The Chilton-Colburn analogy describes the relation between K_d and τ_w using equation 2-20 [22, 80, 105] :

$$K_d \approx \left(\frac{\tau_\omega}{\rho}\right)^{0.5} \quad \textbf{(2-20)}$$

$$Kd \approx 17.24 \left(\frac{\tau_\omega}{\rho}\right)^{0.5} S_c{}^{2/3} \quad \textbf{(2-21)}$$

Sc= the dimensionless Schmidt number, is expressed as the ratio of the viscosity (μ), to the product of density (ρ), and diffusion coefficient (D_j), for the active species, j. For Sc>100:

$$Sc = \frac{\mu}{\rho D_j} \quad \textbf{(2-22)}$$

2.11 Test Methods to Evaluate the Hydrodynamic Effect

Several techniques have been developed to evaluate the effect of flow on corrosion, including the carbon dioxide corrosion method. Many methods with a variety of approaches have been applied to hydrodynamic conditions especially for steel corrosion in turbulent flow systems. The rotating cylinder electrode (RCE), recirculating flow loop, rotating cage and the submerged jet impingement (SJI) are systems that applied widely in corrosion studies. This is because these methods can be used to investigate a structure's corrosion performance under laminar and turbulent flow with electrochemical equipment [15,16,23,27,58,108].

2.11.1 The rotating cylinder electrode (RCE)

The rotating cylinder electrode is a popular methods used to investigate the effect of flow on corrosion because this process is easily controlled and inexpensive [109]. In RCE, the test specimens are mounted side by side onto a (metal) rod that can be rotated and controlled at a given speed to provide a hydrodynamic effect to the subject material.

The transition from laminar to turbulent flow takes place at lower rotation rates, and hydrodynamic conditions are produced over the electrode surface. The rotating cylinder has the advantage that the whole velocity regime from homogeneous laminar to turbulent can be examined in equal adjustment [17,23,110,111]. Alawadhi & Robinson [15] assembled a novel RCE that consisted of hollow cylindrical samples (Figure 2-23) which were taken from each of region of the weldment (PM, HAZ and WM).

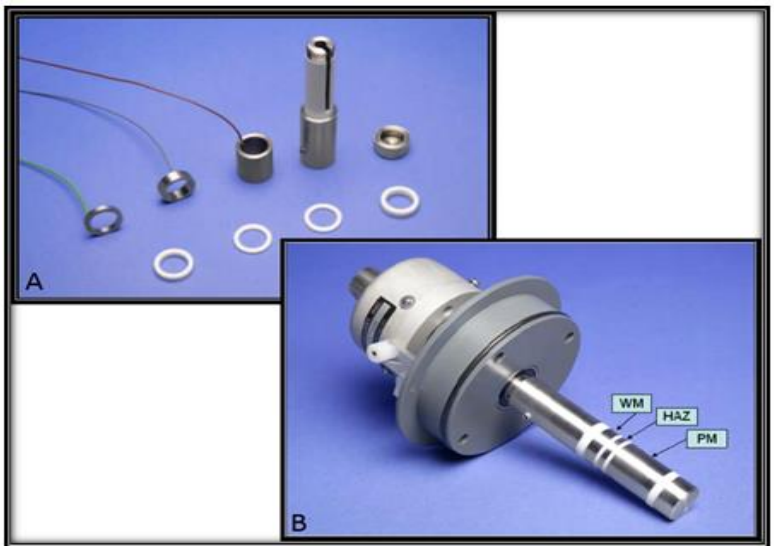

Figure 2-23 Assembly of a rotating cylinder electrode (RCE): (A) detail parts and (B) complete target that consists of the weldment [15]

Table 2-4 Advantages and disadvantages for corrosion testing using rotating cylinder apparatus [106]

Advantages	Disadvantages
Equation for mass transfer and wall shear stress well defined	Wall shear stress > 300 Pa is difficult to achieve
Fully developed wall shear stress is uniform over the entire surface	Testing is single phase liquid only for the equations to apply
Electrochemical tests, electrical resistance probes and coupons can be used	Maintaining good electrical contact with the rotating electrodes is difficult
Easy to use with no pumps or valves required	Testing under high pressure is difficult

RCE is commonly used for evaluating flow accelerated corrosion in a single phase liquid environment. Silverman [106] summarises the basic advantages and disadvantages of this method in Table 2-4.

2.11.2 Recirculating Flow Loop

Recirculating flow loops are conventional laboratory tests for evaluating the effects of flow in steel pipes. The technique was developed from the pipe-flow method. A recirculating flow loop set up is shown in Figure 2-24.

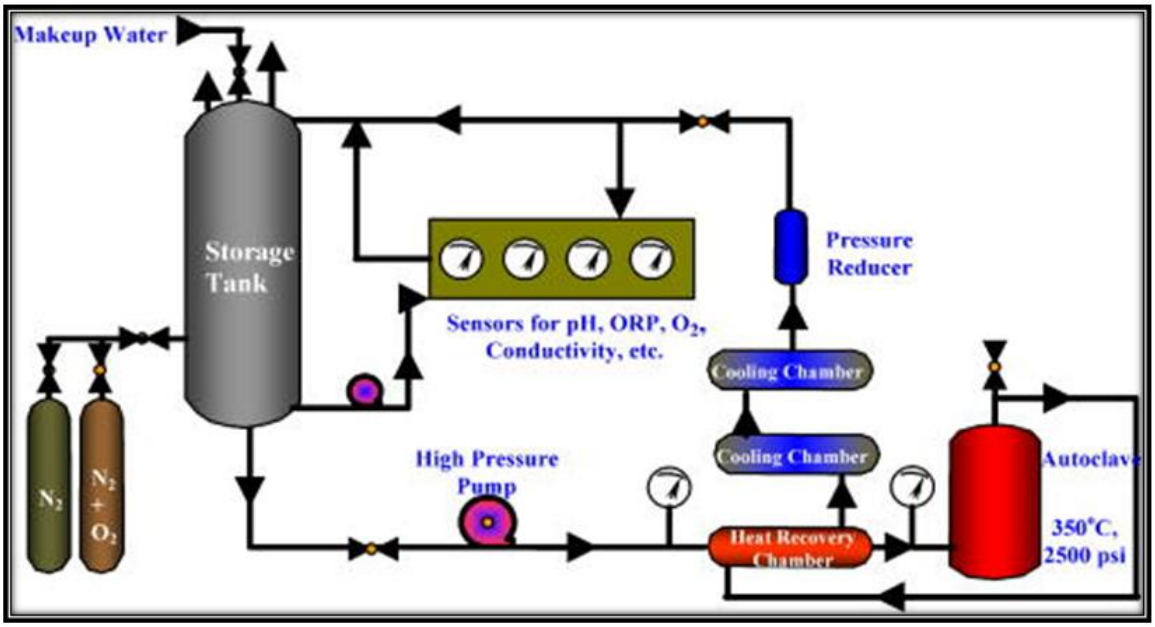

Figure 2-24 Flow loop system to study the hydrodynamic effect [27]

This experimental test consists of pipeline systems which recirculate the brine solution from a storage tank through a planned corrosion test system. The samples (electrically insulated coupons) can be placed inside a chamber (autoclave) making it possible to conduct a test at high temperatures and pressures whilst carrying out electrochemical analysis simultaneously.

Recirculating flow loops exist in a wide range of designs and sizes. The test section diameter can range from half an inch to four inches and greater. Diameter is an issue for both single phase and multi-phase systems.

The advantages and disadvantages of recirculating flow loops to evaluate flow effects are outlined in Table 2-5.

Table 2-5 Advantages and disadvantages for corrosion testing using recirculating flow loop apparatus

Advantages	Disadvantages
Equations for mass transfer and wall shear stress well established	High fluid requirements for both gas and liquid
Fully developed wall shear stress is uniform over the entire coupon	High liquid pumping and/or gas compression requirements
Electrochemical tests, electrical resistance probes and coupon can be used	High construction costs and operating costs along with high technician time
Simulation of multi-phase flow	Obtaining high shear stress is difficult

2.11.3 Rotating Cage

The rotating cage (RC) is also a tool used for evaluating the CO_2 corrosion at high temperatures and pressures in oil & gas fields. The RC methodology has practical advantages for assessing uniform and localised corrosion, and has been shown to be a more stringent test than others since some inhibitors (at a given concentration) loose effectiveness beyond a critical flow intensity [19,112].

The test protocol includes finding rotation speeds at which flat coupons showed similar surface marks of erosion corrosion as encountered in field failures. In the second step, corrosion inhibitors are identified to prevent erosion/corrosion under the same conditions as evaluated in the non-inhibited brine. The rotating cage adjustment of specimens incorporates the advantage that dissimilar carbon steel compositions could be tested in the same test as the same corrosion inhibitor under high pressures and temperatures (Figure 2-25).

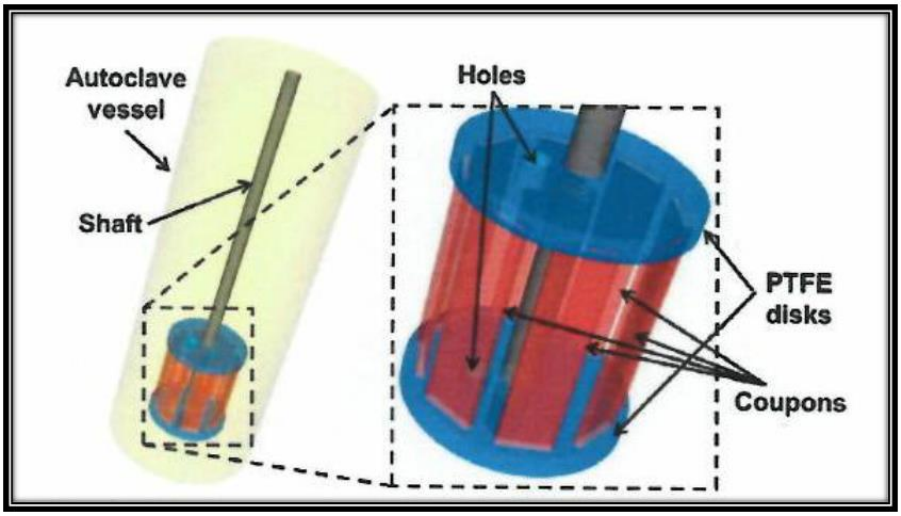

Figure 2-25 Rotating cage construction [112]

High turbulence zones exist in the gaps between the rotated coupons and that the critical flow intensities, which initiate erosion/corrosion cannot be quantified with existing equations. On the other hand, corrosion inhibitors evaluated under such "undefined" flow conditions always performed well in the field. Since then, the rotating cage has been successfully used in a multitude of investigations, specifically designed to test and evaluate corrosion inhibitors for oil & gas field applications under high pressure/temperature conditions [112–114].

Table 2-6 Advantages and disadvantages for corrosion testing using rotating cage [23]

Advantages	Disadvantages
Different alloy compositions could be tested in the same experiment	Equations for mass transfer and wall shear stress not established
Easy test, coupons can be produced easily and Low cost	Electrochemical tests, electrical resistance probes and coupon can not be used

2.11.4 Submerged Jet Impingement (SJI)

Jet impingement is one of the leading methods that offer an experimental approach to study hydrodynamic characteristics within pipelines. The hydrodynamic nature of the flow in pipelines is very important since the fluid flow velocity, dropping pressure, water cut and the rate of water condensation significantly affect the corrosion inhibitor performance on the solid surface of the steel. A particular concern is the development of slug flow. Slug flow is a temporary disturbance, in which, when a slug passes a point, the flow is severely disturbed, but then normalised after the slug passes-through [14]. The slug is a multiphase flow pattern that develops in pipeline systems which link the wells on the sea bottom to production platforms in the surface on oil & gas productions.

Previous research was conducted by Orazem [115] using a submerged axisymmetric impinging jet to monitor the effect of large fluid velocity on corrosion and to identify the effect of hydrodynamics and shear stress on the erosion/ corrosion of steel. Orazem's study used pipeline-grade steel in a high shear condition with brine saturated in CO_2 at 1 atm and at temperatures of 30 and 60^{o}C using a commercial potentiostat (Figure 2-26). Three regions of behaviour were monitored. At low jet velocities, the polarization resistance decreased with increasing fluid flow, and mass transfer is controlled by diffusion through a film. However, at intermediate jet velocities, the value of polarisation resistance is not dependent on velocity, suggesting that mass transfer is managed by diffusion via an active layer. Further, the surface films were removed by hydrodynamic effects, at the higher velocities. The submerged axisymmetric impinging jet is a recommended experimental system for monitoring the influence of hydrodynamics and mass transfer activity on the corrosion of steel.

Efird [27,102] conducted a simulation using a jet impingement tool by initiating a step change in the jet velocity rate. A flow environment is established for a circular jet impinging on a flat plate with the jet's central axis normal to the plate. A jet impingement target (JIT) is used for flow accelerated corrosion testing

considering the hydrodynamic characteristics of a jet impinging on a flat plate as shown in Figures 2-26 and 2-27. The fluid flow (from the jet nozzle) across a flat surface contains characteristic flow regions that are definable.

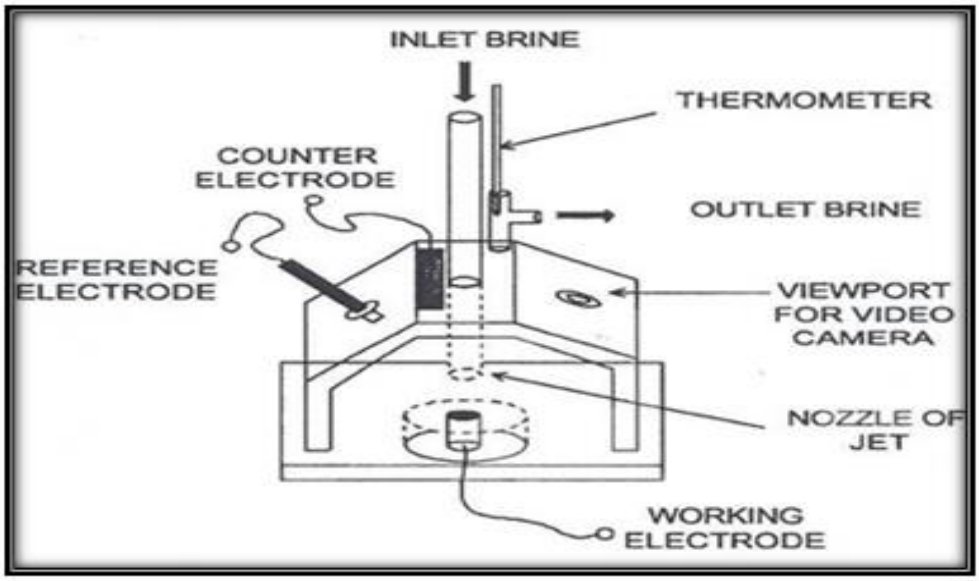

Figure 2-26 Schematic of the SJI experimental test cell [115]

Three regions are identified in Figures 2-27 and 2-28 as the centre (A), beneath the JIT nozzle, inner ring (B) and outer ring (C); in which different hydrodynamic conditions are experienced:

Centre (A) : stagnation region (no-flow)

inner ring, B : high radial velocity and high turbulence

outer ring, C : lower velocity and low turbulence

The hydrodynamic characteristics of jet impingement on a flat plate display the location of the test ring in the flow field and the properties of the flow regions. Efird's study [24] tested three hydrodynamic regions experimentally with a circular target (Figure 2-28) for carbon steel electrodes separated by dielectric regions.

Using the SJI method, the working electrode is placed just below the jet, and the corrosive fluid flows continuously to impinge the surface of the target and creates a hydrodynamic effect. This test can produce accurate and reproducible data when the test ring is properly installed, and the wall shear stress is determined.

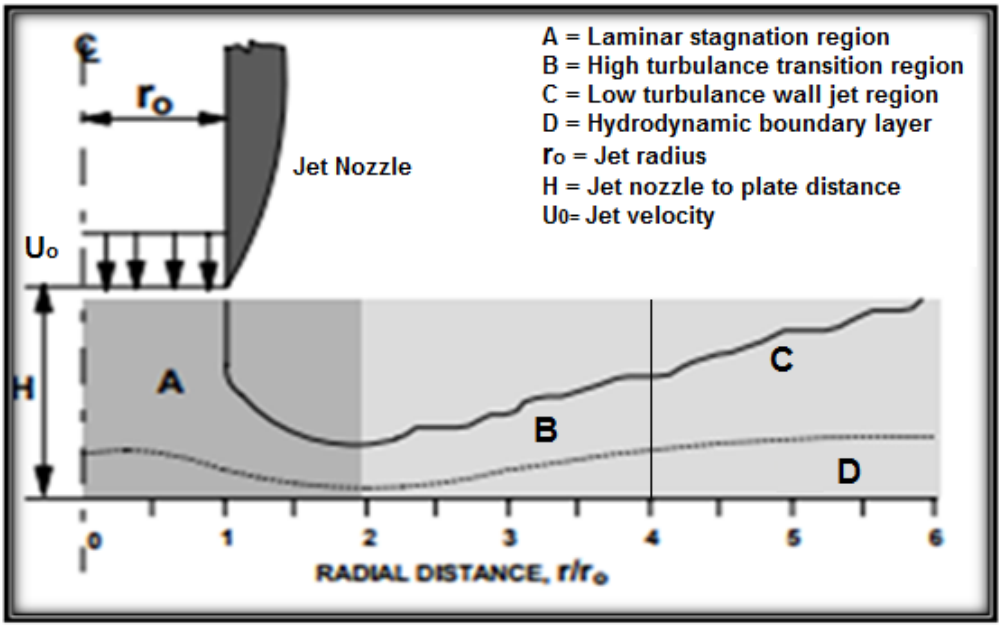

Figure 2-27 Hydrodynamic Characteristic of Jet Impingement [24]

The change in the rate of corrosion of carbon steel was constantly recorded at different flow rates. The assessment results of two chemical inhibitors on carbon steel in a common offshore service condition indicate that a large increase in wall shear stress is followed by a sharp acceleration in the rate of corrosion [24].

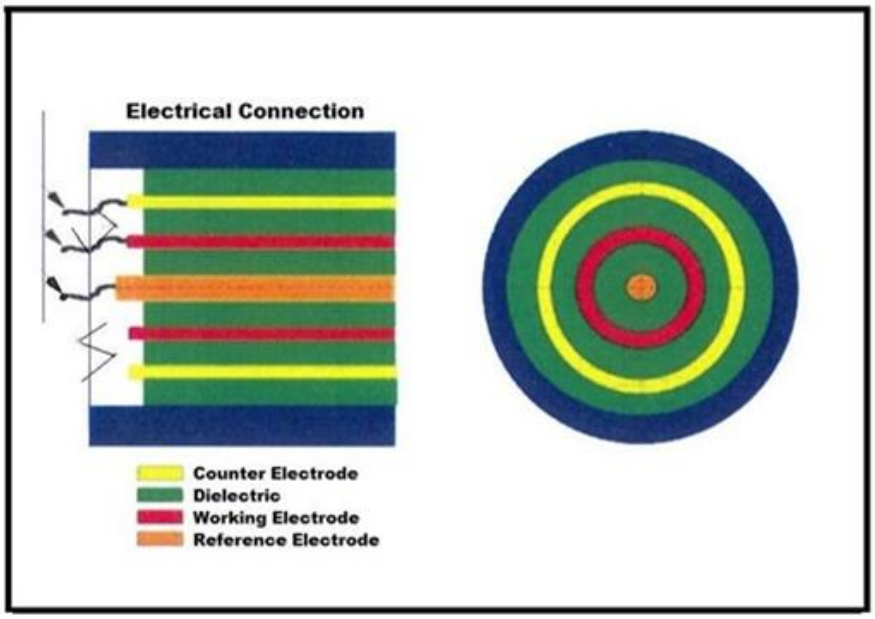

Figure 2-28 Hydrodynamic Region SJI Target [24]

The equation for wall shear stress in the wall jet area is proposed below [116]:

$$\tau_{\omega} = 0.179\,\rho \mathrm{Uo}^2 \mathrm{Re}^{-0.182} \left(\frac{r}{r_0}\right)^{-2} \quad \textbf{(2-23)}$$

The jet Reynolds number is defined as:

$$\mathrm{Re} = \frac{2\mathrm{r}_0 \mathrm{U}_0}{\vartheta} \quad \textbf{(2-24)}$$

Where r is the radial distance from the jet centre line and r_o is the jet radius.

Adegbite *et al.* [13,14,97] adapted the jet impingement target at Cranfield University to look at preferential weld corrosion. Each ring (or hydrodynamic region) was made up of WM, HAZ, and PM approximately in a ratio of 2:1:8 respectively as shown in Figure 2-29. In this way, weld corrosion was investigated by measuring galvanic and self-corrosion in no-flow and with flowing conditions. Initially, the HAZ is anodic and corroded preferentially to the PM and the WM. However, with a flow rate of 5 m/s, a sharp current reversal changed the HAZ to cathodic where it was protected by currents from the PM and WM.

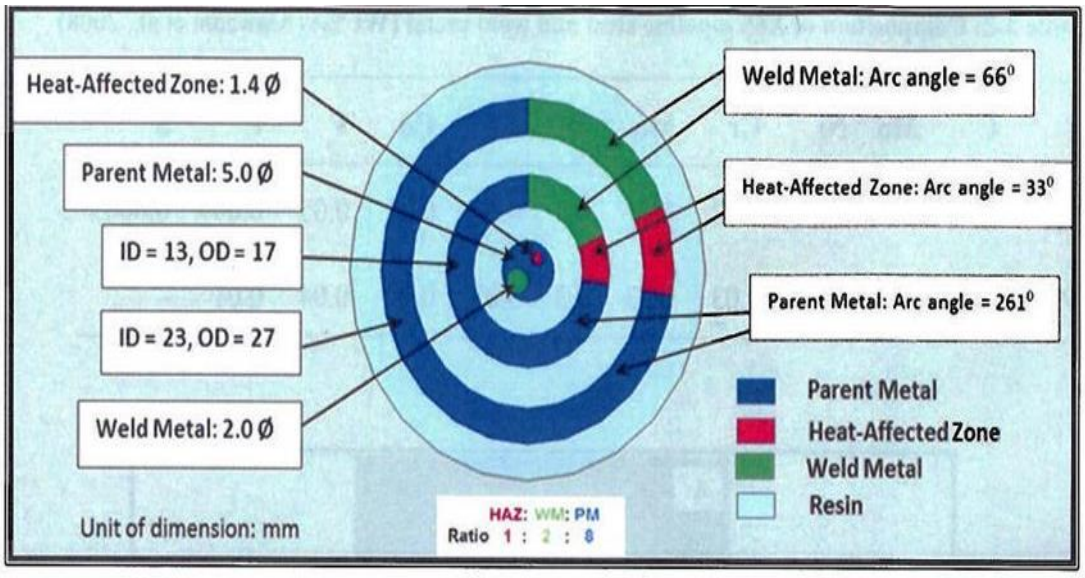

Figure 2-29 Jet impingement target design [13]

Adegbite correlated the reversal behaviour to displacement of an active inhibitor layer. The wall shear stress on the surface was 72 N/m^2 and this value was

comparable with another study (70 N/m^2) on the same material from Alawadhi and Robinson [15]. However, in this research, only the inner ring results were explored fully. In no-flow conditions, the galvanic current characteristics of each weld section was found to be slightly different. This was not expected since all the electrodes are at the same condition. Such changes were attributed to differences in chemical composition of the material or challenges during construction or fabrication [14].

2.11.5 Computational Fluid Dynamic (CFD) Simulations using Submerged Jet Impingement

It has been explained in the previous section that there is a difference in flow rate characteristics in each region of the submerged jet-impinged target (Figure 2-27). Figure 2-27 illustrates a model, introduced by Efird [102], that shows the flow rate characteristics when the fluid impinges perpendicularly on a circular plate which has been equipped with the working electrodes placed in different regions. Efird found that there was a difference in flow rates between regions A, B and C; where A (centre) has the lowest flow rate, followed by zone C (outer) and then zone B; which has the highest intensity of flow, due to higher turbulence comparing to areas A and C.

Zhang & Cheng [117], carried out computational fluid dynamic simulations (CFD) for flow over seven electrodes mounted on to a plate. He discovered that the maximum velocity of the fluid flows downstream from the region where the jet comes into contact with the surface of the electrode-infused plate in which the position of the seven microelectrodes is marked with number 1-7 that has different impact angles (Figure 2-30).

The CFD simulation process was carried out using a CFD software package (Solidworks 2009). In this simulation, the fluid condition was assumed to be incompressible, and the ƙ-ε turbulent model was applied to complete the simulation, where ƙ is defined as turbulent kinetic energy and ε is correlated with the local rate of dissipation. 10 % of turbulence intensity, 1 J/Kg of turbulent

kinetic energy (ƙ) and 1Wkh of turbulent dissipation (ε) were set. Table 2-7 shows the initial conditions for CFD simulation parameters:

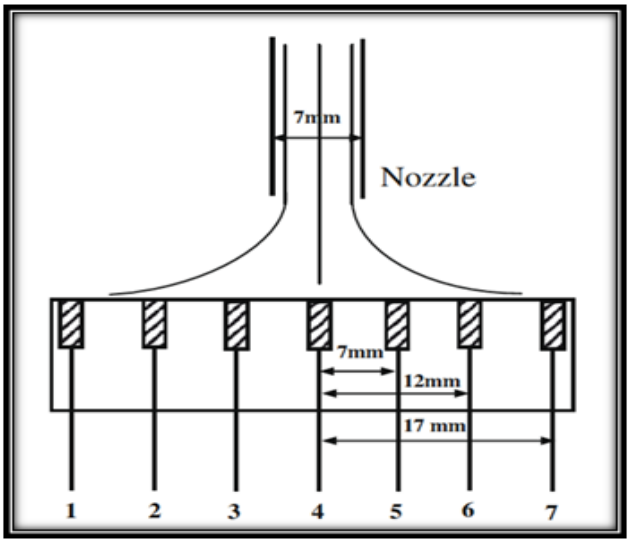

Figure 2-30 The set-up of micro-electrodes under fluid impingement [117]

Table 2-7 CFD running parameters from Zhang & Cheng [117]

Parameters	
Fluid velocity	3 m/s
Resolution of grid	0.4 mm
Electrode roughness	10 µm
Pressure	101.325 Pa
Flow type	Turbulent

CFD simulation results show that there is a slight difference in flow velocity and shear stress values in each point along the radial direction with normal (90 °) impact of the impinging fluid.

Zhang and Cheng [117] found that the performance of electrodes under the impinging flow is basically divided into 4 different working areas, namely: central laminar area, transition area, jet wall area, and boundary layer area. In the centre area where the micro-electrode 4 is placed, the flow is basically laminar on the electrode surface, and the main velocity component changes (from axial to radial), with a point of stagnation at the centre. The shear stress that defines as

isothermal loss due to fluid friction due to contact with stagnant walls, is reactively low in this location.

Later, increasing the radial distance to the transition area is accompanied by a rapid increase in the velocity of fluid flow which peaks at around x / d = 1

x is the radial distance from the centre of the electrode
d is the diameter of the jet nozzle

Shear stress increases to the maximum value, with the turbulence intensity increasing above the electrode surface. Flow patterns are displayed with high turbulence (high shear stresses) and large velocity gradients on the electrode surface. It is therefore unexpected that the mass transfer rate in the transition area is higher than the area of laminar stagnation. Therefore, the transition region is of primary importance to study the effect of fluid flow on corrosion in high turbulent regions. It can be seen that in region 5 & 3, where maximum velocity occurs, the shear stress is higher than in region 4 where the jet comes into contact with the plate (Figure 2-31 & 2-32).

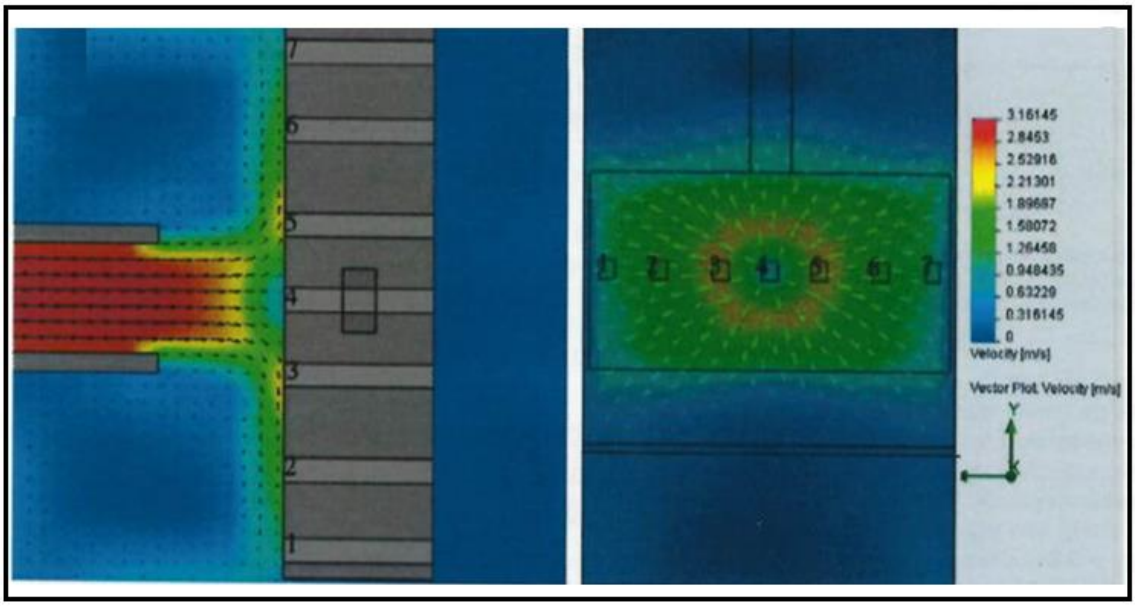

Figure 2-31 Velocity profiles at flow rates of 3 m/s from CFD simulation [117]

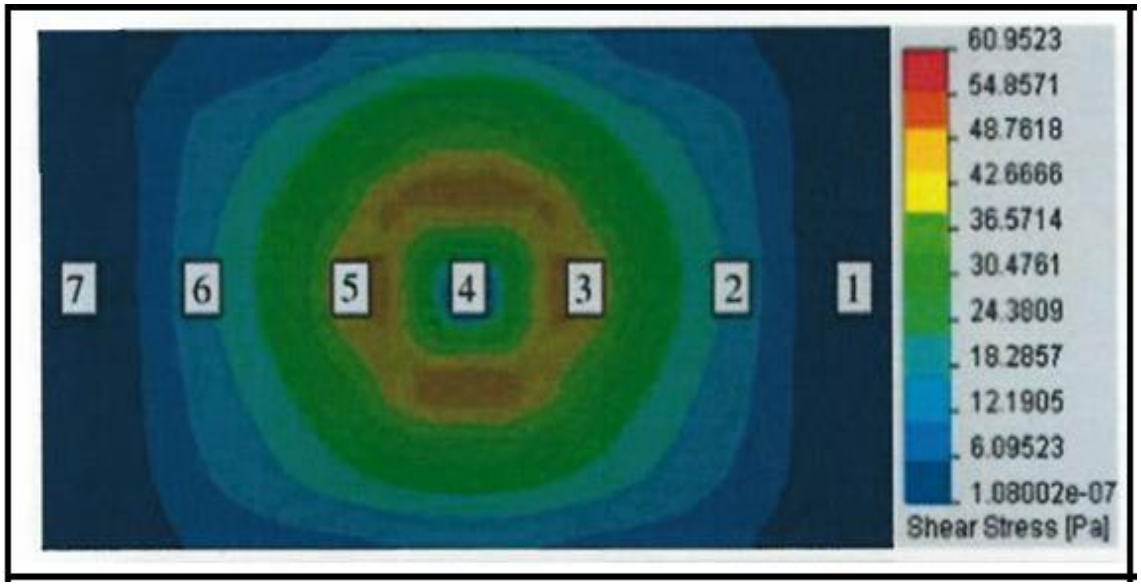

Figure 2-32 Shear stress contours for the electrode-mounted plate [117]

At a radial distance further from the centre, (area 1, 2 and 7, 6), the fluid velocity and the shear stress decrease due to low turbulent intensity in line with increasing jet wall thickness. The shear stress intensity is directly proportional to the rate of corrosion. A decrease in mass transfer rate and shear stress results in a decrease in the steel corrosion rate. In the boundary layer area, the resulting velocity and shear stress decrease further, resulting in a decrease in the steel corrosion rate. The simulation results are supported by findings from previous studies that show the variation of velocity and shear stress for each electrode placed in different areas of a jet impingement target [102,104,118].

2.12 Corrosion Prevention

All industries have an objective to increase their profit margins by minimising cost, but must take in account the security and safety aspects of their staff. In the petroleum and petrochemical industries, the use of steel is very common, especially during the installation of process facilities. H_2S and CO_2 gases that are carried away during production can increase the chances of corrosion. That in extreme situations may damage the production facilities. Pipeline ccorrosion generally occurs in the weldment area that exists after the welding process [46].

To address this problem, it is necessary to develop several methods of corrosion prevention to extend the lifetime of the material. There are several methods to minimize corrosion of a metal surface. Every method has different characteristics and objectives. Generally, the approach to control corrosion is to acquire a better understanding of the corrosion mechanisms involved [119].

There are four primary methods for corrosion control and corrosion protection [4]:

1. Materials selection and design
2. Protective coatings
3. Cathodic and anodic protection
4. Application of corrosion inhibitor(s) in different environments

Generally, effective corrosion control is obtained by combining two or more of these methods. Corrosion control should be considered at the design stage of a given facility or system. The methods selected must be appropriate for the materials, for the configurations, and the types and forms of corrosion which must be monitored. Of the four methods, corrosion inhibitors are commonly used because they can be applied or changed directly without disrupting a process [6].

2.13 Corrosion Inhibitor

Corrosion inhibitors are materials that when mixed to in a corrosive environment, will minimise the corrosion. Inhibitors are added to corrosive media such as acids, cooling waters, steam, and other fluids, either continuously or intermittently. The concentration of inhibitors can vary from 1 to 15,000 mg/L [120]. In oil and gas industry, the range of inhibitor concentration used is from 10-200 ppm [121].

The inhibitor works by forming a thin film layer on the metal surface to inhibit electron exchange between a metal surface and corrosion media. Some inhibitors work by forming large deposits and by coating metals. The latter initiates corrosion reactions so that metal corrosion takes place very fast and

produces products that will be adsorbed on the metal surfaces to form a passive layer [122].

One of the advantages of using a corrosion inhibitor is the simple procedure. The inhibitors can be directly added during the process without a shutdown procedure, so the production process is not disrupted.

The use of corrosion inhibitors is popular in many industries such as in oil & gas companies, petrochemical, and heavy manufacturing companies. The most of corrosion inhibitor consumption is in the oil & gas industry, especially in refineries. In the shipping industry, the application of corrosion inhibitors is also increasing. Inhibitors added as an ingredient into the paint solution before directly painted on the wall or the vessels of ships to protect those areas from corrosion attacks [2].

The use of inhibitors has been shown to significantly decrease the corrosion rate, thus providing a direct impact on the cost reduction caused by corrosion attacks. The success of inhibitor protecting metals from corrosion in petroleum industry has saved about 15-35% from the $2.5 trillion total corrosion cost in 2013 [123].

2.13.1 Classification of Corrosion Inhibitors

There are many types of inhibitors that can be used for preventing corrosion reactions and these can be classified based on the mechanism employed. In general, the inhibitor can be classified into two groups: interface inhibitors and environmental scavengers (conditioners) as described in Figure 2.33 [124].

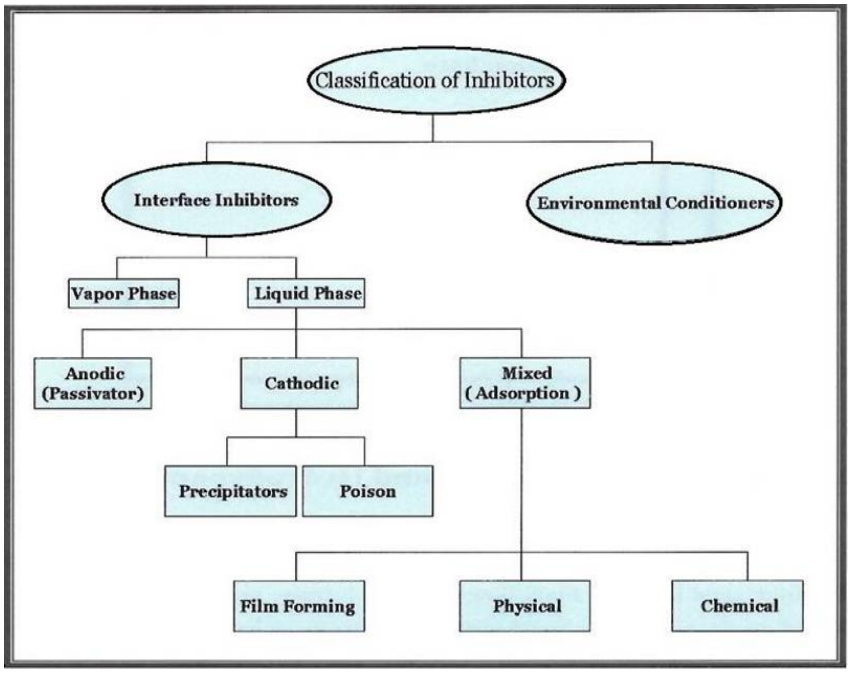

Figure 2-33 Classification of Inhibitor [124]

An environmental scavenger is a type of inhibitor that contains active chemical compounds that can eliminate or deactivate undesirable compounds. For example, the addition of hydrazine compounds into a sealed package to capture remaining residual oxygen. The objective is to improve safety and extend the shelf life of a product because the presence of oxygen in small concentrations can have a negative effect, such as a microbial contamination or by initiating a corrosion reaction. Interface inhibitors consist of three different types of inhibitor which are anodic, cathodic and mixed inhibitors, each inhibitor indicates how the inhibitor prevents the corrosion reaction from taking place.

2.13.1.1 Anodic Inhibitor

Anodic inhibitors can typically form passive protective films which delay the anodic reaction (Figure 2-34A) by making E_{corr} (corrosion potential) more positive. These inhibitors are commonly used in neutral medium where soluble corrosion outputs, such as oxides, hydroxides, or salt are produced. For example, 2,5-bis(3-pyidyl)-1,3,4-thiadiazole is an anodic inhibitor that may facilitate the formation of passive film that inhibits the anodic metal dissolution reaction [125]. Corrosion

could be accelerated rather than inhibited if the concentration of anodic inhibitor is insufficient. The critical concentration above which inhibitors are effective depends on the properties and concentration of the aggressive ions [124].

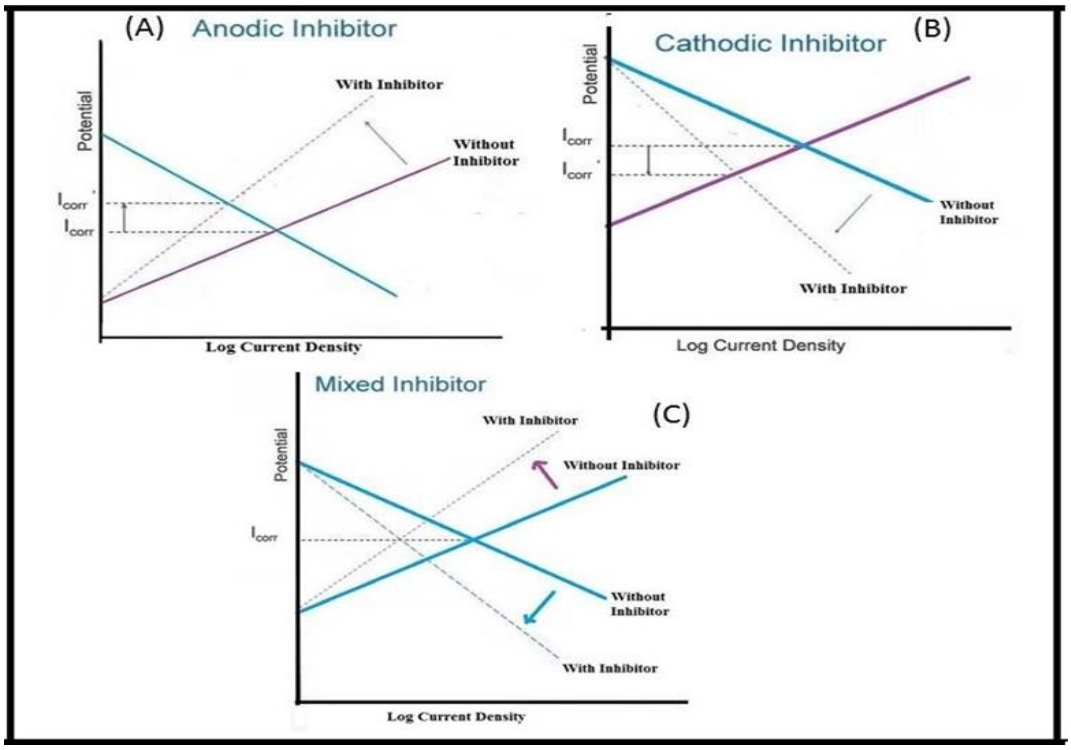

Figure 2-34 Evans diagram showing corroding systems with(A) anodic inhibition; (B) cathodic inhibition and (C) mixed inhibition [124]

2.13.1.2 Cathodic Inhibitor

Cathodic inhibitors work by shifting the corrosion potential to be more negative (cathodic site) as shown in Figure 2-34B. Cathodic inhibitors use hydrogen ion reduction to form H_2 gas, or reduction of O_2. These conditions create the environment directly adjacent to the cathode to become alkaline. As a consequence, some ions such as zinc, magnesium and calcium will precipitate as oxides to create a protective film on the metal surface. There are several ways of inhibition by polarisation of the cathodic reaction, such as oxygen scavenging, cathodic poisoning and cathodic precipitation. However, in acidic mediums, using cathodic poisons can cause a serious drawbacks, initiating hydrogen blistering and hydrogen embrittlement [124]. 2-napthalene sulfonic acid and salicylic acid hydrazide are examples of cathodic inhibitors [126,127].

2.13.1.3 Mixed Inhibitors

Most mixed inhibitors are organic compounds used in many industries, including in oil and gas. These inhibitors have different mechanisms compared to anodic and cathodic inhibitors, so that this type of inhibitor cannot be explicitly determined as an anodic or cathodic inhibitor (Figure 2-34C). The nature of mixed inhibition is determined by the ability of the inhibitor to be adsorbed on the metal surface and minimize direct contact with the electrolyte. Several factors influence the mixed inhibitor performance such as the structure of the inhibitor, the surface charge of metal, and the type of corrosion media (electrolyte) [128].

The adsorption mechanism of a mixed inhibitor on the metal surface can be classified in three categories; physical interaction (physisorption), chemical interaction (chemisorption), and a protective film mechanism. Physisorption is a physical interaction between inhibitor ions or dipoles and the active charge of the metal surface. If the metal surface has a positive charge, it will react with an anion from the inhibitor. Inversely, when the surface of the metal is negatively charged, it will interact with a cation from the inhibitor.

The physisorption mechanism is relatively weak interaction, and the ability of the inhibitor to adsorb on the metal surface is temporary (desorbed easily). The physisorption mechanism between the inhibitor and metal surface has a low activation (Gibbs free) energy and is relatively independent to the temperature [129]. Chemical interaction (chemisorption) is a more powerful and effective interaction compared to physisorption due to the inhibitor molecules being chemically adsorbed on the metal surface. In terms of electrochemical reactivity, the interaction involves the transfer and sharing of charge between the inhibitor molecules and the surface of the metal. Most of the mixed inhibitors are organic compounds that have phi (π) electrode pairs, providing more free electrons that can be transferred and shared with the metal surface.

Chemisorption is a slow and complicated process due to the complexity of charge-transfer electrons between metal and the inhibitor. This interaction produces higher activation energy compared to physisorption, and the inhibitor molecules are adsorbed on the metal surface and therefore there is less possibility for it to be displaced [38,47].

Film formation refers to a process of forming a good corrosion product as a thin film on the surface of the steel. This protective film acts as a physical barrier and limits the electrochemical reaction or charge transfer between electrolyte and metal surface. One compound that acts as a protective film is $FeCO_3$ [130]. More detail about $FeCO_3$ film formation from CO_2 corrosion is explained later in this chapter (2.16).

To understand about the nature of adsorption, the various adsorption related isotherm equations have been used to study adsorption mechanisms, and one such is the Langmuir equation. The proportion of the surface covered by the adsorbed substance is proportional to its concentration, as expressed in the following equation:

$$\frac{\theta}{1-\theta} = K_{ads} C \qquad \textbf{(2-25)}$$

Rearranging, the final form of the Langmuir adsorption equation will obtain:

$$\frac{C}{\theta} = \frac{1}{K_{ads}} + C \qquad \textbf{(2-26)}$$

Where, C is the inhibitor concentration, θ is the surface coverage and K_{ads} is the adsorption equilibrium constant.

2.14 Factors Affecting Corrosion Inhibitor Performance

The inhibitors in extreme environments such those found in the oil and gas industries has been undertaken for many years and shown that use of corrosion inhibitors is one of the best ways to protect the metal from corrosion [124,131,132].

Some studies also state that in the case of oil and gas pipelines, corrosion inhibitors can be utilized when a newly installed pipeline is commissioned or during operation [59,60]. Application of inhibitors to pipeline steel during operation creates a different challenge and sometimes may affect the inhibitor performance. Meng et al [100] showed that, the effectiveness of the inhibitor depends on physical and chemical factors such as steel composition and microstructure, water chemistry, pH, organic acids, water/oil ratio, temperature, CO_2, and H_2S partial pressure, flow regimes and flow pattern.

2.14.1 Effect of microstructure and composition

A pipeline used in the upstream petroleum industry must have strong mechanical properties, especially in the weld area connecting the pipe, so the pipeline is expected to operate for a longer period and is also resistant to corrosion attack [135]. The main factors that improve mechanical resistance are the microstructure and chemical composition of the material [63,64]. The microstructure plays a significant role in forming protective film layers such as $FeCO_3$ in a CO_2 environment or a film layer with a chemical inhibitor [135].

An experiment conducted by Lopez [138] studied the performance of inhibitors for two dissimilar microstructures (annealed, quenched and tempered). A carbon steel with the composition shown in Table 2-8 was used.

Table 2-8 The composition of carbon steel used by Lopez (2005) [138]

Mn	C	Si	Cr	Cu	Ni	Mo	P	S	Fe
0.99	0.38	0.33	0.17	0.99	0.04	0.02	<0.01	<0.01	Balance

Two different heat treatment processes were used for annealed and, quenched and tempered (QT) samples. The result shows that the two dissimilar microstructures have different characteristics in terms of their corrosion response. Electrochemical analysis using impedance spectroscopy (EIS) and linear polarisation resistance (LPR) found that the annealed samples have a stronger corrosion resistance than QT. When annealed samples are exposed to

the corrosive media, the corrosion activity produces an increase in the area of cementite (Fe_3C). The inhibitor interacts with laminar cementite and the adsorbed molecules block the active site from further cathodic reactions. Therefore, in quenched and tempered samples the inhibitor presence results in a delay in the precipitation of the film and does not provide strong protection that is normally caused by cathodic blocking.

Paolinelli *et al.* [139] studied the additional effect of adding 1% chromium (Cr) to the C-Mn steel on inhibitor performance. He used two different steels tubes with different compositions, particularly 1% and 0.17 % Cr for tubes (A) and (B) respectively as seen in Table 2-9.

Table 2-9 The composition of carbon steel used by Paolinelli [139]

Cr %	Mn	C	Si	Cr	Cu	Ni	Mo	P	S	Fe
(A) 1	1.01	0.39	0.26	1.02	0.08	0.04	0.19	0.001	0.002	Balance
(B) 0.17	0.99	0.38	0.33	0.17	0.09	0.04	0.02	0.01	0.01	Balance

EIS measurements showed tube A has a higher corrosion rate than tube B. EDX shows that the addition of Cr greatly influences the microstructure and is detrimental to the performance of the inhibitor used. Cr enrichment in the C-Mn steel increases the corrosion product too.

2.14.2 Effect of Temperature

The effect of temperature is a crucial factor on inhibitor performance and there are many studies that have been carried-out to evaluate this phenomenon [38,140–145]. It was found that the temperature not only affects the corrosive medium but, it also has a significant influence on the inhibitor response, both physically and chemically [141].

The behaviour of corrosion inhibitors at higher temperature was explored using the flow loop test by Gulbrandsen and Kvarekval [145]. The laboratory testing

condition was set up with a temperature at a range of 60-150 ^{o}C, a pressure of 1 bar, and a pH 5, in a brine solution with 1 % sodium chloride. It was found that the rate of corrosion has a positive correlation with temperature, where the inhibited corrosion rate generally increased with increasing temperature [145].

El-Nabey & Khamis [146] conducted research on mild steel, with the chemical composition of 0.27 C, 0.70 Mn, 0.05 S, 0.50 P and 0.35 Si (wt.%), to evaluate inhibitor performance (benzaldehyde thiosemicarbazone) at various concentration over temperatures ranging from 25 to 600 ^{o}C via impedance spectroscopy. At a low inhibitor concentration (<5 x 10^{-4} M), the protection efficiency decreases with temperature increase (Figure 2-35). Increasing temperature leads to desorption of adsorbed inhibitor molecules from the surface. From this plot we can see that the maximum inhibitor concentration for best efficiency is 5 x 10^{-4} M. Increasing the concentration beyond this value results in low efficiency, this means that constant absorption of the compact layer will not occur at higher temperatures [146].

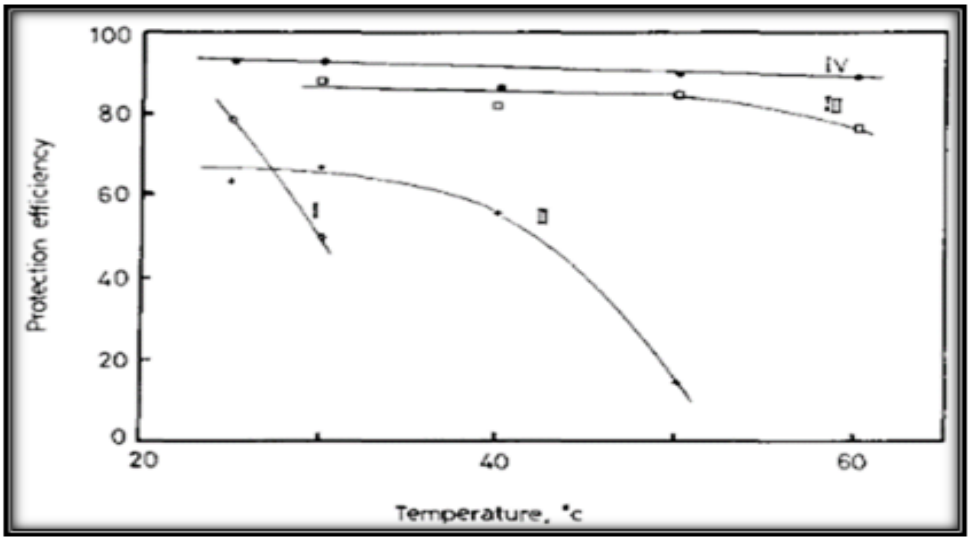

Figure 2-35 Variation in protection efficiency with temperature for inhibitor concentration: curve I (1 x 10^{-4} M), curve II (3 x 10^{-4} M), curve III (5 x 10^{-4} M), curve IV (1 x 10^{-3} M) [146]

2.14.3 Effect of Velocity

The effect of flow is an important parameter, particularly in an oil and gas production. A higher flow rate is associated with a turbulent flow of oil and gas

inside the pipeline. When the flow changes from laminar to turbulent, it may result in an increase of corrosion activity due to more active mass transfer process between the steel surface and the brine solution as a corrosion media [147]. More detrimental conditions appear if a protective layer is not formed or mechanically removed due to the high flow velocity. At this condition, the corrosion rate will significantly rise and sometimes, localised corrosion will occur [50].

Sorkhabi and Asghabi [148] investigated the inhibition effect of L-methionine (I-MTI) as an environmentally friendly organic inhibitor under no-flow and flowing conditions at different rotation speeds using ST 52-3 steel in a 1 M H_2SO_4 solution (Figure 2-36).

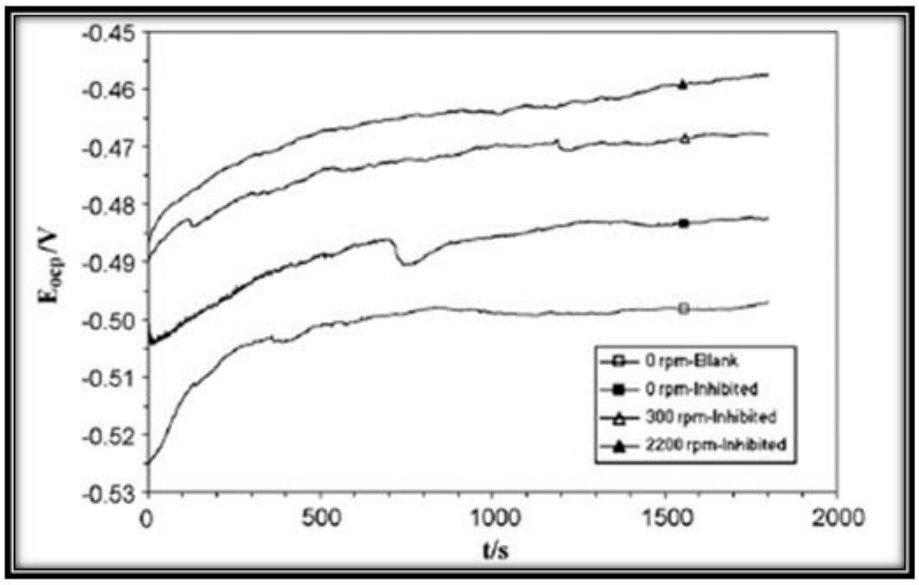

Figure 2-36 Potential (OCP) with time in uninhibited and inhibited solution [148]

Figure 2-36 shows that, in a no-flow condition, the open circuit potential (OCP) is stable at -0.51 V and becomes more positive when the flow rate increases in an inhibited condition (eg 300 and 2200 rpm). From the result, it can be seen that at low rotation speeds (0rpm) the inhibition efficiency is reasonably constant, while at 2200 rpm, the inhibitor efficiency increases. The chemical mechanism of the inhibition is shown in the equation below:

$$Inh_{(aq)} + xH_2O_{(ads)} \leftrightarrow Inh_{(ads)} + xH_2O_{(aq)} \quad \textbf{(2-27)}$$

The inhibitor combines with Fe^{2+} on the steel surface to form metal inhibitor complexes:

$$Fe \rightarrow Fe^{2+} + 2e \quad \textbf{(2-28)}$$

$$Fe^{2+} + Inh_{(ads)} \rightarrow [Fe\text{-}Inh]_{(ads)}^{2+} \quad \textbf{(2-29)}$$

At low concentrations, the inhibitor molecules (methionine) are insufficient to form complexes. At high concentrations of methionine, more molecules become available for complex formation and significantly improve the inhibition process. To summarize the factors affecting inhibition performance during a flowing condition, these conclusions were made [148]:

- At higher velocity, mass transport of inhibitor molecules is increased causing more inhibitor to be present at the metal surface and the inhibition performance will increase.
- Mass transport of metal ions (Fe^{2+}) increases from electrode surface to the bulk of solution and the amount of $[Fe\text{-}Inh]^{2+}$ decreases, hence the inhibition performance decreases.
- High flow velocity produces high shear stress and this removes the inhibitor layer.

2.14.4 Effect of Inhibitor Concentration

Inhibitor concentration is a crucial factor that influences the performance of inhibitor when applied in a corrosive environment. The optimum concentration of inhibitor in a corrosive environment needs to be maintained from the outset and during operation so that any depletion of inhibitor concentration will not cause detrimental corrosion activity such as localised corrosion attack [144].

A study of the effect of inhibitor concentration by Nesic [149] found that insufficient inhibitor concentration can initiate the corrosion reaction and create an unsafe condition compared to the uninhibited environment. A high concentration of inhibitor will not always inhibit the corrosion rate. In certain conditions, when the concentration is too high, the inhibitor may not work properly

due to the abundance in molecules inside the solution. Sometimes precipitation (coagulation) will reduce the inhibitor performance too. Therefore, the optimum concentration of an inhibitor that provides the highest efficiency is required.

Efird [150] has studied the effects of increasing the concentration of corrosion inhibitors with constant wall shear stress (Figure 2-37). He found that, corrosion rate decreases when more inhibitor molecules are in the corrosion medium.

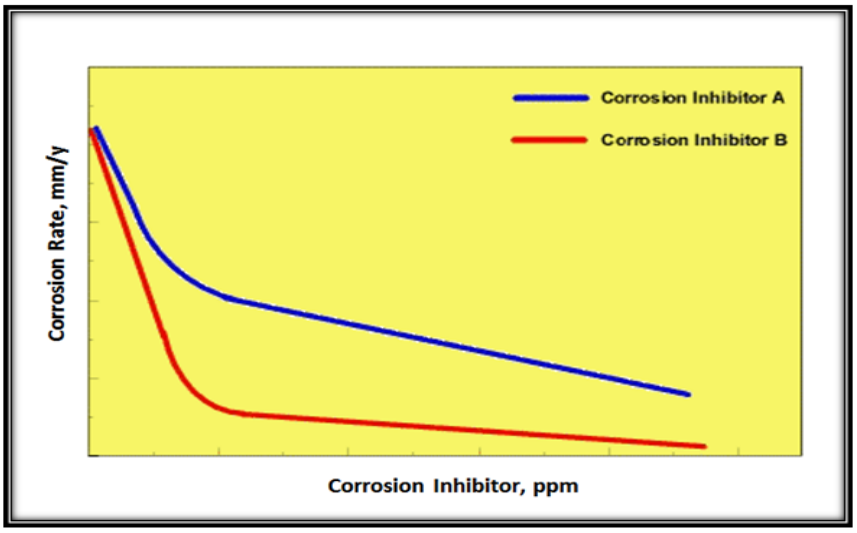

Figure 2-37 Effect of corrosion inhibitor concentration on corrosion rate [150]

2.15 Methods of Evaluation of Corrosion Inhibition

The performance of inhibitors to inhibit the corrosion process can be evaluated with several analytical methods that have good validity and reproducibility. Each technique has advantage and disadvantages so that the use of multiple methods for evaluating inhibitor performance is the best way to get a reliable results [46].

Mass loss measurements remain the most commonly used methods of evaluation of the corrosion environment [47,151–153]. Other methods include polarisation measurements and AC impedance techniques [15,58,154–156]. Mass loss is a conventional method which compares the sample weight before and after the corrosion process. It can be applied to all range of pH values (0-14). However, this method has low accuracy and is only suitable for general corrosion. Corrosion

rates calculated from mass losses can be misleading when corrosion is highly localised, such as pitting or crevice corrosion.

Polarisation measurements and AC impedance techniques are leadings method used for evaluation corrosion inhibition due to shorter experimental durations compared to mass loss. These techniques have given a significant contribution to the electrochemical field, particularly for corrosion assessment. However, to interpret the data, care is highly needed due to the complexity of the corrosion processes [157]. Further as data tends to be acquired quickly, there is a need to ensure data gathered over short durations (minutes and hours) are representative of steady state behaviour and representative of long term duration (months and years) and changes in environment over time.

2.15.1 Potentiodynamic Polarisation Measurements

Potentiodynamic polarisation techniques are based on electrochemical evaluation of the rate of corrosion reactions that spontaneously occur in the electrode or solution interface. The corrosion process starts when a steel is immersed in a solution. The electrochemical reaction takes place by transfer of electrons between steel surfaces via reduction and oxidation process mechanisms (redox). The corrosion reaction occurs at the anodic sites while reduction occurs at cathodic sites. Cathodic currents are considered to be negative (protective) and the anodic currents are normally positive (corroding).

Potentiodynamic polarisation techniques are fundamental techniques, and there are several approaches to evaluate the data based on polarisation measurements for determining corrosion rates such as Tafel-slope extrapolation (Tafel plots) [158,159] and linear polarisation resistance [160].

2.15.2 Tafel Plots

Tafel polarisation curves for a corrosion system can be constructed knowing charge transfer polarisation. The plots are additively composed from a partial

anodic curve of metal oxidation and partial cathodic curve of reduction of an oxidant from solution. In practice, a Tafel plot can be produced by polarising the steel surface with (for example) 0.3 volts in the anodic (positive direction) and cathodic (negative direction) from the open circuit potential (OCP) as shown in Figure 2-38.

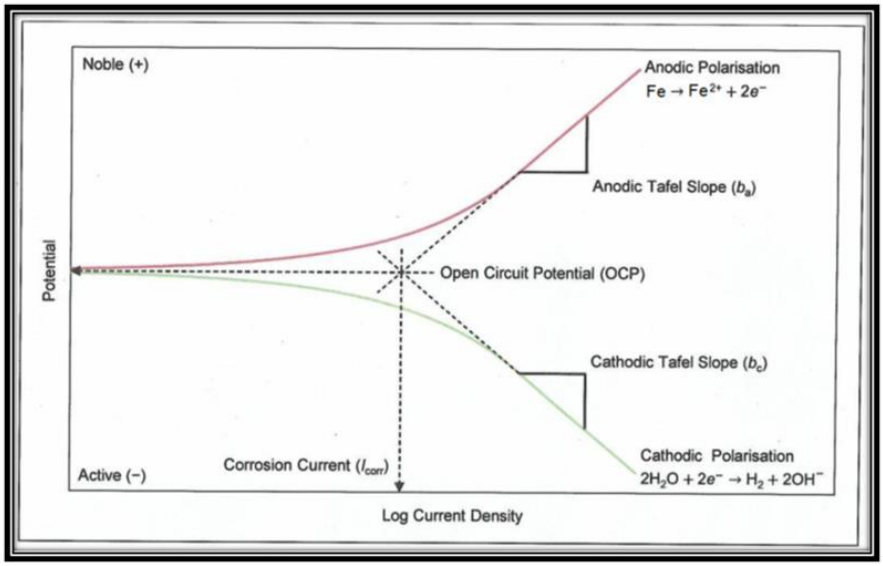

Figure 2-38 A Tafel plot extrapolation diagram of steel [161]

A potential scan rate could be 0.1 – 1.0 mV s^{-1}. The resulting current is plotted on a logarithmic scale. The corrosion current, i_{corr} is obtained from a Tafel plot by extrapolating the linear portion of the curve to E_{corr}.

According to the Tafel equation:

$$\eta = \beta \log \frac{i}{i_{corr}} \quad \textbf{(2-30)}$$

where η is the overvoltage, that is the difference between the potential of the sample and its corrosion potential, β is the Tafel constant, i is the current corresponding to the overvoltage and i_{corr} is the corrosion current, in μA.

$$\eta = \beta(\log i - \log i_{corr}) \quad \textbf{(2-31)}$$

When it is plotted against log i, this equation should give a straight line with a slope of β.

When η=0 (at E_{corr}) then,

$$\log \frac{i}{i_{corr}} = 0 \quad \text{or} \quad \frac{i}{i_{corr}} = 1 \quad \text{or} \quad I = i_{corr} \qquad \textbf{(2-32)}$$

From the Tafel plot diagram, ba and bc can be calculated for both the anodic and cathodic parts of the Tafel and are expressed in mV/decade. The information on βa and βc values are essential when an inhibitor was applied to the corrosive media and to know whether the inhibitor used is an anodic or cathodic inhibitor.

2.15.3 Linear Polarisation Resistance

Linear Polarization Resistance (LPR) is a direct electrochemical technique to monitor the corrosion process in a corrosive environment. This technique is fast, needs a short response time and could produce accurate data [160]. Another advantage from this method is that it is non-destructive, so therefore, the samples used in LPR experiments are reusable for future experiments.

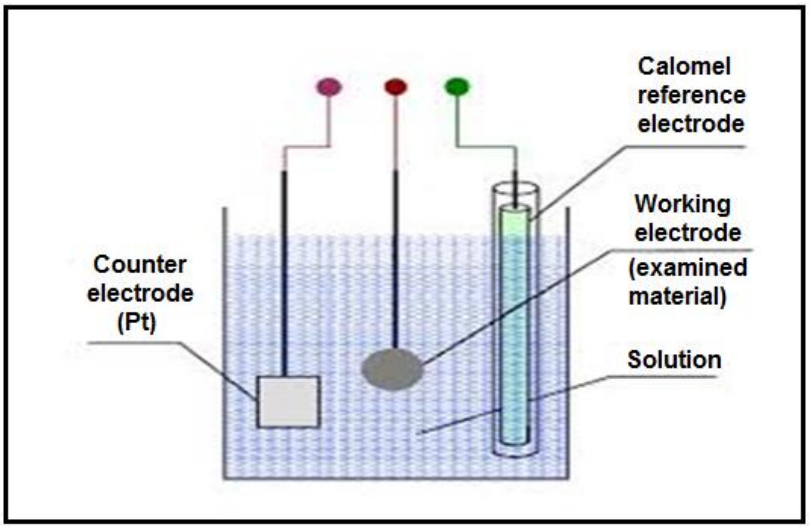

Figure 2-39 Linear Polarisation Resistance corrosion cell [162]

To produce LPR data, a three electrode set-up is used on the corrosion system including a reference electrode (a calomel electrode Ag/AgCl), counter electrode (platinum) and a steel surface as the working electrode (Figure 2-39).

A small potential difference (typically in the order of ±10mV) is induced on the electrode, and its response in terms of current is measured and plotted against this potential difference (Figure 2-40).

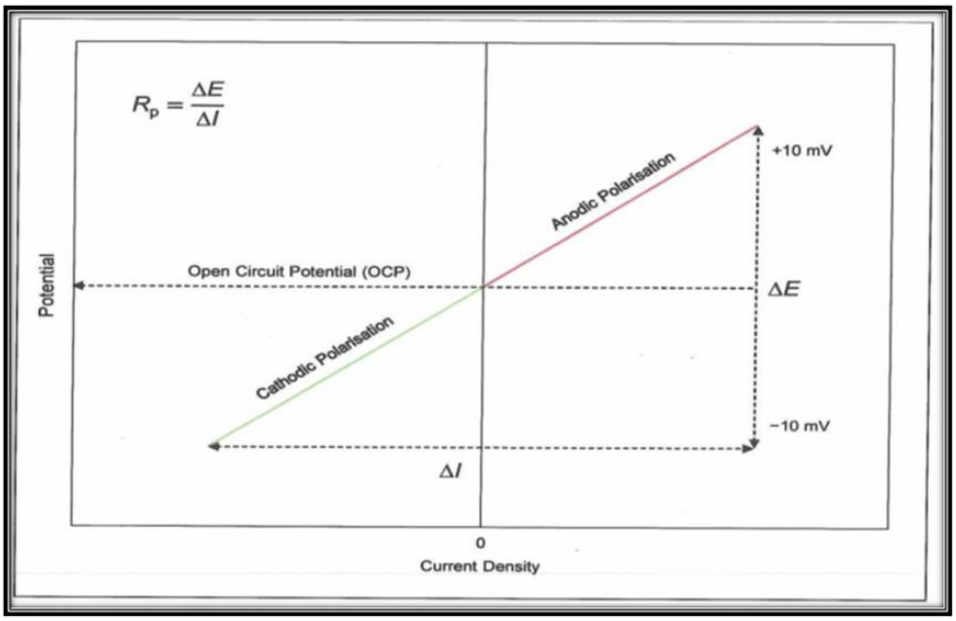

Figure 2-40 Linear Polarisation Resistance plot [163]

The relationship between R_p and the corrosion rate is inversely proportional. When the working electrode corrodes faster, metal ions pass easily into the brine solution. A tiny difference in potential is induced between the electrodes, this produces a response in the form of a high current, and therefore, a lower LPR value is associated with a high current density [4]. To measure the LPR value, the data between potential with current density is plotted. The gradient from the linear regression equation is considered as the LPR value and it is used to calculate the rate of corrosion using equation 2-34.

From Figure 2-40, the potential of the working electrode changes and a current flows between the working and counter electrodes. The R_p value of a material is

the gradient of the potential and the current density (ΔE/Δi) curve at a free corrosion potential. This results in the polarisation resistance R_p, which can be related to the corrosion current using equation 2-34:

$$R_p = \frac{\Delta E}{\Delta i} = \frac{B}{i_{Corr}} \quad \textbf{(2-33)}$$

Where R_p : polarisation resistance (Ωcm^2)

I_{corr} : corrosion current density (A/cm^2)

B : Stern-Geary constant that can be related to the anodic (b_a) and cathodic (b_c) Tafel slopes with equation 2-35:

$$B = \frac{b_a b_c}{2.3\,(b_a b_c)} \quad \textbf{(2-34)}$$

The anodic and cathodic Tafel constants can be measured by performing a full polarisation scan as shown below (Figure 2.41).

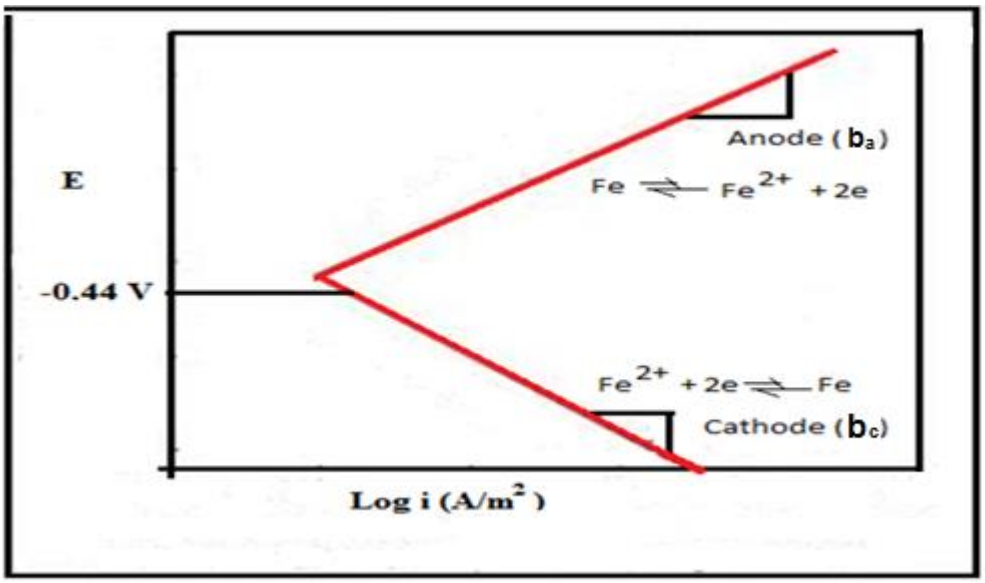

Figure 2-41 Activation polarization diagram for steel (Fe) reaction [5]

The Stern-Geary constant is reliant on a given corrosion system however, it can also be directly investigated separately via a different experiment. The corrosion rate (metal dissolution) can be calculated from Faraday's law based on the kinetic energy of the cathodic and anodic reactions (equation 2-36).

$$\mathrm{CR} = \frac{M}{n}\rho P(i_{corr}) \quad \textbf{(2-35)}$$

Where:

CR = Corrosion rate of metal (metal dissolution)

i_{corr} = current density

ρ = density of the element (material) being oxidized

M = metal atomic weight

P = Faraday constant (96,485 $Cmol^{-1}$)

(M/n) = the equivalent weight of the element (material) being oxidized,

2.16 Electrochemical Impedance Spectroscopy Measurements (EIS)

EIS is used to complement the Linear Polarisation Resistance (LPR) measurements and confirm the self-corrosion rate values. EIS uses similar principles to LPR, however, this technique is better used for validating the LPR results, and vice versa [164].

Similar to LPR measurements, analysis using EIS measurement is carried out using the open circuit potential (OCP) of +/- 10mV and frequencies ranging from 20 kHz to 0.05 Hz. The corresponding currents and frequencies are recorded and used to calculate the impedance of the corrosion processes.

The Nyquist diagram describes a series of data, and every point represents the magnitude and direction of the impedance vector at a certain frequency. The x-axis is the real impedance (Z') or the resistive part while, the y-axis is the imaginary impedance (Z") or the capacitive part.

The resulting vector for impedance is

$$Z = Z' + jZ'' \quad \textbf{(2-36)}$$

Both real and imaginary impedances measured at different frequencies via the Nyquist plot/diagram (Figure 2-42A). Impedance measurement is represented by

a large frequency range as shown in Figure 2-42A, area A is a region in which the frequency (MHz-KHz) is at its highest while, area B is a region of low frequency (Hz-µHz).

An example of the Nyquist plot with its equivalent circuit is shown in Figure 2-42 A and B. After describing the plot, an extrapolation of the right side of the semicircle is undertaken to find the horizontal axis. The diameter of the semicircle extrapolated in the Nyquist plot represents the charge transfer resistance (R_t) and this value is equivalent to the polarisation resistance (R_p) value from LPR measurements. The smaller the diameter of the semicircle, the lower the resistance, R_p, and hence, the higher the corrosion rate.

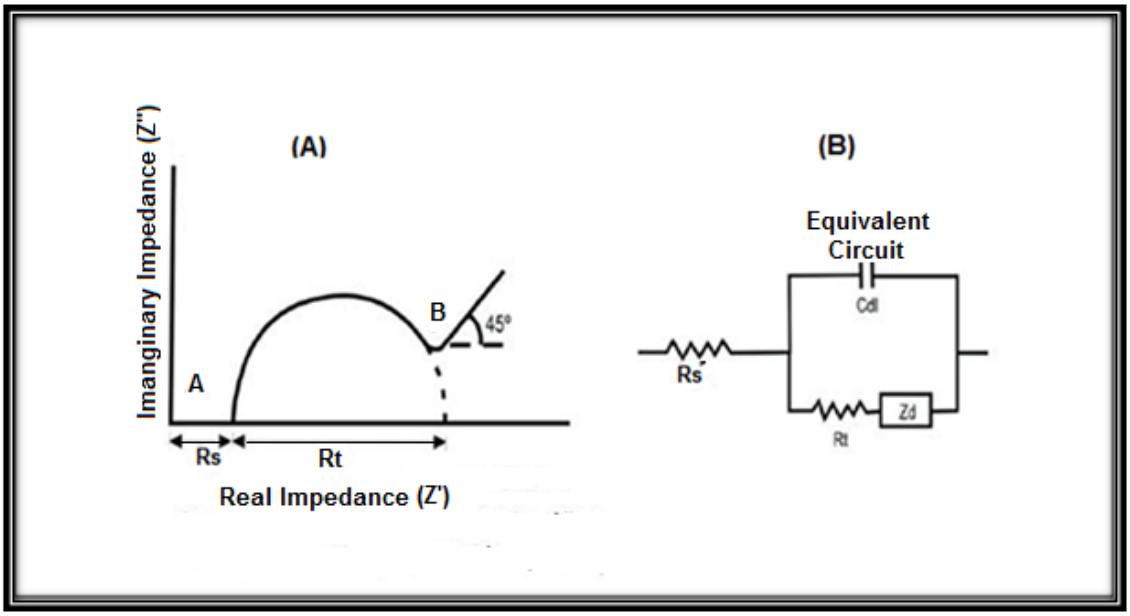

Figure 2-42 Nyquist plot and its equivalent circuit [165]

EIS, or Nyquist plots, are used to investigate the corrosion mechanism and to identify the influence of surface films that result from either the corrosion process or the action of the inhibitor. The intensity of the R_t (or R_p) value can then be found by subtracting the value of the R_s that was acquired from the high-frequency response.

EIS analysis can detect the formation of a protective film on the steel surface. The presence of a protective film, like an oxide in CO_2 corrosion can be identified from the shape of the Nyquist plot since it displays a different response. This

corresponds to the superposition of two curves or semicircles, where, one is associated with corrosion of the steel and another correlates with the protective film layer (Figure 2-43). The smaller semicircle is the surface layer, and the larger curve is the corroding metal, although this is not always the case.

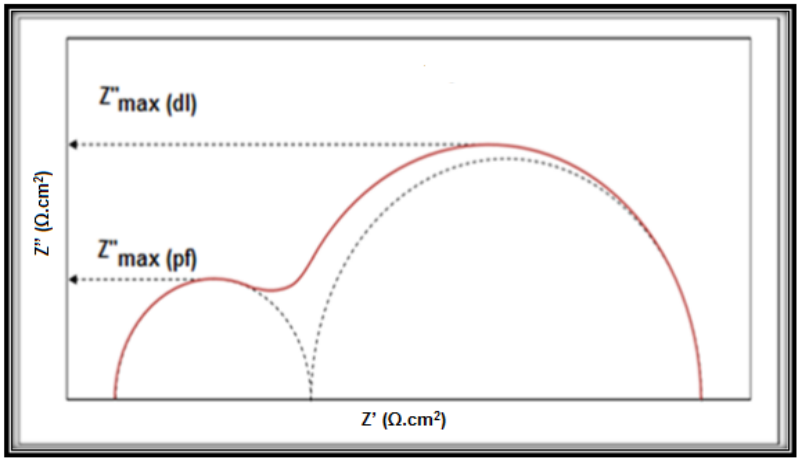

Figure 2-43 Typical Nyquist plot when a protective film exists [126]

The equivalent circuit for a protective film is more complex than a circuit without a film (Figure 2-42B). Figure 2-44 shows components R_{pl} and C_{pl} represent the resistive and capacitive behaviours of the surface layer or film.

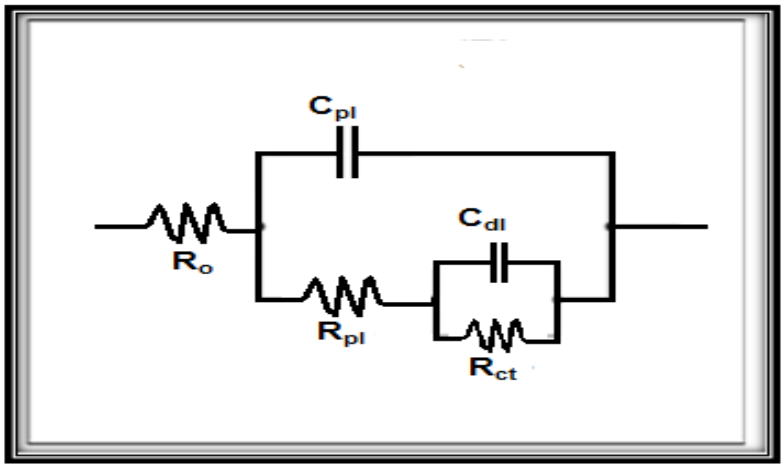

Figure 2-44 Nyquist diagram and its equivalent circuit, showing the effect of a surface layer or coating [126]

2.17 Adsorption Isotherm Studies

The amount of inhibitor adsorbed on the metal surface can be calculated by the inhibitor efficiency. The adsorption of the inhibitor is determined by the residual charge on the metal surface and also the structure and chemical properties of the inhibitor itself.

Adsorption is commonly described through isotherms, that is, the amount of adsorbate (inhibitor) on the adsorbent (steel) as a function of its liquid concentration at constant temperature. Adsorption isotherm studies are a way of supporting and understanding the inhibitor adsorption mechanism to protect the material from a corrosion. Detailed information regarding the interaction between inhibitor and the X65 metal weldment can explained from such a study.

A CORRTREAT 10-569 inhibitor was used in earlier work [14–16] and is also used in this research, Nofrizal. A different weldment has been used in this so as to later allow comparison of results. To examine the adsorption behaviour of this CORRTREAT inhibitor 10-569 on the weldments saturated with CO_2 under no-flow and flowing condition, an adsorption isotherm was plotted.

Data from linear polarization resistance (LPR) was calculated by using the equation below to calculate the slope of isotherm adsorption [5]:

$$\frac{C}{\theta} = \frac{1}{K_{ads}} + C \qquad \textbf{(2-37)}$$

$$\Delta G^{o}_{ads} = - RT \ln C_{water} K_{ads} \qquad \textbf{(2-38)}$$

Where, C is the concentration of inhibitor, θ is the surface coverage determined by IE/100, K_{ads} is the adsorption equilibrium constant and ΔG^{o}_{ads} is the standard Gibbs free energy, R is molar gas constant, T is the temperature, IE is the inhibitor efficiency and C_{water} is the concentration of water in 1000 g/L.

The fraction of the surface covered (θ) is found by the ratio of IE/100 as a function of the logarithm of the concentration (log C) of CORRTREAT 10-569. It has to be plotted and fitted to several adsorption isotherms.

The value of Gibbs free energy (ΔG^{o}_{ads}) can identify whether the inhibitor works on the metal surface with a physical or chemical approach. When ΔG^{o}_{ads} values are around −20 kJ mol^{-1}, the interaction between metal surface and the molecule inhibitor is likely to be physisorption. This process is associated with electrostatic interactions between the charged centres of inhibitors and charged metal surfaces [46,166]. Values more negative than -40 kJ mol^{-1} are considered as chemisorption, as this involves charge sharing or transfers from the inhibitor molecules to the steel surface to form a coordinate type of bond [47,166].

2.18 Chapter Summary

This chapter has reviewed challenges of using high strength low alloy (HSLA) steels for pipelines, valves, and joining systems in the oil and gas industry in environments where 'sweet' corrosion can occur. The microstructural characteristics from welding high strength pipeline materials are explored and the current understanding of the response of HLSA material in 'sweet corrosion' and key influencing factors have been set out including the challenges of corrosion in pipelines. Techniques to monitor corrosion rates were considered including the submerged jet technique for assessing the effect of turbulent flow. In addition, the information regarding oilfield inhibitors applied at various velocities and wall shear stresses used from previous studies were highlighted.

The next chapter outlines the experimental work undertaken in this work to evaluate the submerged jet impingement technique, the benefits and drawbacks when applied to corrosion behaviour of HSLA weldments across a range of fluid velocities and changes in environmental conditions.

3 METHODOLOGY

This chapter will explain the preparation and construction of a submerged jet impingement (SJI) in order to study the behaviour of a HSLA steel weldment in a range of sweet corrosion environments. This includes the effect of flow, of dissolved oxygen and of a corrosion inhibitor commonly used in the oil and gas fields. The electrolyte under which the experiments were performed is a sea salt solution saturated with carbon dioxide.

Tests using a flow loop and electrochemical measurement techniques (LPR, galvanic, and EIS) carried out assess the corrosion performance of X65 carbon steel weldment are described. Finally the methods used for surface characterisation of the corroded surface are also set out.

3.1 Preparation and construction of a submerged jet impingement target

A submerged jet impingement (SJI) target was prepared from a sample of the parent metal X65 pipeline steel using a multi-pass welding process (submerged-arc welding / SAW). The chemical composition of the parent metal (PM) X65 and the weld metal (WM) are shown in Table 3-1.

Table 3-1 The X65 pipeline steel composition, PM (I) and WM (II) (Wt. %)

	C	Si	Mn	P	S	Cr	Mo	Ni	Al	Cu	Nb	Ti	N
I	0.07	0.3	1.51	0.01	<0.005	0.02	0.01	0.39	0.037	0.26	0.02	<0.01	0.005
II	0.07	0.3	1.59	0.01	0.007	0.03	0.11	0.27	<0.01	0.1	<0.01	<0.01	0.005

A weld of 210 x 60 mm^2 area and 30 mm thickness was produced (Figure 3-1A). The weld sample was polished using different grades of abrasive paper from 240 up to 1200 grit, rinsed with deionized water, and flushed with iso-propanol to remove excess grease then dried before being etched in 10 % nital (Figure 3-1B). The macrostructure of X65 weld metal is shown in Figure 3-1C showing the parent metal (PM), weld metal (WM) and heat affected zone (HAZ).

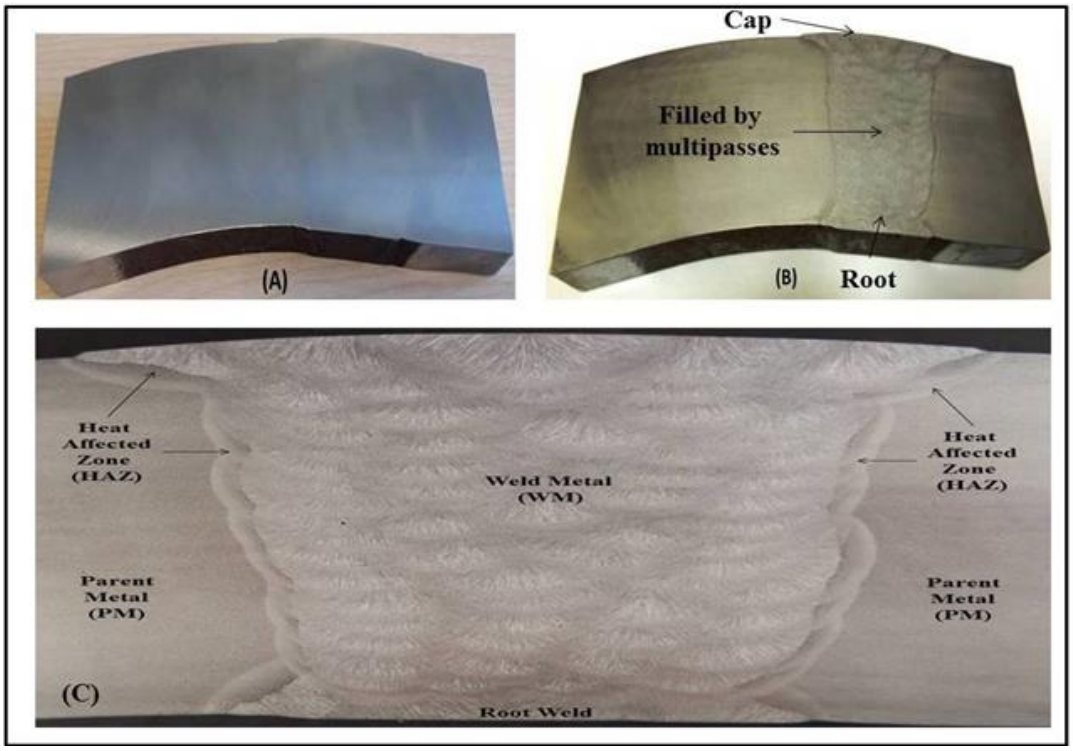

Figure 3-1 (A) Plate after welding, plate etched in 10 % nital (B) and (C) the PM, the WM and the HAZ macrostructures

The SJI target for this study was made up of carefully selected fragments of the parent metal, the heat affected zone and the weld metal using a target design from a previous study by Adegbite [13] (Figure 3-2).

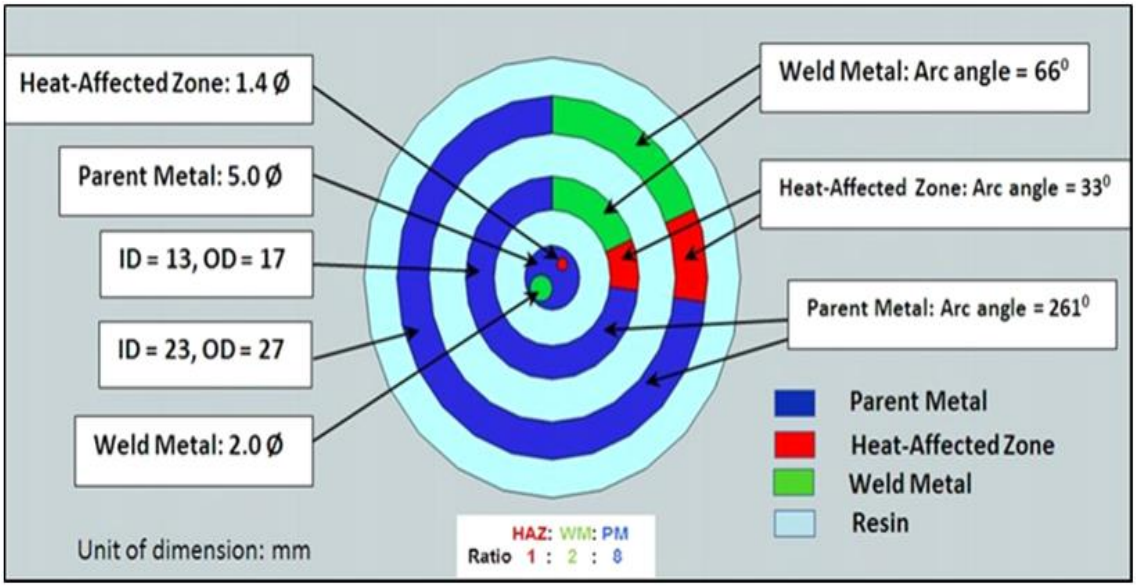

Figure 3-2 Design of the submerged jet impingement target [13]

The X65 carbon steel pipeline weldment was cut by using an electrical discharge machining (EDM) to create surface areas of the WM:HAZ:PM in the ratio of 2:1:8 respectively (Figure 3-2 and Table 3-2). The cut pieces of each electrode are shown in Figure 3-3.

Figure 3-3 The cut pieces of metal from the weldment after electrical discharge machining (EDM)

Table 3-2 Area of each electrode in the submerged jet impingement target

	Weld specimens (cm^2)		
	PM	WM	HAZ
Outer	1.1383	0.2878	0.1439
Inner	0.6829	0.1727	0.0864
Centre	0.1492	0.0314	0.0154

All nine pieces of cut metal (3 PM, 3 HAZ and 3 WM) were each attached to wires to create electrodes. Each piece was electrically isolated from the neighbouring section using polytetrafluoroethylene (PTFE) insulation before joining and assembling together. Rings of increasing diameter were constructed with 3 electrodes: PM, HAZ and WM. The rings were concentrically assembled and the target filled with insulating resin as shown in Figure 3-4. Finally, a long cable with the insulated wires was used to connect the electrodes. The sequence of the preparation steps in constructing the SJI target are shown in Figure 3-5.

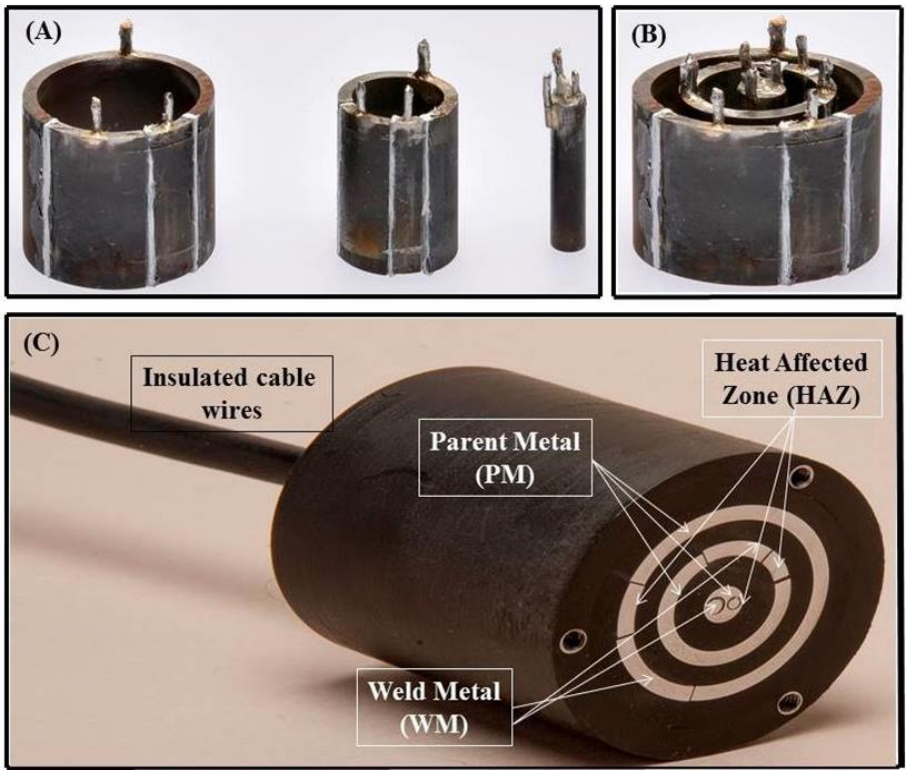

Figure 3-4 Isolated electrode rings (A), ring positioning (B) and (C) SJI target

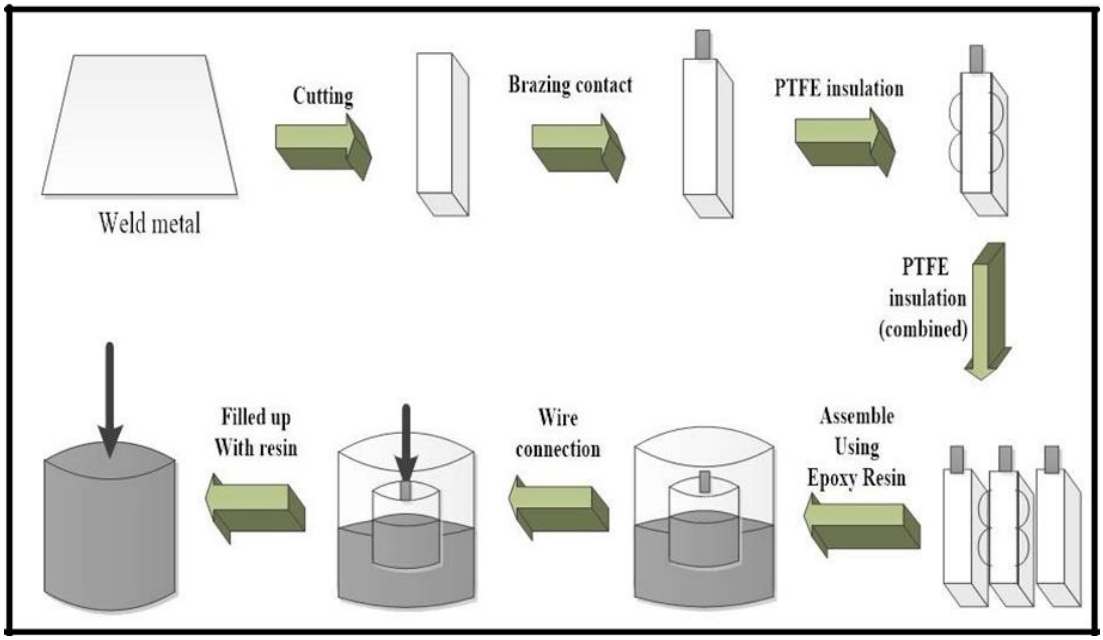

Figure 3-5 Sketch of SJI target preparation

3.2 Experimental Plan

Laboratory experiments were conducted to examine the corrosion behaviour of the weldment using the SJI target. In order to do that, electrochemical measurements were performed in no-flow and flowing brine in uninhibited and inhibited conditions. The corrosion environment used is brine solution prepared from 33.33 g/l of Tropic Marin sea salt with a chemical composition as Table 3-3.

Table 3-3 The elemental composition in weight % of Tropic Marin sea salt

Compounds	%
Calcium (Ca)	1.1
Chlorine (Cl)	49.0
Magnesium (Mg)	3.5
Potassium (K)	1.1
Sodium (Na)	27
Sulphur (S)	2.2

CORRTREAT 10-569 supplied by Clariant Oil Services, UK is the inhibitor used in this study. The main composition is ethanadiol, 2-butoxy ethanol and a fatty acid amine in a water/glycol solvent. A range of concentrations (0-40 ppm) were used to determine the optimum concentration to give maximum inhibition efficiency. Although the inhibitor has now been superceeded, it is used as an example of a typical oilfield inhibitor and to compare results with previous studies.

To prepare the inhibitor in parts-per-million (ppm) with a concentration, for example of 30 ppm, the quantity of inhibitor needed to produce a concentration of 30 ppm is 30×10^{-6} or 0.03 ml per litre. So, for a 4 litre solution of brine in the corrosion cell, 0.12 ml of inhibitor is needed to produce a 30 ppm brine solution.

3.2.1 Equipment within the corrosion cell and SJI flow loop

To undertake electrochemical analysis of a corroding weldment, a range of equipment was needed as outlined in Table 3-4. This is used to measure the galvanic and self-corrosion rate for each electrode on the SJI target.

Table 3-4 A list of equipment used for the SJI flow loop

Equipment used
• Centrifugal pump • Peristaltic (tubing pump) • A Zero-Resistance Ammeter, Galvo-Gill 12 connected to data logging PC (from ACM Instruments. Grange-over-Sand-UK • Computer-controlled potentiostat (from ACM Instruments. Grange-over-Sands-UK • A 1.5 corrosion glass cell with nylon lid • Counter (secondary) platinum electrode. The platinum electrode paddle type with gauze wire 0.12mm, 250 mesh per cm^2 and 2.5 grams in weight and total area of 8.4 cm^2 • Calibrated saturated calomel (SCE) as a reference electrode, with connection into the cell through a lugging capillary probe • Thermometer • Gas bubbler (3 units) • Micro pipettes • Spirit (bubble) level • Three equal lengths of 5 mm stainless steel rods • Gas flow meter • Water container (cooling system)

3.2.2 Submerged Jet Impingent Flow Loop

The experimental setup is schematically shown in Figure 3-6. A flow loop was connected with electrochemical tools to monitor the corrosion process. It is equipped with two gas lines to flow oxygen-free nitrogen and CO_2 gases into the brine solution contained within a water cooled glass cell (No.5). The SJI target is placed inside the glass cell beneath the jet which is part of the pumped flow loop. Two electrodes; namely a calomel reference electrode and a platinum counter electrode, are connected to the system. A thermometer and gas bubbler is also added to the glass cell (Figure 3-6).

Before measuring the galvanic and self-corrosion currents, the SJI target was ground using different grades of abrasive paper (240 up to 1200 grit), rinsed with deionized water, flushed with iso-propanol then dried. The target was placed

directly beneath the jet nozzle of 5 mm diameter inside glass cell within the flow loop (Figure 3-6). Figure 3-7 shows the experimental setup inside the glass cell.

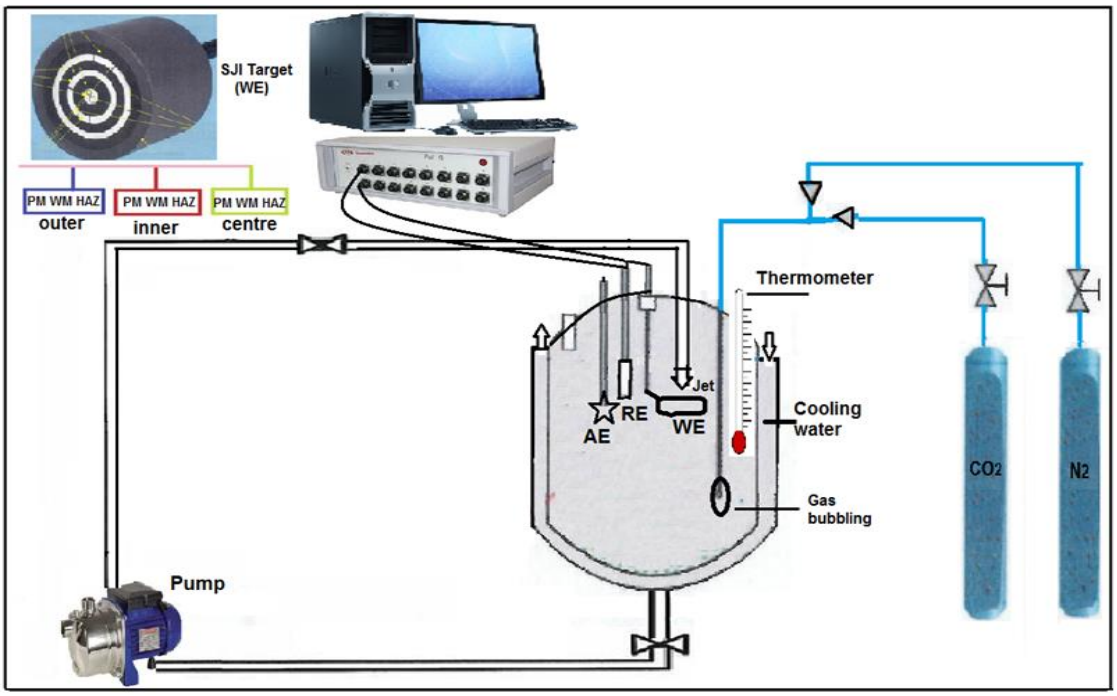

Figure 3-6 SJI experimental layout

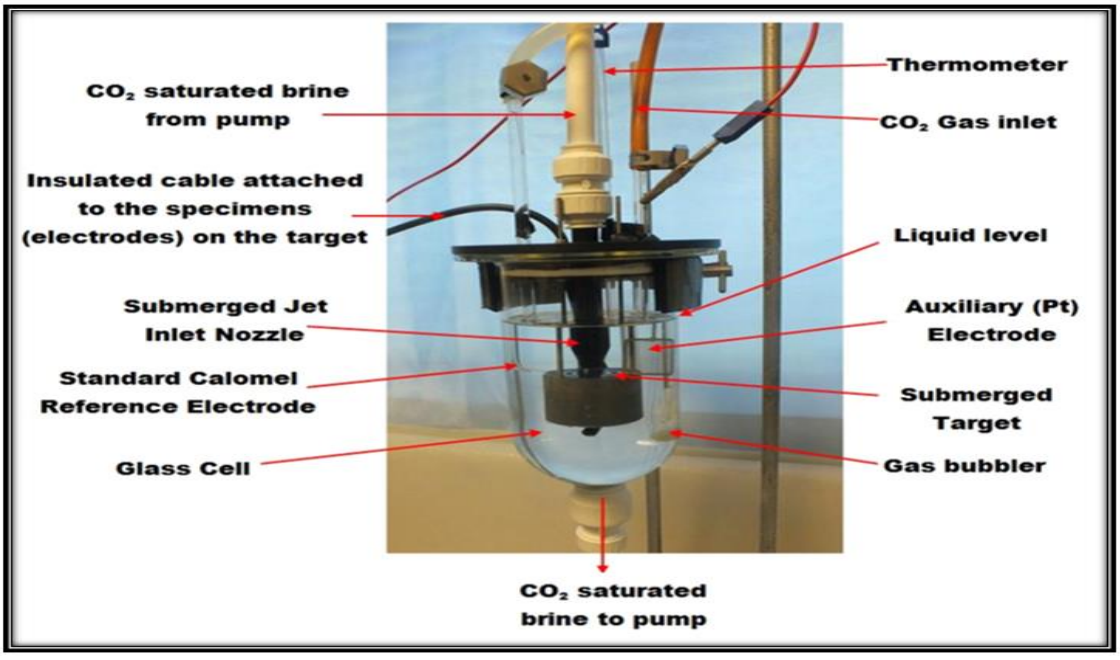

Figure 3-7 Detail of the glass cell, showing the target in the SJI setup

Nitrogen gas was bubbled into the brine solution for several hours to remove dissolved oxygen. Once a satisfactory potential had been achieved, the nitrogen feed was replaced with CO_2 which was the bubbled into the corrosion cell continuously. A CO_2 partial pressure of 1 bar was maintained, and test solution pH of 4.0 was observed in all the experiments. Temperatures of 25 ^oC in still and flowing conditions were maintained using a water cooled jacket. Flow rates were determined by monitoring the water flow at different pump settings and jet velocities 0 to 10 $m.s^{-1}$ calculated from the pipe diameter.

In this study, a typical oilfield corrosion inhibitor with different concentrations was added to the brine solution to identify the optimum concentration for reducing the corrosion rate. Later, to understand the effect of oxygen dissolved in brine solution, the air (compressed gas) was deliberately added into the glass cell at 1 bar, to imitate specific conditions of oxygen and CO_2 dissolved in seawater.

The experimental scenarios in this study are summarised in Table 3-5.

Table 3-4 Experimental environment and flow conditions

	Uninhibited brine		**Uninhibited brine**	
Velocity (ms^{-1})	**Saturated with CO_2**	**Saturated with CO_2**	**Saturated with CO_2**	**Saturated with CO_2**
0	√	√	√	√
2	√		√	
5	√	√	√	√
8	√		√	
10	√	√	√	√

3.2.3 Electrochemical Measurements

Galvanic and self-corrosion measurements were carried out to monitor the rate of corrosion of each electrode of the SJI target in coupled and uncoupled conditions. The method is described below in sections 3.2.3.1 and 3.2.3.2.

3.2.3.1 Galvanic Measurements

The SJI target was immersed in the glass cell within the flow loop and each electrode of the target in the outer, inner and centre monitored. Electrochemical

measurements were taken to measure the galvanic effect from each electrode while deaerating the sea salt water (brine solution) with nitrogen in a non-flowing condition. After 3 hours, N_2 was replaced with CO_2 and bubbled into the brine solution and galvanic measurements were recorded for 24 hours continuously.

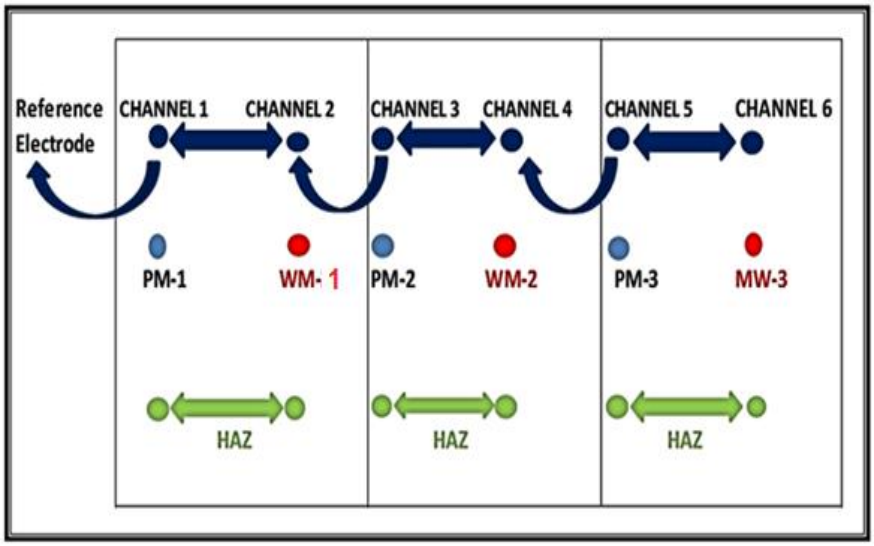

Figure 3-8 Electrical connections of the working electrodes to the ZRA

The galvanic current of each electrode in the weldment was measured using a zero resistance ammeter (ZRA), with several channels that connect the experiment to a PC which then records data every minute. For the nine electrode sections in sets of 3 in each of the 3 locations of the SJI target, the currents from the PM to the HAZ and from the WM to the HAZ were recorded on 6 ports of the ZRA (Figure 3-8). The working electrodes were coupled, with the HAZ short-circuiting all channels. The standard calomel electrode (SCE) reference electrode was connected to all channels in the similar procedure as the HAZ. Since the three working electrodes (PM, HAZ, WM) were in the short circuit condition, the total of their galvanic currents are zero. Their galvanic currents were established from the following relationship:

$$I_{PM} + I_{HAZ} + I_{WM} = 0 \quad [58] \tag{3-1}$$

$$I_{HAZ} = -I_{PM} - I_{WM} \tag{3-2}$$

The current density for each weld region was measured to calculate the corrosion rate, found by dividing current with electrode area (Table 3-2). They are converted to metal loss from the mathematical relationship shown in Equation 3-3 and Appendix C:

$$1\ \mu A/cm^2 = 0.0116\ mm/y \text{ for steel} \quad [13] \qquad \textbf{(3-3)}$$

3.2.3.2 Self-corrosion Measurements

Self-corrosion, the rate by which an electrode corrodes (by itself) in an uncoupled condition, of each weld section, in the nine electrodes of the submerged jet impingent (SJI) target, were analysed using linear polarisation resistance measurements. The LPR was determined from every section in SJI target as working electrodes while a standard calomel electrode (SCE) and platinum acted as a reference and counter electrodes, respectively. A long term sweep technique was used to scan each uncoupled electrode from 10 mV (SCE) below the open circuit potential (OCP) to 10 mV (SCE) above the OCP. The changes of current during the process were recorded every second. The resulting current plot exhibited a straight line with an inverse slope, a measure of the corrosion rate., the temperature of inside the flow loop was maintained at a range of 25 ^{o}C.

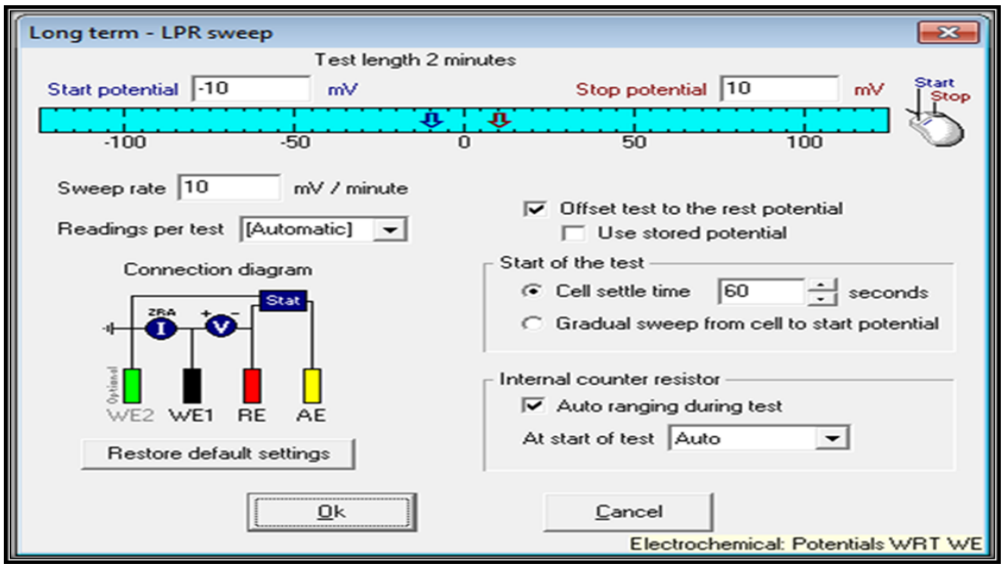

Figure 3-9 LPR Sweep parameters from Gill AC software

The LPR display is as shown in Figure 3-9. The uncoupled electrode rapidly establishes its OCP and the potential was then scanned at 10 mV min^{-1}, and the current response was recorded.

The self-corrosion rates measured by the LPR technique for the three regions on the SJI target were compiled. The resulting potential/current density plot exhibit a straight line (slope) and the gradient is inversely related to the corrosion rate. This results in the polarisation resistance R_p, which is related to the corrosion current using equation 3-4:

$$i_{corr} = B/(R_p) \quad [163] \qquad \textbf{(3-4)}$$

Where:

R_p = polarisation resistance (Ωcm^2)

i_{corr} = corrosion current density (A/cm^2)

B = the LPR constant for the material. B value of 26 was used taken from references as outlined in Appendix C with an example calculation [72,108,201,202].

3.2.3.3 Electrochemical Impedance Spectroscopy (EIS) Measurements

For more information regarding electrochemical interactions within the weldment, electrochemical impedance spectroscopy (EIS) was employed. The electrochemical cell was electrically connected to a computer controlled potentiostat and the EIS parameters were analysed using OCP with amplitude of 10mV AC potential and using a frequency range of 0.005 Hz to 20 kHz in. The solution resistance value *(R_s)* was subtracted from polarisation resistance (*R_p)* to give the *R_{ct}* (charge-transfer resistance) used to calculate the corrosion rate in mm/year [163].

$$R_{ct} = R_p - R_s \quad [163] \qquad \textbf{(3-5)}$$

EIS analysis also used to identify formation of surface films, such as iron carbonate, as a coating that develops on the surface of the electrode after the corrosion process as explained in Chapter 2.

3.2.4 Surface Characterisation

The surface analysis and chemical composition of surfaces formed after immersion were analysed by a combination of scanning electron microscopy (SEM) and energy dispersive X-ray spectroscopy (EDX). Other analytical methods such as focused ion beam (FIB), X-ray diffraction (XRD), and raman spectroscopy are used to gather information on the weldment surfaces. The visual data received from all of these analysis techniques were used to understand any film formation and relate with data from electrochemical analysis to develop a further understanding of the development of weldment corrosion.

3.2.4.1 Scanning Electron Microscopy (SEM-EDX)

SEM is a qualitative surface analysis technique used to observe surfaces of carbon steel samples exposed to a brine solution saturated with CO_2 in a range of conditions for 20 hours. Samples for SEM analysis were prepared from parts of the X65 carbon steel weldment.The weldment sample with the PM, HAZ and the WM was mounted as shown below in Figure 3-10.

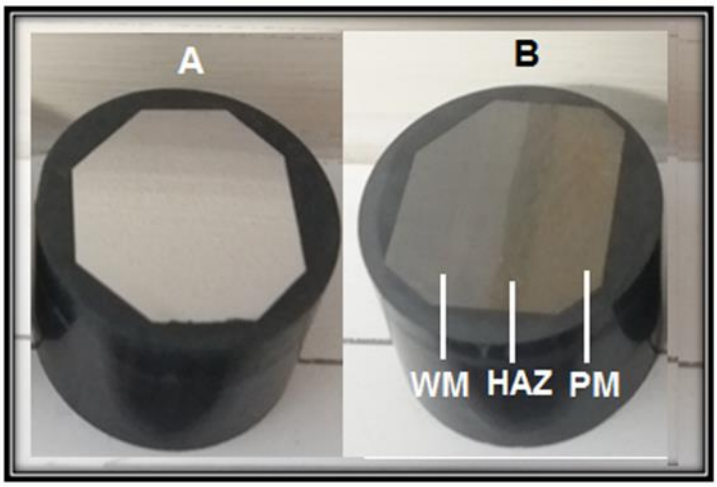

Figure 3-10 The weldment sample for surface analysis

Figure 3-11 Image of the Philips-XL30 ESEM with EDX

Before analysis, the corroded sample was rinsed and cleaned with isopropanol and deionised water, dried and stored in a desiccator prior to the SEM analysis. Analysis was performed using a Philips-XL30 SEM with energy dispersive x-ray analysis (EDX) as shown in Figure 3-11. The data obtained was analysed with Aztec software from Oxford Instruments.

3.2.4.2 Focused Ion Beam (FIB)

The focus ion beam (FIB) was employed to observe the effect of the corrosion process in the near and sub surface. FIB uses a beam of gallium ions (Ga^{+}) instead of a beam of electrons, to mill the sample surface. During the milling process, ions are removed from the specimen surface. The interaction of the ion beam with the sample results in the generation of secondary electrons which can be used for imaging. The equipment at Cranfield University was a dual beam FIB-SEM TESCAN LYRA3 using an energy beam of 5 keV (Figure 3-12). Before cutting an exposed section to see the near surface, the samples were coated with a thin layer of Pt coating (~10 – 20 nm) to protect the surface from further damage by the ion beam. During imaging by the focused ion beam materials is removed material from the surface and surrounding area.

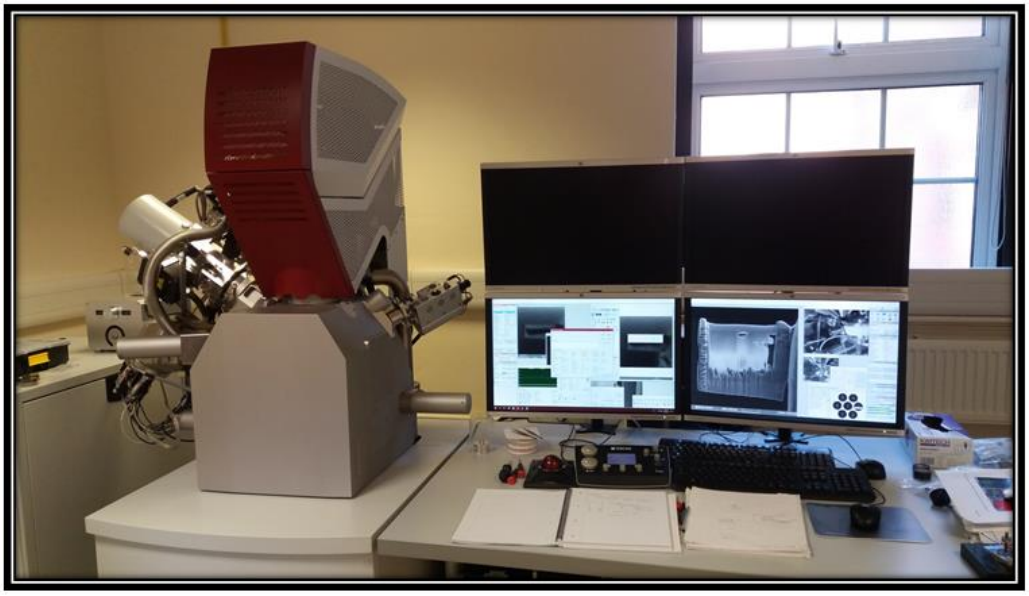

Figure 3-12 TESCAN LYRA3 Focused Ion Beam (FIB)

3.2.4.3 X-ray Diffraction Measurements

XRD is a technique that can be used to obtain structural information from crystalline structures within the sample. The data from x-ray analysis is essential to link the surface of the corrosion products to their chemical composition. This technique is powerful when analysing the crystallography corrosion products and can support data from other studies.

The main principle of the X-ray diffraction is that it uses Bragg's law to determine d spacing of crystalline structures (Equation 3-6, Figure 3-12) [167].

$$n\lambda = 2d \sin \theta \quad \textbf{(3-6)}$$

Where, the (θ) is the angle of the X-ray beam that has been diffracted depends on the distance (d) between the atomic planes in the crystal and the wavelength (λ) of X-rays [4,33,120].

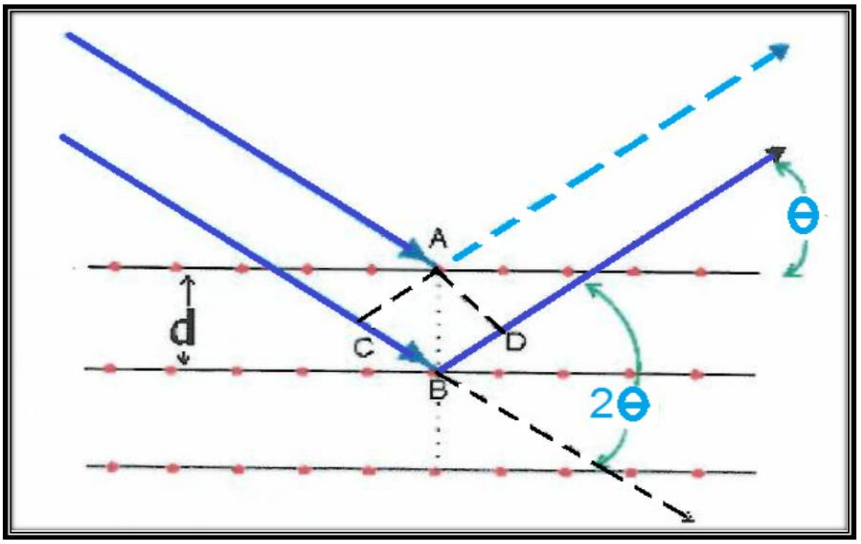

Figure 3-13 Mechanism of X-ray diffraction [167]

In this study, an XRD instrument (Siemens D5005) was used for direct XRD measurements of the corroded surface with CuKα at a wavelength of 1.5406 Å (Figure 3-14). The software analysing the operational system is Diffrac^{plus} XRD commander (version 2.4.1, 2005).

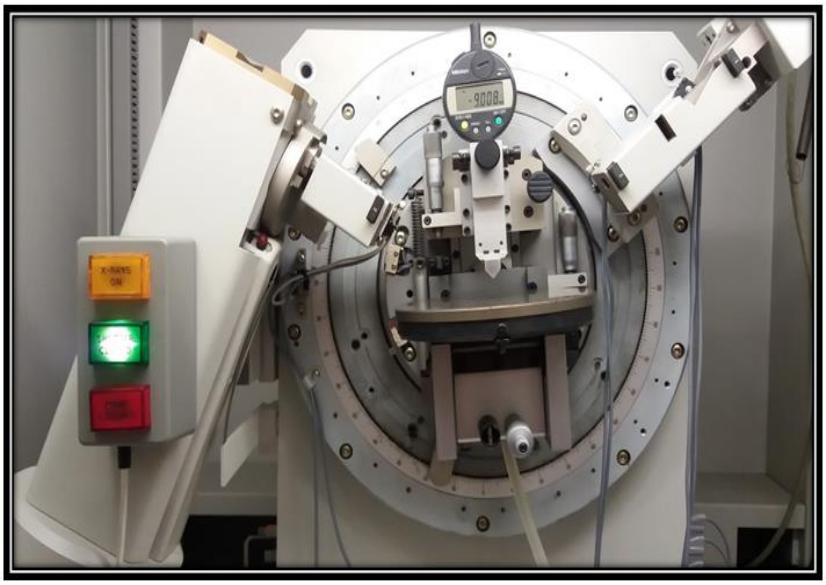

Figure 3-14 Brucker 5005 XRD system

3.2.4.4 Raman spectroscopy

Raman spectroscopy was applied to study the type of corrosion product produced after the corrosion process. The Raman band frequency is specific for every corrosion product (Table 3-5).

Table 3-5 Characteristic of Raman adsorption from iron carbonate [169,170]

Oxide	Band Frequency (cm-1)										
Magnetite (Fe_3O_4)		292 w*	309 w			535 w		666 s			
Goethite (α-FeOOH)		245 m	300 s	387 s	481 m	549 w					
Akageneite (β-FeOOH)		248 w	300 m	386 m	413 w	483 w	542 w				
Lepidocrocite (ϒ-FeOOH)		248 s	347 w	378 m			526 w				
Feroxyhyte (δ-FeOOH)								679 w, br			
Hematite (α-Fe_2O_3)	225 s	243 w	300 s		409 m	495 w	611 m	656 w			
Maghemite (ϒ-Fe_2O_3)		256 w	284 w	334 s, br	376 s, br	500 s, br	625 m, sh	654 s, br	711 s		
Ferrihydrite ($(Fe_2)_3$. 3 H_2O)						507 w, br	615 w		712 w, br		
Cementite (Fe_3C)										1340 b	1580 b

Raman analysis was conducted using a Horiba Jobin-Yvon LABRAM confocal-Raman spectrometer equipped with an Nd-YAG laser (100 mW, 532.2 nm) and diffraction gratings of 1800 grooves mm^{-1} (Figure 3-16). A corroded sample was placed on a glass slide and detection was undertaken with a Peltier-cooled, slow-scan, CCD matrix detector. Laser focusing and sample viewing were performed through an Olympus BX 40 microscope fitted with a 100x objective lens. The data was analysed with Lap-spec 5 software with scans of 0 - 2000 cm^{-1}.

Figure 3-15 Raman spectroscopy set up

3.3 Chapter Summary

The submerged jet impingement target was designed to study the effect of flow on weld corrosion using electrochemical techniques. The galvanic (coupled) and self-corrosion (un-coupled) measurements were obtained in typical flowing and non-flowing environments that would simulate oilfield conditions. Surface characterisation of the corrosion product was undertaken using analytical techniques (XRD, SEM-EDX, FIB and etc.) to better understand the characteristics of the corrosion products and residual surface.

4 CORROSION OF THE WELDMENT WITHOUT FLOW

This chapter will discuss the effects of coupled (galvanic) and uncoupled (self-corrosion) interactions between the parent metal (PM), heat affected zone (HAZ), and the weld metal (WM) in uninhibited brine solution saturated with CO_2 without flow. The PM, the HAZ and the WM have different potentials when exposed in a corrosive environment. In coupled conditions, one of the parts of the weldment or an electrode may act as an anode, and another part of the weldment can act as the cathode. Measuring the galvanic interaction between electrodes such as the PM, the WM, and the HAZ serves as a broad indicator of changes in the weldment behaviour and/or local environment and corrosion rate.

The uncoupled (self-corrosion) rate of each electrode, was measured using Linear Polarisation Resistance (LPR) directly after measuring the coupled effect between the PM, the HAZ and the WM. The total corrosion rate of the material is calculated from the sum of the coupled and uncoupled corrosion rates. EIS is measured to complement the LPR values and confirm the self-corrosion rate values. The SEM-FIB technique is used to assess the surface of each part of the weldment before and after the corrosion process.

For the purpose of clarity, the electrode in the outer ring that consists of the PM, HAZ and the WM has been selected for discussion in this chapter. The assessment of all nine electrodes from all parts of the SJI target will be considered in Chapter 8.

4.1 Galvanic Corrosion Measurements

Galvanic corrosion measurements were performed in still conditions in a brine solution deaerated with oxygen-free nitrogen. A temperature of 25-28^{o}C was maintained throughout the tests. The progress of deaeration was monitored by recording the electrode potential. During the initial deaeration with nitrogen, the galvanic couple potential between the WM and HAZ decreases gradually from -530 mV to -730 mV as shown Figure 4-1 as dissolved oxygen is removed. The

potential of the PM/HAZ reached approximately -730 mV (SCE) during this period, and this is similar to the WM/HAZ. This value indicates that the brine solution was well deaerated and there was no dissolved oxygen present [14].

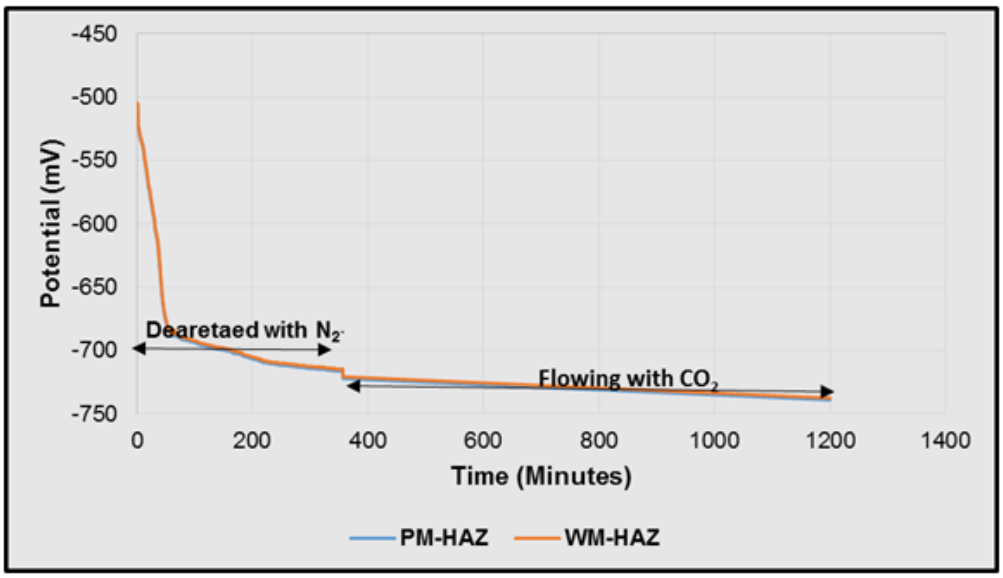

Figure 4-1 Corrosion potential of galvanically coupled PM-HAZ in the outer ring in non-flowing brine solution saturated with CO_2

When CO_2 is bubbled into the cell, there is a further small active shift in the electrode potentials to -740 mV (SCE). This is presumably as the carbon steel electrodes are attacked by the carbonic acid, and this is accompanied by an associated increase in the galvanic current. The galvanic currents and corrosion behaviour with time are given in Figure 4-2.

Figure 4-2 shows the current at each weld electrode in the outer region. The PM, the WM and the HAZ are shown in blue, red and green respectively. The activity below zero, or negative currents, as with the WM and HAZ, indicates a noble or protective condition. Activity above zero line with a positive current indicates an active condition representing anodic behaviour (or loss of metal ions).

In the coupled condition, the PM (given in blue) is the anodic constituent in the outer ring. This condition ascertains that corrosion of the PM offers sacrificial protection to other weld regions, especially for the WM in an uninhibited stagnant

or still brine solution saturated with CO_2. It is also noted that the HAZ, over time, is becoming less protective but remains cathodic.

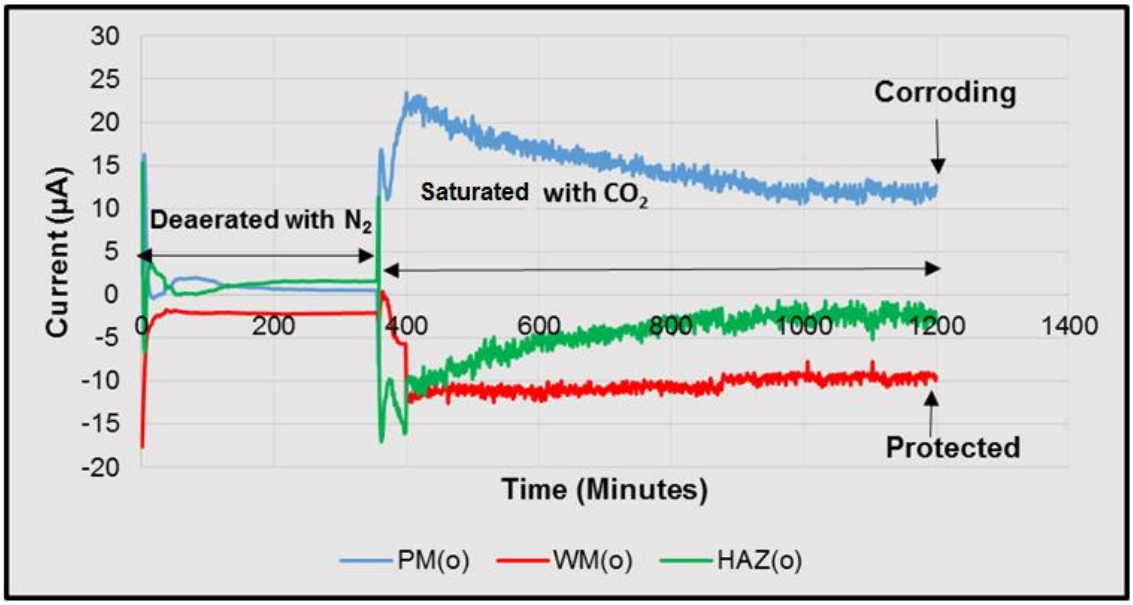

Figure 4-2 Galvanic current for outer ring exposed to deaerated brine solution saturated with CO_2 in a no-flow condition

Figure 4-2 shows the galvanic current in the brine solution with CO_2 is higher than in the deaerated stage with N_2, indicating that the weldment (X65 steel) is susceptible to galvanic corrosion in this condition. However, after CO_2 has passed for several hours, the currents gradually decrease and reach a steady state. This could be due to the initial increased activity on the surface, depending on the rate of exchange of ionic activity reaching the surface and/or formation of a film or corrosion product on the surface of the weld. Such a corrosion product could act as layer that protects the surface from further corrosion.

In Figure 4-3, the reduction in activity of the PM is notable with a gradual decrease in the value of galvanic current density toward the zero line. In previous studies, in the no-flow condition, the decrease in galvanic current density for each weld after exposure for several hours in uninhibited brine solution saturated with CO_2 is reported to be due to the presence of a carbonate film [15,16,168].

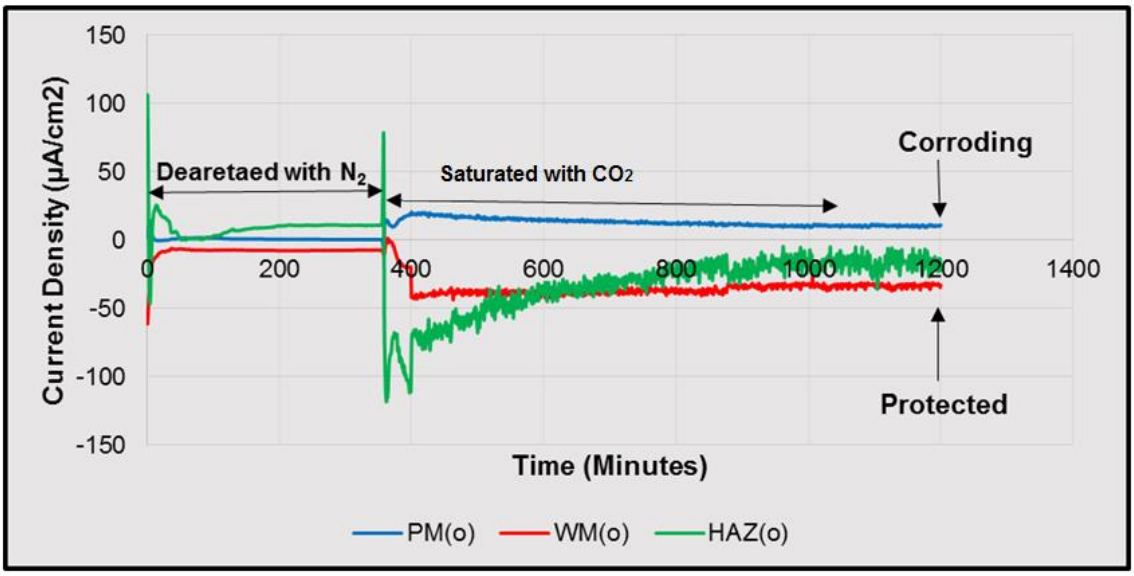

Figure 4-3 Galvanic current density in the outer ring exposed to deaerated brine solution saturated with CO_2 in the no-flow condition

The characteristics of galvanic interactions between the PM, WM, and the HAZ when coupled in this experiment show similar trends to previous studies reported in literature [13,15,22,58]. Tests conducted by Barker et al. [22] found that for a five hour exposure in a no-flow condition, the X65 PM remains in a corroding, anodic position whereas WM containing 1% nickel is protected and cathodic.

In addition, Alawadhi and Robinson [15], obtained similar results for ten days exposure in sweet corrosion (CO_2) conditions. The WM has a negative current and is protected compared to the active PM and also an active HAZ. Adegbite et al. [13] used a SJI target and for X65 in a no-flow condition, the WM is protected by the corrosion current of both the PM and also an anodic HAZ.

4.2 Self-Corrosion Measurements

Self-corrosion rates were evaluated from the Linear Polarisation Resistance (LPR) of each weldment for the outer electrode in the uncoupled state directly after galvanic measurements were completed. The values of the open circuit potential (OCP), anodic (βa) and cathodic slopes (βc) slopes, corrosion current (I_{corr}) and LPR were obtained during the measurements. An example of changes in current with potential for the outer ring in the no-flow condition is shown in Figure 4-4. The three electrodes (the HAZ, the WM, and the PM) have different

gradients. Figure 4-4 depicts the linear regression values of each electrode, it relates to an Rp value, which is used to calculate corrosion current density, (I_{corr}).

In an uncoupled state, the PM was found to be the most noble with the highest potential value compared to the WM and the HAZ. Figure 4-4 shows the potential of the HAZ is intermediate between that of the PM and the WM. This is understandable as the chemical composition of the parent metal and the HAZ are close and are only different in microstructure.

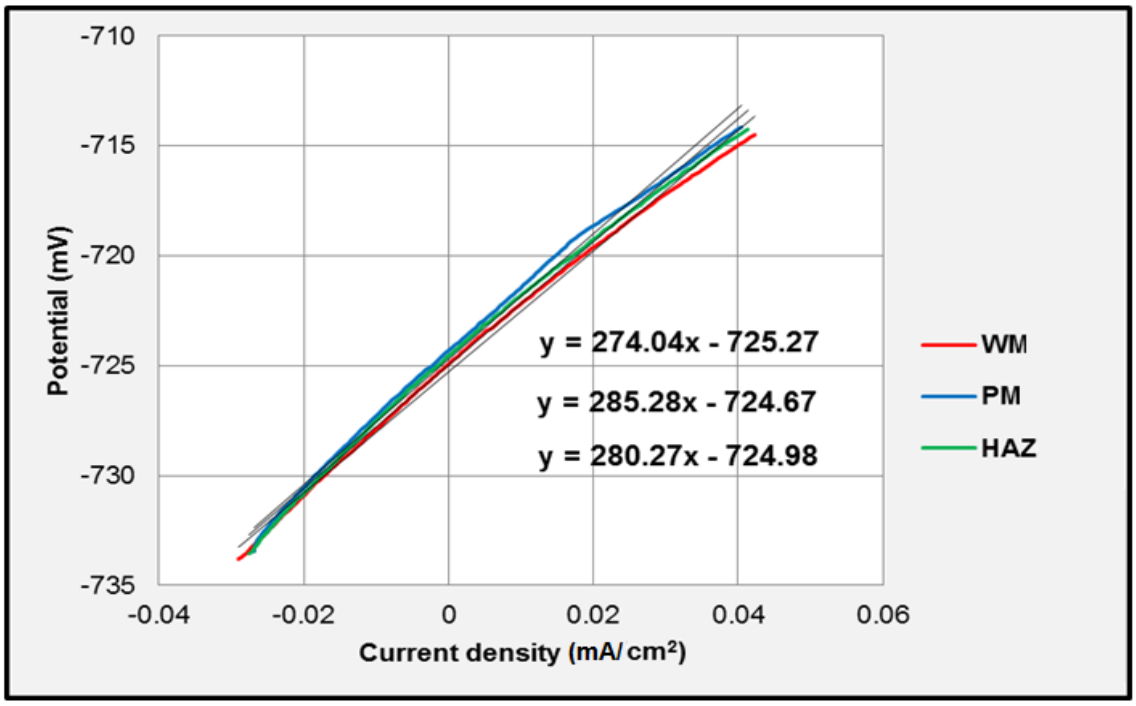

Figure 4-4 Plot of cyclic sweep measurements for weldment sections on the outer ring in brine solution saturated with CO_2 in a no-flow condition

Figure 4-4 was used to construct Table 4-1. Table 4-1 indicates that the values of corrosion potential (E_{corr}) of the PM, HAZ, and the WM are very close to each other (in the range -724 to -725 mV). The values of corrosion current density (I_{corr}) in the outer ring are in the range 93 to 95 µA/cm^2. This very close similarity is

expected in a no-flow situation, as all of the electrodes are placed in an identical environment.

Table 4-1 LPR characteristics (taken from Figure 4-4) for the outer ring of the target in uninhibited no-flow saturated with CO_2

	Weld section	Ecorr (mV)	Icorr (μA/cm^2)
Outer	PM	-724.6	91.1
	HAZ	-724.9	92.8
	WM	-725.3	94.9

The self-corrosion rates calculated from the Rp values (Figure 4-4) and equation 3-4 in the outer ring are given in Figure 4-5. In this (and other) experiments, the standard deviation was calculated from repeats, in this case 3 to 4, of each experiment, and represented as error bars on the plots to indicate the variability of data and reported in tables to indicate the error or uncertainty in a reported measurement.

The WM is the slightly anodic component when uncoupled, and it has highest self-corrosion rate compared to the PM, and HAZ in the uninhibited brine solution with CO_2 at ambient temperature without flow.

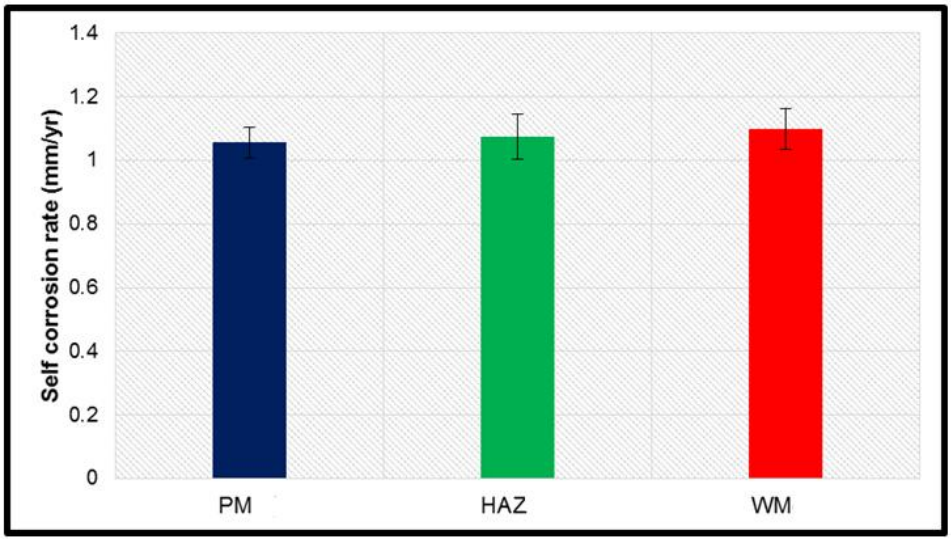

Figure 4-5 Self-corrosion rates of the weld section on the outer electrodes in brine solution saturated with CO_2 in a no-flow condition

Self-corrosion is defined as a rate of corrosion of each weld region by itself , when every electrode is in an uncoupled condition. Figure 4-5 shows the uncoupled corrosion rate of X65 in the outer ring is in the range ± 1 mm/year for the PM, the HAZ and the WM.

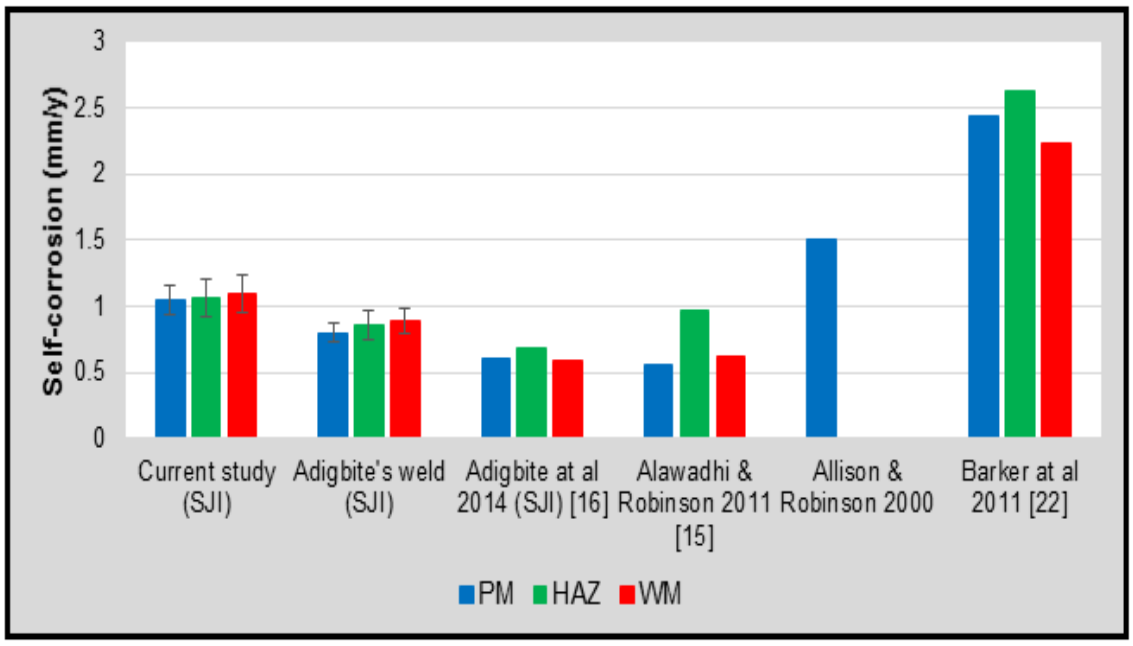

Figure 4-6 Self-corrosion rates of the current study with an X65 weldment and comparison with literature results.

The self-corrosion values in this study using an X65 steel weldment are compared with research results in the literature (Figure 4-6). Other studies reported below use weldments with different compositions. However the X65 parent metal values should be very similar. Two studies report using the same X65 weldment in a no-flow condition in brine saturated with CO_2. Alawadhi & Robinson [15] use a rotating cylinder electrode to obtain results for PM, WM, and HAZ of 0.6; 0.6 and 1.0 mm/year in no-flow condition. Adegbite et al. [13] using an SJI target, found a similar corrosion rate for PM and WM of 0.6 mm/y. These values are comparable with Alawadhi & Robinson, however, the HAZ shows a higher corrosion rate of 0.9 mm/y. Allison & Robinson [168], assess vented flexible liners

for corrosion protection of X65 pipeline, and report a corrosion rate of the parent metal of 1.5 mm/y obtained without flow, (Figure 4-6).

The target from a previous study at Cranfield (Adegbite [16]), was analysed using the current SJI flow loop in this work. The rate of corrosion of every part of the weldment is comparable with current research with values 0.8, 0.87 and 0.83 for PM, HAZ, and WM, respectively. Barker et al. [22], however, finds a static self-corrosion rate double than that of the previous study with the HAZ, PM, and WM at 2.4; 2.4 and 2.2 mm/y respectively. This difference is considered in Chapter 7. However Alawadhi & Robinson [15], Adegbite et al. [16] and Barker report that the HAZ is most active component after exposure to corrosive media. Results from the current study and later evaluation of Adegbite's target in the current flow loop, found that the WM was the most active component compared to the PM and HAZ. Further discussion about the comparison of results is given in more detail in Chapter 9.

4.3 Electrochemical Impedance Spectroscopy (EIS)

Nyquist plots from EIS analyses for the three uncoupled weld regions in the outer electrode ring are shown in Figure 4-7. The diameter of the semicircle represents the charge transfer resistance (R_t), broadly equivalent to the polarization resistance (R_p) measured in the LPR technique above from which the corrosion current density and self-corrosion rate can be obtained using Equation 4-1.

$$Rp = B/ (i_{corr}) \quad \textbf{(4-1)}$$

Figure 4-7 shows the solution resistance (R_s) and that the R_t values of the PM, the WM, and HAZ are similar to each other in appearance (shape). The shape and size of the Nyquist plots are all very similar, although there are small differences in values. The PM and the HAZ have the lowest charge transfer resistances as they exhibit slightly smaller semi-circles compared to the WM. The WM has the largest semi-circle corresponding to a smaller self-corrosion rate.

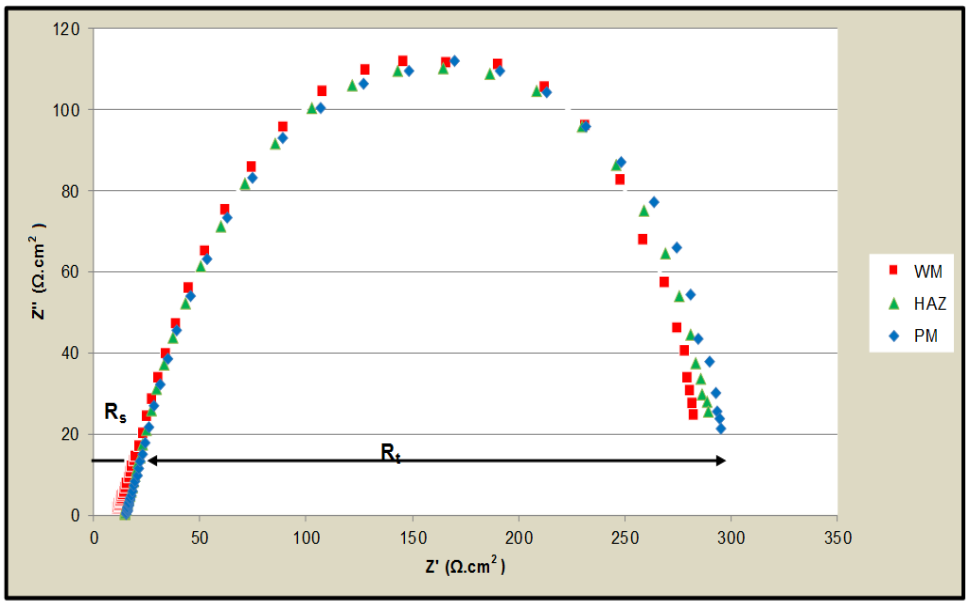

Figure 4-7 Nyquist plots of weld sections of the outer ring in a no-flow condition in brine saturated with CO_2

The EIS quantitative values of R_s+R_t are reported in Table 4-2 with the LPR measurements (gradients taken from Figure 4-4). From electrochemical impedance analysis, the corrosion rates of each part of the weldment were very similar at 1.05, 1.03 and 1.0 mm/y from the PM, the HAZ and the WM respectively (Table 4-2). These are in good agreement with self-corrosion rates calculated from the LPR measurements.

Table 4-2 EIS characteristic values of the outer ring weldments without flow

Flow	Weldments	R_s	R_t	R_s+R_t	LPR value	Corrosion Rate (mm/y) EIS	Corrosion Rate (mm/y) LPR
0(m/s)	PM	9.2±0.52	281.2±1.7	295.3	285.3	1.02±0.24	1.04±0.23
	HAZ	8.7±0.47	285.5±2.3	289.7	280.2	1.03±0.33	1.07±0.32
	WM	7.4±0.6	295.4±3.1	283.2	274.1	1.05±0.21	1.08±0.39

As Figure 4-7 shows just one semicircle in the plot for every electrode, there is no evidence of the formation of a protective carbonate film. This condition is understandable as the experimental conditions in this study of 30° C and pH 4 do not support the formation of a carbonate film. The formation of carbonate film is usually formed when the temperature is above 50 ^{o}C [75,169].

4.4 Total Corrosion

The total corrosion rate for every weld section (the PM, the HAZ and WM) of the outer ring in the no-flow condition is calculated from the sum of the galvanic corrosion rate and self-corrosion rate as in Equation 4-2. Figure 4-8 illustrates these corrosion rates, giving the contributions from the galvanic corrosion and self-corrosion. The error bars are from 3-4 repeated experiments.

$$CR_{Total} = CR_{Galv} + CR_{Self} \quad \textbf{(4-2)}$$

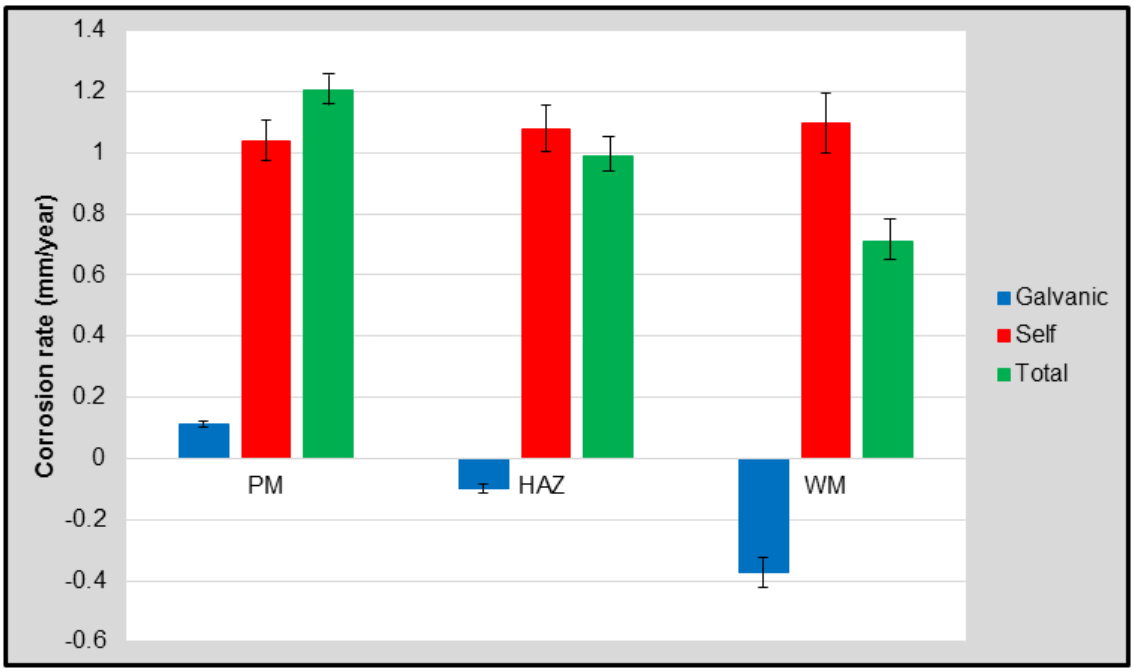

Figure 4-8 Total corrosion rate in weld sections on the outer ring in uninhibited brine solution saturated with CO_2 without flow

The self-corrosion rates in the outer ring of the WM, the HAZ and the PM, although with small variability, are in the range 1.0-1.1 mm/y. The contribution from self-corrosion (red) is the most significant contribution compared to the galvanic corrosion (blue). The overall galvanic protection of the WM results in a lower total corrosion rate. Thus in the outer electrode, the WM was slightly more noble, with a lower total corrosion rate, compared to the PM and the HAZ. The total corrosion of WM in the outer was on average 0.7 mm/y. The PM has highest total corrosion rate at 1.2 mm/y, and this condition ensures that its corrosion offers sacrificial protection to other weld regions in uninhibited brine solution with

CO_2 at ambient temperature without flow. However, although the total corrosion of weld metal is lower than that of the parent metal, this condition does not guarantee the protection of the WM from PWC because the corrosion may shift to the HAZ, as previously occurred in some oil and gas facilities [16,60].

4.5 Surface Characterisation (SEM-EDX, FIB, XRD and Raman spectroscopy)

To monitor the change of morphology and to investigate the details of chemical composition of the weld and/or a carbonate or oxide that could form on the surface of the weld and to understand the mechanism of corrosion, SEM and elemental analysis using energy dispersive spectrometry (EDX) is employed. Other characterisation techniques were carried out in support of the elemental analysis. These include X-ray diffraction (XRD) to analyse any corrosion product which had formed over the regions of the weldment. Focused ion beam (FIB) and Raman spectroscopy were also employed in this study.

4.5.1 Scanning Electron Microscopy (SEM-EDX)

A weld specimen was immersed in brine saturated with CO_2 in still conditions, without an electrical connection for 20 hours. Figure 4-9A shows the weld before the immersion process and Figure 4-9B shows a change of colour on the weld surface to dark grey across the weld after the corrosion process.

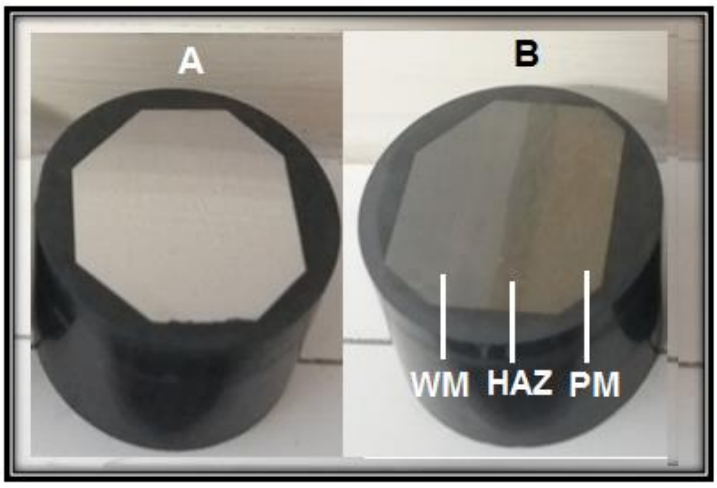

Figure 4-9 The weldment surface, (A) weldment before corrosion process and (B) after immersion in brine saturated with CO_2 for 20 hours

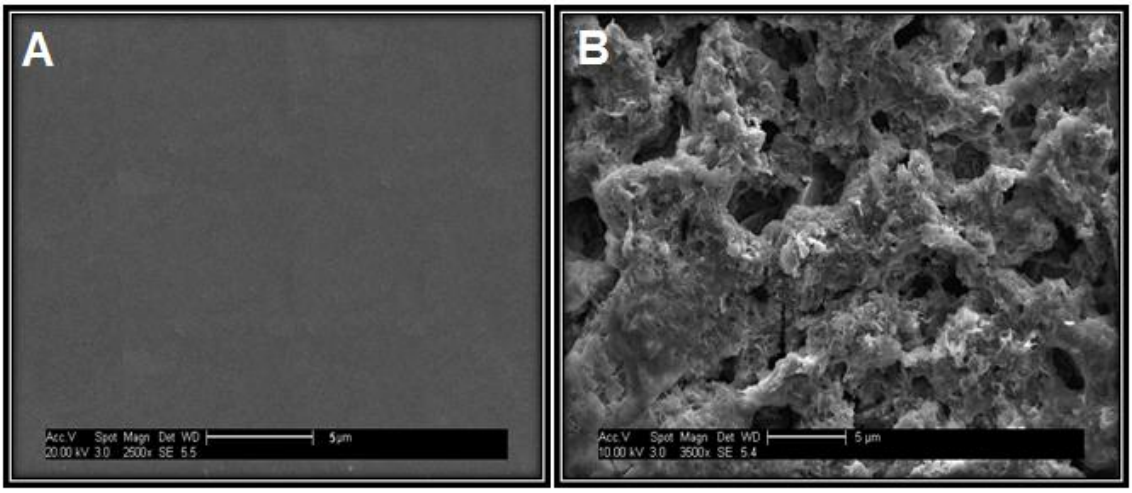

Figure 4-10 SEM images for weld metal (WM) (A) before immersion and (B) after 20h immersion in brine saturated with CO_2

Subtle visual differences in the corrosion area between the WM, the HAZ and the PM regions are seen with the SEM when the weld surface was examined. Figure 4-10 are SEM images for the WM after immersion in brine solution saturated with CO_2 for 20 hours. In Figure 4-10A, the surface is smooth after being ground and cleaned before immersion in brine. In Figure 4-10B it can be seen that a corrosion reaction has taken place after the immersion step. A porous structure has formed.

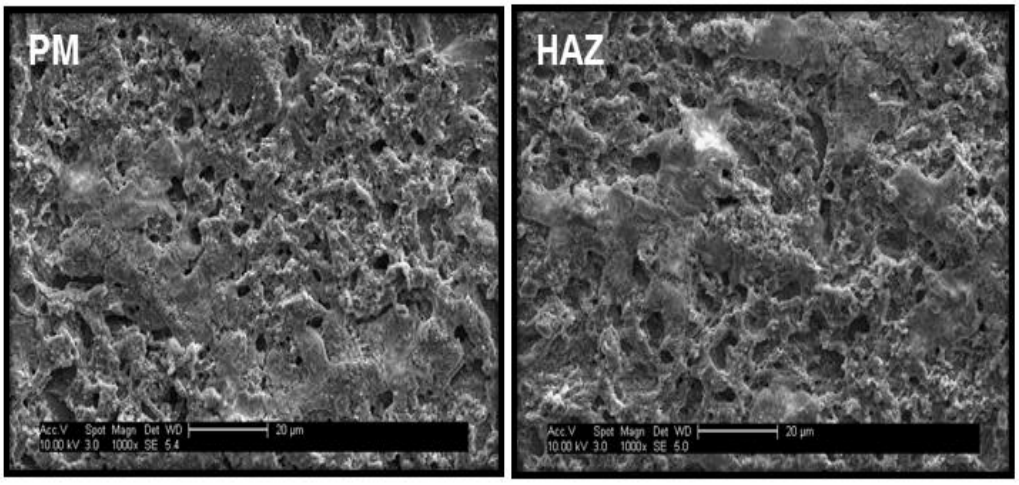

Figure 4-11 SEM images (PM and HAZ) in brine saturated with CO_2 without flow

The corroded surfaces of the PM and the HAZ are shown in Figure 4-11. It can be seen that the surface appears to be vulnerable to corrosion and is non protective with a porous structure at the surface (Figure 4-11). The results of self-

corrosion in no-flow conditions are equivalent for PM, WM and HAZ where the corrosion rate is about 1 mm/y.

The chemical composition of every part of the weldment was analysed by EDX. Table 4-3 summarises the elemental composition of the PM, WM and HAZ surfaces before and after 20 hours exposure.

Table 4-3 EDX (PM and WM) in uninhibited brine saturated with CO_2 without flow

Elements	PM (wt %)		WM (wt %)	
	Not corroded, unexposed, ground	Corroded weld without flow	Not corroded (unexposed, ground)	Corroded weld without flow
C	0.7	6.7	0.9	6.4
Si	0.1	0.2	0.3	0.2
Mn	1.6	1.4	1.7	1.6
Ni	0.3	0.4	0.2	0.3
Cu	0.2	0.3	0.2	0.2
Fe	97.1	90.8	96.7	91.2
Total	100	100	100	100

The concentration of carbon determined from a ground PM surface is 0.7 wt. %. However, after exposure in a corrosive media (brine), the carbon content increased to 6.7 wt. % (Table 4-3). There was no indication of oxygen present on the surface of the steel and the EDX spectra is given in Appendix B. The existence of cementite (Fe_3C) is inferred due to the relative increase of carbon content and this is supported by the EDX scan of elemental distribution through the layer of corrosion product in a no-flow environment. The effect of exposure to brine reduced the concentration of iron (Fe) from 96-97% in an unexposed polished weld to about 90 wt. % after 20 hours exposure.

The overall elemental concentration of the PM, WM and the HAZ in the no-flow environment is very similar and this is supported by the electrochemical measurement, particularly by the LPR (self-corrosion) analysis that gives a similar corrosion rate in each part of the weldment (±1 mm/year).

The thickness of the surface modification after the immersion process is evaluated by the FIB analysis. Figure 4-12 below shows the thickness of the likely

cementite corrosion product (between 0.35-0.5 µm) after exposure. At a corrosion rate of 1 mm/y it is likely that the network of cementite is much thicker (estimated to be around 2.7 µm) and it is likely that the platinum surface used to protect the FIB section has masked the full thickness. The SEM images (Figure 4-10B) show a mixture of shallow and deep pores, and section though shallow pores may have been taken.

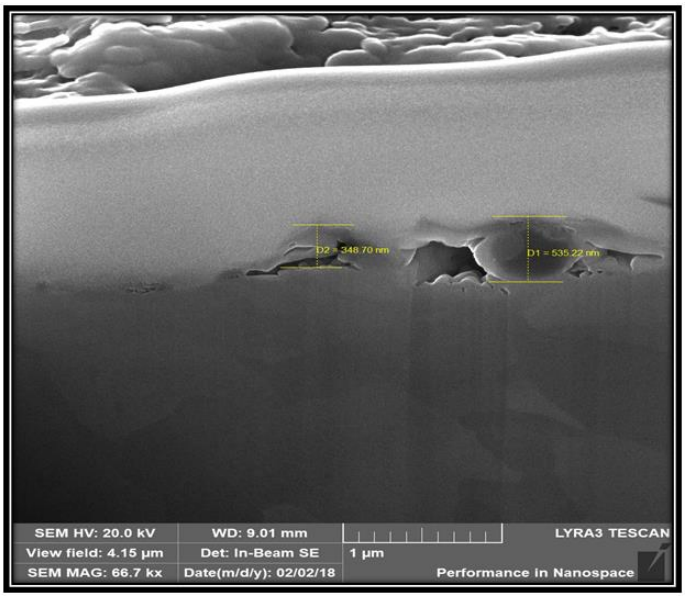

Figure 4-12 Through thickness FIB section of weld metal exposed to stagnant brine solution saturated with CO_2 showing a porous surface substructure (0.5 micron deep) on top of X65 with an over layer of deposited Pt (light colour).

While the tests are very short, they are representative of behaviour at steady state. While the impact of corrosion activity does not seem very significant but represents activity during the production process when maintenance or commissioning activities take place. It is also clear that no protective film has developed on the weldment surface. A similar observation was found in previous studies on weldment surface [15, 56]. They also failed to observe any protective film formation at no-flow environment.

4.5.2 X-Ray Diffraction Analysis

XRD of the weld before and after the corrosion process is shown in Figure 4-13. The weldment was analysed as a function of relative intensity at angles (2θ) after 20 hours of immersion under artificial seawater and saturated with CO_2 at 30 ^oC. It shows the main peaks of iron associated with ferrite from the X65. Initially iron carbonate was expected from this test. However, the X-ray diffraction did not detect the presence of the carbonate film as a corrosion product.

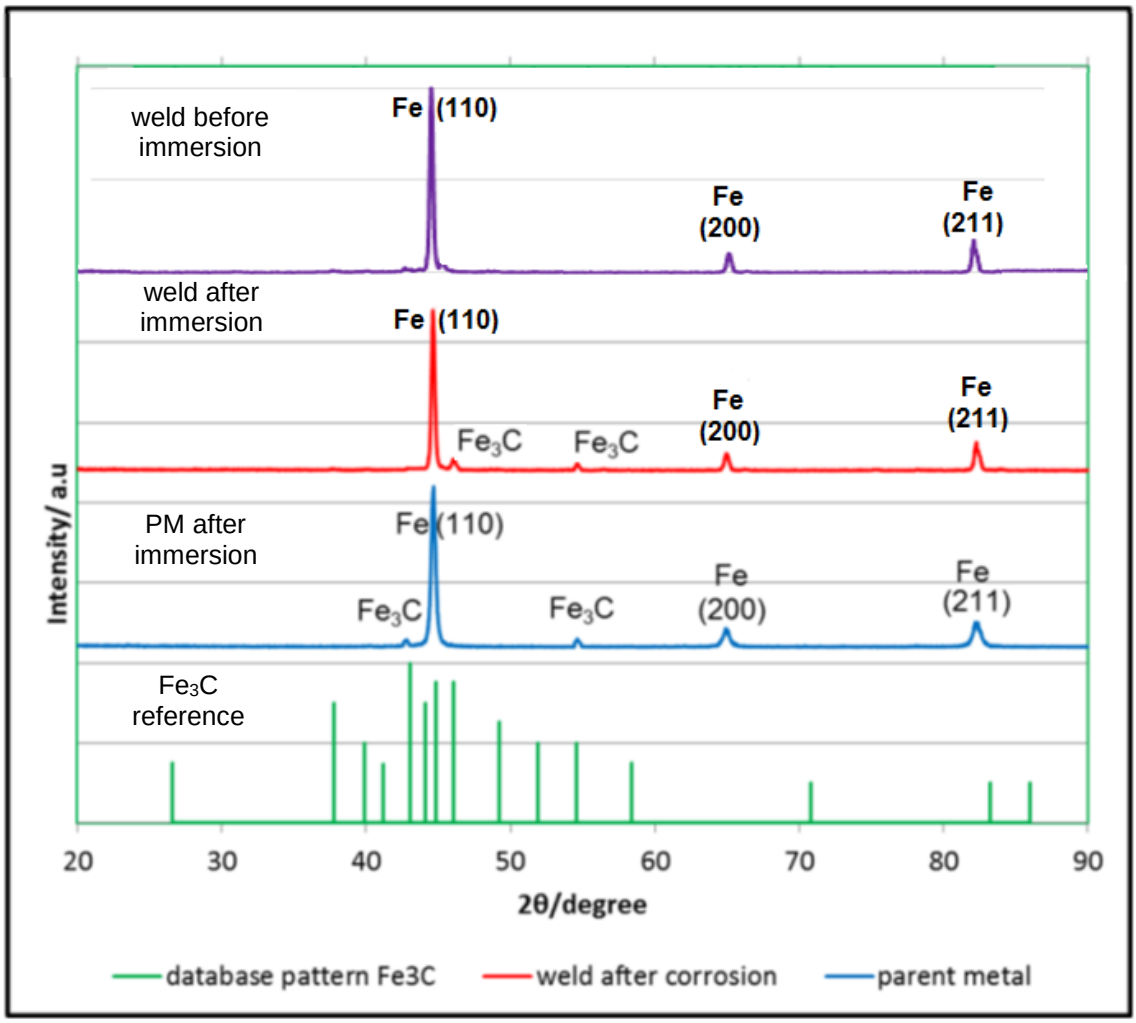

Figure 4-13 XRD pattern for cementite formation on the weld metal (WM) in uninhibited brine solution saturated with CO_2, without flow

XRD analysis supports the presence of Fe and Fe_3C at the exposed weldment surface for both the parent and the weld area samples when immersed at 30^o C. In stagnant uninhibited brine saturated with CO_2, only three peaks assigned to

cementite were observed by XRD. The several smaller peaks are related to Fe_3C formation on the weld surface shown in the reference pattern in Figure 4-13.

To support the results from previous analysis and to confirm the elemental composition of the weldment, Raman spectroscopy was adopted to identify the compounds by obtaining the vibrational mode that is specific to the chemical bonds in molecules. Figure 4-14 shows the Raman spectra for corrosion product of WM, PM and HAZ areas after the corrosion process.

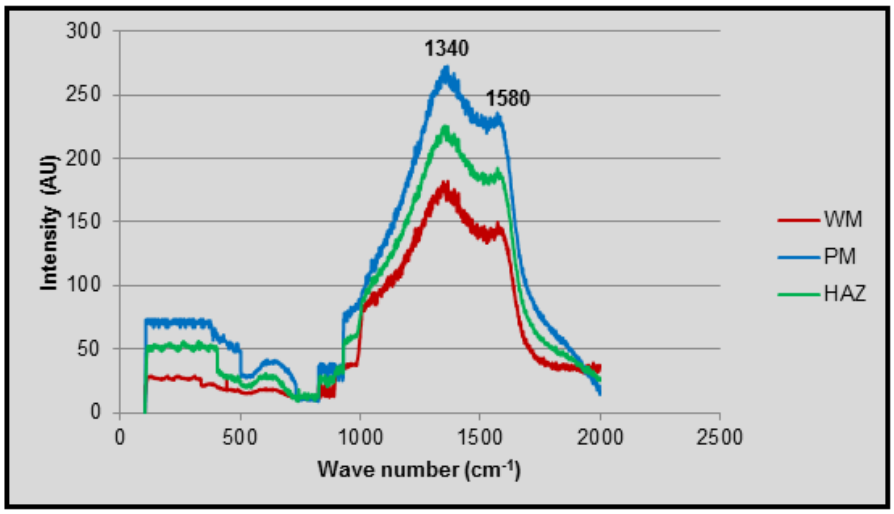

Figure 4-14 Raman spectra for corrosion product on the parent metal (PM) in uninhibited brine saturated with CO_2 without flow.

Figure 4-14 shows absorption peaks at 1340 and 1580 cm^{-1} which are characteristic of cementite Fe_3C (reported in Table 3-5) [170,171]. Fe_3C is observed in each part of the weldment with a different intensity. A tiny peak appears at 676 cm^2 that could be associated with residual Fe_3C (cementite).

From the surface characterisation it can be seen that a porous surface rich in iron carbide (Fe_3C) remains on the surface of the entire weldment. This is likely to have developed from dissolution of the ferrite and the weldment surface is extremely vulnerable to further corrosion attack. Studies by Adegbite et al. [13] and Alawadhi & Robinson [15] found a similar result when using X65 pipeline in brine solution saturated with CO_2 at ambient temperature. Both of these studies identified cementite (Fe_3C) network on the metal surface and suggested a depletion of iron through anodic reaction leaving the more noble cementite.

No evidence of an iron carbonate film was found at the controlled temperature of 30 ^{o}C used in this test. It is likely that an iron carbonate film may develop at higher temperatures. Forerro et al. [174] investigate corrosion scale formation on X70 and X80 pipeline steel in the CO_2 environment at 25 to 80 ^{o}C. It was found from this work, the protection of the steel was more noticeable when temperature was increased. At temperatures of 25 ^{o}C, no film formation occurred and when the temperature reached 60 ^{o}C, the corrosion rate was minimal due to the formation of carbonate film that protects the steel from further corrosion [173].

4.6 Chapter Summary

- ✓ The corrosion performance of weldment sections placed at the outer ring of the SJI target have been evaluated in uninhibited brine solution saturated with CO_2 at a no-flow condition by measuring the galvanic (coupled) corrosion current and self-corrosion current (uncoupled) to calculate the total corrosion rate.
- ✓ In a coupled condition, the parent metal was the anodic constituent in the outer ring. This condition ascertains that corrosion of the outer PM may offer sacrificial protection to other weld regions, especially for the outer WM in uninhibited no-flow brine saturated with CO_2.
- ✓ Surface characterisation of the weld under no-flow condition indicates that an iron carbide (Fe_3C) network remains on the surface of the specimen. This is likely to have developed from dissolution of the ferrite.

5 EFFECT OF FLOW IN DEAERATED UNINHIBITED BRINE SOLUTION

The corrosion behaviour of the submerged jet impingement (SJI) target in flowing environments is discussed in this chapter. The behaviour of the SJI target was monitored for different flow rates of the brine solution (2, 5, 8 and 10 m/s). For clarity, this chapter discusses one flow rate and one location on the SJI target specifically 10 m/s at the outer electrode. The assessment of other flow rates and their interaction with nine electrodes from all parts of the SJI target is discussed in Chapter 8 with reference to the target hydrodynamics.

5.1 Galvanic Corrosion Measurements

The effect of a flowing environment is evaluated on the weldment with a jet of CO_2 saturated brine at a velocity of 10 m/s applied to the SJI target. Similar to the no-flow condition, the progress of deaeration is monitored by recording all the electrode potentials, which become more electronegative as dissolved oxygen is removed.

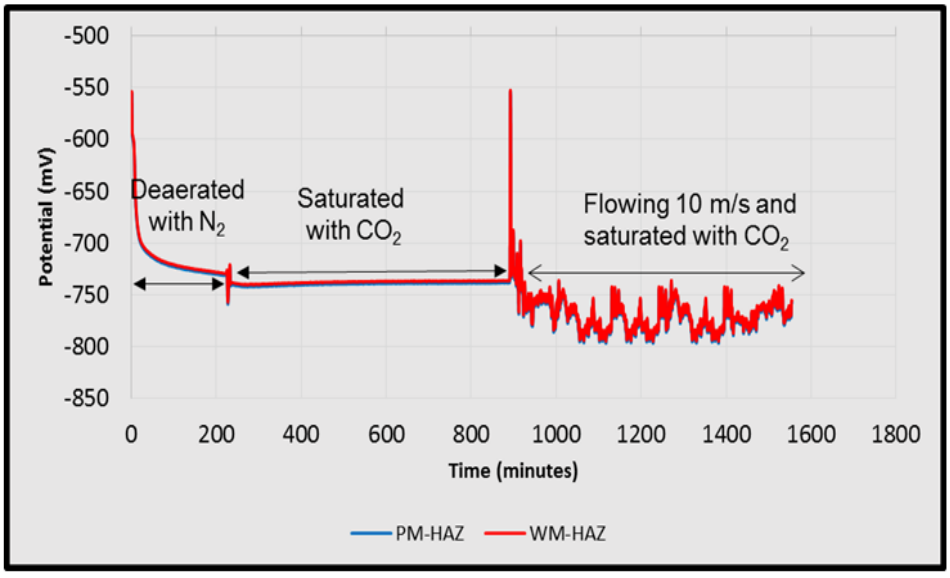

Figure 5-1 E_{corr} of PM-HAZ and WM-HAZ galvanic coupled in no-flow uninhibited brine solution saturated with CO_2, then a flow rate of 10 m/s commenced

Figure 5-1 shows the potential of the PM/HAZ and WM/HAZ couples during the deaeration stage. When deaerated with nitrogen, the galvanic potentials

decrease from -550 mV to -740mV. The brine solution is considered to be well deaerated when the potential reaches -740 mV (SCE), and thus, in these initial experiments, there is no dissolved oxygen present [97].

When CO_2 is bubbled into the cell, there is was further active shift in the electrode potential to -742 mV (SCE) as the weldment electrodes were attacked by carbonic acid. After flowing CO_2 into the static solution for 6 hours, the flow of the brine solution with a jet velocity of 10 m/s commenced (with the aid of a pump) directed onto the SJI target. Turbulent flow was generated on the target by the submerged jet. Thus, an active corrosion reaction between the target and brine solution was supported by a decrease in potential to be more negative in a range -745 to -775 mV.

A current density for each part of the weldment is calculated to measure the corrosion rate. Figure 5-2, shows the variation in current densities of the weld sections in the outer ring for CO_2 saturated brine at 10 m/s.

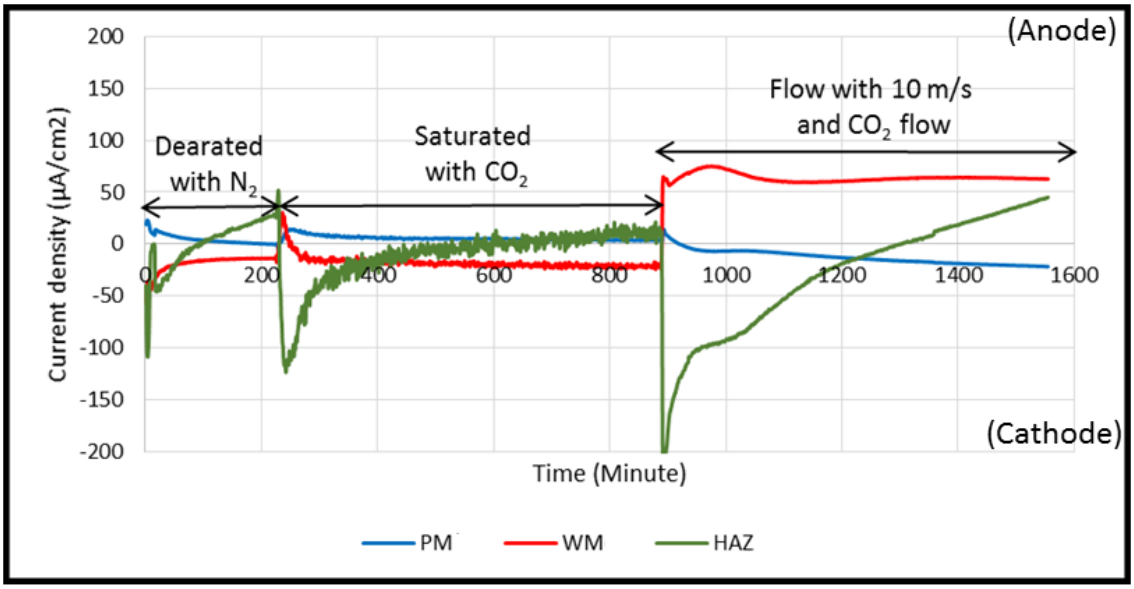

Figure 5-2 Current density of weld sections in the outer ring of the SJI target exposed to deaerated brine solution saturated with CO_2, later flowing at 10 m/s

The WM instantly becomes the anodic component in the couple as the solution starts flowing. This condition is not beneficial to the weld, and if sustained over a long time, this condition would result in severe preferential corrosion of the WM.

Figure 5-2 shows the influence of adding CO_2 is accompanied by a small increase in the galvanic current for the parent metal. The PM is anodic (positive current) and the other two weld regions WM and HAZ are cathodic (negative currents) and therefore partially protected from corrosion. The HAZ over time becomes more anodic.

When CO_2 saturated brine starts flowing with a jet velocity of 10 m/s, there is a reduction in the PM current. The transition to flowing seawater is indicated by the change of characteristics of the WM, immediately anodic from cathodic behaviour. The change in the WM provides protection to the PM and HAZ.

The galvanic current density was observed at the end of the period from values of corrosion current density of WM, HAZ and PM are 60, 45, and -25 $\mu A/cm^2$, respectively. The characteristics of galvanic (coupled) interactions between the PM, WM, and the HAZ when coupled occurring in this experiment have similar trends to previously reported studies on X65. Research by Martinez, et.al, [99] found that the WM (0.7 % nickel) is protected by the galvanic current of PM and WM in a still condition. However, in a flowing condition at 1000 rpm the WM became anodic corroding preferentially.

Tests conducted by Barker et al. [22] found that over 5 hours of immersion in a no-flow condition, the PM remained in anodic whereas WM containing 1% nickel was cathodic. However, the situation changed once in a flowing environment where the WM and HAZ became anodic and vulnerable to preferential corrosion. Alawadhi and Robinson) [15] also obtained similar results. Their experiment ran for three days in sweet corrosion (CO_2) conditions using an RCE at 1000 rpm. Their results showed the WM (0.7 % nickel) is anodic for two days but, on day 3 the position shifted and the HAZ had a slightly positive current compared to the WM. Research by Adegbite *et al.* [13] , was conducted with a similar SJI target with 0.7 % nickel in the weld. The same results are achieved in a flowing condition where the WM and HAZ corroded and protected the PM from corrosion attack.

5.2 Self-Corrosion Measurements

Uncoupled or self-corrosion rates were evaluated from LPR cyclic sweeps of each part of the weldment in the uncoupled condition after the coupled or galvanic measurements were finished. Similar to the method for the no-flow condition, the values of the open circuit potential (E_{corr}) Tafel anodic (βa) and cathodic (βc) slopes, corrosion current density (I_{corr}) and LPR were obtained.

Figure 5-3, shows cyclic sweep measurements for the HAZ, the PM, and the WM showing slightly different gradients (different LPR values). At 10 m/s the electrode behaviour differs the no-flow condition. The WM is active with the lowest LPR value or highest corrosion current density. I_{corr} for the PM, the HAZ and the WM with a 10 m/s jet are 157, 175 and 192 µA/cm^2 respectively, compared with 91-95 µA/cm^2 under static (no flow) conditions. Thus, a flowing environment increases the corrosion current density.

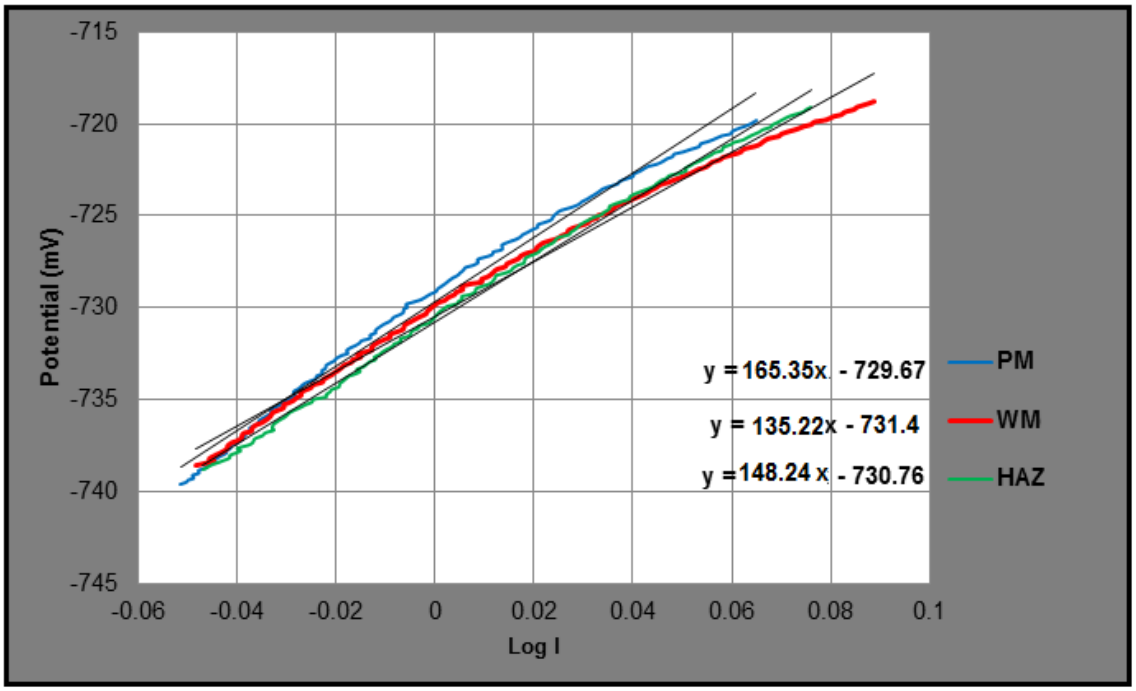

Figure 5-3 Plot of cyclic sweep measurements for the weldment sections on the outer ting in brine solution with 10 m/s flowing condition saturated with CO_2

Table 5-1 LPR characteristics for the outer ring of the target in uninhibited brine with CO_2 at 10 m/s (taken from Figure 5-3)

	Weld section	E_{corr} (mV)	i_{corr} (μA/cm^2)
Outer	PM	-729	157.3
	HAZ	-730	175.9
	WM	-730	192.0

LPR characteristics for the outer ring of the target in uninhibited brine with CO_2 at 10 m/s from Figure 5-3 are given in Table 5-1. The values of corrosion current density (i_{corr}) in the outer ring with flowing conditions are in the range 157-192 μA/cm^2 which are significantly higher than in without flow (91-95 μA/cm^2). This behaviour is expected as in a flowing environment mass transfer opportunities from metal to electrolyte are increased. In this state, the interaction between cations and anions is greater and produces a higher corrosion rate compared with the still condition.

The self-corrosion rate at 10 m/s flowing conditions is given in Figure 5-4. The self-corrosion rate of the PM and HAZ were close to each other (1.9 -2.0 mm/y). This value is understandable as they have the same chemical composition but differ in microstructure. The WM has the highest self-corrosion rate at about 2.2 mm/y. This means the WM has lower corrosion resistance compared to the PM and HAZ under the studied flowing conditions.

The tendency of WM or HAZ to be more anodic in turbulent uninhibited brine occurs in all previous studies even with different welds or steel compositions. Based on the compositions for this study given in Table 3-1, the WM has a slightly lower Ni content (0.24 wt%) compared to the PM (0.36 wt%).

In Figure 5-5, self-corrosion rates of an X65 steel weldment from a flowing condition are compared to previous research reported in the literature. The comparison is complex due to variations weld composition, flow and local environment with the differing techniques. In a flowing condition, the shear stress plays a significant role on the rate of corrosion rate of the weldment.

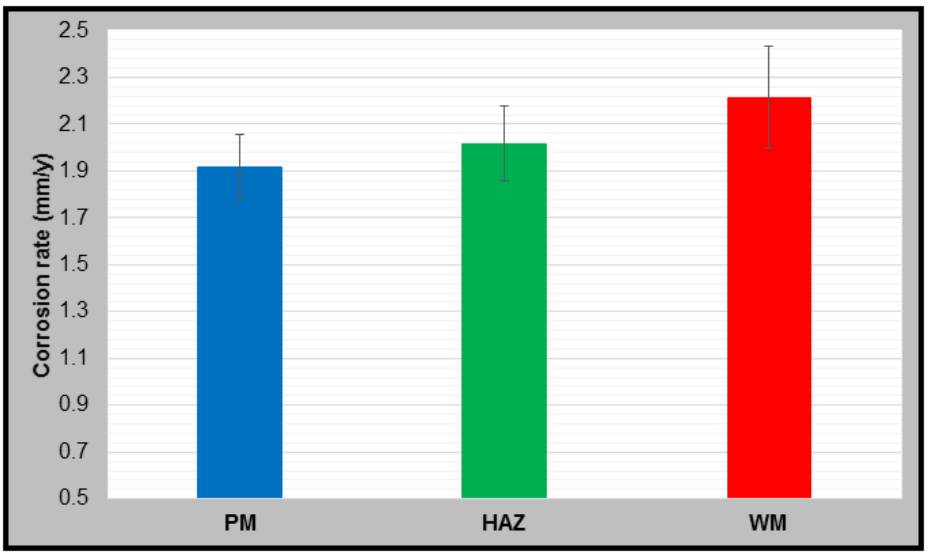

Figure 5-4 Weldment self-corrosion rates in brine saturated with CO_2 at 10 m/s

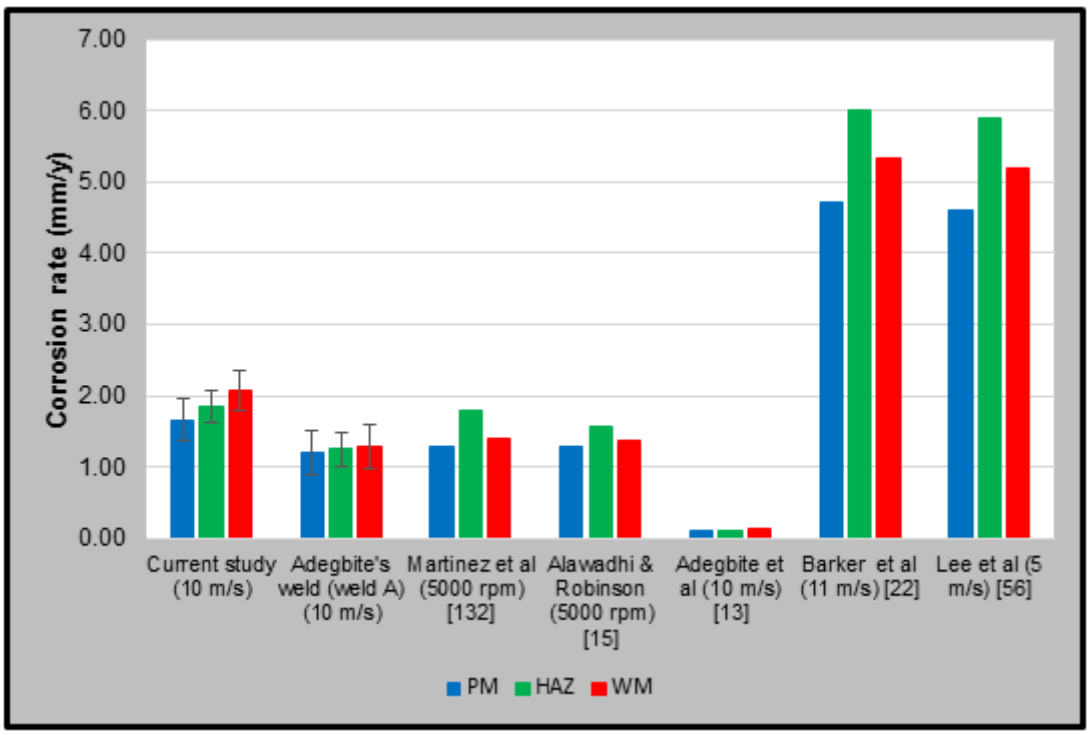

Figure 5-5 Self-corrosion rates from the current study on X65 weldment and comparison with literature

Although in most studies weldments of different composition are used, three studies report using the same X65 weldment. Martinez et al [99] uses a rotating cylinder electrode at 5000 rpm (70 Pa shear stress) and reports results for PM, HAZ, and WM of 1.3; 1.8 and 1.4 mm/year. Alawadhi & Robinson [15], using the

same method as Martinez, at 5000 rpm (70 Pa shear stress), found similar corrosion rate results for WM and PM of 1.3 and 1.4 mm/y, while the HAZ has a high corrosion rate at 1.6 mm/y (compared with Martinez) despite the lower flow rate.

Barker *et al.* [22] found that the corrosion rate of PM, WM and HAZ in uninhibited brine saturated with CO_2 with the electrolyte flowing at 11 m/s was 4.7; 5.3 and 6.02 mm/y respectively. Another study from Lee et al. [60] using at velocity 5 m/s resulted in corrosion rates for the PM, HAZ and WM in a range 4.2-6.2 mm/y. For both of these studies, while the trend is equivalent, the results are high compared to other reported studies. Likely explanation for the high rates could be from the position of the weldment compared to the jet or more likely, the presence of a very small amount of dissolved oxygen in the system which will accelerate a corrosion reaction at the anodic side. These possibilities are further discussed later in Chapter 6 and Chapter 9.

A significant difference was found in Adegbite's *et al.* [13] research. He uses a similar flow rate to this current study (10 m/s or 280 Pa of shear stress). Corrosion rates for the PM, the HAZ and the WM are in a range 0.13-0.19 mm/y. The results are 10% lower than rates determined in the same work [13] at a no-flow condition. This result is significantly different from work of others using the same material (X65).

As this work was undertaken at Cranfield, the SJI target from Adegbite's research was available, was cleaned and transferred to the flow loop used in this current research. The corrosion rates obtained, on Adegbite's target, called Target A, for the PM, the WM and the HAZ are 1.2, 1.3 and 1.35 mm/y respectively. The new experimentally determined corrosion rates obtained with Target A are comparable with rates reported by Alawadhi [58] and Martinez *et al.* [99] which both use similar weld composition. However, the new experimentally determined corrosion rates on Target A are different to the earlier reported results from Adegbite [13] in his earlier research (0.13-0.19 mm/y). There are a number of possible explanations for this, including a different flow loop, and these are discussed in Chapter 9.

The results from all studies gathered above, show that attacks on the HAZ or WM are a common occurrence in weldments in uninhibited flowing brine saturated with CO_2. Attack on the WM or the HAZ occurs in flowing conditions in every study even though each weldment was manufactured from an X65 carbon steel with a different chemical composition or different microstructure. Comparison of results from the current target (Target N) and Target A, are an opportunity to examine differences in weld metal composition and/or deposition method when in the same corrosive environment. Further discussion is provided in Chapter 9.

5.3 Electrochemical Impedance Spectroscopy Measurements

Nyquist plots from an impedance study in the outer electrode ring with deaerated brine (saturated with CO_2) at 10 m/s are shown in Figure 5-6, and the results for the PM, WM and HAZ placed in the outer ring are shown in Table 5-2. The WM had the lowest charge transfer resistance (R_t) of around 147.6 $\Omega.cm^2$ at 10 m/s. The highest rate of self-corrosion is experienced by the WM (2.2 mm/y) compared to the PM (1.8 mm/y) and HAZ (2.0 mm/y). The R_s+R_t values for the PM and the HAZ at 182 and 160 $\Omega.cm^2$ respectively, were found.

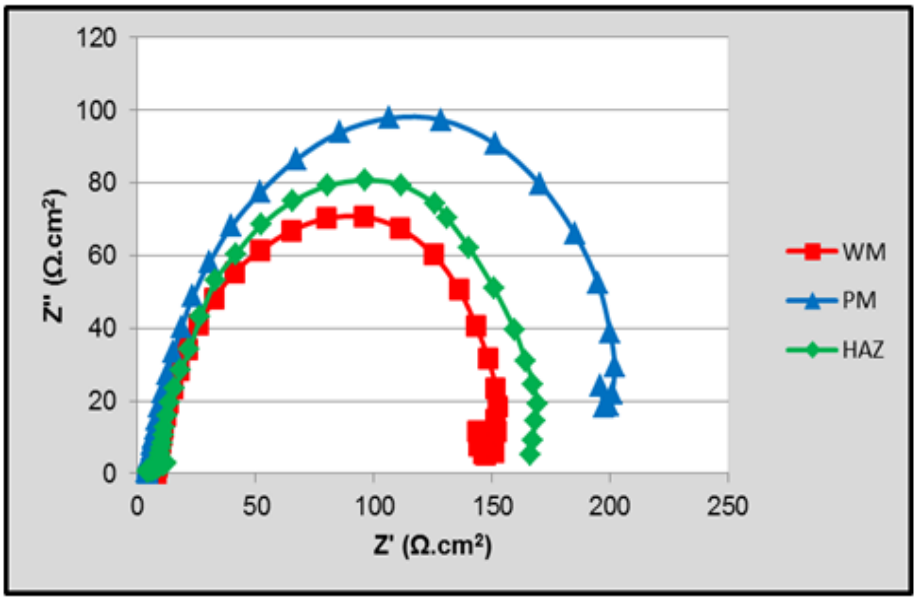

Figure 5-6 Nyquist plots of weld sections of the outer ring in brine saturated with CO_2 flowing at 10 m/s

In a similar way to the no-flow condition, there was no evidence of a very resistive film at high frequencies. This suggests no film formed on the metal surface at the time of measurement. The quantitative values of R_t are comparable to the LPR measurements (gradients in Figure 5-3). From impedance analysis, the WM has the highest corrosion rate of 2.17 mm/y at 10 m/s and this supports the self-corrosion rates calculations from the LPR measurements (2.2 mm/y).

Table 5-2 Impedance measurement for outer ring at 10 m/s

Flow	Weldment area	R_s	R_t	R_s+R_t	LPR value	Corrosion Rate EIS (mm/y)	Corrosion Rate LPR (mm/y)
10 (m/s)	PM	4.8±0.77	173.2±2.8	178.4	165.4	1.70±0.14	1.82±0.21
	HAZ	5.8±0.56	150.5±2.4	156.3	148.7	1.91±0.13	2.06±0.11
	WM	6.9±0.81	131.7±2.6	138.5	132.4	2.12±0.22	2.22±0.25

5.4 Total Corrosion Rate

The total corrosion rate for each section of the weldment is calculated from the sum of coupled (galvanic) corrosion and uncoupled (self) corrosion measurements. The overall corrosion rates for each electrode in the outer ring in a flowing brine environment saturated with CO_2 at 10 m/s is shown in Figure 5-7.

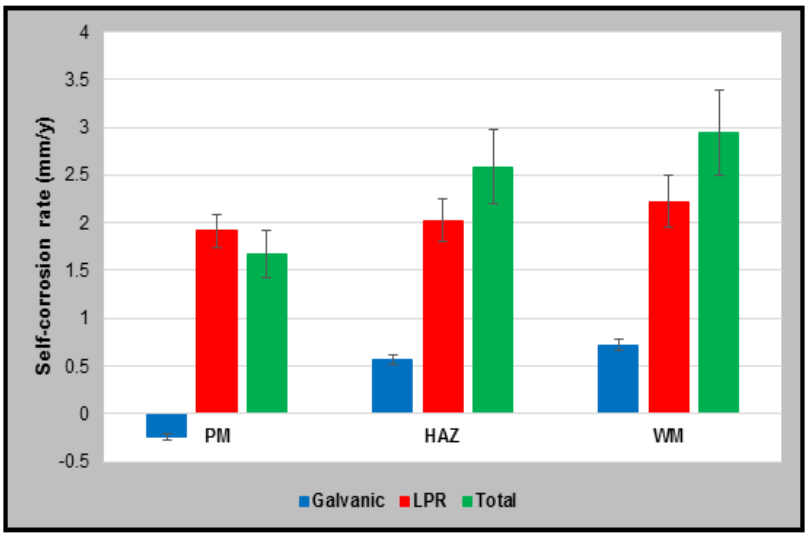

Figure 5-7 Corrosion rate in weldment on the outer ring region in brine solution saturated with CO_2 at 10 m/s

The total corrosion rates (in green) of the WM in each electrode in the outer ring exceeded that of the PM and HAZ. In contrast, the PM and HAZ will corrode less than the WM, in some cases at 30-23% of the rate of the WM. Thus in an environment of uninhibited brine saturated with the CO_2 at 10 m/s, preferential weld corrosion (PWC) is expected to occur.

Figure 5-7 shows galvanic protection of the PM results in a slight reduction of the total corrosion rate. Thus in the outer electrodes, the PM is noble, with a lower total corrosion rate, compared to the WM and the HAZ. The self-corrosion rates of the WM, the HAZ and the PM differ, with values in the outer rings in the range 1.9, 2.0 and 2.2 mm/y for the PM, the HAZ and the WM, respectively. There was a significant increase in self-corrosion compared to stagnant conditions as described in the previous chapter. However, the difference in self-corrosion between the three electrodes is not too high because the three electrodes are located in the same hydrodynamic region.

The total corrosion rate of PM and HAZ in the outer region is in the range 1.7-2.5 mm/y. The WM has highest total corrosion rate at 2.8 mm/y, and the weld is vulnerable to corrosion in the oil and gas process from preferential or localized corrosion in the weld area.

5.5 Surface Characterisation

For surface analysis purposes, a weldment sample was exposed to SJI with uninhibited brine solution saturated with CO_2 for 20 hours under a flowing brine solution at 10 m/s. After that, the weldment was washed with deionised water, rinsed using isopropanol and dried. The surface was then analysed with SEM. The aim was to assess the morphology and composition of the corroded surface (corrosion product) as if it was the SJI target.

Figure 5-8 shows SEM micrographs of the PM, the WM and the HAZ. In the flowing environment, the surface of the WM and the HAZ appear rough and damaged, less on the PM. Pits and cracks have formed in the absence of inhibitor especially in the HAZ and WM. In the flowing conditions, due to high shear stress, areas of the weldment were unprotected resulting in greater material loss than

no-flow conditions. Material dissolution with the removal of ferrite leaves cementite regions at the surface. The result is similar to that of Hu *et al.* [174] using X-65 at flow rate 7 m/s. They note material dissolution is the dominant process rather than material removal through particle impingement [175].

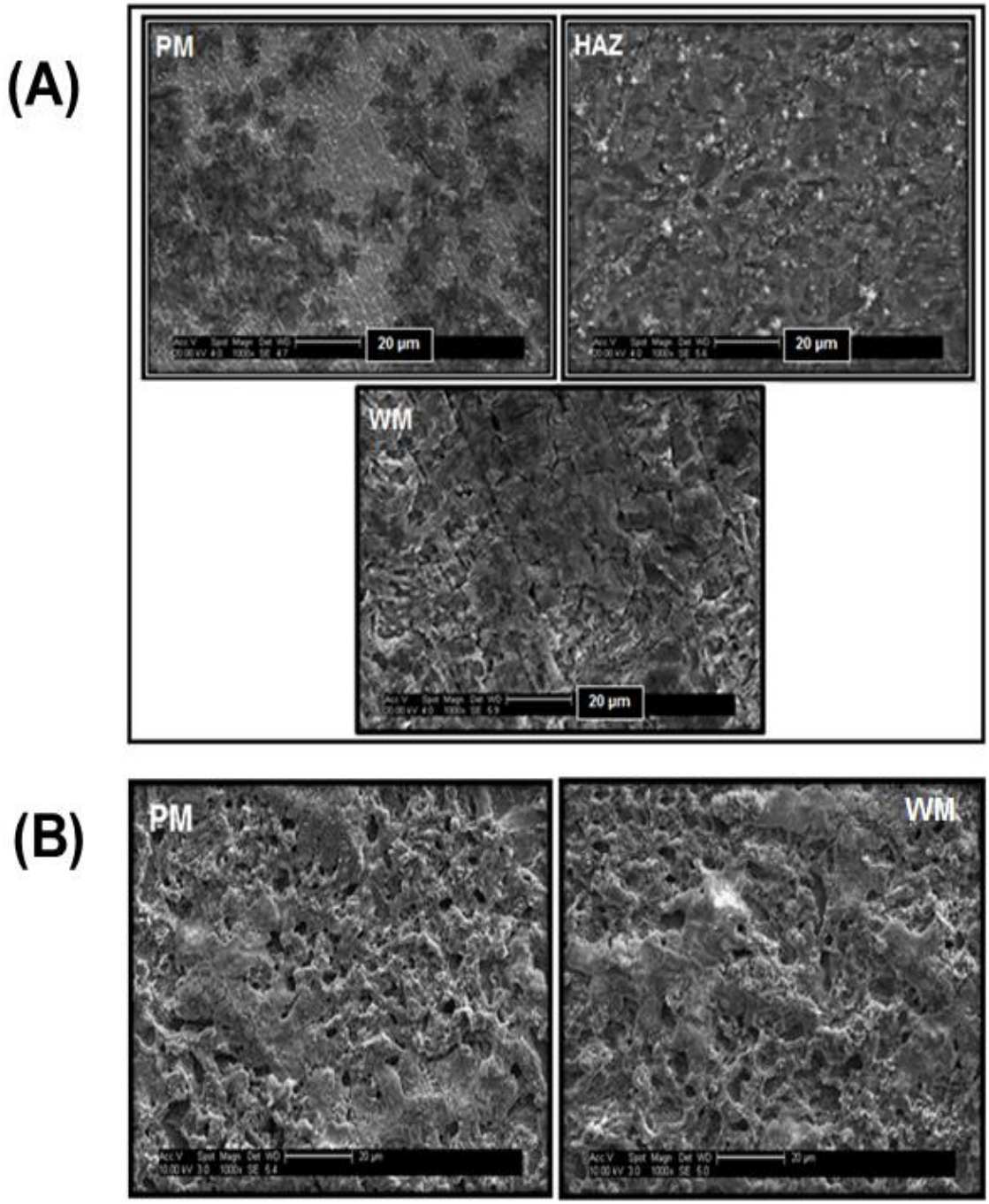

Figure 5-8 Typical SEM micrographs of the weldment after exposure to brine saturated with CO_2 (a) at 10 m/s (b) with no flow

The surface elemental composition from EDX spectra are given in Table 5-8, with the elemental composition of the PM, the WM and the HAZ after corrosion. The accumulation of carbon in flowing conditions is significant compared to no-flow conditions. The carbon concentration on the weldment was 15.1, 15.3 and 19.6 wt % for the PM, the HAZ and the WM respectively.

The concentration of Fe in the weldment decreases with the corrosion reaction and more Fe dissolves in the brine solution. In this case iron (Fe) depletes from 91, 90 and 90 wt% for the PM, HAZ and the WM in no-flow condition to 82, 81 and 77 for PM, HAZ and WM respectively with flow. The decrease in Fe concentration in flowing conditions is accompanied by a rise in carbon, 40-50% higher than with no-flow. Similarly, to without flow, there is no indication of oxygen presence on the steel. This supports the argument that the corrosion mechanism is primarily related with the dissolution of Fe without the formation of oxygen containing film or corrosion products on the corroded surface.

Table 5-3 EDX analysis of the weldment in the outer ring in uninhibited brine

Elements	PM (wt %)		WM (wt %)	
	Not corroded (no immersion)	Corroded with flow	Not corroded (no immersion)	Corroded with flow
C	0.7	15.4	0.9	19.8
Si	0.1	0.2	0.3	0.2
Mn	1.6	1.4	1.7	1.6
Ni	0.3	0.4	0.2	0.3
Cu	0.2	0.3	0.2	0.2
Fe	97.1	82.3	96.7	77.9
Total	100	100	100	100

The elemental compositions in Table 5-3 support those from electrochemical measurements showing the WM has a higher corrosion rate with more Fe dissolving into the corrosive media. In this condition formation of protective film on the weldment surface such as $FeCO_3$ is not favoured.

SEM studies in the literature on coupled weldments exposed in flowing conditions also reported the absence of a protective film $FeCO_3$ despite higher temperatures to this study [14,15,58]. The study of Alawadhi & Robinson [15] was performed

at flowing condition of RCE at 5000 rpm, and 50 ^{o}C. The SJI study by Adegbite et al. [13] was at 30-40^{o}C.

FIB sections were taken to observe the effect of fluid turbulence on the SJI target, reproduced on weldment surfaces. Figure 5-9 is a FIB section of the weld metal.

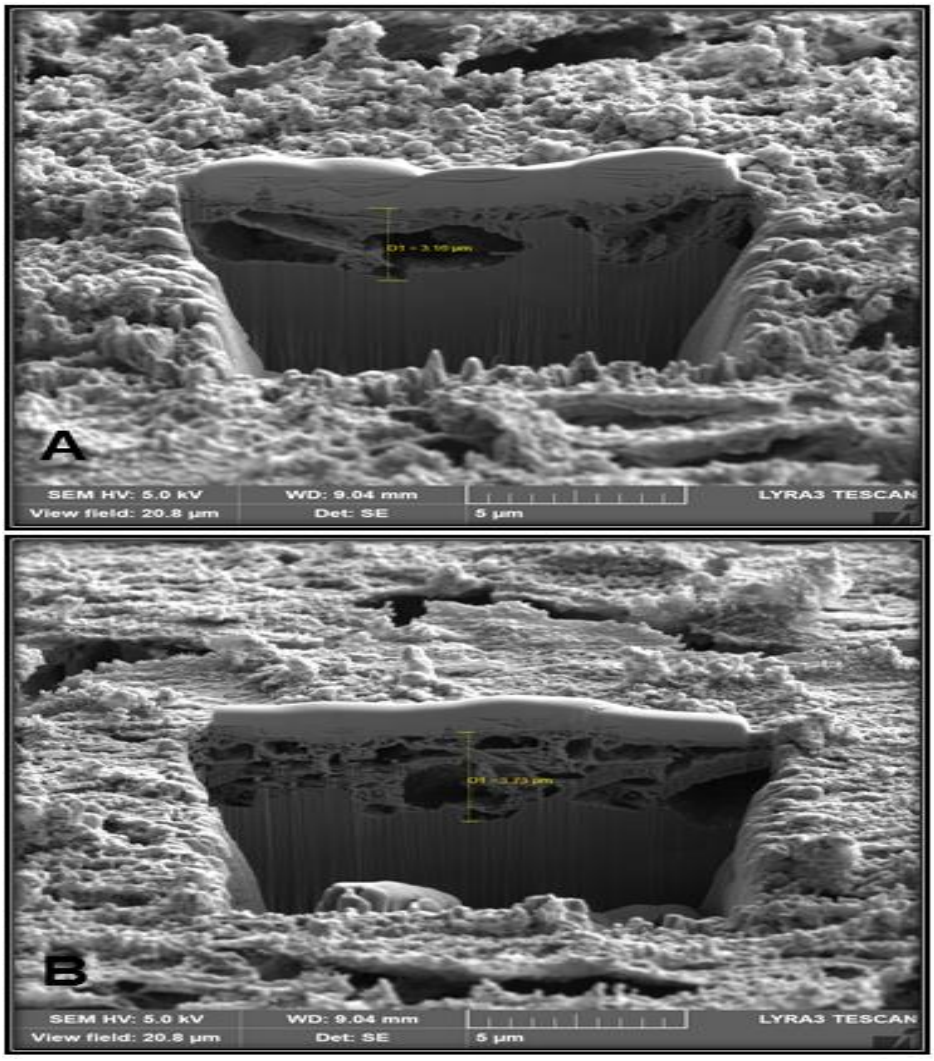

Figure 5-9 The FIB micrograph of the parent metal (A) and the weld metal (B) in uninhibited flowing 10 m/s saturated with CO_2

A porous and significantly depleted zone at the near surface is observed beneath a protective Pt layer. This depleted zone is about 3.8 µm thick for the WM (Figure 5-9A) and 2.5-3 µm thick for the PM (Figure 5-9B). These values are about 10 times that found for all weldment sections in no-flow conditions, which were in the

range 0.3 to 0.6 µm. This supports the accelerated corrosion measured using the electrochemical method particularly with self-corrosion measurements.

Barker et al. [176] found that the PM was more noble than the HAZ and the WM. They noted that the effect of microstructure and the composition play a significant role during the corrosion process. Similar results were found by Alawadhi and Robinson [58] who used the RCE method at 5000 rpm. They found a lower corrosion rate on the PM compared to HAZ and WM in flowing conditions. However they argued that a $FeCO_3$ film and cementite phase could reinforce the protective film and anchor it to the PM.

To ascertain the nature of the depleted zone, XRD analysis was employed. Figure 5-10 shows the XRD analysis of the weldment in deaerated brine saturated with CO_2 under flowing conditions for 20 hours. Cementite peaks, similar to the standard, are determined. It is likely that an external framework (skeleton) of cementite (Fe_3C) separates from the pearlite after Fe is dissolved from the corroded matrix of the metal.

As expected the intensity of cementite peaks found on surfaces in a flowing environment are greater, particularly on the weld metal, than those determined in a no-flow environment. This is due to the flow or increased mass transfer and thus, more Fe will dissolve and leave a high accumulation of cementite on the weldment surface. Unknown peaks that appear are likely to be a result of another corrosion product. However no evidence of a $FeCO_3$ film was found in this study.

Raman analysis is used to study the corrosion product that forms on the same electrode surface as above. Figure 5-11 shows the Raman spectra consist of several peaks identified as cementite. Overall, the peaks characteristics are similar to those in no-flow conditions. Two peaks at wave numbers 1360 and 1575 cm^{-1} are associated with absorption characteristics of cementite (Fe_3C). Similar to the XRD analysis, the peak intensity of each part of the weldment at a flow is greater than in no-flow conditions as a result of the turbulence. Despite the porous framework of cementite on the surface results in a greater increased surface area

and channels further brine solution into the near surface of the weldment inducing accelerated corrosion rates.

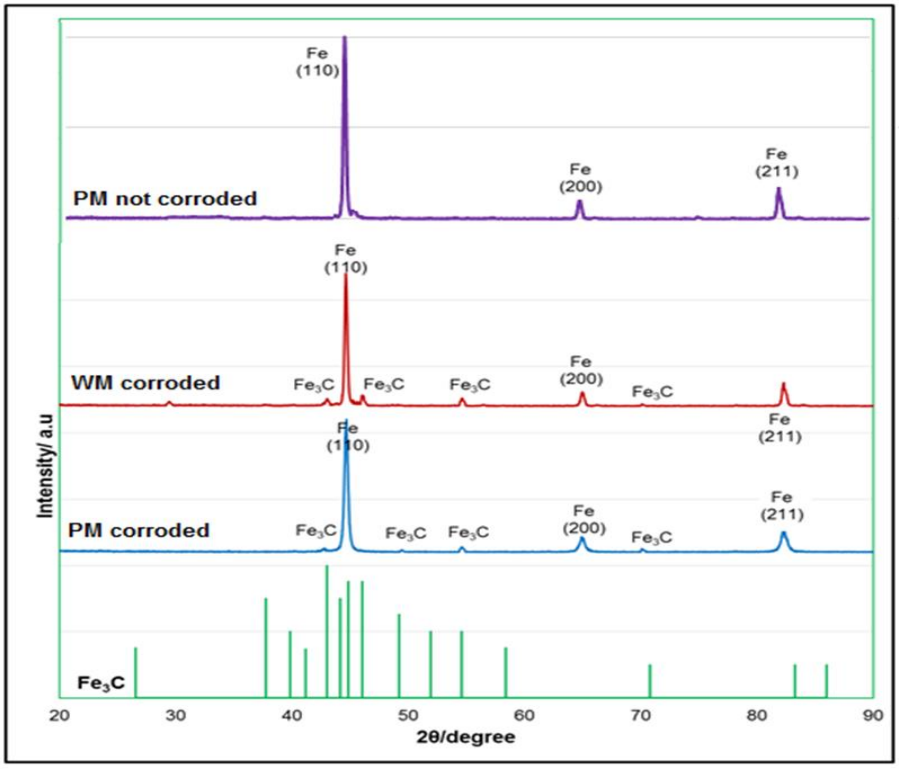

Figure 5-10 X-Ray diffraction spectra of the weldment after corrosion process in deaerated brine saturated with CO_2 at 10 m/s

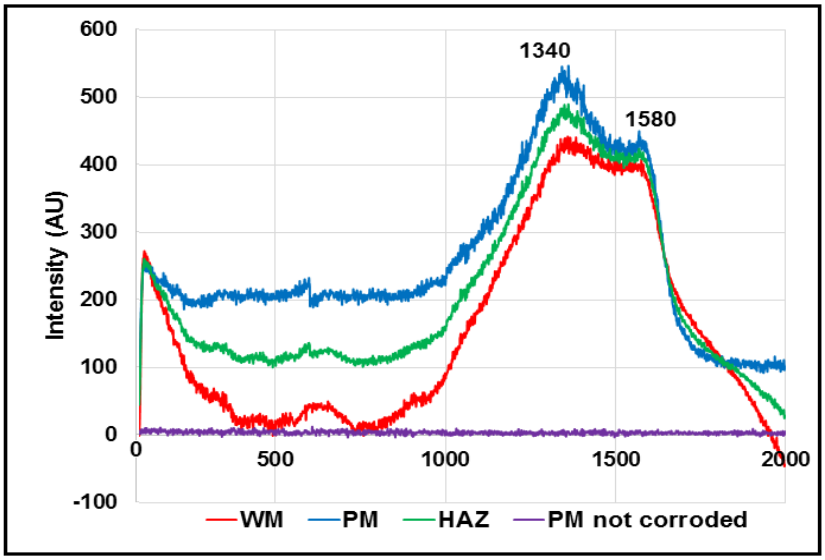

Figure 5-11 Raman peaks characteristic of cementite observed in deaerated brine saturated with CO_2 at 10 m/s

5.6 Chapter Summary

. From these experiments, it can be summarised that:

- ✓ In artificial sea-water saturated with CO_2 at flowing conditions of 10 m/s, the weld metal becomes anodic and preferentially corrodes in comparison to the parent metal. The PM and HAZ will corrode less than the WM, in some cases at 30-23% of the rate of the WM. Thus in an environment of uninhibited brine saturated with the CO_2 at 10 m/s, preferential weld corrosion (PWC) is expected to occur.
- ✓ Galvanic corrosion plays a significant contribution to the total corrosion in a flowing environment where the WM and the HAZ are anodic. As the current density is calculated from the current divided with each electrode area, a tiny area of HAZ and WM will produce a high current density. Therefore, they corrod faster compared to the PM and result in PWC.
- ✓ A porous, hollow framework of iron carbide (Fe_3C) develops in the near surface of the weld in flowing conditions.

6 EFFECT OF INHIBITION WITH AND WITHOUT FLOW

This chapter will discuss the performance of the SJI target with an oilfield corrosion inhibitor added to brine saturated with CO_2 in both no-flow and flowing conditions. The oilfield corrosion inhibitor, CORRTREAT 10-569 is used for comparison with previous work [13,15,16]. The weldment (PM, WM, and HAZ) behaviour is monitored using galvanic measurements, LPR and EIS.

SEM-EDX and FIB analysis are employed to characterise the surface before and after the corrosion process. XRD and Raman analysis is used to identify the formation of any film on the weldment surfaces. Fourier Transform Infra-Red spectroscopy (FT-IR analysis) is undertaken to analyse the qualitative nature and the chemical structure of an inhibitor (CORRTREAT 10-569). The corrosion rates determined in the inhibited environment are compared to results in an uninhibited condition using the SJI target. In this way the influence of a range of flow rates is assessed so the likely behaviour of this weldment in an oil production pipeline environment is considered.

6.1 Characterisation of CORRTREAT 10-569 using FTIR analysis

Based on information from the Material Safety Data Sheet (MSDS), the composition of CORRTREAT 10-569 comprises several chemicals such as ethanadiol, 2-butoxy ethanol and a fatty acid amine (Figure 6-1). FTIR analysis is performed to confirm and identify active functional groups (shown in Figure 6-2) in the inhibitor.

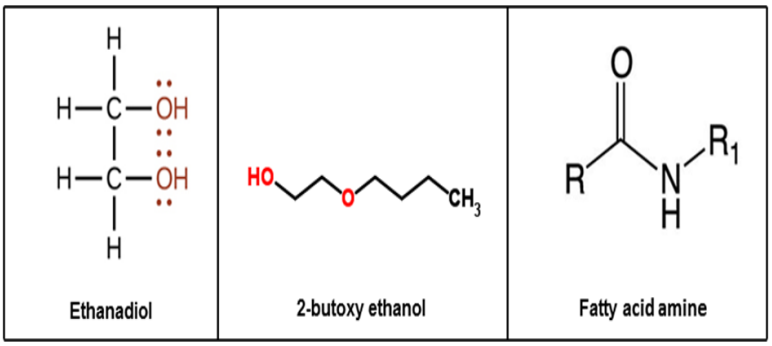

Figure 6-1 The structure of ethanadiol, 2 butoxy-ethanol and fatty acid amine

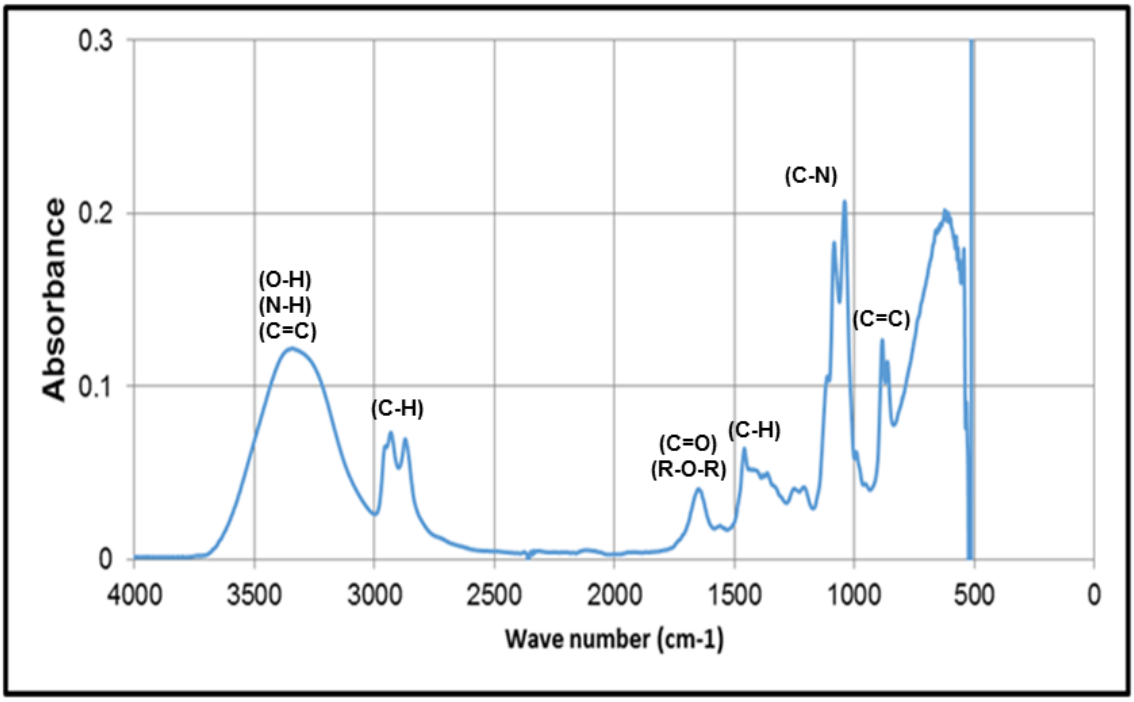

Figure 6-2 FTIR spectra of CORRTREAT 10-569

Infra-Red (IR) absorption peaks are shown in Figure 6-2 and reference peak values attributed to the expected functional groups given in Table 6-1. A broad absorption band between 3000 to 3500 cm^{-1} showed the existence of hydroxyl group (O-H), amine group (N-H) and (C-H) absorption. Peaks appearing around 1000 to 1600 cm^{-1} are related to the presence of carbonyl (C=O), (C-O), (C-C) and (C-N) [177].

All the functional groups were identified as anticorrosion substances that are classified as organic corrosion inhibitors, and these were reported in many studies [13]. An inhibitor is adsorbed into the metal surface to form a thin layer and prevent the diffusion process by minimising ion transfer between the solution and the metal. The metal is then said to be passivated.

The organic inhibitor (Figure 6-1) used in this research contains hydrophilic (polar) and hydrophobic (non-polar) parts. The inhibition mechanism is explained as the polar component (O-H and N-H) which binds to the metal surface by an adsorption process. Whereas, the non-polar (alkyl) part of the inhibitor aggregates with other free hydrophobic groups in the solution [15].

Table 6-1 Typical IR absorption position and intensity attributed to a range of functional groups [177]

Functional Group	*Absorption Location*	*Absorption intensity*
Hydroxyl (O-H)	3400-3600	strong
Amine (N-H)	3300-3350	strong
Amine (C-N)	1180-1300	medium
Carbonyl (C=O)	1650-1700	medium
Alkane (C-H)	2850-2970	strong
	1340-1470	medium
Alkene (C=C)	3010-3100	strong
	650-900	strong
Ether (R-O-R)	1650-1750	medium

The inhibitor generally controls corrosion by forming thin films that modify the environment at the weld surfaces. Another mechanism consists of causing the metal to corrode in such a way that a combination of adsorption and corrosion product forms a passive layer [120] and restricts easy access to the surface therefore acts as a barrier to further attack. This is discussed a little in Chapter 9.

6.2 Optimisation of Inhibitor Concentration in Still (No-Flow) and Flowing Conditions

The inhibitor CORRTREAT 10-569 is applied to support protection of the weldment from corrosion. Optimisation of the CORRTREAT 10-569 concentration was conducted to determine the optimum concentration that can reduce the corrosion rate for the conditions required; at no-flow and flowing condition in brine saturated with CO_2.

LPR measurements of the weldment is carried out using the inhibitor to measure the self-corrosion rate as a percentage of inhibitor efficiency (IE %) and determine the optimum concentration of the inhibitor. The percentage of inhibitor efficiency calculated from different concentrations (0 to 30 ppm) in a non-flowing environment is reported in Table 6-2 and shown in Figure 6-3. For comparison the results for a jet velocity of 10 m/s are also given in Figure 6-3.

Table 6-2 Inhibitior efficiency (% IE) of weldments in the outer ring in still brine saturated with CO_2

	Concentration (ppm)	E_{corr} (mV)(SCE)	I_{corr} (μA/cm^2)	Efficiency (%)
Parent metal (PM)	0	-724.6	91.2	-
	5	-692.4	22.3	75.5±3.3
	10	-678.8	17.7	80.6±3.1
	20	-657.1	15.8	82.7±2.9
	30	-635.7	10.7	88.3±2.2
	40	-647.4	12.9	85.8±3.0
Heat Affected Zone (HAZ)	0	-724.9	92.8	-
	5	-695.3	24.9	73.2±3.7
	10	-680.2	18.6	79.9±2.9
	20	-659.5	14.9	83.9±2.5
	30	-637.5	11.5	87.6±2.2
	40	-645.5	13.2	85.7±2.6
Weld metal (WM)	0	-725.3	94.9	-
	5	-696.7	26.1	72.5±2.4
	10	-682.8	20.2	78.7±2.8
	20	-660.5	16.8	82.3±2.5
	30	-638.8	12.5	86.6±3.1
	40	-643.6	15.5	83.6±3.4

For both non-flowing and flowing brine, the results in Figure 6-3 show a positive correlation between the concentration of CORRTREAT 10-569 and the inhibitor efficiency of the weldment until the concentration reaches 30 ppm. For no flow, the percentage of inhibition from the PM, the WM and the HAZ is increases slightly from 72 % at 5 ppm to about 88 % at 30 ppm. The inhibitor efficiency of increases as the concentration increases. This condition is expected as the amount of adsorbed inhibitor on the weldments rise. This reflects the effective protection of the weldment surface from carbonic acid attack. At concentrations above 30 ppm, the inhibitor efficiency starts to decrease, presumably because saturation occurs at higher inhibitor concentrations, so that the inhibitor does not work effectively. From this study, the maximum % IE is obtained with a CORRTREAT 10-569 inhibitor concentration of 30 ppm for the weldment in the outer ring range from 88-87%.

The inhibitor efficiency (% IE) calculated in the current study is comparable with the results obtained by Alawadhi & Robinson [15] who obtained an inhibitor

efficiency of 78, 88 and 83% for the PM, WM, and HAZ respectively, in similar conditions without flow using the same oilfield inhibitor.

A jet velocity of 10 m/s was used to analyse the performance of the SJI target using LPR to measure the self-corrosion rate at each electrode on the outer ring. At 10 m/s the maximum % CORRTREAT 10-569 efficiency was obtained at an optimum concentration of 30 ppm and ranges from 82-85%.

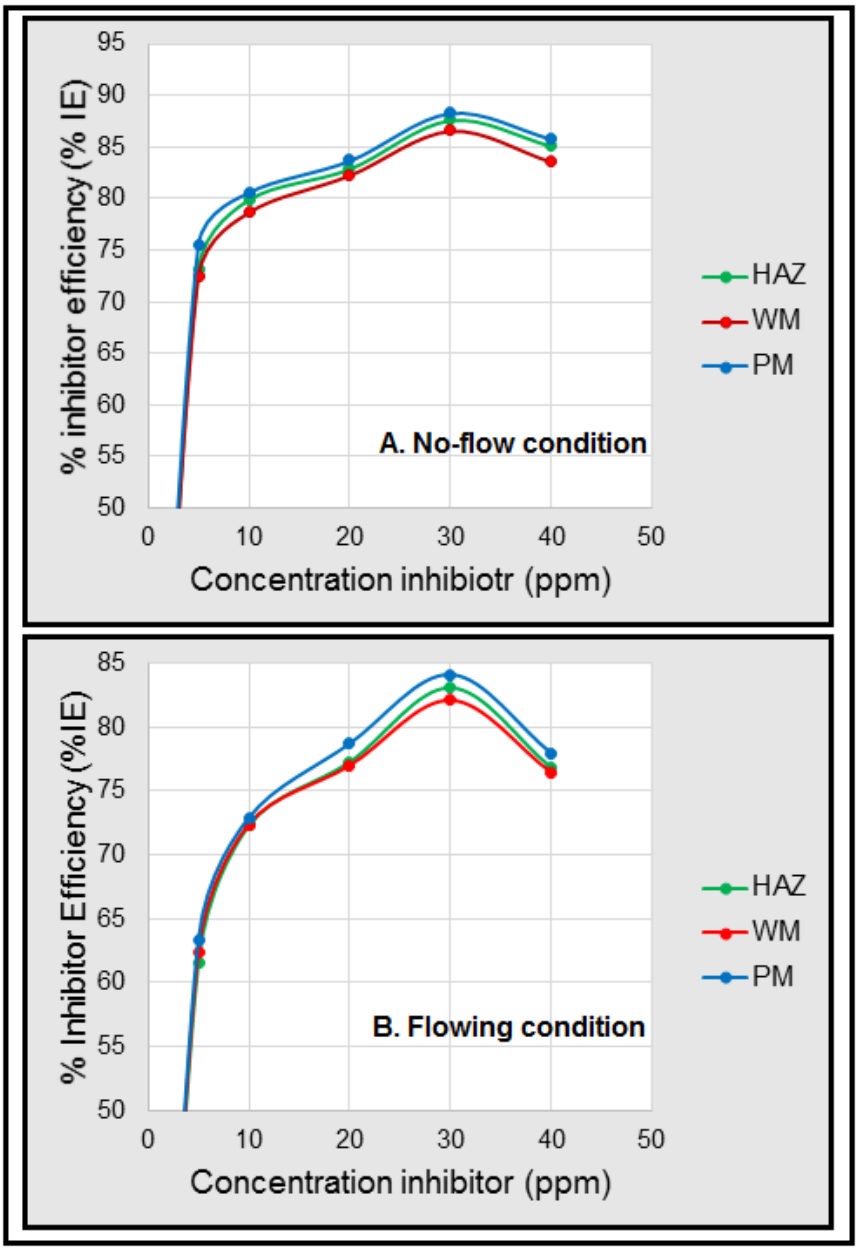

Figure 6-3 Efficiency of inhibitor at different concentrations (A) without flow and (B) with flow

The inhibitor efficiency in flowing brine is slightly lower than without flow. Under flowing conditions surface adsorption may be influenced by the shear stress. It is now a dynamic condition with turbulent flow and as a consequence, the total adsorption and/or the adherence of inhibitor molecules (or a film) to the weldment surface appears to be less effective under flow than in tranquil, quiet conditions.

An inhibitor concentration of 30 ppm is found to the optimum for both conditions evaluate and used to evaluate the corrosion of the weldment in both inhibited flowing and non-flowing brine environments saturated with CO_2.

To calculate the inhibitor efficiency, data for the outer and inner electrode is recorded assuming both electrodes have a large area compared to the centre electrode so the error is minimised. The maximum inhibitor efficiency on the parent metal in the outer electrode is 88 % while the inner electrode is 81 %, Thus the inner electrode has lower inhibitor efficiency compared to the outer, presumably linked to the expected higher turbulence on the inner electrode.

6.3 Application of CORRTREAT 10-569 as a Corrosion inhibitor without flow

The current characteristics from the galvanic, LPR and impedance analyses after the addition of 30 ppm of CORRTREAT 10-569 inhibitor are explored in brine saturated with CO_2 with no-flow. The effect of inhibited brine saturated with CO_2 on the weldment was monitored by calculating the total corrosion rate of each working electrode without flow. Following exposurure, surface analysis was conducted using the SEM-EDX, FIB, XRD and Raman spectroscopy.

6.3.1 Galvanic Measurement

Galvanic corrosion currents of the coupled weldments in inhibited still brine saturated with CO_2 are plotted against time in Figure 6-4. In a deaerated condition, the first couple of WM-HAZ has an anodic current which shows preferential corrosion of the WM with respect to the HAZ. The HAZ-PM couple has a negative current showing the HAZ corrodes preferentially to the PM.

Figure 6-4 shows that, after the deaeration stage, as CO_2 is bubbled into the brine, the order of the size of currents associated with each electrode changes such that the PM becomes anodic and corrodes preferentially. The HAZ and the WM become cathodic and are protected by the PM current. The order is similar to that in an uninhibited environment where the WM is slightly cathodic to the HAZ and the PM, but the current produced is very different. In an inhibited condition, the current obtained with the PM is 4 µA, while uninhibited, it is 20 µA.

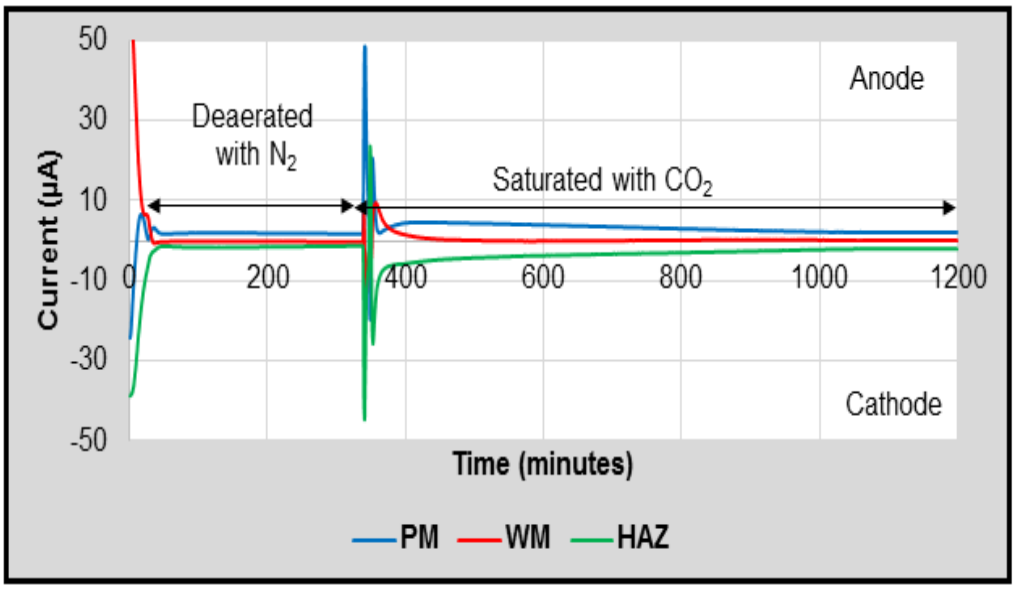

Figure 6-4 Galvanic density of PM, HAZ and WM exposed to inhibited deaerated brine without flow

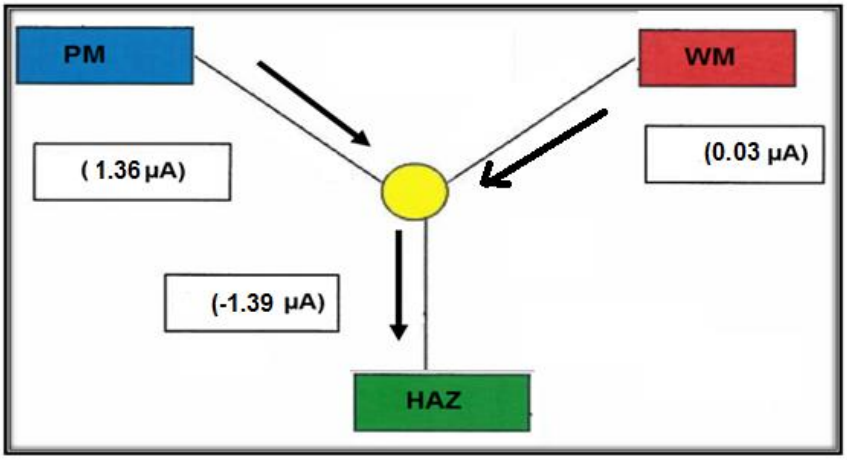

Figure 6-5 The flow of galvanic current in still inhibited brine saturated with CO_2

Figure 6-5 shows the values and the flow of current during the corrosion process after 20 hours of exposure. The corrosion current of the HAZ (-1.39 µA) is calculated from the value of I_{corr} (corrosion current) of the parent metal (1.36 µA) and the WM (-0.03 µA).

The galvanic corrosion measurements show that the inhibitor decreases the overall current density (Figure 6-6) and hence, decreases the corrosion rate. This shows that the inhibitor affects all galvanic currents for each region, and the WM remains cathodic, protecting the weld from corrosion. The weld surface is covered by adsorbed inhibitor molecules resulting in the formation of a protective layer which decreases the electron transfer between the metal, the immediate modified surface and the corrosive media.

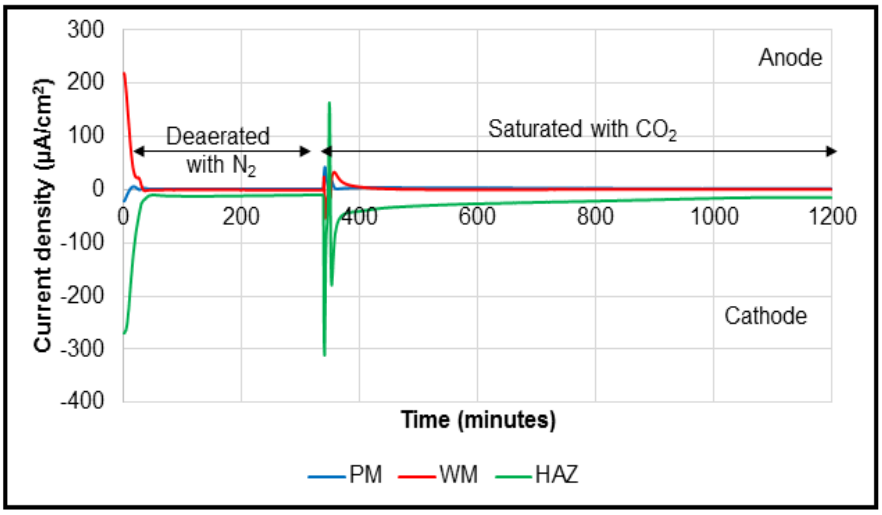

Figure 6-6 Galvanic current density for PM, HAZ and WM exposed to deaerated inhibited still brine solution

6.3.2 Self-Corrosion Measurements from LPR

A typical plot of current density with potential for the outer ring in a non-flowing inhibited brine is shown in Figure 6-7. The HAZ, the PM, and the WM have different gradients (different LPR values).

The PM is a passive (noble) component with a high LPR value and a low corrosion rate. The LPR values for the PM, HAZ and WM in still inhibited brine saturated with CO_2 are 1916, 2219 and 2286, respectively.

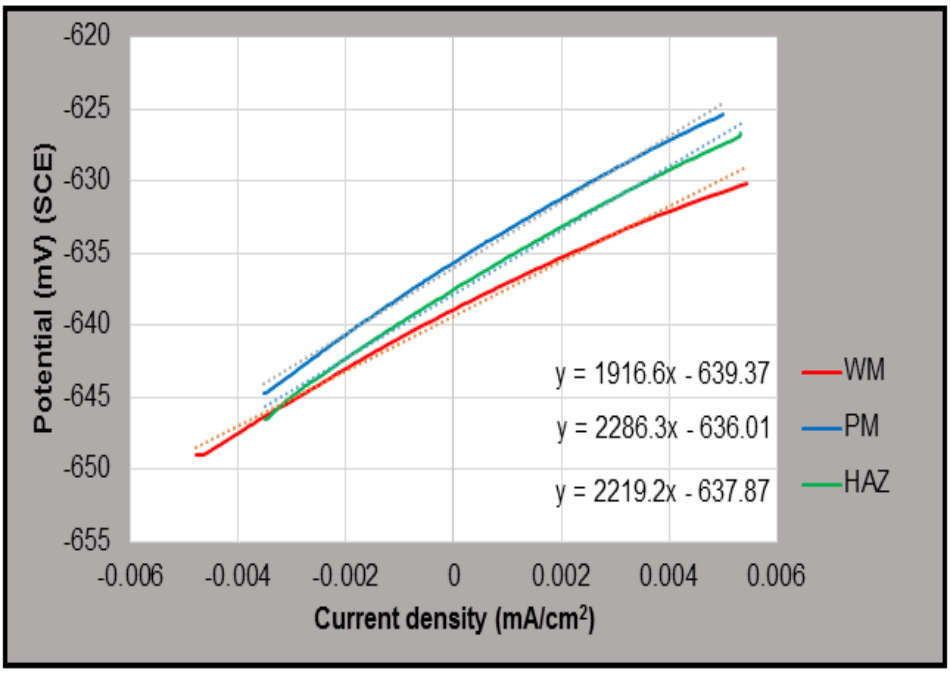

Figure 6-7 Plot of cyclic sweep measurements for weldment sections on the outer ring in still brine solution saturated with CO_2 with inhibitor.

Table 6-3 LPR characteristics (taken from Figure 6-7) for the outer ring of the target in inhibited still brine solution saturated with CO_2.

	Weld section	E_{corr} (mV) (SCE)	I_{corr} (µA/cm^2)
Outer	PM	-635.7	11.4
	HAZ	-637.5	11.7
	WM	-638.8	13.6

Table 6.3 confirms this behaviour for inhibited still brine solution saturated with CO_2. Average OCP values for the uninhibited condition are -724.6, -724.9 and -725.3 mV for PM, HAZ and WM respectively as shown in Table 4-1. Conversely, OCP in the inhibited brine are more positive with values in the range - 635 to -638 mV. The I_{corr} in with the inhibitor decreases rapidly compared to in the uninhibited environment from 90 µA/cm^2 to 11 µA/cm^2.

This behaviour is supported by Figure 6.8 which shows the OCP characteristics in an uninhibited and inhibited condition. With the addition of an anodic inhibitor, the potential becomes more positive, and the current decreases significantly. This is similar to the behaviour observed in this work with a shift to more positive E values by about 90 mV and reduced current by 79 µA/cm^2. Thus it seems likely that CORRTREAT 10-569 is an anodic inhibitor.

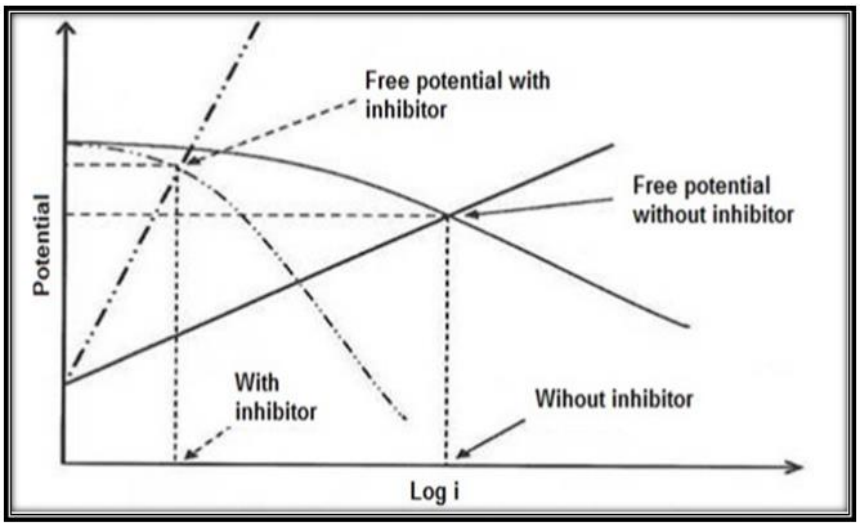

Figure 6-8 Representative Tafel plot of the change in corrosion potential with and without an anodic inhibitor [131]

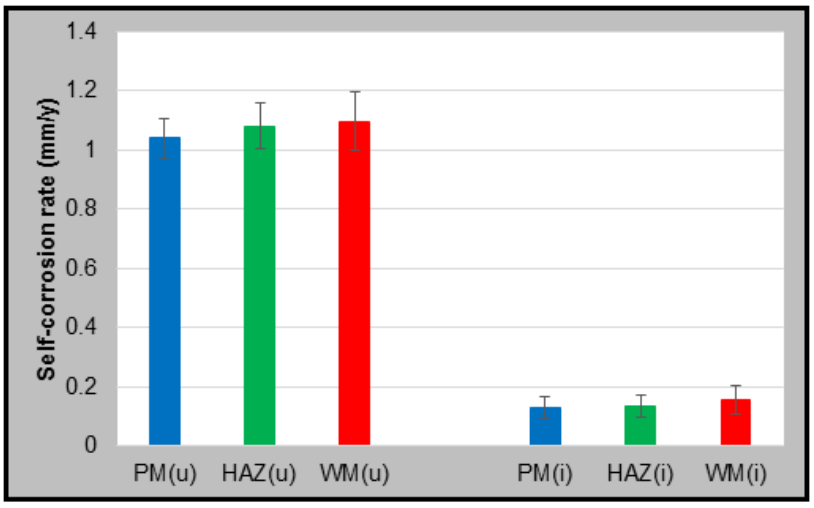

Figure 6-9 Self-corrosion rate of weldment in outer ring inhibited compared to uninhibited no-flow environment

The self-corrosion rates calculated from the LPR values of the Tafel plots in the outer ring are given in Figure 6-9. The trend is similar to the uninhibited condition where the WM is the slightly anodic component in the couple compared to the PM and HAZ. From Figure 6-9, the propensity of the WM to corrode is higher than the PM and HAZ. However, the oilfield inhibitor used reduces the rate of corrosion significantly for all working electrodes in the outer ring (~0.1 mm/y) by about 90 % compared to the uninhibited corrosion rates (~1 mm/y).

The uncoupled self-corrosion rates in the inhibited environment in this study are compared with research previously reported in literature with X65 steel welds (Figure 6-10). Barker et al. [22] used two types of inhibitors (Inhibitor A and B) in his work. Both inhibitors work well with an efficiencies in the range of 83-95%. These values are comparable to the current study.

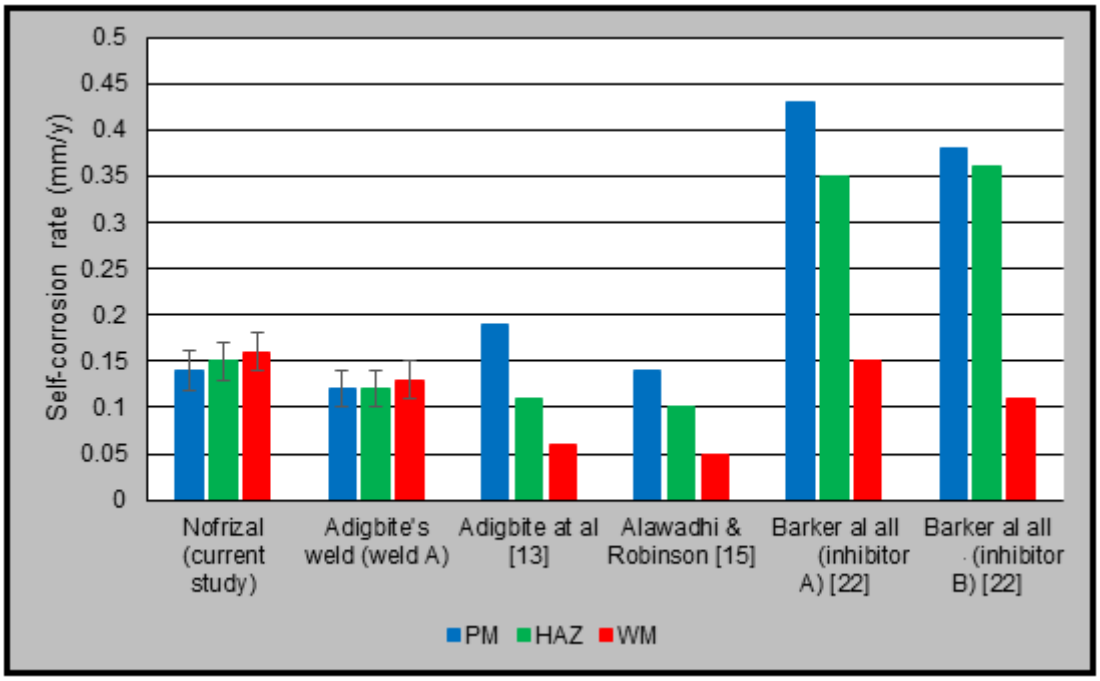

Figure 6-10 Comparison data of self-corrosion in inhibited no-flow condition

Other studies from Alawadhi & Robinson [15] and Adegbite et al. [13] use the CORRTREAT as used in this research. Alawadhi & Robinson report the inhibitor efficiency at 78-88% while Adegbite record the % IE at 90-93%. Based on this information, the inhibitor works well to significantly inhibit the corrosion reaction

of X65. For galvanic corrosion the inhibitor decreases the overall current density and hence the corrosion rate.

In general terms, the overall self-corrosion rates of weld metal with inhibitor are reduced to similar values around 0.1 mm. There is an exception for Barkers reported results for PM and HAZ. Generally while results for Barker et al. [22] (for other conditions) are on the high side however the trends are very similar to other researchers. In all cases except in this research, the weld metal is well protected compared to the rest of the weldment when in a no flow situation. In comparison, reported results in uninhibited weldments with non-flowing brine (Figure 4-7), show the differential between weld metal and PM to be proportionally lower and rates of PM and WM to be very similar to each other. However it can be said that although the trend for the proportionally higher WM rate in this research compared with PM is shown with two weldments, the reduction in corrosion rates overall indicates effective inhibition.

Adegbite's target (weld A) provides a result with a corrosion rate range from 0.1-0.15 mm/y. With this target the the WM has a slightly higher corrosion rate compared to the PM and the HAZ whilst in Adegbite's work on this same target, the PM is reported to corrode faster compare to the HAZ and WM. Four studies conducted at Cranfield University using the same oilfield corrosion inhibitor show a corrosion rate reduction around 80% despite using different weldments and an exposure duration. One implication is that the inhibitor used has good stability.

6.3.3 Electrochemical Impedance Measurement (EIS)

Nyquist plots for the three weld regions in the outer electrode ring are shown in Figure 6-11. The diameter of the implied semicircle represents the charge transfer resistance (R_t). The R_t is equivalent to the LPR values from the self-corrosion rate measurements. In the inhibited condition, the Nyquist plot (Figure 6-12) does not show complete semicircles at the low frequency region (at the far right hand side). Nevertheless, the charge transfer resistance is found using fitting software for determining R_t values. When a 45° line, is observed (Warburg) diffusion should be considered, specifically unrestricted diffusion to a large planar electrode [164].

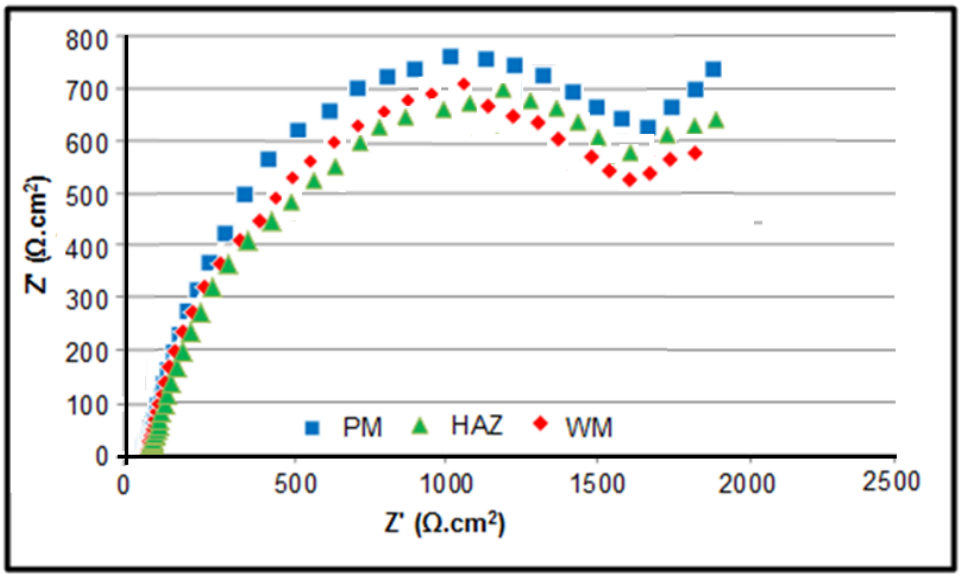

Figure 6-11 EIS characteristics for the weldment in the outer ring in inhibited brine saturated with CO_2 without flow

Water describes the Warburg impedance is the diffusional impedance for the diffusion layer of infinite thickness. The impedance depends on the frequency of the potential perturbation. At high frequencies, the Warburg impedance is small since diffusing reactants don't have to move very far. At low frequencies, the reactants have to diffuse farther, increasing the Warburg-impedance. With Warburg impedance, an electrochemical cell can be decribed by a Randles equivalent circuit [164].

The resistance values from two methods (LPR and EIS) show good agreement (Table 6-4). From this EIS result, the WM in the outer ring in stagnant conditions has the lowest charge transfer resistance (smallest semicircle), indicating the highest rate of self-corrosion. This is confirmed in Figure 6-7 (red line)

Table 6-4 EIS characteristics of the weldment in the outer ring without flow.

Flow	Weldments	R_s	R_t	R_s+R_t	LPR value	Corrosion Rate EIS (mm/y)	Corrosion Rate LPR (mm/y)
0 m/s	PM	47±0.92	2251±2.9	2298	2386	0.13±.0.02	0.13±0.04
	HAZ	52±0.87	2134±3.5	2186	2223	0.14±0.05	0.13±0.03
	WM	49±1.15	1830±4.4	1879	1916	0.15±0.04	0.16±0.04

6.3.4 Total Corrosion

A summary of the corrosion rates for each working electrode of the SJI target is shown in Figure 6-12. The total corrosion rates in the inhibited brine without flow is significantly reduced (>80%) compared to the uninhibited condition. The total corrosion rate values (green) without flow for PM, HAZ and WM are 0.17; 0.06 and 0.003 mm/y, respectively. In comparison the total corrosion rates in uninhibited brine are 1.2, 0.1 and 0.7 mm/y for PM, HAZ and WM, respectively. The WM has the lowest total corrosion rate compared with the PM and the HAZ.

Figure 6-12 shows the WM has the lowest total corrosion rate in both the inhibited and uninhibited condition without flow. The combination of a high negative galvanic corrosion rate and small positive self-corrosion of the WM, in the stagnant environment, indicates that the WM is adequately protected by currents from the HAZ and the PM. Based on this result, the CORRTREAT 10-561 inhibitor is working effectively to reduce the corrosion rate of each weld significantly, providing protection to the WM and the HAZ from preferential weld corrosion.

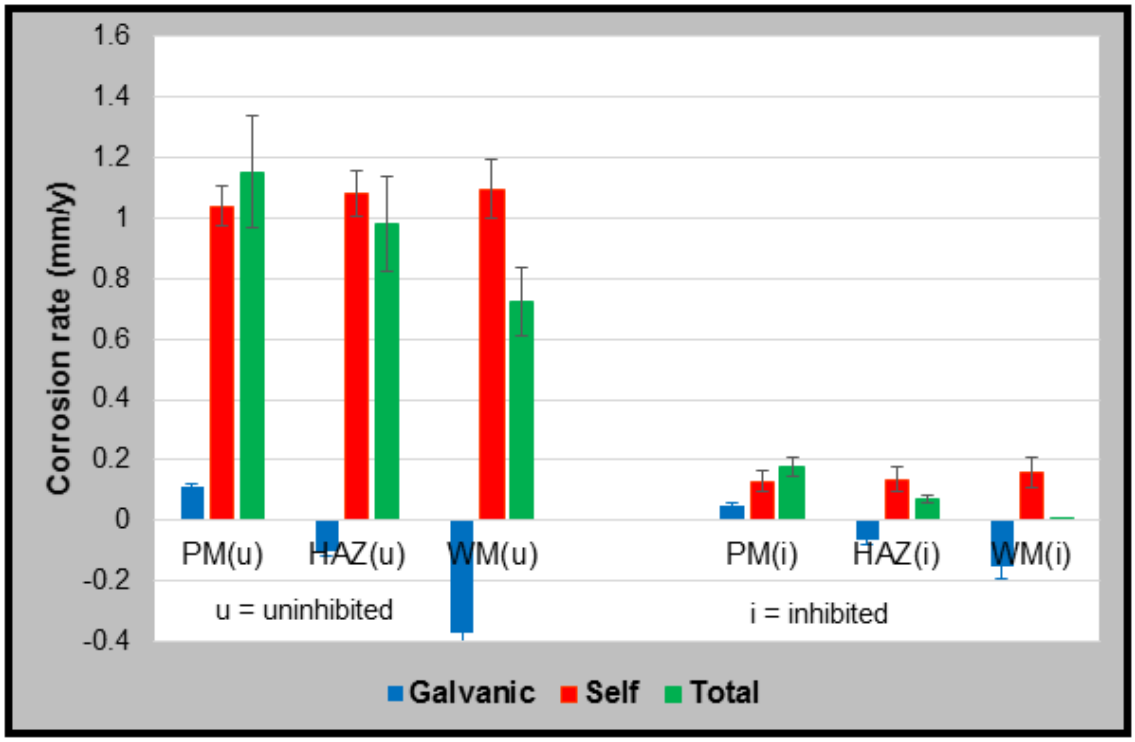

Figure 6-12 Total corrosion for the weldment in still brine saturated with CO_2 on the outer ring in uninhibited and inhibited conditions

The total corrosion rate in this study, without flow, is compared with previous studies that use different weldments and different inhibitors show a similar trend, wherein preferential welding corrosion is negligible in still inhibited brine saturated with CO_2 [16,58,60,178]. Based on the above results, the application of CORRTREAT 10-569 is compatible to use in a variety of offshore production systems to mitigate the rate of corrosion in stagnant or still conditions.

6.4 Surface Characterisation

The effect 30 ppm of inhibited solution in still brine saturated with CO_2 to the weldment is analysed using SEM and FIB techniques. Following 20 hours exposure, to the inhibited solution, the surface is cleaned, using firstly deionised water, then iso-propanol and dried with warm air.

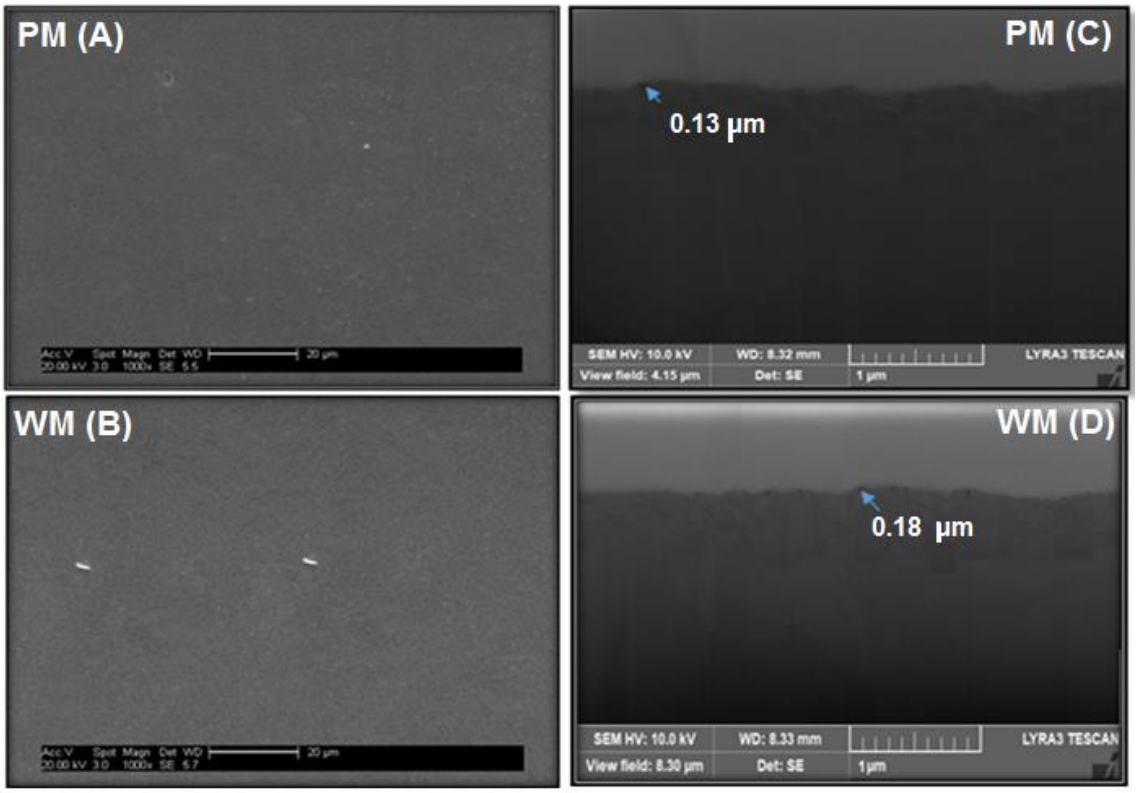

Figure 6-13 The SEM (A, B) and FIB images (C, D) for the PM and the WM after exposure in 30 ppm inhibited brine saturated with CO_2 after 20 hours

Figure 6-13 shows images taken from the SEM and FIB from the exposed surface. SEM images in Figure 6-13 (A, B) show a steel surface with very little apparent modification following exposure in comparison to the uninhibited

condition (Figure 5-8). Figure 5-8 shows significant metal (Fe) dissolution in the carbonic acid environment. The inhibitor minimises the metal loss significantly and the surface is left smooth and free of cracks or cavitation.

Focused ion beam (FIB) analysis is used to determine the characteristics of any surface layer or corrosion product layer (CPL) after the exposure. Figure 6-13 C and D are FIB micrographs from a surface exposed to inhibited no-flow conditions, with a bright protective platinum film deposited on the surface for protection against the ion beam. Figure 6-13 C & D shows a CPL thickness for the PM and the WM of 0.13 and 0.18 µm respectively. These values were lower than CPL in the uninhibited environment at a range of 0.3-0.4 µm (Figure 4-13). The FIB analysis supports the results from SEM characterization. From the examples above (Figure 6-13) it is concluded that the CORRTREAT oilfield inhibitor 10-569 protects the weld from corrosion attack in a still, non-flowing environment of brine saturated with CO_2.

6.5 Effect of Inhibitor Concentration in Flowing Environment

The effect of inhibited condition from the weldment in a flowing environment is assessed using 10 m/s. The current characteristics from galvanic, LPR and impedance measurements from the addition of 30 ppm inhibitor CORRTREAT 10-569 are explored. The effect of inhibited brine saturated with CO_2 is monitored by calculating the total corrosion rate of each working electrode in the no-flow and high turbulence region. Later, surface analysis is conducted by using the SEM-EDX, FIB, XRD and Raman spectroscopy.

6.5.1 Galvanic Measurement

The typical galvanic behaviour of the target at 10 m/s with the inhibitor is different to that in a stagnant environment thought to be a result of shear stresses on the target surface. The galvanic current at 10 m/s (associated with a shear stress of 280 Pa) is presented in Figure 6-14. In still, inhibited brine deaerated with N_2, the PM current reduces significantly from 54 to 10 µA. This indicates inhibitor film formation on the weld surface. After 200 minutes, the current becomes more stable. In this situation, the PM is slightly anodic and protects the WM and the

HAZ. After 400 minutes, the movement of brine at 10 m/s begins. A small current increases with PM in an anodic region, but after 200 minutes, the current decreases slowly until at the end of exposure the PM is cathodic.

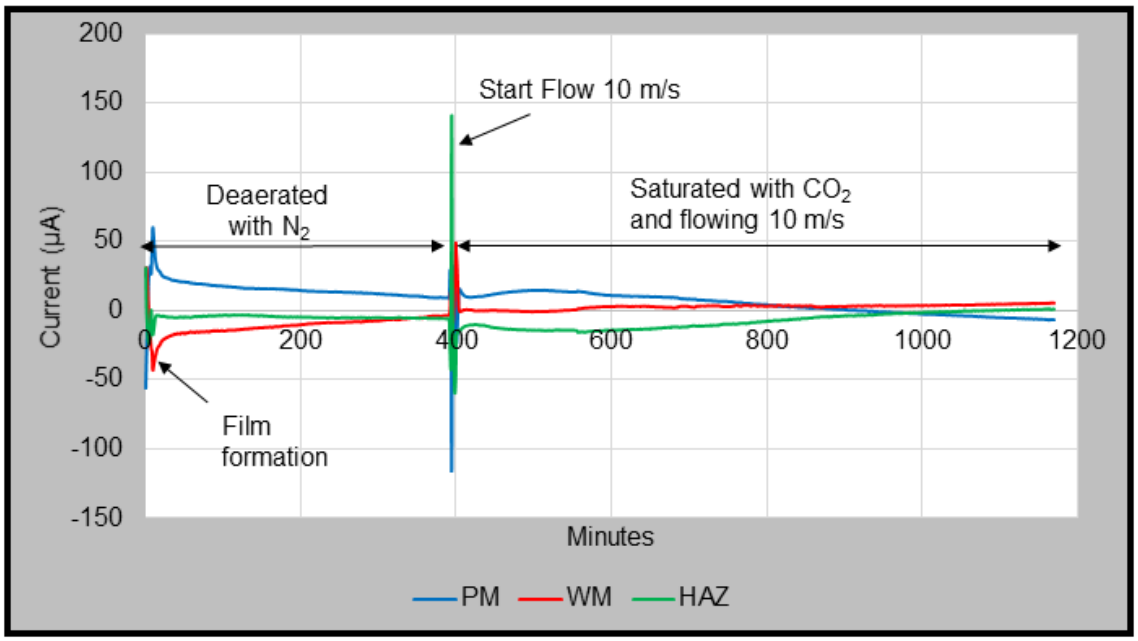

Figure 6-14 the characteristic of galvanic current inhibited flowing 10 m/s saturated with CO_2

Figure 6-15 describes the average galvanic current at the end of the exposure of the weldment where the total anodic (positive) currents from the weld metal and HAZ are similar to the negative currents (cathodic) of the parent metal.

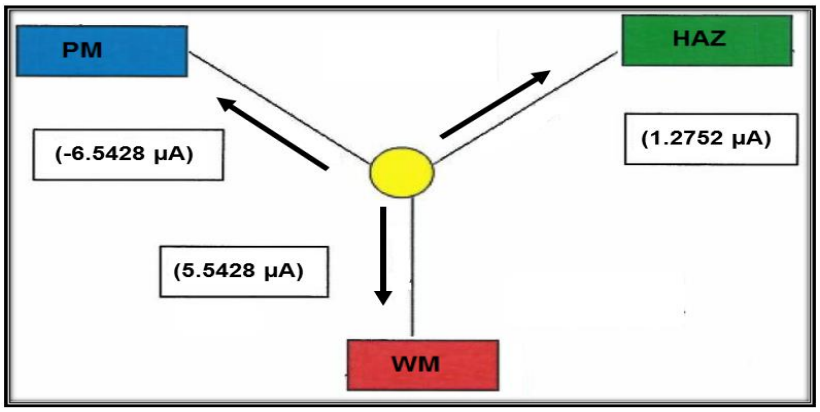

Figure 6-15 Average galvanic currents for flowing 10 m/s uninhibited brine saturated with CO_2

Figure 6-16 describes the current density of each electrode inhibited at 10 m/s. The WM has a high current density compared to the HAZ and the PM, so the WM may experience preferential weld corrosion. However, when this result is compared with the uninhibited conditions at 10 m/s, the corrosion rate of each uninhibited electrode is reduced significantly. With the WM in particular, the current density decreases from 63 µA/cm^2 in uninhibited conditions at 10 m/s to 18 µA/cm^2 in the inhibited flowing environment.

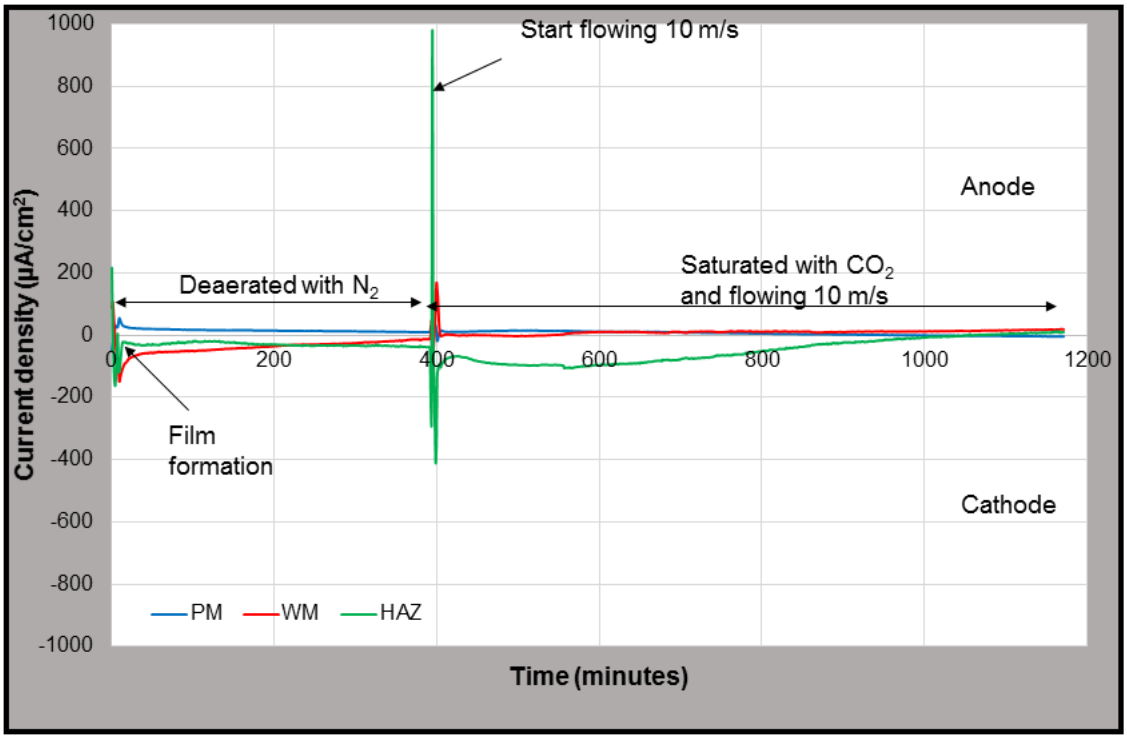

Figure 6-16 The current density of each electrode in inhibited flowing 10 m/s saturated with CO_2

From these results, it can be seen that the addition of the CORRTREAT 10-569 inhibitor is effective to minimise the rate of corrosion of the weld in flowing environments. The galvanic behaviour is similar to previous research in an inhibited environment at 10 m/s. Previous researchers found that the WM was anodic while the corrosion current density reduces significantly compared to an uninhibited environment at 10 m/s [13,16].

6.5.2 Self-corrosion Measurements from LPR

The self-corrosion of the weldment in inhibited brine saturated with CO_2 at 10 m/s condition from LPR measurement is shown in Figure 6-17. From linear regression, the R_P values of each electrode are found in the flowing inhibited condition. They are larger compared to the uninhibited flowing condition, meaning that the corrosion rate had reduced significantly in the presence of the inhibitor.

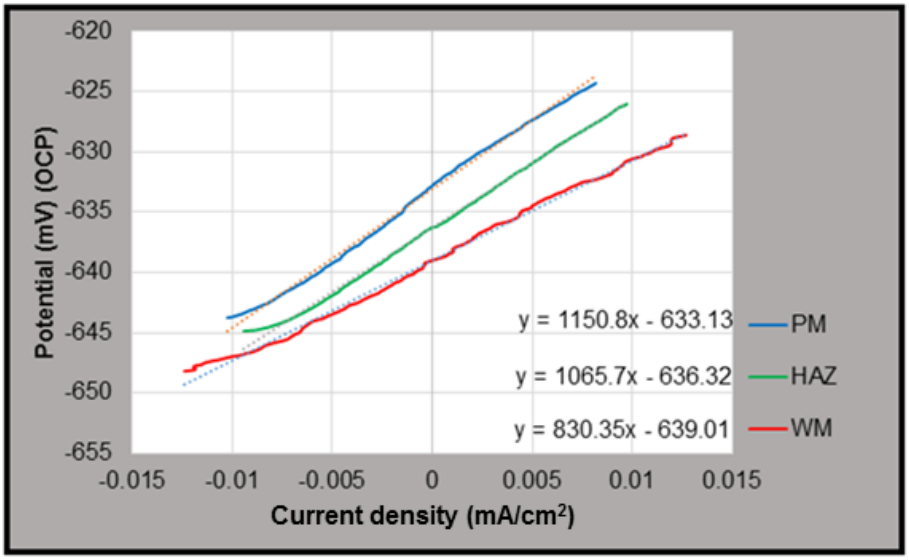

Figure 6-17 The self-corrosion of the weldment in outer ring at flowing inhibited condition and saturated with CO_2

The characteristics of the weldment in an inhibited flowing environment, from the Tafel plot, are summarised in Table 6-5.

Table 6-5 Tafel plot characteristic of the weldment inhibited flowing condition

	Weld section	E_{corr} (mV)	I_{corr} (μA/cm^2)
Outer	PM	-652.8	22.6
	HAZ	-656.3	24.4
	WM	-658.9	31.3

In the inhibited no-flow condition, the self-corrosion is 80 % less than at the corrosion rate in an uninhibited environment. The associated metal loss due to

self-corrosion in flowing environment for the WM is 0.36 mm/y followed by the HAZ and the PM; at 0.28 and 0.36 mm/y respectively (Figure 6-18).

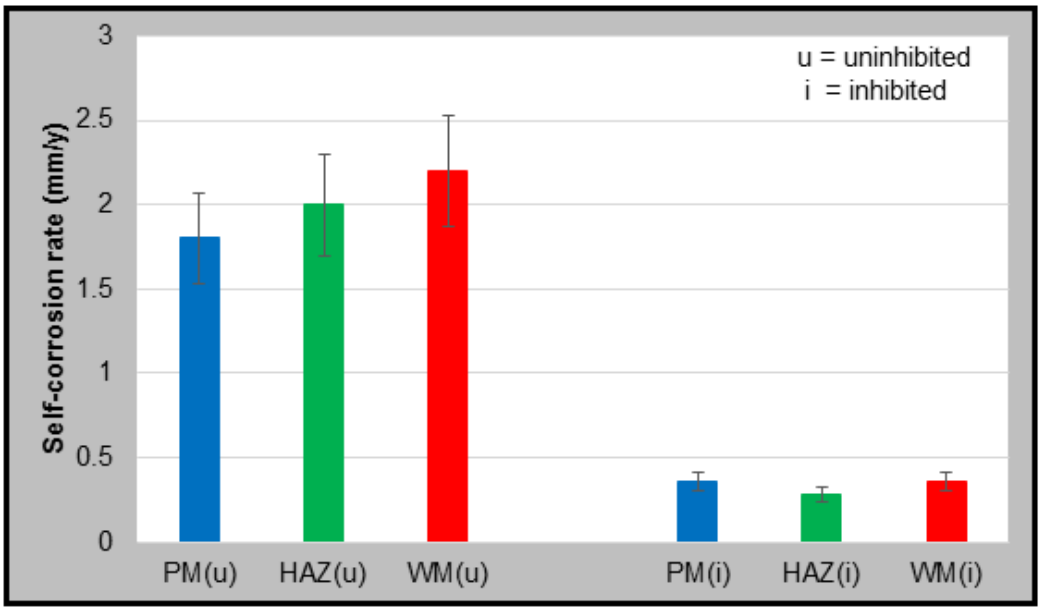

Figure 6-18 Self-corrosion of weldment in the outer ring, both inhibited and uninhibited at 10 m/s

The reduction of corrosion rate in inhibited condition for the PM, the WM, and the HAZ in a range 75-80 % is lower than the uninhibited flowing condition.

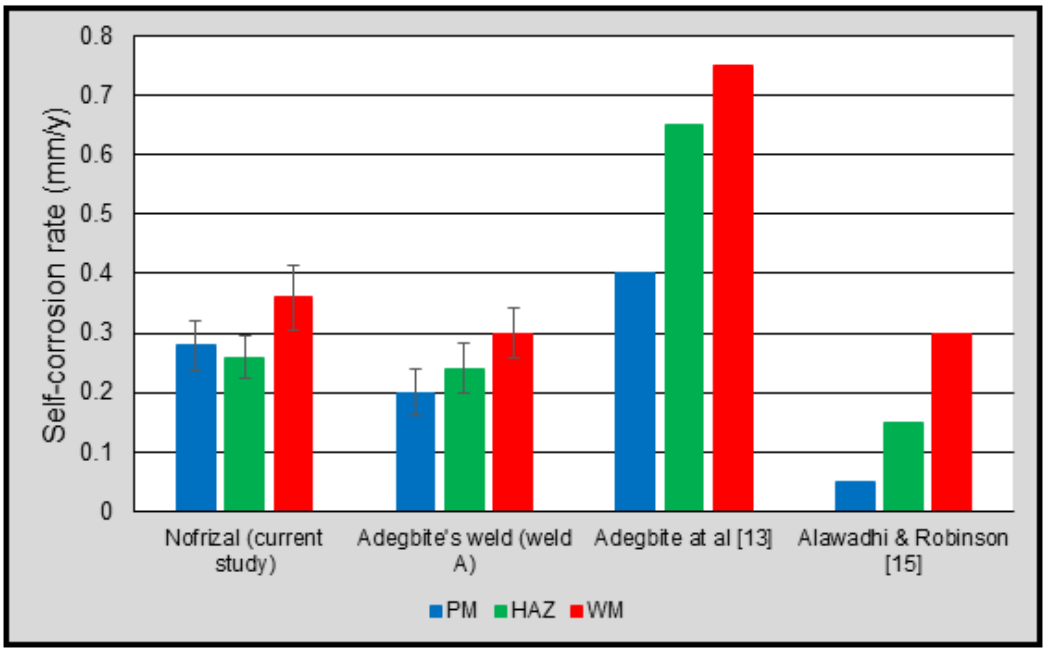

Figure 6-19 Comparison data of self-corrosion in inhibited a flowing condition

The self-corrosion rate of other studies on an X65 weldment; different techniques and conditions are used (Figure 6-19 and Table 6-6).

Table 6-6 refers to the SJI and RCE (rotating cylinder electrode) techniques used to monitor the corrosion reaction in a flowing environment. It is calculated (from equation 2-20) that the SJI method generated a maximum shear tress value of 280 Pa at some point on the target. A study from Adegbite *et al.* [13], on target A, also used in this study, shows a higher corrosion rate in comparison with this study. A different temperature was used; Adegbite used a temperature of 40 ^{o}C which is higher as compared to 25 ^{o}C in this study using his target. However, when Adegbite's weldment was analysed with a 25 ^{o}C as the present study, the corrosion rate was comparable.

Table 6-6 Comparison result flowing inhibited saturated with CO_2

Ref	Method	Flow rate	T (^{o}C)	σ (Pa)	Corrosion rate		
					PM	HAZ	WM
Current	SJI	10 m/s	25	280	0.26	0.28	0.36
Current (weld A) [used in 13]	SJI	10 m/s	25	280	0.20	0.24	0.30
Adegbite et al [13]	SJI	10 m/s	40	280	0.4	0.65	0.75
Alawadhi & Robinson [15]	RCE	5000 rpm	70	70	0.05	0.15	0.3

Table 6-6 refers to the SJI and RCE (rotating cylinder electrode) techniques used to monitor the corrosion reaction in a flowing environment. It is calculated (from equation 2-23) that the SJI method generated a maximum shear tress value of 280 Pa at some point on the target. A study from Adegbite *et al.* [13] on target A, also used in this study, shows a higher corrosion rate in comparison with this study. A different temperature was used Adegbite used a temperature of 40 ^{o}C which is higher as compared to 25 ^{o}C in this study using his target. However,

when Adegbite's weldment was analysed with a 25 ^{o}C as the present study, the corrosion rate was comparable.

A study by Alawadhi and Robinson [15] used an RCE method in inhibited conditions at a rate of 5000 rpm. A lower corrosion rate is seen compared to the other studies reported by researchers (Table 6-7), even though this experiment was conducted at 70 ^{o}C at an estimated shear stress of 70 Pa. As comparison, with RCE at 11000 rpm, the calculated maximum shear stress is around 270 Pa.

6.5.3 Electrochemical Impedance Spectroscopy (IES)

The Nyquist plots for the three weld regions in the outer electrode ring are shown in Figure 6-20. The R_t is equivalent to the LPR values from the of the self-corrosion rate measurements (Table 6-7). In the inhibited flowing condition, the Nyquist plot fit is similar to that in no-flow inhibited environment. The fit was unable to follow a full semi-circle, particularly in high frequency areas. However, appropriate R_t values can still be measured by a fitting tool. At the high frequencies a 45° line, is observed and this is attributed to unrestricted diffusion ie Warburg diffusion [164].

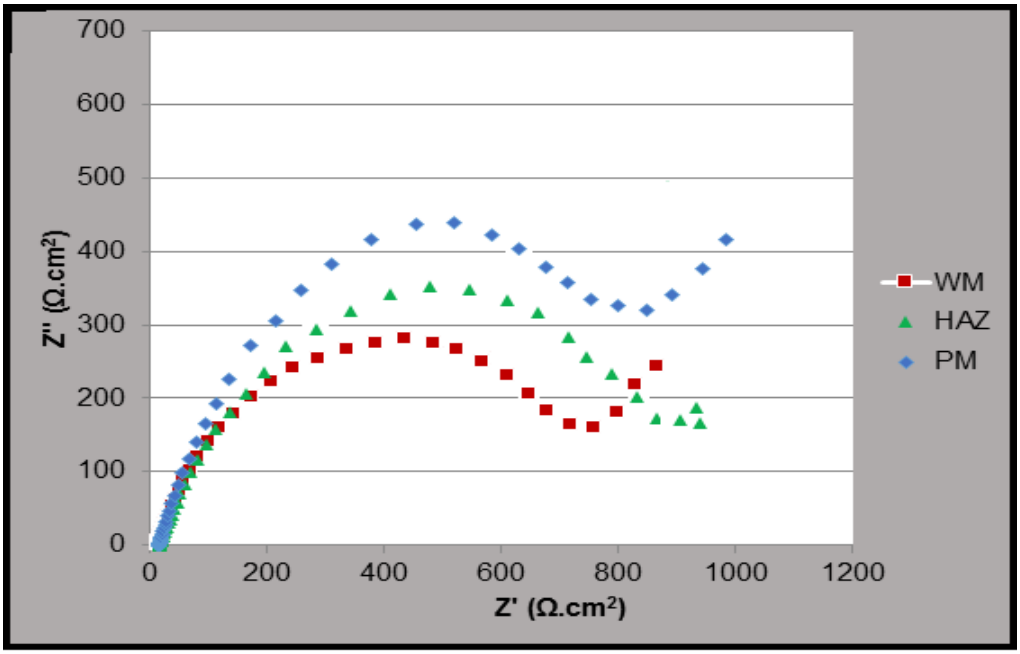

Figure 6-20 EIS analysis for the weldment in an inhibited flowing environment

From the EIS results (shown in Figure 6-20), the WM in the outer ring with stagnant conditions has the lowest charge transfer resistance (R_t) which correlates with the highest corrosion rate (0.35 mm/y). The PM has the highest R_t and therefore the lowest corrosion rate (0.29 mm/y). The resistance values obtained with both methods (LPR and EIS) show good agreement (Table 6-7).

Table 6-7 EIS and LPR comparison of the inhibited weldment at 10 m/s

Flow (m/s)	Electrodes	R_s	R_t	R_s+R_t	LPR value	Corrosion Rate (mm/y) IES	Corrosion Rate (mm/y) LPR
10	PM	35±1.2	1080±5.6	1115	1150	0.27±.0.043	0.26±0.039
	HAZ	41±1.6	984±6.5	1025	1065	0.29±0.049	0.28±0.005
	WM	43±1.9	817±5.8	860	830	0.35±0.051	0.36±0.005

6.5.4 Total Corrosion Rate

A summary of the corrosion rate on each working electrode of the SJI target in inhibited flowing environment is shown in Figure 6-21.

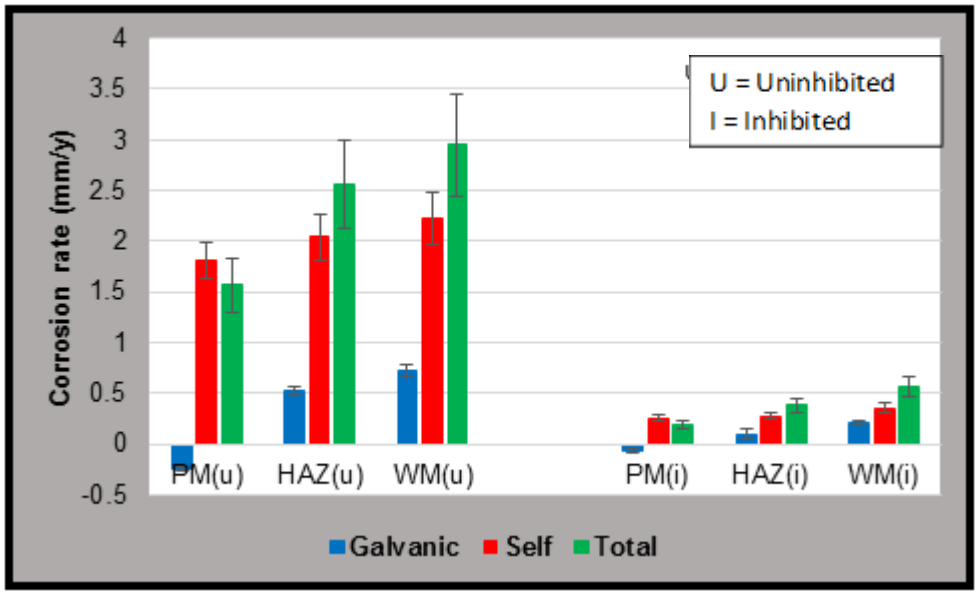

Figure 6-21 Total corrosion of the weldment in uninhibited and inhibited brine saturated with CO_2 at 10 m/s

The total corrosion rate of each section of the weldment in the inhibited brine with a flow rate of 10 m/s is significantly reduced compared to the uninhibited condition. The total corrosion rates (green) for 10 m/s inhibited condition are 0.2, 0.4 and 0.6 mm/y for the PM, HAZ, and WM respectively. In comparison, uninhibited values are 2.0, 2.1 and 2.2 mm/y for the PM, HAZ, and WM respectively. In the inhibited condition at 10 m/s, the WM and the HAZ have the highest total corrosion rates compared to the inhibited stagnant condition. This means that, at high flow rates, PWC is possible. This result is in good agreement with other findings [13,15,16,178].

6.6 Surface Characterisation

To look at the detail of the weldment surface after the corrosion process, the specimen of weld was analysed by SEM after being exposed for 20 hours of inhibited brine saturated with CO_2 in flowing environment. Figure 6-23A and B shows the SEM analysis for PM and WM with 30 ppm inhibitor with flow.

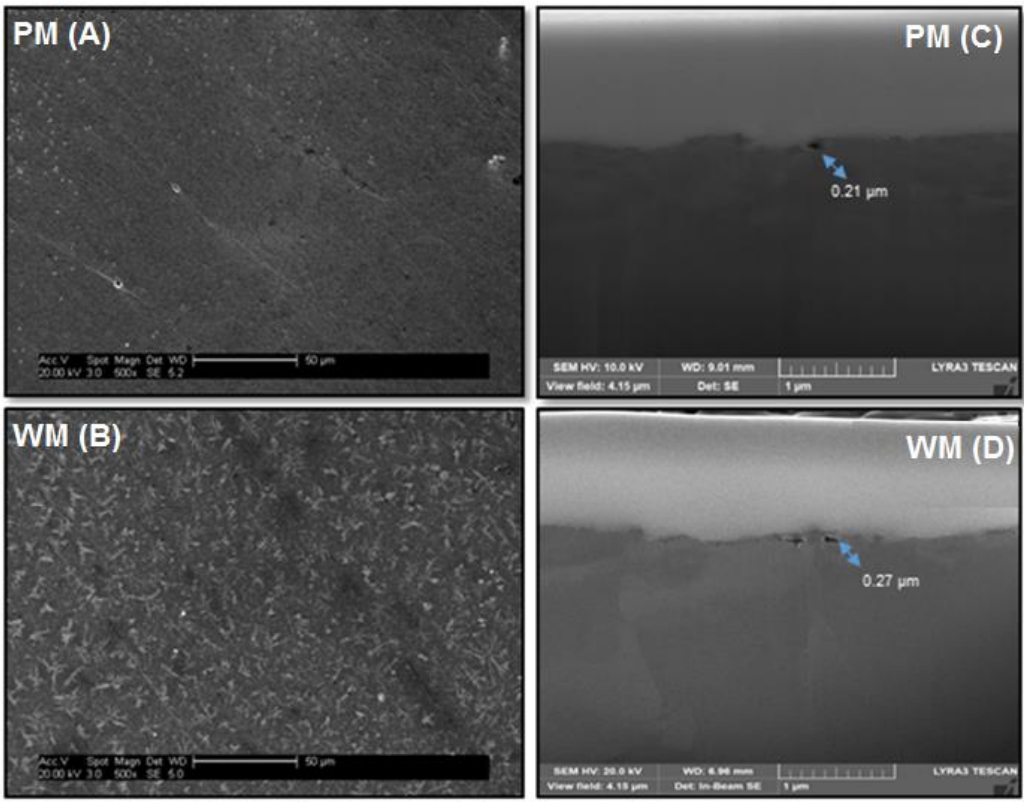

Figure 6-22 The SEM and FIB analysis of the PM and the WM after exposed with inhibited brine 30 ppm saturated with CO_2 and 10 m/s for 20 hours

SEM images show that excellent protection has been offered to both material, with the WM appearing more protected as the original polishing marks are still to be seen. There was a significant improvement on the weld surface as compared to uninhibited no-flow condition (Figure 5-8). The SEM result supports the electrochemical measurement, especially in total corrosion measurement which shows that the WM possess a higher corrosion rate in flowing inhibited brine saturated with CO_2 as shown in Figure 6-23.

Figure 6-23C and D showed the FIB performance under inhibited flowing conditions. The thickness of corrosion the product in the PM and the WM were reduced significantly from about 3 µm (in uninhibited flowing) to about 0.28 µm (inhibited flowing environment). The FIB analysis supports the result from SEM characterization and electrochemical measurement. It can be concluded that CORRTREAT oilfield inhibitor 1059 is also suitable for corrosion protection in an oilfield flowing environment.

6.7 Chapter Summary

The inhibition efficiency of CORRTREAT 1069 has been evaluated for the weldment of X65 using an optimum concentration of 30 ppm under no-flow and flowing conditions saturated with CO_2.

In term of objectives, the electrochemical and non-electrochemical analysis was employed and from this chapter, it can be summarised:

- ✓ The results with inhibitor showed that it could be applied in an oilfield production due to its higher efficiency in a flowing environment.
- ✓ In an inhibited condition and flowing conditions, the total corrosion rate of the PM was higher than total corrosion of the WM and the PM, so that the weldment in no-flow inhibited is free from PWC attack.
- ✓ The surface analysis supports the electrochemical measurement to evaluate the performance of CORRTREAT inhibitor in no-flow and flowing condition saturated with CO_2

7 EFFECT OF DISSOLVED OXYGEN WITH FLOW

The presence of oxygen is one of the most significant issues in production and transportation of oil in pipelines due to its potential to cause a hazard. Oxygen reacts with metal as part of a natural process, modifying (or degrading) the metal into its more chemically stable oxide or hydroxide. The dissolution of oxygen in drilling fluids is a significant cause of drilling-pipe corrosion. There is a possibility that sources of oxygen are in the water phase and carbon dioxide as a result of leaking pump seals, casing, and process vents. Laboratory explorations of pipeline corrosion using submerged jet impingement have been conducted to mimic the effect of oxygen contamination to see if SJI can be used to understand this phenomenon.

7.1 Effect of Dissolved Oxygen in Uninhibited Condition

Jet impingement experiments were carried out, in which air was deliberately admitted to the flow loop to investigate the effect of oxygen. The effect of dissolved oxygen in uninhibited brine containing CO_2 was analysed without flow and again at 10 m/s. To investigate an effect, three conditions were with artificial sea water saturated with CO_2:

(a) fully deaerated

(b) fully deaerated, then aerated with 20 cm^3/min of air

(c) not deaerated, then aerated with 20 cm^3/min of air.

It is expected that with 20 cm^3/min of air, the volume of oxygen dissolved inside the brine is 4.2 cm^3/min due to the comparison between oxygen and nitrogen is 21:69 %.

All conditions were as previously with a jet of 10 m/s in the flow loop. Artificial seawater is considered to be well deaerated when its potential reaches -740 mV (SCE). Therefore, in these initial experiments, for condition (a) and (b), there is no dissolved oxygen present. To monitor the effect of oxygen contamination, electrochemical analysis from the SJI target was recorded and surface analysis performed to analyse the corrosion product after exposure.

7.1.1 Galvanic Measurements

The galvanic effect on the X65 steel in the SJI target in uninhibited brine saturated with CO_2 is studied at 10 m/s whilst adding oxygen to the flow loop. Figure 7.1 describes the galvanic current and galvanic current density characteristics when 20 cm^3 oxygen was added after fully deaerating the brine with nitrogen.

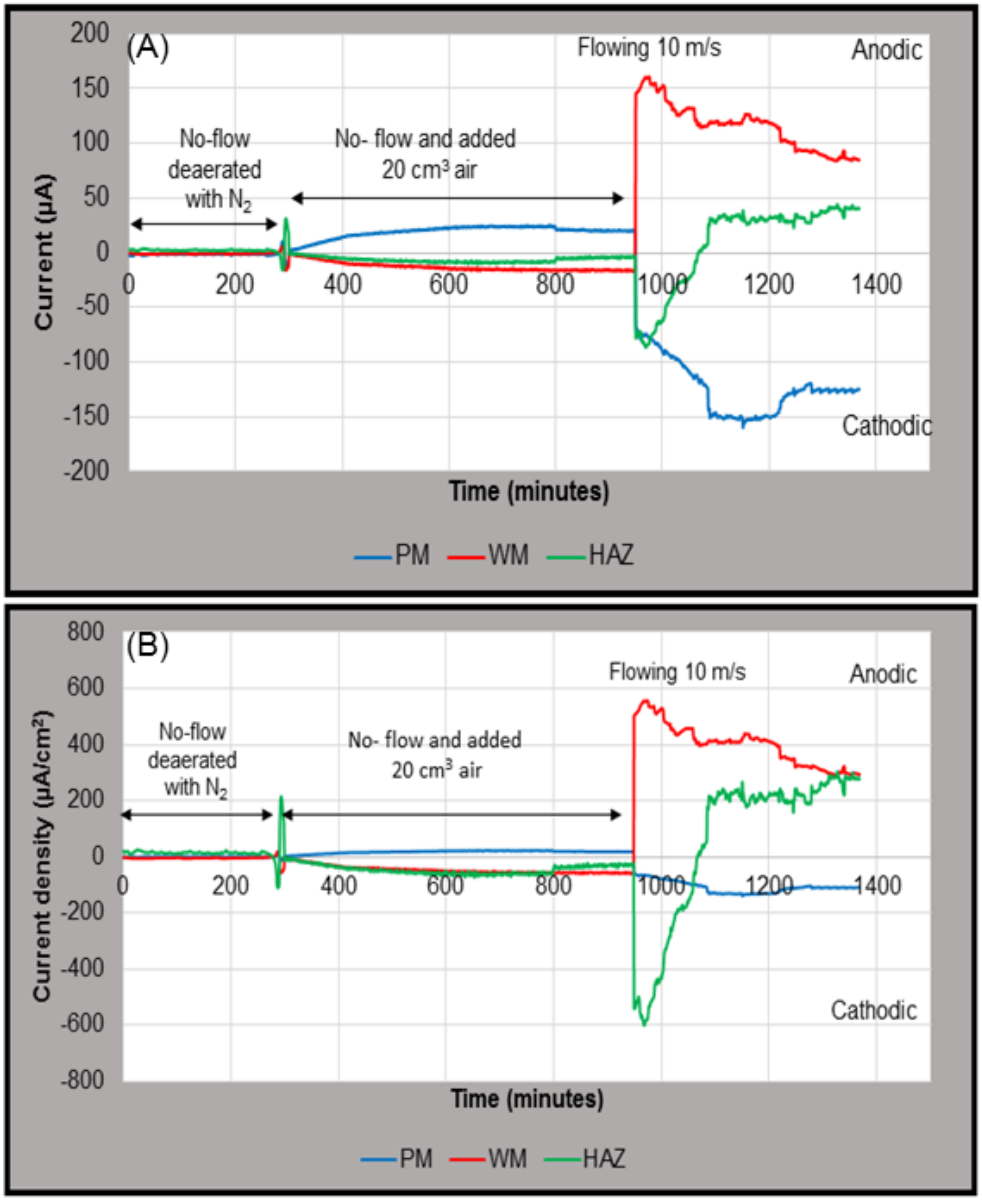

Figure 7-1 X65 weldment (outer ring) in deaerated uninhibited brine with CO_2 at 10 m/s when 20 cm^3 of O_2: (A) galvanic current and (b) galvanic current density

Figure 7-1(A) shows the galvanic currents for each electrode are very low in the fully deaerated environment. The presence of 20 cm^3 of air after fully deaerating the brine with nitrogen without flow, the PM is in an anodic position with 20 µA of current which may be sufficient to protect the weld metal and the heat affected zone. When brine impacts on the target at a velocity of 10 m/s, a significant change of galvanic current was observed, mainly for the weld and the HAZ (with associated currents of 84 µA and 40 µA respectively). This shows that the weld metal and the HAZ are corroding faster, now protecting the PM. The galvanic current density for each electrode is presented in Figure 7.1(B). After over 6 hours of flowing brine, the WM has a high current density around 294 µA/cm^2 and HAZ at 276 µA/cm^2. These current densities are significantly enhanced (5 times higher) compared to a fully deaerated flowing condition with no dissolved oxygen (Chapter 5). This suggests that the weld and the HAZ regions are less protected by a high oxygen concentration that naturally drives the corrosion reaction. As Figure 7-2(A) and (B) shows severe corrosion is experienced when the weldment is exposed to flowing brine with some dissolved oxygen, in this case with 20 cm^3.

The initial part section of Figure 7-2(A) show the situation with stagnant brine and a small amount of air. The PM (blue line) is anodic and provide protection to the WM and the HAZ around 45 µA. However, when the pump is started and the turbulent brine reaches the target, the galvanic current increases and the weld and HAZ become anodic and corrode. The WM and the HAZ remain anodic to the end of this exposure (6 hours) and a current is generated that is 50% higher compared to a fully deaerated environment. The more significant current density produced at the weld (414 µA / cm^2) and the HAZ (315 µA / cm^2) in Figure 7-2 B shows that without deaeration, the effect of dissolved oxygen causes more severe corrosion due to an abundance of dissolved oxygen in the brine solution. Adegbite et al. [13] studied the effect of oxygen with an SJI target in flowing conditions. From this study also observed that an addition of air increased the anodic current density.

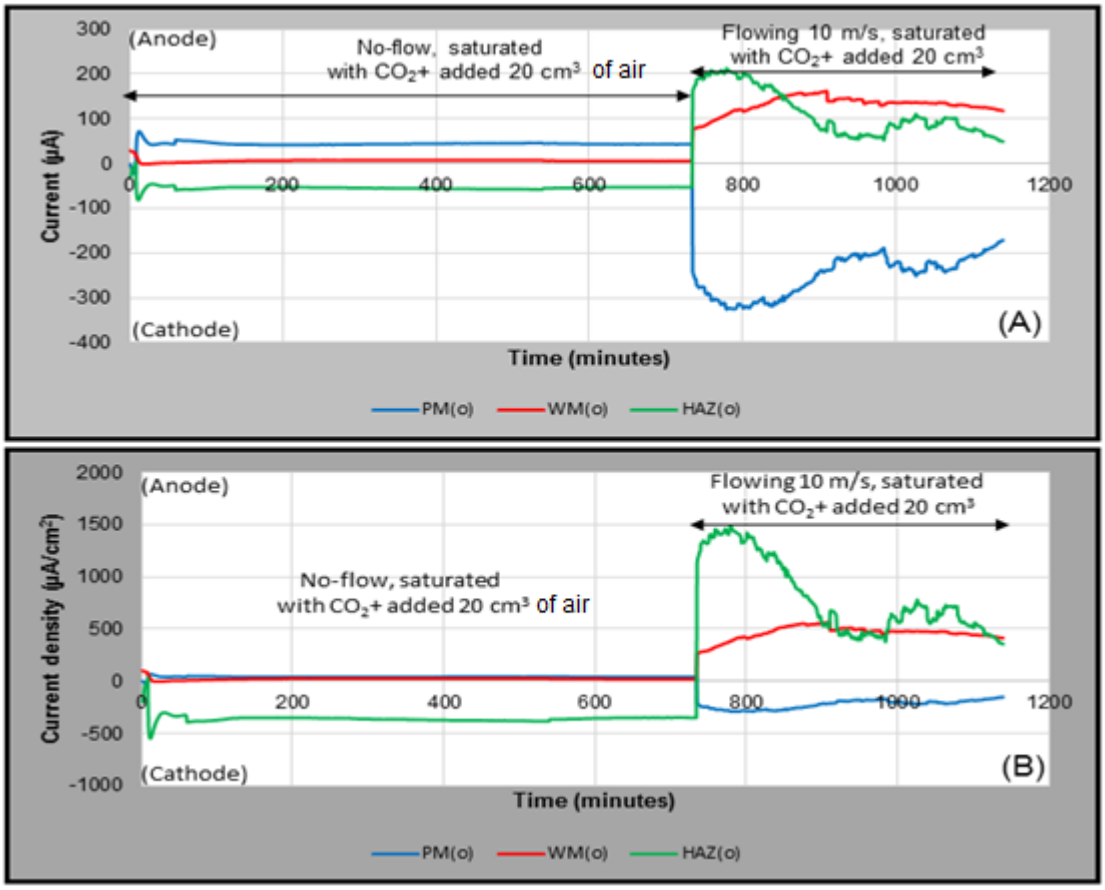

Figure 7-2 The X65 (outer ring) in non-deaerated uninhibited brine with CO_2 at 10 m/s and 20 cm^3 of O_2: (A) galvanic current and (B) galvanic current density

7.1.2 Self-corrosion Measurements

The significant contribution of dissolved oxygen on self-corrosion rate of the weldments at 10 m/s is depicted in Figure 7-3. In the uncoupled state, the PM, which was non-deaerated with an addition of 20 cm^3 air had the highest corrosion rate due with a low LPR (65.8). The effect of 20 cm^3 air addition (or 4 cm^3 oxygen) almost doubles the corrosion rate compared to when deaerated (Figure 7-4). When there is no deaeration, the corrosion rate is three times the rate of the fully deaerated corrosion rate. The corrosion rates are significant and detrimental to all of the weldment electrodes with oxygen present in flowing sea water, and the amount of dissolved oxygen in the non-deaerated solution appears to have been greater than 16 cm^3 from the increase in LPR compared to air added to a deaerated solution. The target surface appeared brown following exposure

indicating iron oxide had formed. Typically, in deaerated conditions a grey dull surface develops following exposure of a reflective grey surface after polishing.

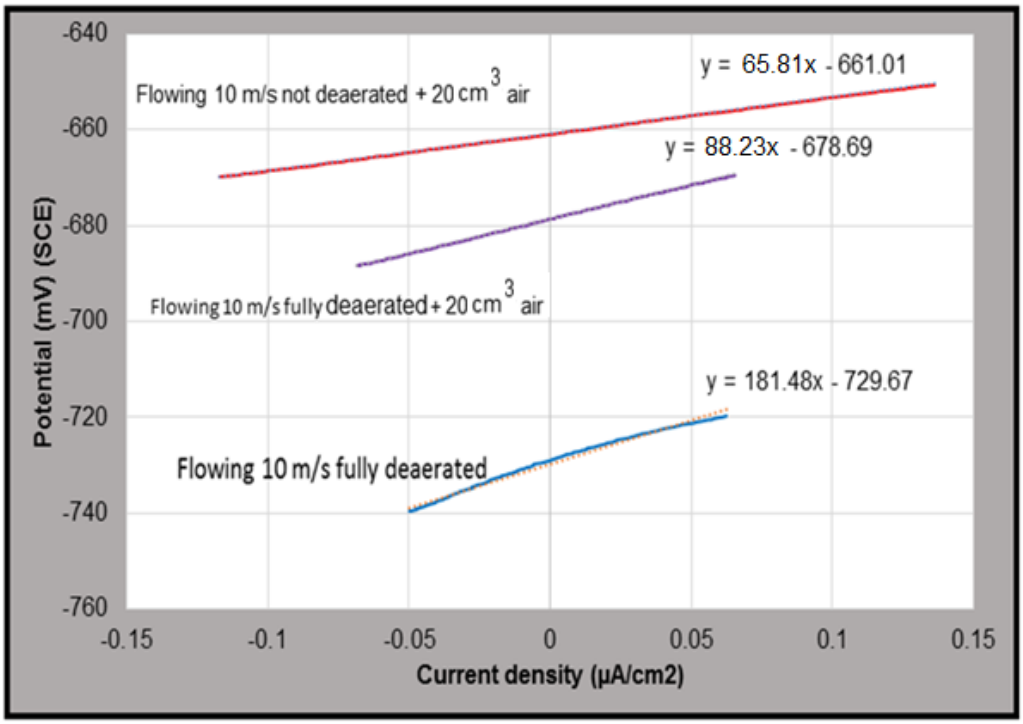

Figure 7-3 The effect of aeration on the LPR values of the weldment in uninhibited brine containing CO_2 at 10 m/s for the PM (outer ring)

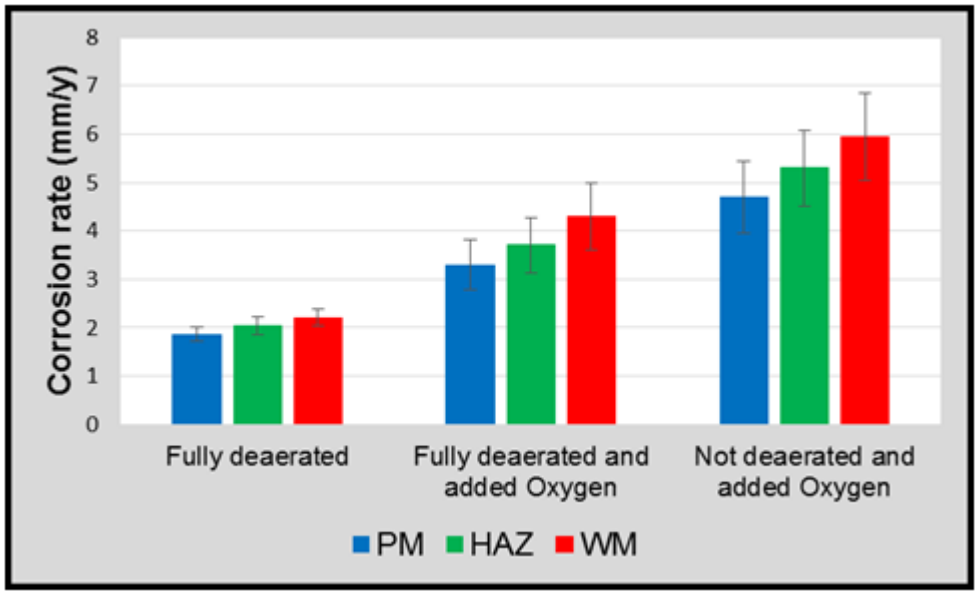

Figure 7-4 Self-corrosion rates of the PM (outer ring) in uninhibited brine containing CO_2 and oxygen at flowing 10 m/s

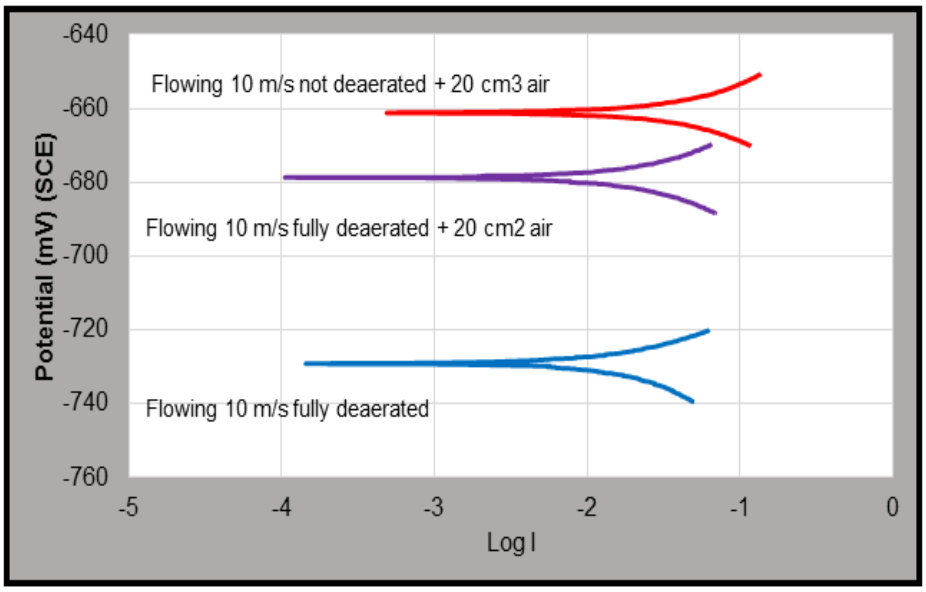

Figure 7-5 Effect of aeration for the PM (outer ring) on the potential in uninhibited brine containing CO_2 at 10 m/s

Figure 7-5 shows the corrosion potential values in the uncoupled condition in brine solution saturated with CO_2, flowing at 10 m/s (the readings were taken from LPR measurements). The corrosion potential (E_{corr}) of the PM in outer the electrode is shown in Table 7-1. The E_{corr} for fully deaerated brine was -729 mV, however, when 20 cm^3 air was added, the E_{corr} changed by 50 mV and by 70 mV for the non-deaerated brine as a result of adding of 20 cm^3 of air into the system. While the E_{corr} is the best parameter for predicting the galvanic corrosion, however, the self-corrosion rate is not necessarily related to the potential, so, the noblest electrode does not always have the lowest corrosion rate.

Table 7-1 LPR characteristic of the weldment taken from Figure 7-3

Corrosion environment	Ecorr (mV)	I_{corr} (µA/cm^2)	LPR
Fully deaerated	-729.3	143.26	181.5
Fully deaerated +20 cm^3 air	-678.2	287.93	90.3
Not deaerated +20 cm^3 air	-661.1	417.47	62.28

The total corrosion rate due to oxygen contamination is shown in Figure 7-6. In general, the presence of oxygen accelerates the total corrosion rate on the weldment. For the WM and HAZ that have smaller areas compared to the PM, corrosion attack is found to be more severe. PWC attack is seen clearly. Figure 7-6 shows the total corrosion rate for WM and HAZ; for a fully deaerated brine (A) is in the range 1.8-2.3 mm/y, for fully-deaerated + 20 cm^3 of air (B) in the range 2-8 mm/y, and for non-deaerated brine with 20 cm^3 of air (C) in the range 3-11 mm/y. These values are very high and significant for surface facilities in oil and gas industries.

In industry, the possibility of oxygen being present during oil and gas production occurs through pump or valve leakages allowing oxygen to access the production line. Based on the information above, due to the harmful effects, the amount of oxygen present should be at a minimum so that the chances of accidents and fatalities are also at a minimum. Prevention of accidents can also prevent high expenditure.

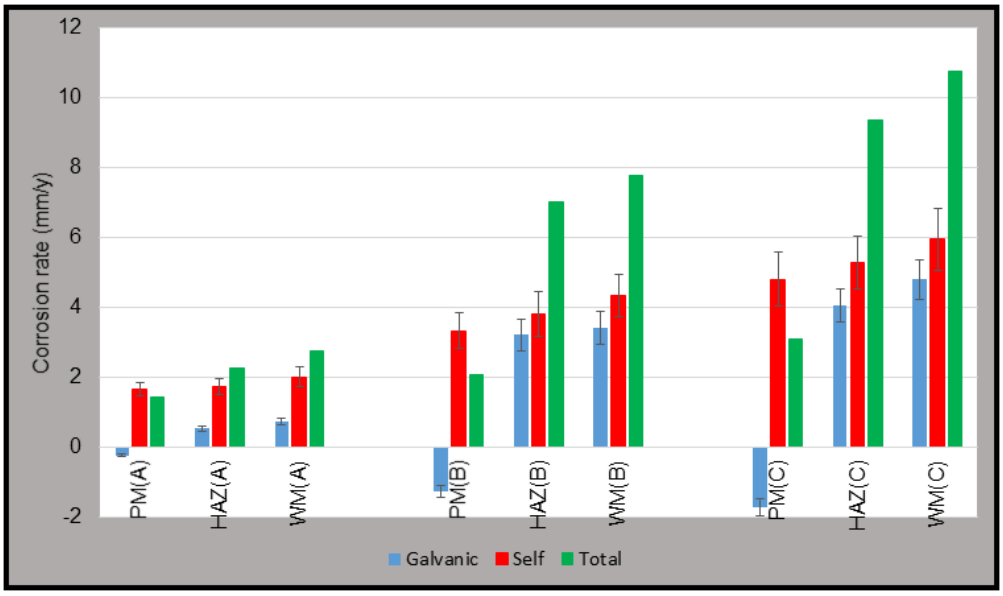

Figure 7-6 Total corrosion rate for the weldment (outer ring) in uninhibited brine saturated with CO_2; for fully deaerated (A); fully deaerated with the addition of 20 cm^3 of air (B); not deaerated added 20 cm^3 air (C)

The effect of oxygen has been studied by several researchers. Notably, this study finds a similar trend with Adegbite et al. [13] with where oxygen contamination accelerates the corrosion rate by approximately 4-5 times compared to an oxygen-free environment. Dong *et al.* [179] also studied the effect of oxygen on N 80 steel and found the current density increases 5 times with 0.05 MPa O_2 added into the system, whilst the corrosion potential increases by 41 mV vs AG/AgCl.

7.1.3 Surface Analysis

Surface analysis was used to monitor the surface of the weldment after the occurrence of the corrosion reaction in the presence of oxygen. SEM analysis was used to observe the surface appearance of the weldment after SJI with uninhibited brine saturated with CO_2 and 20 cm^3 of air. Figure 7-7 shows SEM micrographs for the weld and parent metal at a magnification of 1000x.

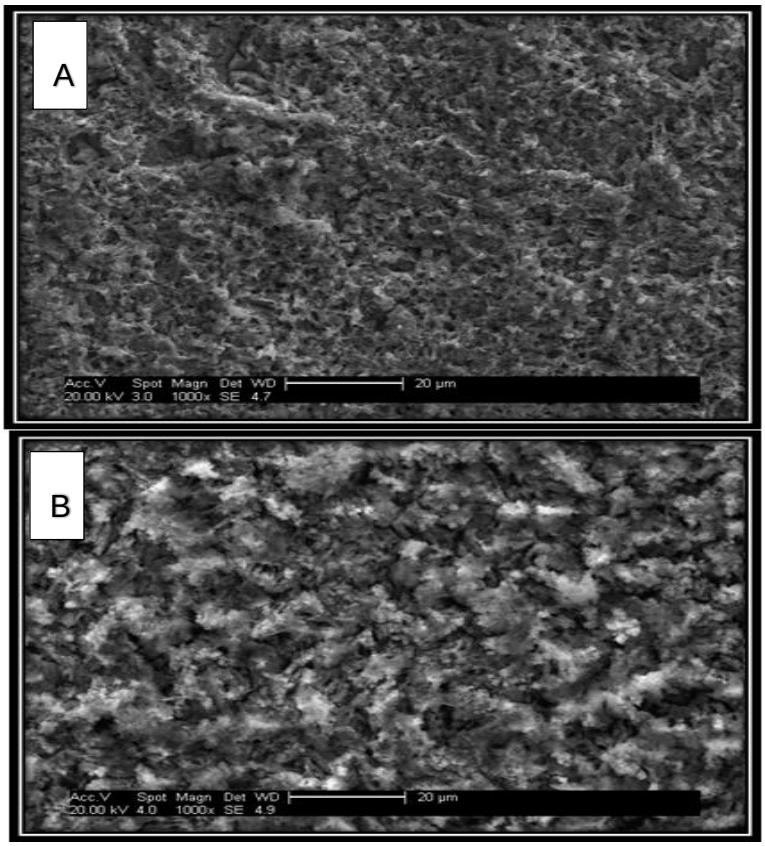

Figure 7-7 SEM micrograph of the PM (A) and WM (B) at 10 m/s in not deaerated uninhibited brine and 20 cm^3 oxygen

From Figure 7-7, it can be seen that in flowing and oxygenated conditions, corrosion attacks appear more intense on welds as compared to the parent metal. The layer of WM (7-7 B) is very rough and some cracks on the surface are visible. The presence of cementite (Fe_3C) was observed on the WM surface. Furthermore, there are some tiny particles (as a result of particle growth) on the weld surface which can be confirmed with XRD analysis.

The chemical properties and composition of the weldment was studied by using the EDX technique in flowing condition for the three different experiment conditions (Table 7-2). Fe reduces from around 90 % (fresh weldment after polished) to 60% (wt) for the PM and the WM. Conversely, oxygen or oxide increases from zero to about 11-13% (wt), and the level of carbon or carbide increases from 1% to around 20% (wt). An accumulation of carbon and oxygen is seen after the weldment exposure with non-deaerated uninhibited brine with an addition of 20 cm^3 of air. The amount of dissolved oxygen actively enhances the corrosion reaction with more activity in the anodic region. A further indicator is the reduction in Fe due possibly to a surface layer enriched with oxygen.

Table 7-2 EDX analysis of chemical composition of the PM and the WM after exposure with uninhibited not deaerated brine flowing at 10 m/s

Elements	PM		WM	
	Not corroded (fresh PM)	Corroded PM Flowing condition	Not corroded (fresh WM)	Corroded WM Flowing condition
C	0.7	16.1	0.9	20.6
Si	0.1	0.2	0.3	0.2
Mn	1.6	1.4	1.7	1.6
Ni	0.3	0.4	0.2	0.3
Cu	0.2	0.3	0.2	0.2
O	-	11.6	-	13.6
Fe	97.1	69.7	96.7	63.5
Total	100	100	100	100

FIB (Focused Ion Beam) analysis was carried out and a micrograph is shown in Figure 7-8. The corrosion attack of the weldment that uses a non-deaerated brine

containing oxygen dissolved in flowing conditions produces a very detrimental effect. The corrosion attack at every weld is very quick as seen in the picture (Figure 7-8). The area exposed to the corrosion attack is around 11 μm, and this attack is four times bigger than the corrosion impact produced at fully deaerated brine at 3.15 μm depth (Chapter 5).

Results from SEM and FIB analysis support those from the data using the electrochemical method, particularly, self-corrosion measurements. Among all the weldment, the WM has the highest rate of corrosion followed by the HAZ and the PM.

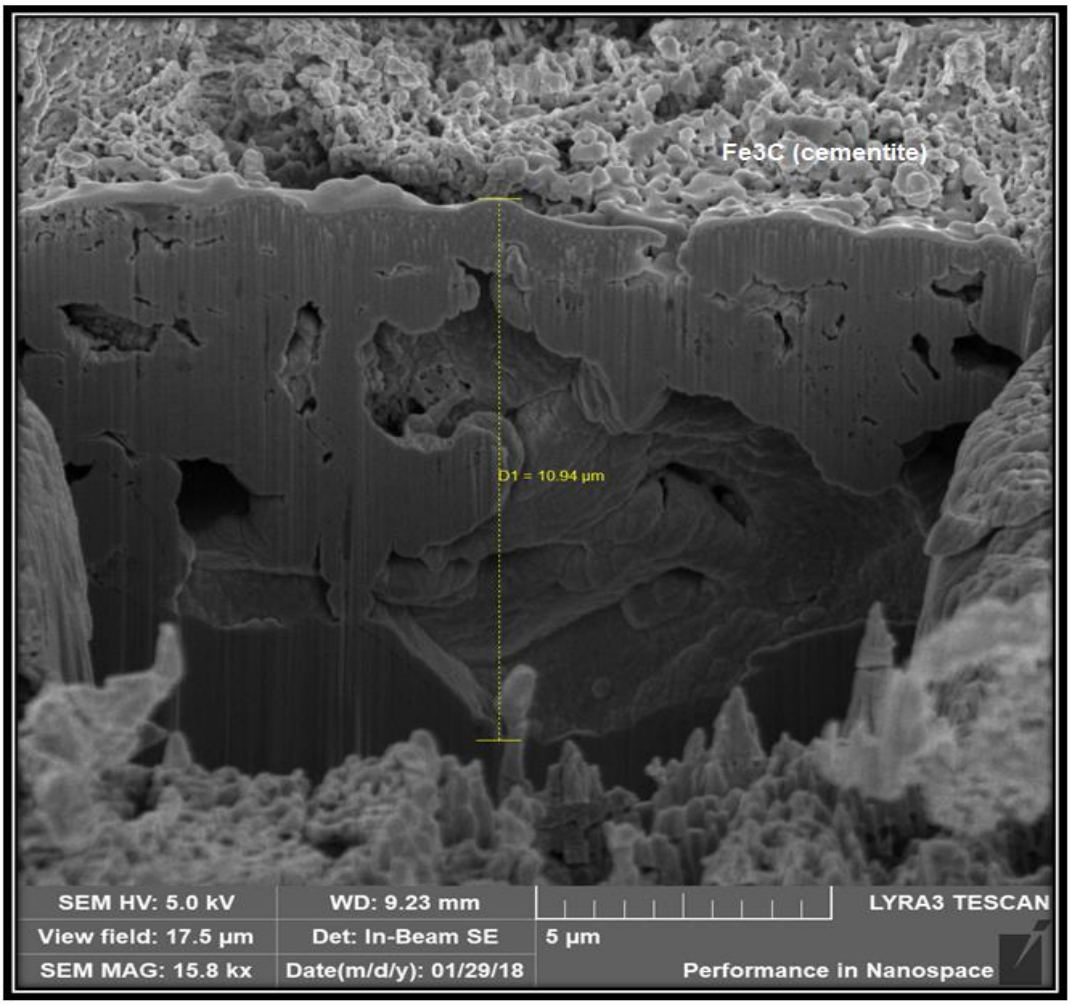

Figure 7-8 FIB cross section of the WM near surface after exposure for 20 hours with uninhibited non-deaerated brine saturated with CO_2 using 10 m/s

A grey film is typically formed on the weld in a brine saturated with CO_2. However, with added air, the surface particularly on the WM is dark grey and appears relatively thick. The surface is essentially porous in structure, and many slightly different fissures are visible on the weldment surface. The surface or surface film appears non-protective and this is consistent with the very high total corrosion rates measured when this film is visible. A similar trend obtained in Figures 7-7 and 7-8 from SEM and FIB analysis to that shown by others in previous studies [14,15,49,66].

XRD results from this surface layer are shown in Figure 7-9 of the weldment after the corrosion process in flowing brine at 10 m/s saturated with CO_2 with the addition of 20 cm^3 of air. Figure 7-9 shows peaks consistent with the presence of cementite when compared to a standard. The intensity of cementite peaks in a flowing environment is greater than in the non-flowing environment.

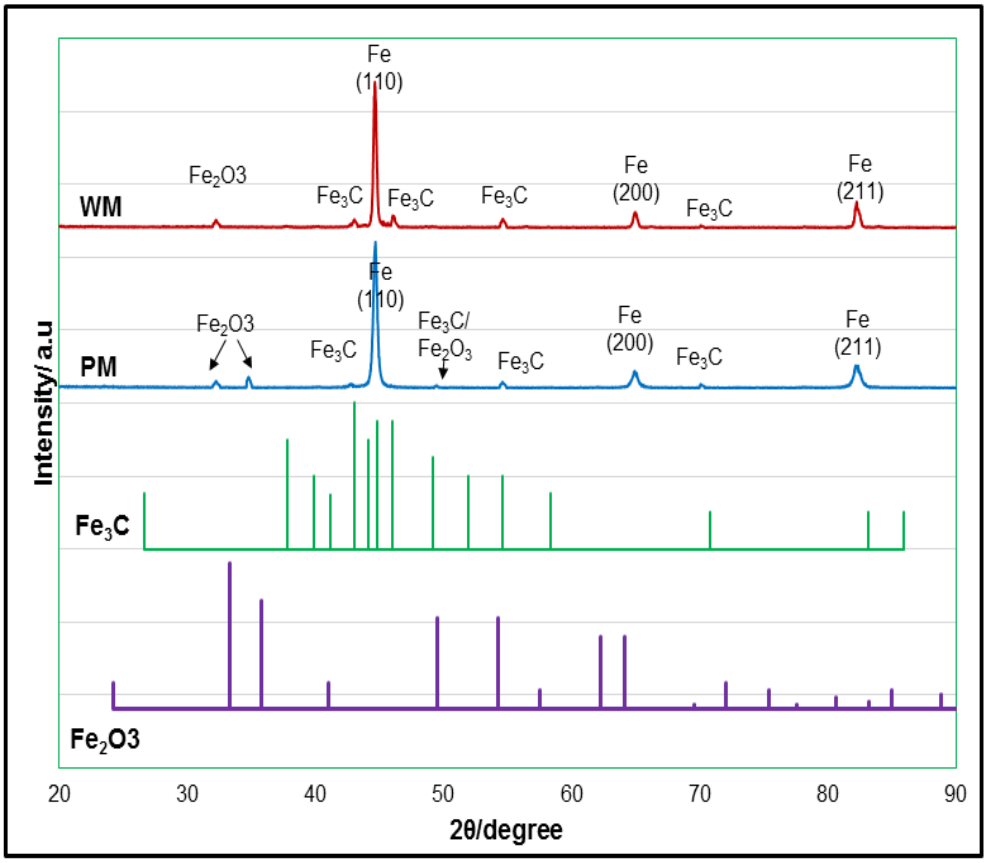

Figure 7-9 XRD spectra of the weldment when exposed with dissolved oxygen non-deaerated at flowing condition brine saturated with CO_2

The X65 weldment is an high strength low alloy steels that consists of two microstructures, namely; eutectoid ferrite and pearlite, where pearlite comprises of ferrite and cementite microstructure. Figure 7-8 is associated with the external framework (skeleton) of cementite (Fe_3C) and suggests that it has a more noble potential than ferrite so that the selective dissolution of ferrite (proeutectoid and eutectoid ferrite) can occur on the weldment and leaves more cementite on the weldment surface [15,139,180–183]. Thus with flowing brine, more ferrite will dissolve and allows cementite to accumulate on the weldment surface.

Figure 7-9, shows that after the weld is exposed to uninhibited brine saturated with CO_2 and oxygen, there are two types of corrosion products formed, namely; cementite (Fe_3C) and hematite (Fe_2O_3). The presence of hematite (Fe_2O_3) is because the oxygen dissolved in the brine solution which allows the reaction between CO_2 and O_2 to occur, is now available to form the stable Fe_2O_3. However, Fe_2O_3 and cementite (Fe_3C) do not protect the surface because they form porous films, and this supports the corrosion rate results obtained during electrochemical measurements. No $FeCO_3$ layer was detected probably due to unsuitable conditions for the formation of $FeCO_3$, in this case low temperature and high pH. The surface has both cementite (Fe_3C) and Fe_2O_3.

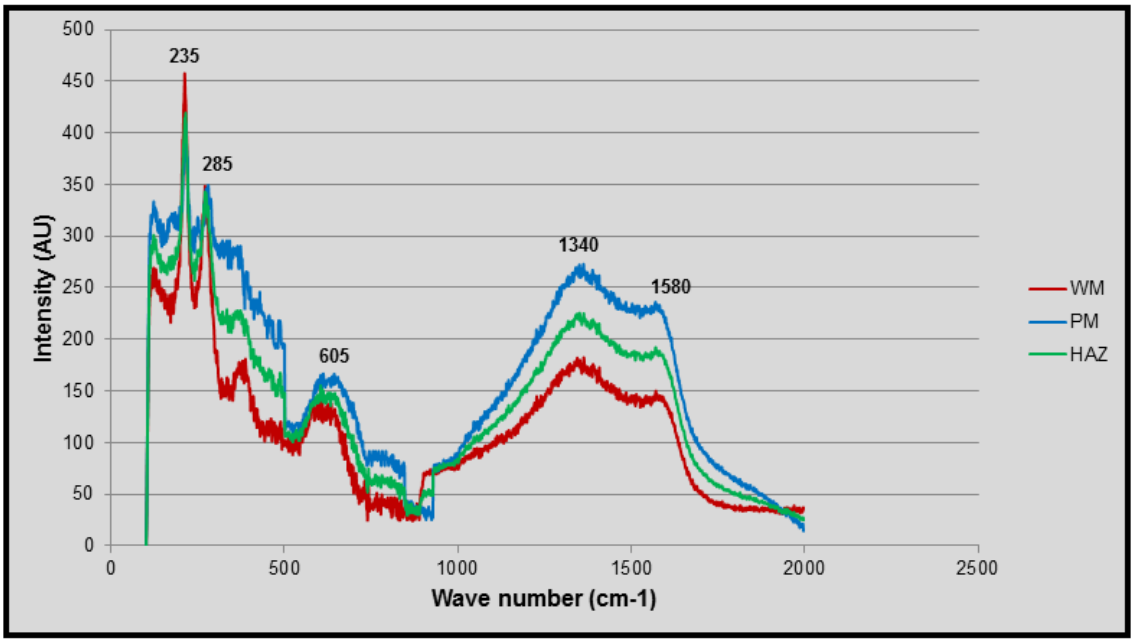

Figure 7-10 Raman peaks of the weldment in non-deaerated brine saturated with CO_2 with added 20 cm^3 oxygen at 10 m/s showing characteristics for cementite

Raman analysis was used to study the corrosion product that formed on the electrode surface after the corrosion process of 20 hours in non-deaerated brine at 10 m/s. Figure 7-10 shows the Raman spectra from the exposed weldment which support the data from the SEM and FIB analysis. Some spectra matched with the standard peaks of cementite (Fe_3C) and hematite (Fe_2O_3). Two peaks are present at wave numbers 1340 and 1580 cm^{-1}, which are characteristic of absorption of cementite (Fe_3C), while the other peaks at 235 and 285 cm^{-1} are attributed to the standard peaks of hematite (Fe_2O_3) as shown in Table 3-5 [170].

7.2 Effect of Dissolved Oxygen in Inhibited Condition

The effect of dissolved oxygen on corrosion of an X65 weldment in inhibited brine saturated with CO_2 was performed using SJI at 10 m/s. The current characteristics of coupled (galvanic) and uncoupled (LPR) parts of the weldment were performed after the addition of 30 ppm oilfield inhibitor CORRTREAT 10-569 so that the total corrosion rate could be calculated. The surface analysis, using the SEM and FIB, was performed to assess the corrosion product after the corrosion process.

7.2.1 Galvanic Measurements

Similar to the effect of oxygen dissolved in uninhibited condition, three different conditions (mentioned previously in this chapter) are compared to monitor the impact of oxygen contamination on the weldment under an inhibited environment. Galvanic currents for inhibited fully deaerated brine at 10 m/s is shown in the previous chapter (Figure 6.15). Figure 7.11 shows the galvanic features of the weldment in an inhibited environment with the addition of air into (A) fully deaerated brine (A), and (B) not deaerated brine.

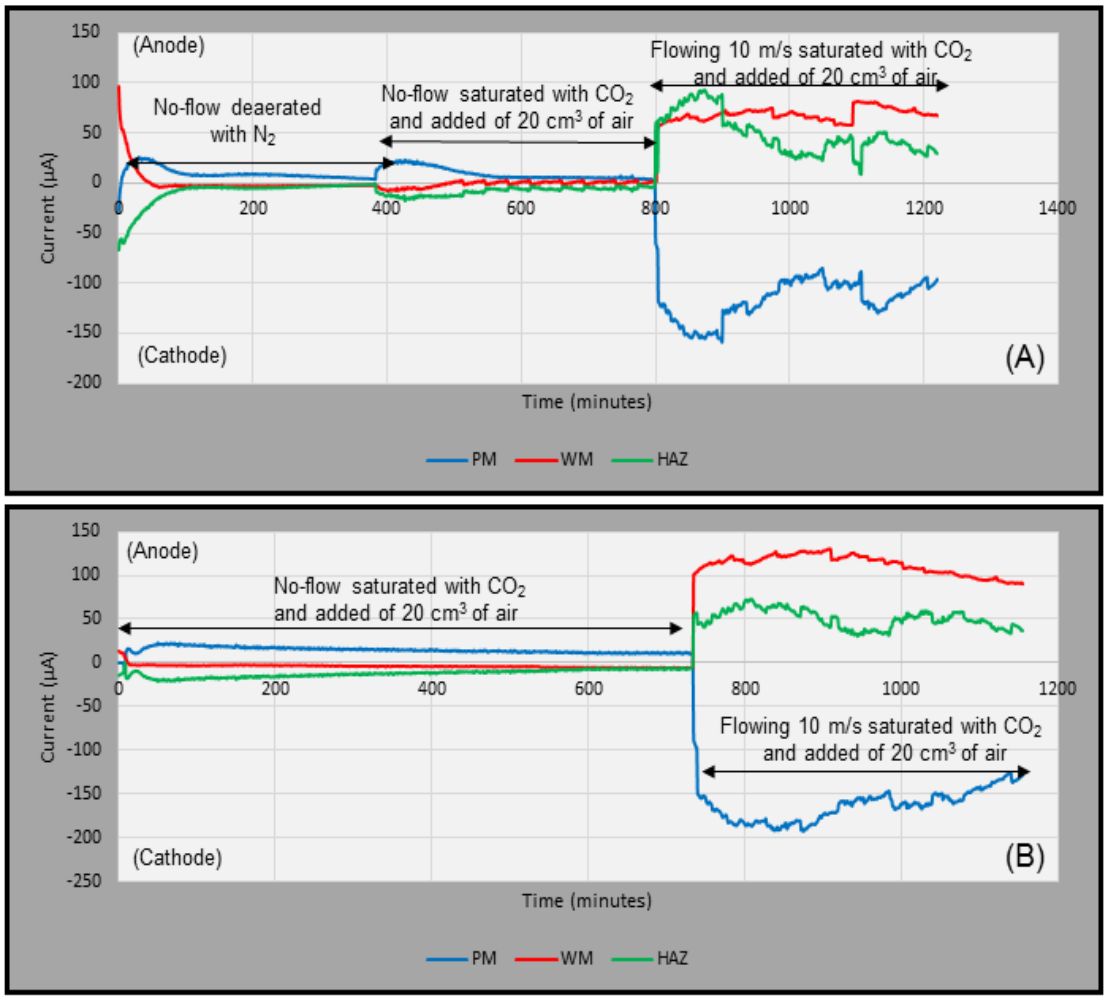

Figure 7-11 Galvanic currents of the weldment in inhibited brine with 20 cm^3 of air into (A) deaerated brine (B) not deaerated brine

When the weldment is exposed to an inhibited brine with dissolved oxygen, the typical galvanic current characteristics are different compared to the uninhibited condition. In Figure 7-11(A), the current during the static, non-flowing state (of the PM), from each electrode at different distances across the target, decreases. This is probably due to the effect of the inhibitor forming a passive film on the X65 surface. At this stage, the parent is anodic while the weld and HAZ are slightly more cathodic. A similar trend is found in Figure 7-11(B), the current from each electrode decreases after several hours perhaps due to the effect of the inhibitor in the brine solution. However, with flow from a jet at 10 m/s the weld (and also the HAZ) have high positive currents. This condition may occur as a result of an adsorbed layer forming on the weld metal that is easily displaced compared to

when the film forms on the parent metal. The current density produced during the flowing state is shown in Figure 7-12.

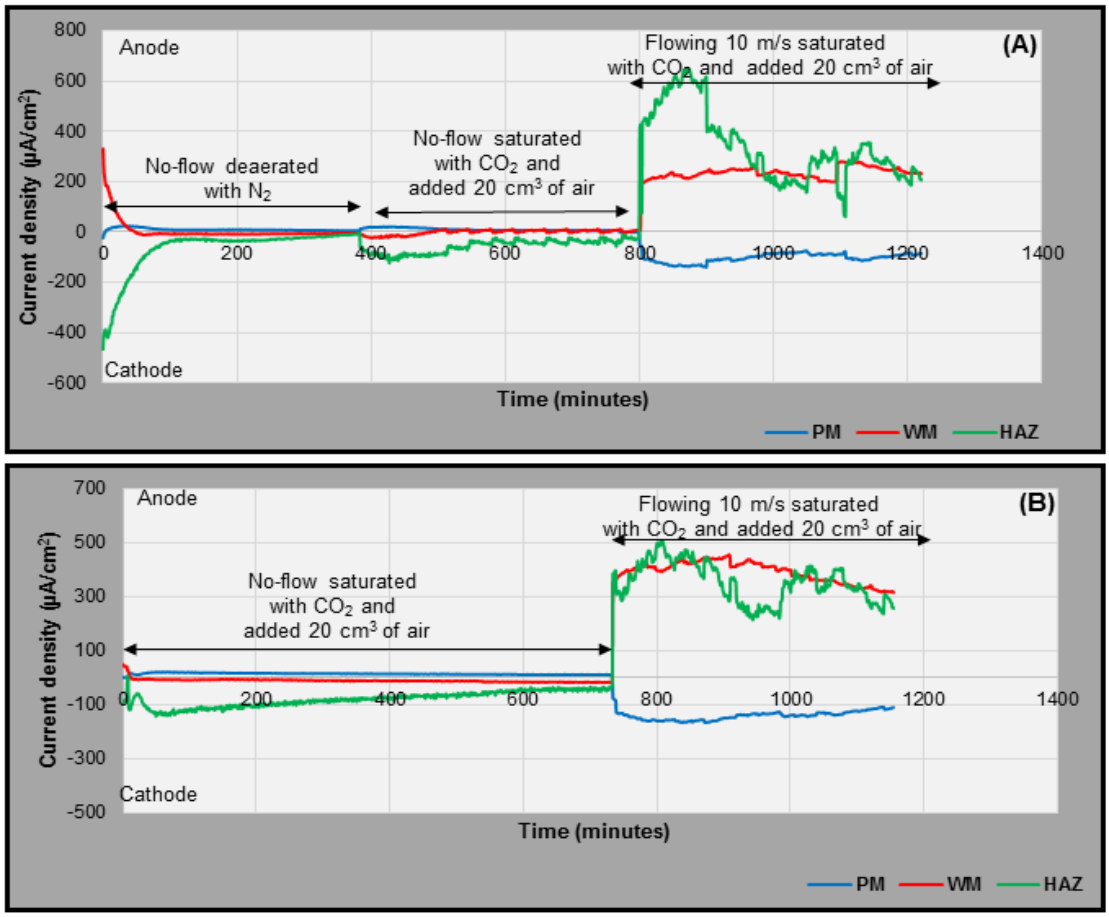

Figure 7-12 Galvanic current density of the weldment in inhibited brine with 20 cm^3 of air with (A) deaerated brine and (B) not deaerated brine

It was found that current densities from the weld with oxygen dissolved in the brine and HAZ in inhibited brine with the deaerated condition after flowing condition were lower than in the not deaerated state (20 cm^3 of air was added). The current densities for the WM and the HAZ in inhibited deaerated condition are 228 and 206 µA/cm^2 respectively. While in a not deaerated condition, the current densities are 287 and 255 µA/cm2 for the WM and the HAZ respectively. The current densities are not significantly reduced compared to the uninhibited flowing condition with dissolved oxygen (only about 25% less). This is very different to a thoroughly deaerated system with no oxygen and an inhibitor, where the current density is significantly reduced (over 80%, as explained in Chapter 6).

Thus the presence of oxygen provides a detrimental effect on an X65 weldment significantly affecting corrosion.

7.2.2 Self-corrosion Measurement

The self-corrosion rate was analysed using linear polarisation resistance (LPR technique) to determine the effect of dissolved oxygen, of an uncoupled electrode, in an inhibited brine (fully deaerated and not deaerated) that was saturated with CO_2 with an addition of 20 cm^3 of air (Figure 7.13 and 7.14).

Figure 7.13 shows the gradient of the PM, the WM and the HAZ in the outer ring whilst immersed in fully deaerated inhibited brine with 20 cm^3 air. The PM has the highest LPR value at 121 followed by the HAZ and the WM at 109 and 87 respectively (Figure 7.13). In non-deaerated brine with 20 cm^3 of air (Figure 7-14), the LPR gradient is lower than in the fully deaerated condition in the range of 66-89 for the PM, the WM, and the HAZ respectively. This may mean that the electrode which was exposed with deaerated-inhibited brine has a higher self-corrosion rate due to exposure in the more reactive and corrosive environment.

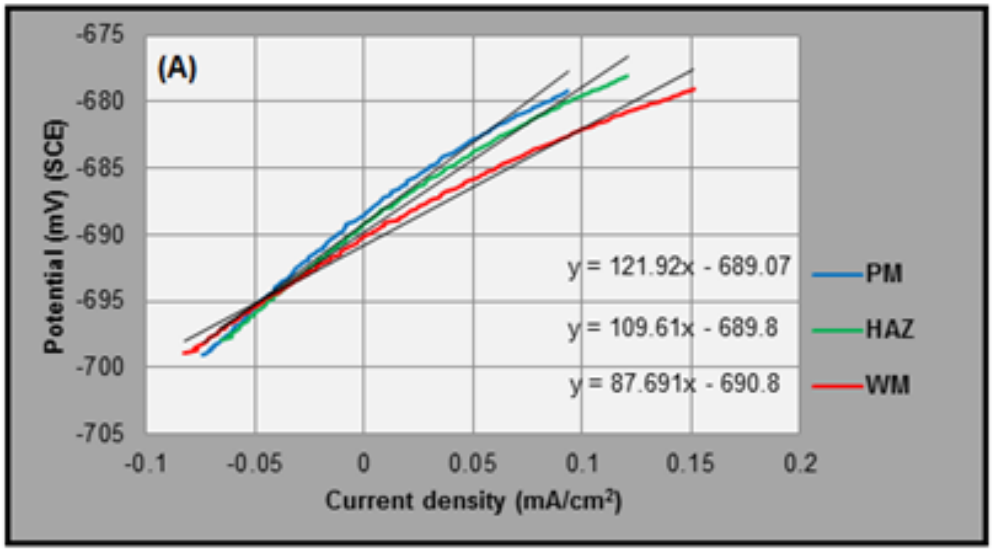

Figure 7-13 The LPR plot for each electrode in outer ring in fully deaerated of inhibited brine with 20 cm^3 of air and flow 10 m/s

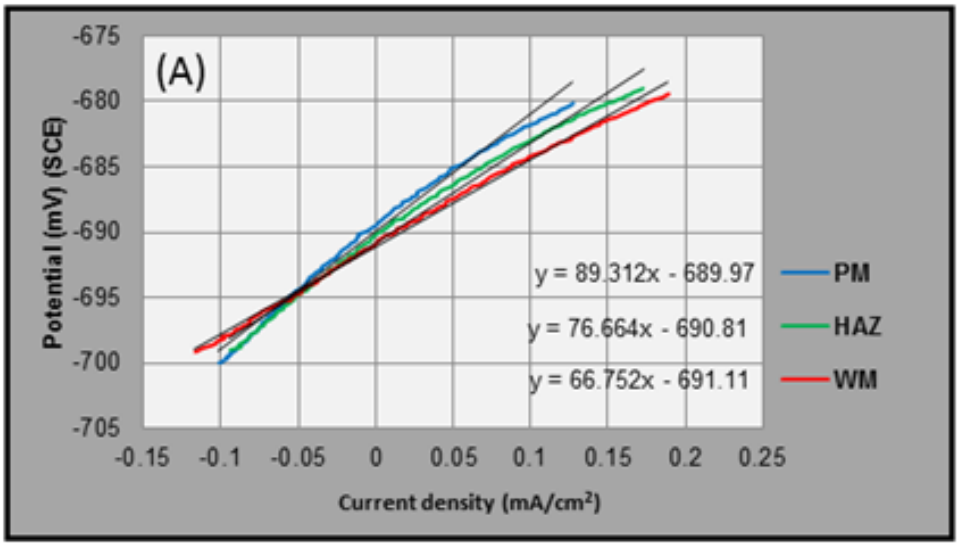

Figure 7-14 The LPR plot each electrode in outer ring in not deaerated of inhibited brine and with addition 20 cm^3 of air and flow 10 m/s

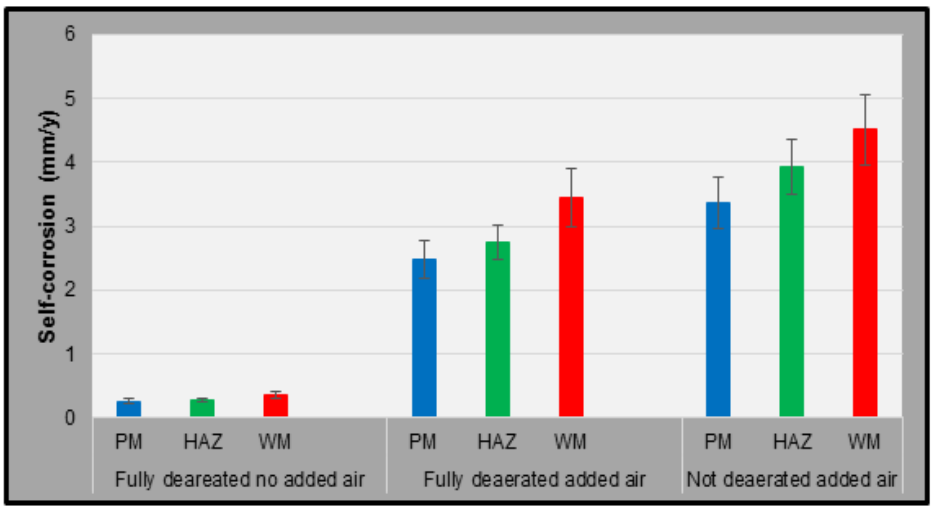

Figure 7-15 Self-corrosion rates of the outer ring electrodes in inhibited brine at 10 m/s with dissolved oxygen in fully deaerated and non-deaerated conditions

Table 7-3 Percentage of self-corrosion rate with oxygen added and flow

	Fully deaerated no oxygen added			Fully deaerated with oxygen added			Not deaerated with oxygen added		
	PM	HAZ	WM	PM	HAZ	WM	PM	HAZ	WM
Uninhibited (mm/y)	1.8	2.0	2.2	4.4	3.7	3.3	6	5.3	4.8
Inhibited (mm/y)	0.2	0.3	0.4	3.4	2.6	2.5	4.5	4.4	3.4
% Self Corrosion reduction	89	88	87	23	30	24	25	17	29

Figure 7-15, shows that the addition of an inhibitor to brine does not have a significant effect on reducing the corrosion rate when brine solution contain a small amount of dissolved oxygen. The self-corrosion rate reduces by 17-30% compared to uninhibited conditions (Table 7-3). The result is completely different when the weldment is exposed to fully deaerated inhibited brine and there is no addition of air. In the absence of dissolved oxygen self-corrosion rates of each part of the weldment are very low.

Similar results are also reported in previous studies in the literature. Additions of oxygen in inhibited conditions in flowing environments were shown to reduce the effectiveness of inhibitors [66]. In some studies, it was found that the addition of inhibitors to an oxygen containing environment can initiate additional corrosion reactions and make the metals corrode more severely [16,65].

7.2.3 Total Corrosion Rate

A summary of the effect of dissolved oxygen in inhibited brine on the weldment is shown in Figure 7-16.

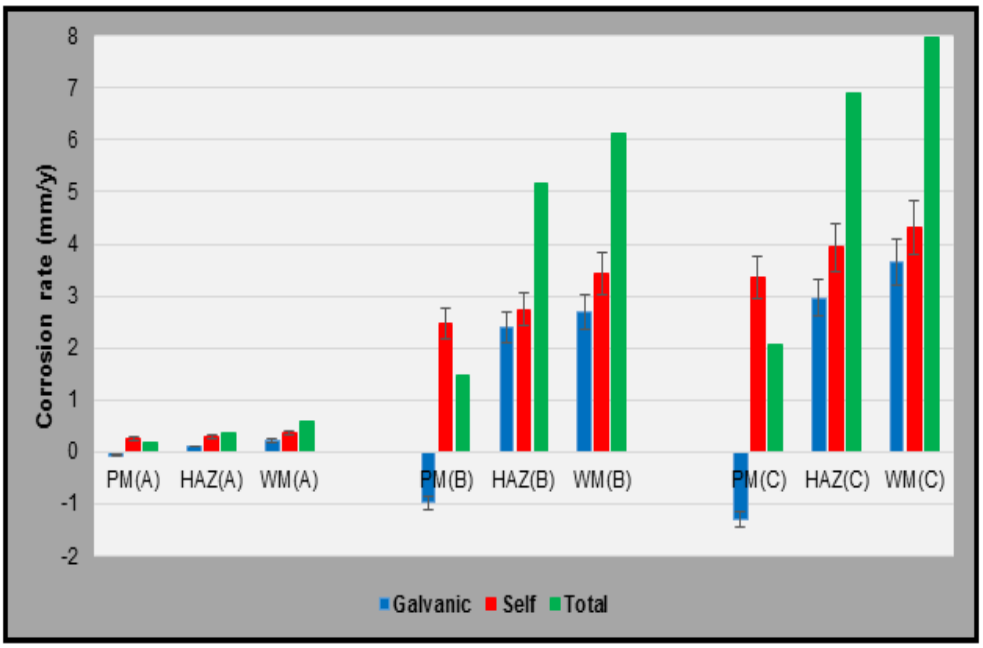

Figure 7-16 The effect of dissolved oxygen on the total corrosion rate in inhibited brine (A) fully deaerated; (B) fully deaerated with air; (C) not deaerated with air

This shows the WM has the highest total corrosion rate in in all conditions compared to the HAZ and the PM. In condition (A) fully deaerated, the total corrosion rate of each electrode is low (0.2-0.6 mm/y). With the addition 20 cm^3 of air in (B) deaerated and (C) non deaerated conditions, the total corrosion for PM, HAZ and WM are in the range 1.5-6 mm/y, and 2-8 mm/y respectively. Thus a ten fold increase in corrosion rate is experienced with a small amount of dissolved oxygen in the system. Occasionally when unexpectedly high corrosion rates are reported, it is possible that the presence of oxygen is responsible. of the potential value, can provide some validation regarding the amount of dissolved oxygen in the system (see section 4.1).

Table 7-4 Percentage of total corrosion rate reduction with oxygen and flow

	Fully deaerated no oxygen added			Fully deaerated with oxygen added			Not deaerated with oxygen added		
	PM	HAZ	WM	PM	HAZ	WM	PM	HAZ	WM
Uninhibited (mm/y)	1.4	2.3	2.7	2	7	7.8	3	9.3	10.8
Inhibited (mm/y)	0.2	0.4	0.7	1.4	5.2	6.2	2	6.8	7.8
% Total Corrosion reduces	86	83	74	30	26	21	33	27	28

Figure 7-16 shows that when air is added into inhibited-deaerated brine (B) and inhibited, non-deaerated brine solution (C), the corrosion rate is high and reduced >20% compared to that in an uninhibited condition (Figure 7-16 (B) and (C)). Conversely, when the weld was exposed to fully deaerated, inhibited brine without oxygen, the corrosion rate by reduced by over 70% (Table 7-4). This phenomenon shows the negative effect of dissolved oxygen in a range of situations, where dissolved oxygen in the environment causes severe corrosive attack. Similar results were obtained from previous studies in inhibited brine conditions, the presence of oxygen reduces the inhibitor performance [49,66].

7.3 Chapter Summary

- The effect of oxygen accelerates the corrosion rate of an X65 weldment in both inhibited and uninhibited brine.
- The effect of 20 cm^3 added air (or 4 cm^3 added oxygen) accelerates the corrosion rate compared to deaerated conditions uninhibited. With air the corrosion rate is almost 4 times greater than the deaerated corrosion rate
- When the air is added into inhibited-deaerated brine, the corrosion rate is higher and could only be reduced to a rate by 20% compared to the uninhibited condition. Conversely, when the weld was exposed to the inhibited brine which was fully deaerated with no oxygen, the corrosion rate reduced by approximately 85%.

8 USE AND ASSESSMENT OF THE SJI TARGET

In previous chapters, the corrosion data presented and discussed was taken from the outer electrode of the submerged jet impingement (SJI) target. In this chapter, electrochemical measurements from electrodes placed in the outer, inner and centre positions are presented to discuss the corrosion effects in no-flow and flowing conditions considering, firstly coupled measurements, followed by, uncoupled data. In flowing environment the corrosion rates at each electrode at velocities of 2, 5, 8 and 10 m/s in the outer, inner and centre are observed. From this, an optimal velocity which may provide minimum corrosion on the target electrodes is identified.

By considering the effect of flow on corrosion, the hydrodynamic characteristics across the SJI target itself are assessed using modelling predictions to validate the findings. A modelling approach to accurately obtain the relationship between the electrode position (on the target) with mass transfer and shear stress on the SJI target is developed.

8.1 No-Flow Condition

In this test, the jet impingement target is immersed in a flow loop and a test conducted to investigate the effect of still or stagnant water on each electrode of the SJI target. Starting from the outer, the inner and centre electrodes respectively, galvanic measurements are carried out while deaeration of the brine solution with nitrogen is performed in a no-flow condition. After 2 - 4 hours, the CO_2 is introduced into the deaerated brine solution and galvanic measurements recorded continuously for 20 hours.

8.1.1 Galvanic Measurements

The galvanic characteristics of each part of the weldment from the outer, inner, and centre electrodes are shown in Figure 8-1. In the deaeration stage with nitrogen, each set of 3 electrodes regardless of the target position show a similar trend where the HAZ is slightly anodic and protects the PM and the WM. A reduction in the galvanic corrosion potential is accompanied by a reduction in

galvanic current. When CO_2 is dissolved in brine, the anodic current of the PM (and the HAZ) protects the WM. This is expected because the PM and HAZ are fabricated with the same elemental composition differing in microstructure.

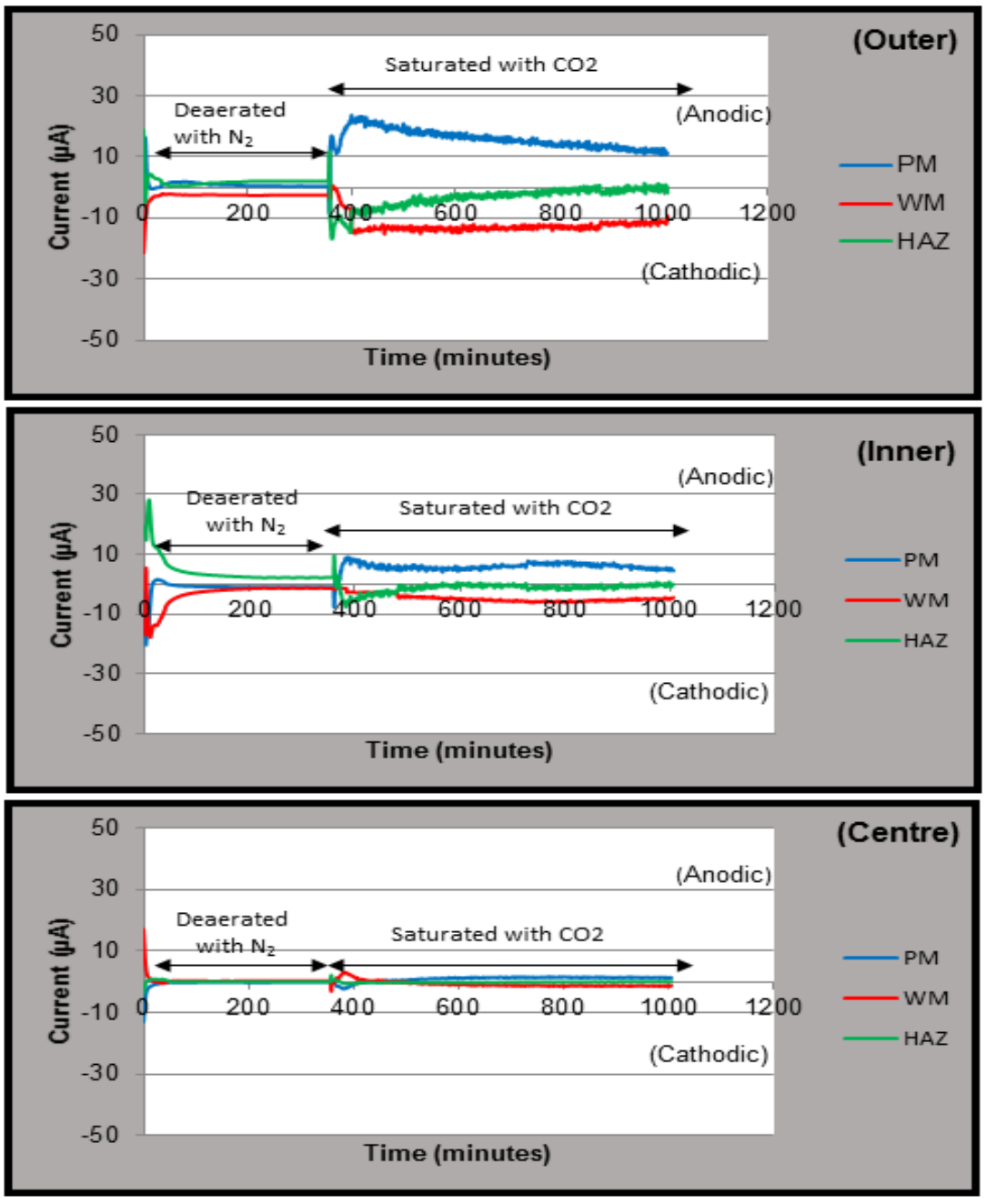

Figure 8-1 Galvanic characteristics of the weldment across the outer, inner and centre electrodes without flow in uninhibited brine saturated with CO_2

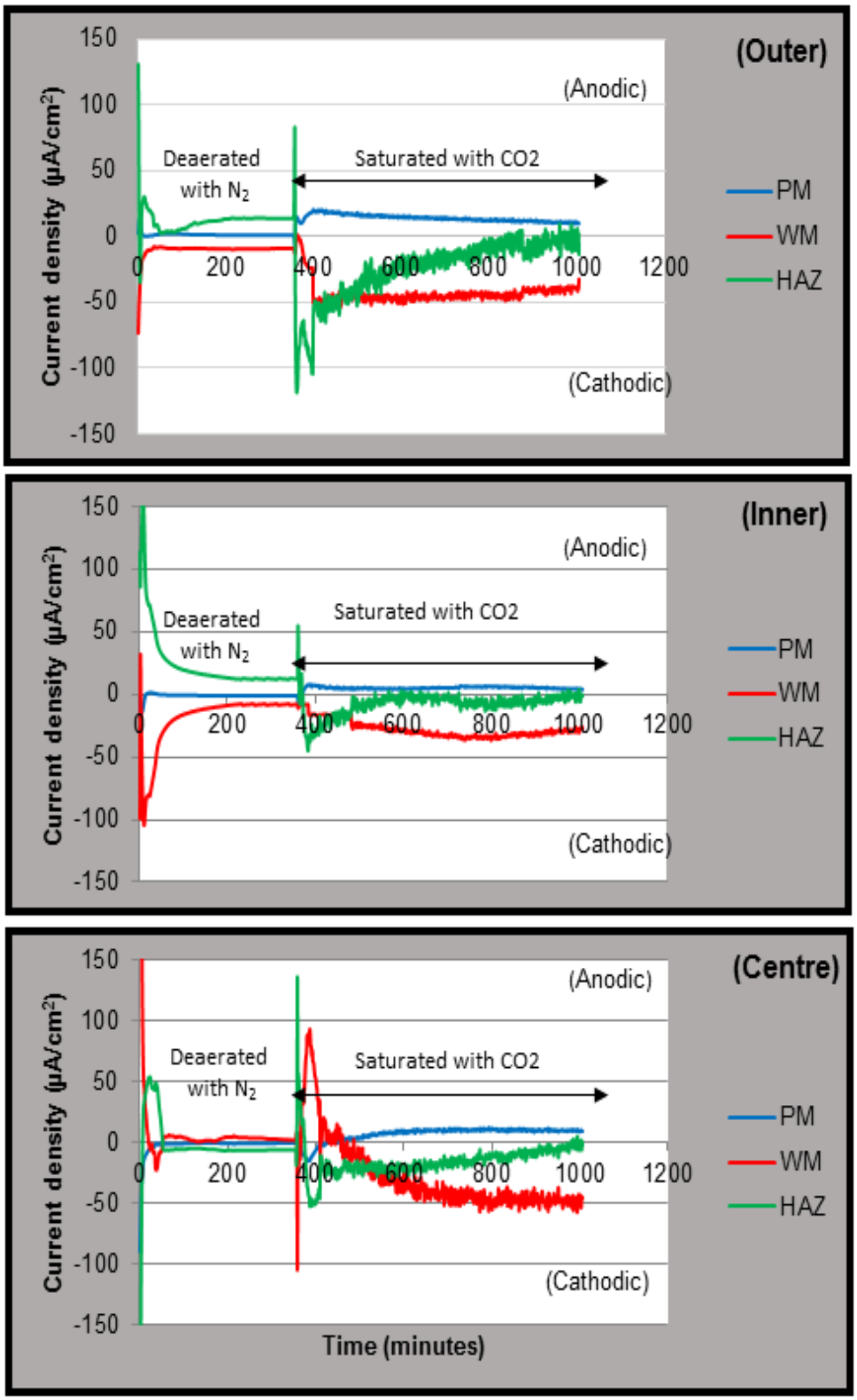

Figure 8-2 Galvanic current density of the weldment of the outer, inner and centre electrode under no-flow uninhibited brine saturated with CO_2

The current density for each part of the weldment across the target was calculated by dividing the current with the electrode area and the results are shown in Figure 8-2. The current density value is used to calculate the galvanic corrosion rates of three weld sections in each hydrodynamic zone of the target. When there is no-flow across the target, the galvanic current density for each weld section is comparable for the outer, inner, and centre electrodes respectively. The current density is in a range of ± 50 μA/cm^2. This result is expected with static flow for all of the electrodes in the same environmental condition and this indicates that the target is working well. From the galvanic corrosion rates, it is favourable for the PM to be the anodic component in the couple. This ensures that its corrosion characteristics offers sacrificial protection to the other weld regions in an uninhibited brine solution with CO_2 at ambient temperature with stagnant water.

This result is in contrast to previous research done by Adegbite on a different and separate SJI target [13]. In this target the HAZ was anodic at the centre and inner ring but cathodic at the outer ring, resulting in a high PM anodic current. This difference between electrode positions with the same hydrodynamic conditions is probably due to the difference in local composition and/or microstructure within the electrode areas, linked to the variance in production or fabrication errors.

8.1.2 Self-corrosion Measurements

Self-corrosion rates were evaluated from the LPR of each working electrode for the outer, the inner and the centre electrode in the uncoupled state directly after galvanic measurements were completed. Figure 8-3 plot the changes in current with potential for the outer, inner and centre electrodes in uninhibited brine without flow. The gradient (LPR values) for each electrode are found to be very close to each other in the range of -274 to -286 mV. The potential of every working electrode in every ring is very similar with the range of potential between -724 to -725 mV and this is likely due to similar conditions without flow.

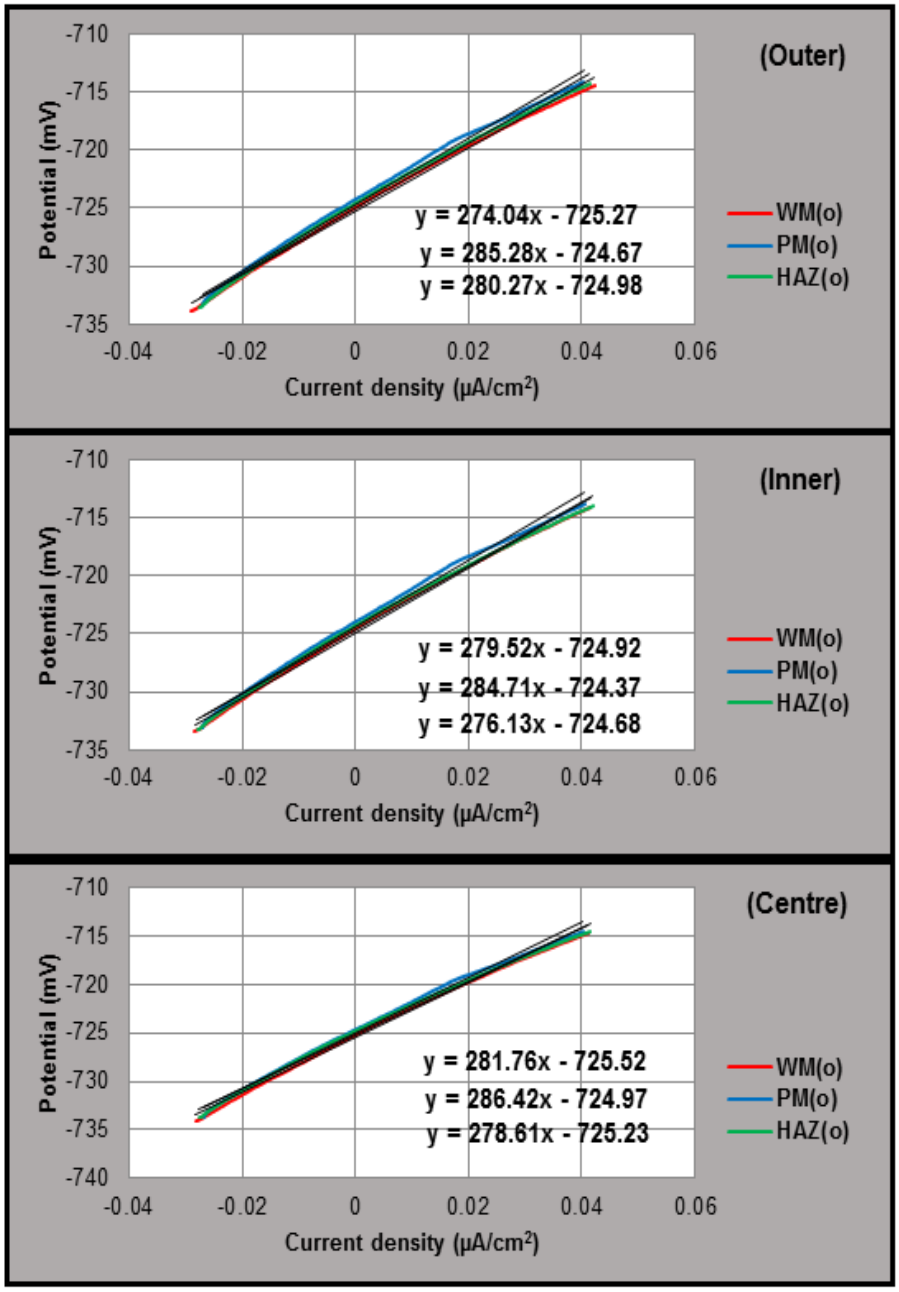

Figure 8-3 Self-corrosion measurements (LPR) of the weldments in the outer, inner and centre electrodes in uninhibited stagnant brine saturated with CO_2.

From the self-corrosion rates in a no-flow environment, the current densities for each electrode are similar at 1-1.2 mm/year.

Figure 8-4 summarises the self-corrosion rates in each weld section of the SJI target in brine saturated with CO_2 in a no-flow condition. Ideally, in a no-flow condition, the self-corrosion behaviour of each electrode in this SJI target should

be similar in the outer, inner and the central electrodes since the hydrodynamic conditions are identical. In this study, the WM (red) is very slightly higher in terms of self-corrosion rates compared to the PM and HAZ for each ring. The difference of self-corrosion rates in outer, inner and centre is very narrow and considered to be equivalent without flow.

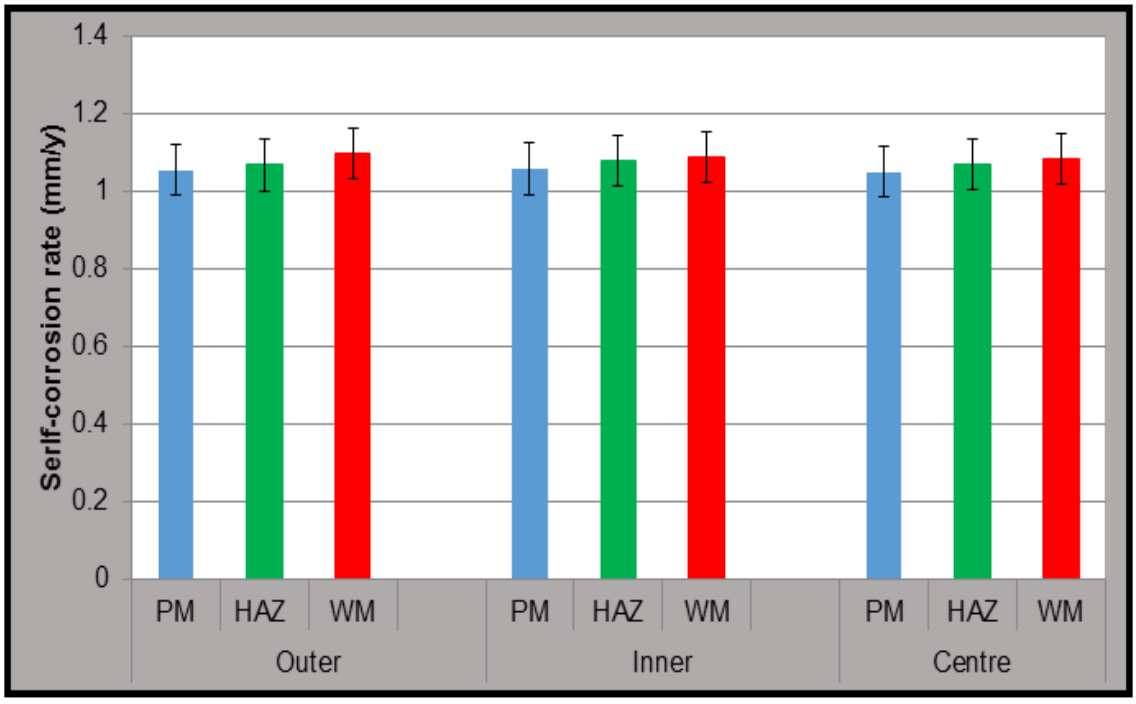

Figure 8-4 Self-corrosion rates of the weldment in the outer, inner and centre electrodes in uninhibited brine saturated with CO_2 without flow.

8.1.3 Total Corrosion Rate

There are different ways of trying to predict the total corrosion rate, however in this study, the total corrosion rate in each weld in the outer, inner and centre electrodes is calculated by adding the self-corrosion rate plus the galvanic corrosion rate. The results of the total corrosion rates for the weldment are shown in Figure 8-5. In all cases, Figure 8-5 shows that the contribution from the self-corrosion (red) is the most significant compared to the galvanic corrosion (blue) in the order of +/-10%. The overall galvanic protection of the WM results in a slightly lower total corrosion rate. Thus, in the outer, inner and centre electrodes, the WM was slightly more noble with a lower total corrosion rate compared to the PM and HAZ. The total WM corrosion in the outer, inner and centre ring was on

average 0.7 mm/y. Although the total corrosion rate of the WM is lower than that of the PM, this condition does not guarantee protection of the WM from PWC because the corrosion may shift to the HAZ. This has previously been reported in oil and gas facilities [8].

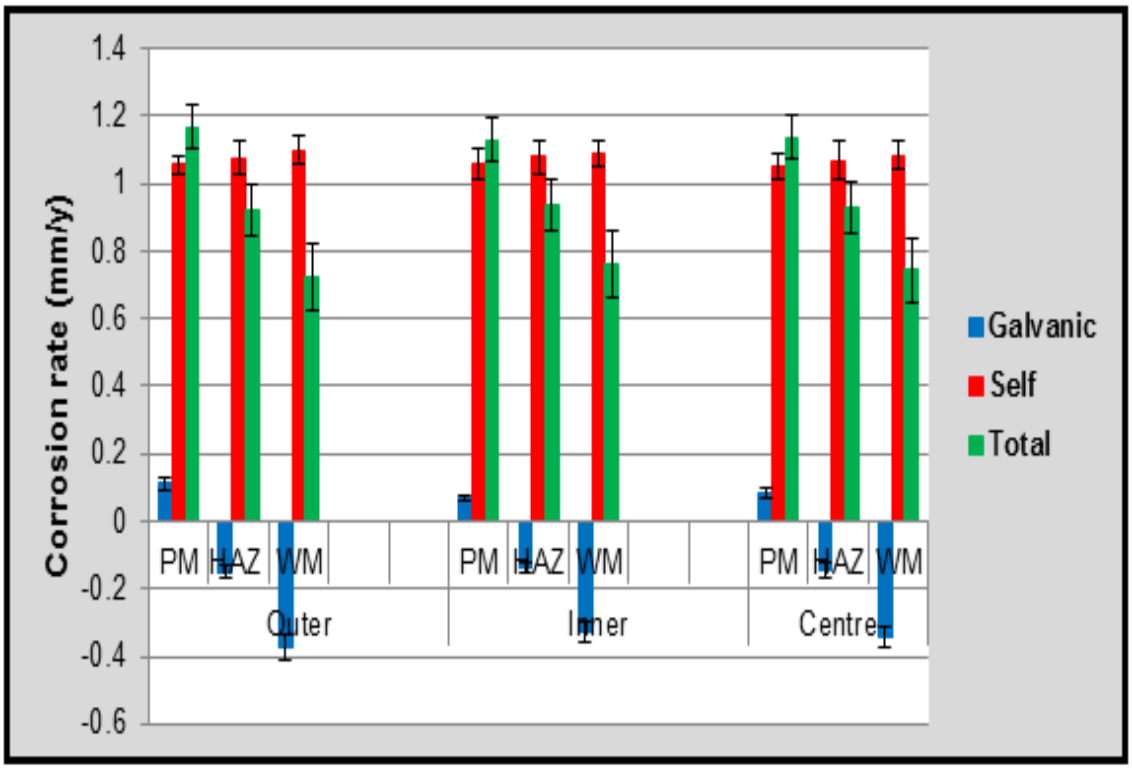

Figure 8-5 Total corrosion of the weldment in outer, inner and centre electrode in uninhibited brine saturated with CO_2 without flow

Without flow, the typical self-corrosion characteristics for each part of the weldment in each electrode ring is expected to be the same, regardless of where the target is located and this is found to be the case. There is consistency of results for each ring in both galvanic and self-corrosion; which indicates that the target is behaving as expected.

8.2 Flowing Condition

The purpose of this study is to understand the performance of a SJI target in a flowing environment when exposed to a high flow rate that simulates likely conditions in oil and gas fields during the production process.

An assessment has been performed to evaluate the effect of hydrodynamic flow on each electrode. Different jet velocity conditions of 2, 5, 8 and 10 m/s are explored which links to an associated variation in wall shear stress. The galvanic and self-corrosion measurements are conducted for every electrode, in the outer, inner and the centre region, to calculate the total corrosion rate at all flow rates. For clarity, a jet velocity of 10 m/s is used as an example to explain the behaviour of the SJI target in the outer, inner and the centre electrode regions.

8.2.1 Galvanic Measurements

Galvanic measurements are carried out while deaeration of the brine solution with nitrogen is undertaken in a no-flow condition.

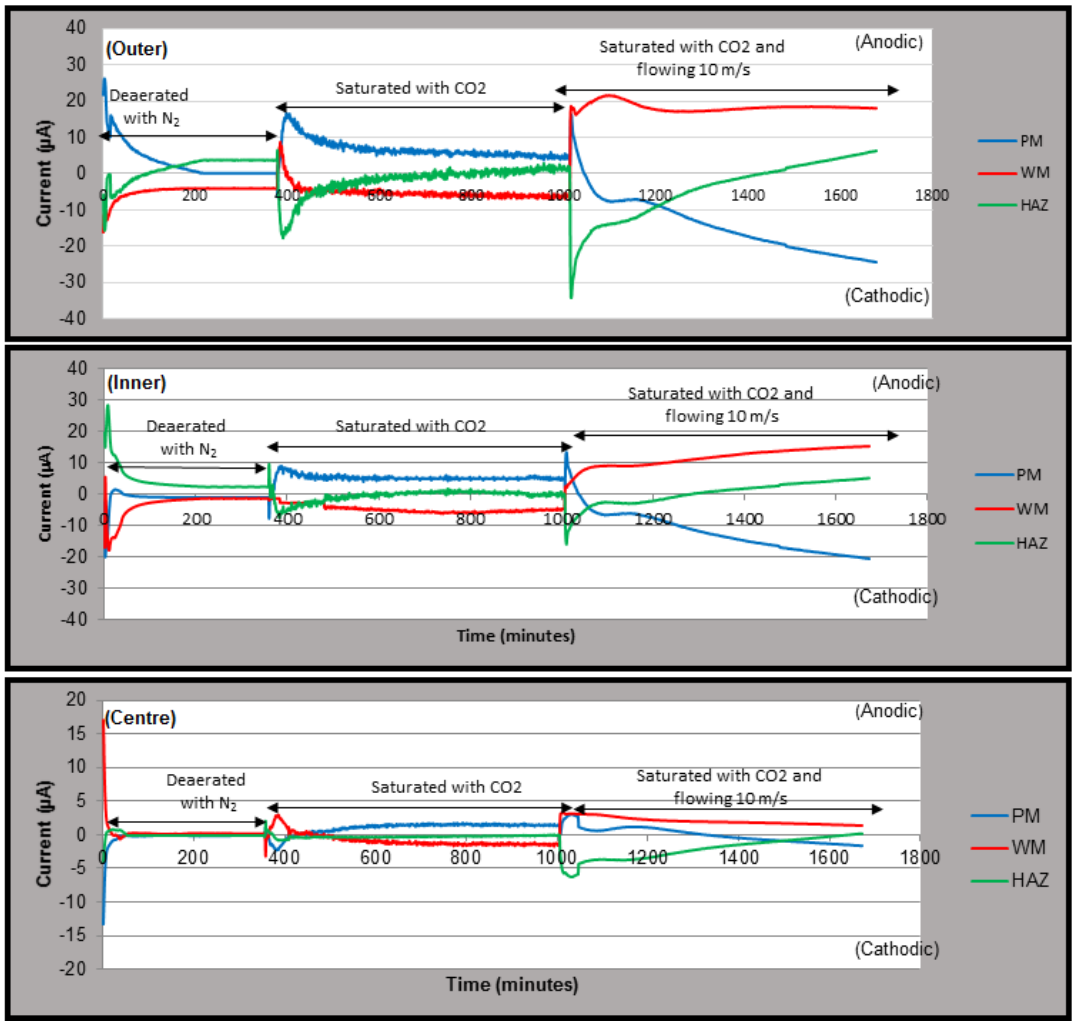

Figure 8-6 Galvanic characteristics of the weldment in uninhibited brine saturated with CO_2 at 10 m/s in the outer, inner and centre electrode regions

After 4 hours, the brine solution is sparged with CO_2 and galvanic measurements recorded for 24 hours continuously.

Figure 8-6 shows the characteristic of galvanic current measurements for the electrodes in each ring at 10 m/s. The plots at each region follow a similar pattern, wherein, at the deaerated stage, the HAZ has a positive current and protects the PM and the WM. The influence of adding carbon dioxide produces an exchange of current and the PM is anodic protecting the WM and the HAZ. The same fluid flowing at 10 m/s gives a significant change of current, particularly at the WM.

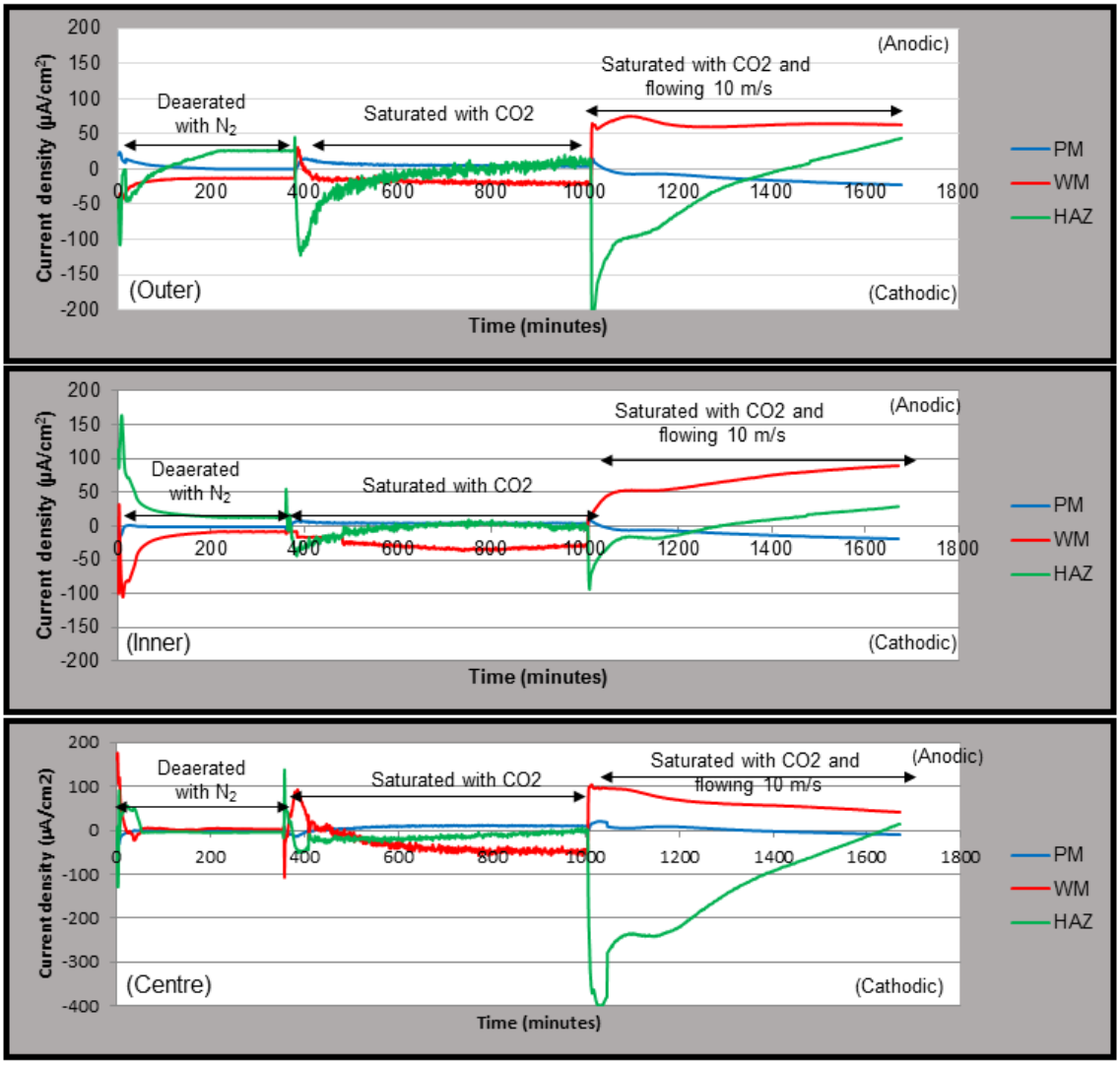

Figure 8-7 The current density of the weldment in centre, outer and inner electrode in flowing 10 m/s uninhibited brine saturated with CO_2

A current density for each weld is calculated to determine the corrosion rate. Figure 8-7, shows the variation in current density of the weld sections in the outer, inner and centre region for CO_2 saturated brine flowing at 10 m/s. The WM instantly becomes the anodic component in the couple, as the solution starts flowing. This condition does not favour the weld, and if sustained over a long time, this current reversal would result in severe preferential corrosion of the weldment. Associated with the flowing solution is an increase in anodic behaviour with time of the HAZ in each region of the SJI target.

The current density of the WM is approximately 30, 90, and 63 $\mu A/cm^2$ in the centre, inner and outer electrode region, respectively after 1700 mins. The inner region shows higher corrosion activity than the outer and centre electrodes. This supports predictions from Efird [102] who describes an inner region of high turbulence in a flowing environment.

The galvanic current produced in centre ring was smaller than the inner and outer. Efird reports that ideally, in the centre electrode, the galvanic currents should be as in the no-flow condition since that there is low turbulence in this central area [18]. However, this was not the case in the experiment conducted in a flowing environment of 10 m/s and corrosion rates are calculated at the end of the experimental period similar to those experienced in the outer ring where some turbulence is also expected.

8.2.2 Self-corrosion Measurements

The self-corrosion rate for all of the electrodes exposed to brine saturated with CO_2 flowing at 10 m/s are recorded after the galvanic measurements finish. Typical potential/current density plots for the outer, inner and centre electrodes at 10 m/s are shown in Figure 8-8. Every electrode has different slope and this is associated with the polarisation resistance (R_p). From the R_p values, corrosion current densities and the self-corrosion rates are obtained and Figure 8-8 and supported by Table 8-1.

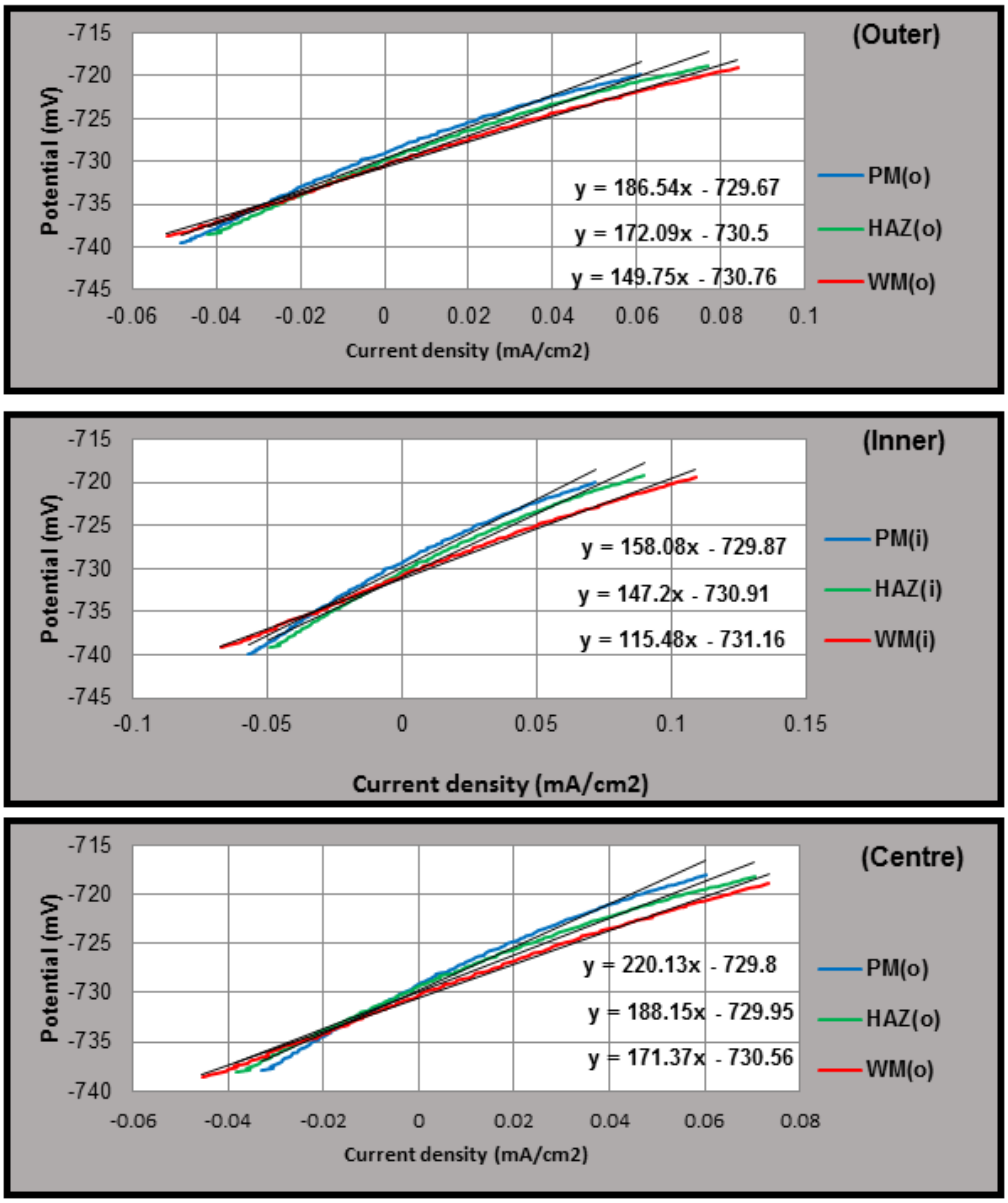

Figure 8-8 Typical self-corrosion profiles of the weldments in outer, inner and centre electrode uninhibited brine saturated with CO_2 at flowing 10 m/s

From Figure 8-8, it can be seen that corrosion current density, I_{corr}, increases in the inner electrode region as compared to the outer and centre electrodes due to the higher hydrodynamic condition in the inner area. The corrosion potential (E_{corr}) for each electrode in the inner region was found to be more negative (more reactive), and it has a positive correlation with the self-corrosion rate.

Table 8-1 Detailed information extracted from Figure 8-8

	Weld section	E_{corr} (mV)	I_{corr} (μA/cm^2)	Corrosion rate (mm/y)
Outer	PM	-729.3	165.8	1.92±0.19
	HAZ	-729.7	177.9	2.06±0.22
	WM	-730.7	191.7	2.22±0.27
Inner	PM	-729.7	193.4	2.24±0.21
	HAZ	-730.1	206.5	2.39±0.26
	WM	-731.1	217.7	2.52±0.34
Centre	PM	-729.0	132.1	1.53±0.25
	HAZ	-729.1	142.5	1.65±0.23
	WM	-730.1	147.7	1.71±0.18

The self-corrosion rates of the weldment corresponding to a jet velocity of 10 m/s is given in Table 8-1. The self-corrosion of PM and HAZ are close to each other. This is understandable because they have the same chemical composition but differ only in microstructure. The WM in every weld section has the highest self-corrosion rate, about 1.76-2.6 mm/y. This means the WM has less resistance as compared to the PM and HAZ. Based on the compositions given in Table 3-1, the WM has a lower Ni composition (0.24 %) compared with PM (0.36%).

8.2.3 Total Corrosion Rate

The total corrosion rates for each electrode in the flowing environment at 10 m/s are shown in Figure 8-9. The total corrosion rates (in green) of the WM at each electrode in the outer, inner and centre ring exceed that of the PM and HAZ. Thus, from these results, in a brine environment flowing onto a weldment at 10 m/s, preferential weld corrosion is predicted to occur. The PM and HAZ will corrode less than the WM, in some cases at 50- 33% of the rate of the WM.

Figure 8-9 clearly shows the effect of local turbulence across the target due to the different positions of each electrode ring. The inner ring corrodes much faster than the outer and also the centre ring.

At 10 m/s the maximum total corrosion rate combining both galvanic and self-corrosion predictions is 3.3 mm/y. This result is likely due to high turbulence at the inner ring. In comparison, the centre electrode is predicted to experience

lowest flow rates and less turbulence, with the total corrosion rate (1.5-2.5 mm/y) at the WM and HAZ being almost halved. The electrode placed in outer region experienced a total corrosion rate of 1.7 – 2.7 mm/y. The observations will be explained in detail with respect to the hydrodynamics across the target, in section 8.3. Section 8.2.4 considers the behaviour at a range of different jet velocities.

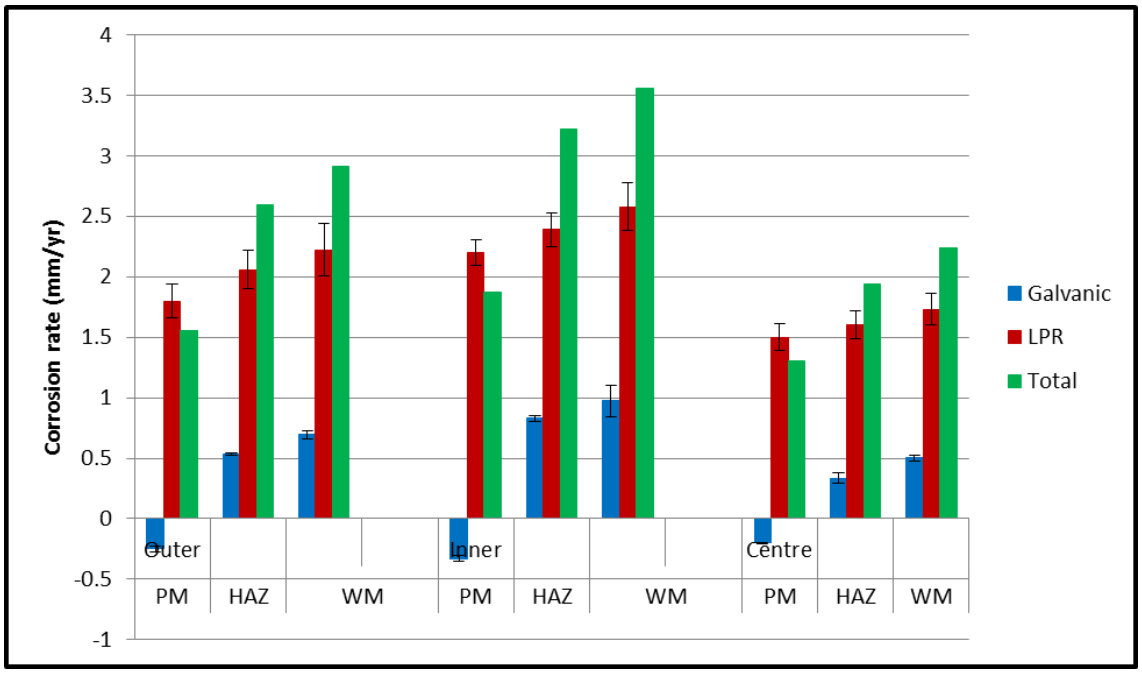

Figure 8-9 Corrosion rates in a weld section at various locations exposed to a jet of brine solution saturated with CO_2 flowing at 10 m/s

8.2.4 Total Corrosion with Jet Velocity in an Uninhibited Condition

Figure 8-10 shows the effect of different jet velocities on the total corrosion rates of the SJI target (outer ring) at flow rates of 0, 2, 5, 8 and 10 m/s. These measurements are estimated (using equation 2.23 and 2.24) to correspond to wall shear stresses of 0, 15, 81, 191 and 286 Pa respectively, on the outer ring of the SJI target. In general, the contribution of the galvanic corrosion rate for each electrode in each weld section is smaller as compared to the self-corrosion rate.

In a no-flow condition (0 m/s), the total corrosion rate of each electrode is relatively low. This result is expected because in a static environment, the initial

corrosion activity remains low near to the surface. Thus in no-flow conditions, the electrochemical environment limits mass transfer resulting in small currents.

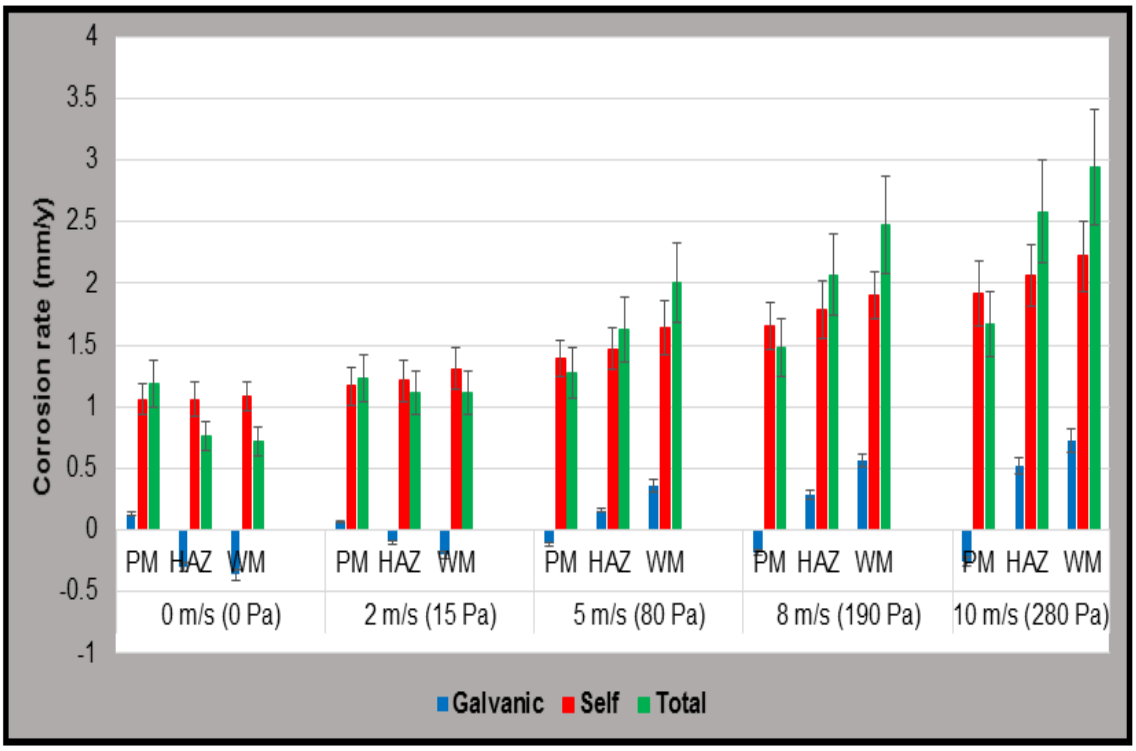

Figure 8-10 A jet velocity of 10 m/s is used as an example to explain the behaviour of the SJI target at the outer ring

At flow rates of 0 and 2 m/s, the total corrosion of the PM is higher than the total corrosion of the HAZ and the WM due to more positive rate of galvanic corrosion. The range of total corrosion of the PM at a flow rate of 0 and 2 m/s is 1.2-1.35 mm/y, higher than total corrosion rate of the HAZ (0.8 to 1.1 mm/y) and the WM (0.7 to 1.1 mm/y). However, at a flow rate of 5-10 m/s, the total corrosion of the WM is higher than the total corrosion rate of the PM and the HAZ. This is due to greater anodic reaction of the WM which gives more protection to the PM and the HAZ (more cathodic). In addition, the total corrosion rate of each electrode at 10 m/s is higher than at other velocities (e.g. 5 and 8 m/s).

It was observed from Figure 8-10 that the total corrosion rate for WM at 5 m/s is up to 2.0 mm/y, while the total corrosion rate at 8 and 10 m/s reaches 2.5 and 2.9 mm/y respectively. The increased rate may be because, in a flowing environment, the surface is continuously replenished and more ionic interactions

and transfer between electrons occur compared to the no-flow or static condition. From these results, it is clear that the current or rate of corrosion increases with flow rate.

At flow rates between 5-10 m/s, the equivalent wall shear stresses are 80-280 Pa. This suggests that electrochemical activity and the current densities are higher; and the total corrosion rate increases with increasing turbulence

Alawadhi & Robinson [15], used a rotating cylinder electrode to monitor the total corrosion of X65 steel PM, WM, and HAZ at flow rates of 500 to 5000 rpm. They found that the corrosion rate has a positive correlation with the flow rate due to a more active mass transfer between anions and cations during the corrosion process. In their study, the rate of corrosion in uninhibited brine at a flow rate of 5000 rpm is 1.7 mm/y, which corresponds to a shear stress of 72 Pa. This is comparable with the result from this study at flow rate of 5 m/s (120 Pa) where the corrosion rate obtained is 1.9 mm/y.

8.2.5 Total Corrosion at Different Flow Inhibited Condition

In this work, the corrosion performance of the SJI target was evaluated using a typical oil and gas inhibitor CORRTREAT 1065 in different flowing environments.

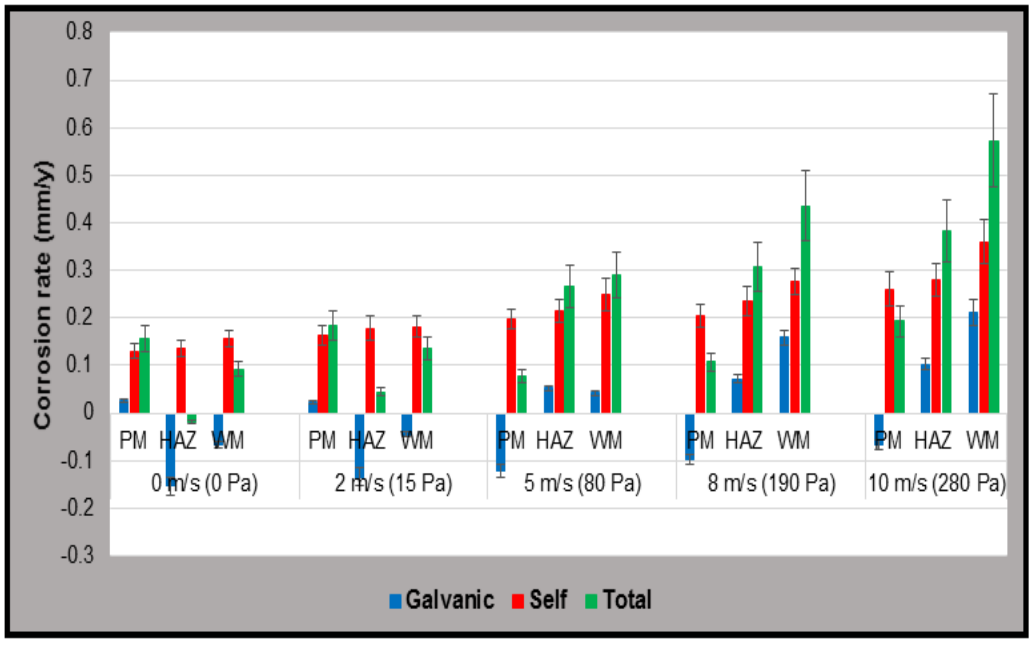

Figure 8-11 Corrosion rates in inhibited solution at velocities of 0-10 m/s (associated with wall shear stresses from 0-280 Pa).

Figure 8-11 shows the performance of the SJI target with the influence of the CORRTREAT inhibitor at different flow rates. From Figure 8-11, it can be seen that the total corrosion rate of the parent material (green bar), in inhibited solution with no flow and 2 m/s, is higher than the total corrosion rate of the HAZ and the WM. At zero velocity 0 m/s, the total corrosion rate of the PM is 0.16 mm/y compared with the total corrosion of the WM plus the HAZ (0.08 mm/y). Similar with a jet velocity of 2 m/s, the total corrosion rate of the PM was 0.19 mm/y as compared to 0.13 mm/y of the WM and HAZ (0.03 mm/y), this shows that the current from the parent material is protecting the HAZ and the WM from corrosion.

Different results were obtained under inhibited jet velocities starting from 5 to 10 m/s. The self-corrosion rates of the WM and the HAZ were higher and accompanied by more positive galvanic currents. In this condition, the total corrosion of the WM and the HAZ is high compared to the total corrosion of the PM. It can be seen that in the inhibited flowing environment, the total corrosion of the WM plus the HAZ at 5, 8 and 10 m/s are 0.6, 0.7, and 1.0 mm/y respectively. This value is higher than the total corrosion rate of the PM, which is 0.1, 0.11, and 0.19 mm/y respectively. The results suggest that the WM and the HAZ are no longer protected by the PM current above 5 m/s.

From the results above, it was shown that the use of CORRTREAT oilfield inhibitor reduces the corrosion rate significantly but does not always protect the weldment from preferential weld corrosion, especially at higher flow rates. The characteristics of corrosion of the SJI target still follows a similar pattern. In the uninhibited condition the jet velocity shows a positive correlation with the rate of corrosion.

8.3 Hydrodynamic Effect on the SJI Target

It has been explained in the section 2.11.4 that there is a difference in the fluid flow characteristics associated with the electrode positions across the SJI target (the centre, inner and outer electrode regions). This section considers the hydrodynamic characteristics across the SJI target by considering the effect of

flow on corrosion. A modelling approach to accurately obtain the relationship of mass transfer and shear stress on the SJI target is developed and discussed.

Efird [24] comments that a large difference is reported between corrosion rates observed in rotating cylinder tests and those in jet impingement test using identical samples and test environments. The corrosion rates in the rotating cylinder test were significantly lower than the jet impingement test. The differences were explained with the concept of steady state mass transfer and disturbed mass transfer. Efird [24] concludes that jet impingement testing is particularly applicable for simulating disturbed flow conditions.

The effect of fluid flow on corrosion, or flow accelerated corrosion, is said to be defined by mass transfer and wall shear stress parameters existing in the water phase contacting a solid wall [24]. Existing fluid flow equations for mass transfer and wall shear stress typically relate to equilibrium conditions and fluid flow can be described when moving in smooth paths or layers as laminar flow. However when fluid flow undergoes irregular fluctuations, or mixing this is described as non-laminar, disturbed or turbulent fluid flow. In turbulent flow the speed of the fluid continuously undergoes changes in both magnitude and direction. Thus corrosion in disturbed flow, with non-equilibrium, steady-state conditions is not addressed by equations representing equilibrium conditions. This section provides a description to relate the results of jet impingement tests with turbulent or disturbed flow directly to corrosion across a target in a flow loop system.

Figure 8-12A illustrates a schematic, introduced by Efird [24], that shows flow rate characteristics when a fluid, contained within a circular jet of known radius, impinges perpendicularly on a flat plate or target. Efird identified that there was a difference in flow between regions A, B and C; where region A is a region of laminar stagnation with no flow, turbulent flow is seen in zone B and zone C. High turbulence is expected across zone B compared with lower flow in C. Electrodes are placed in each of these zones as shown in Figure 8-12 B, and these can be

described as the centre electrode (zone A), inner electrode (zone B) and outer electrode (zone C).

In the current research reported in this thesis, an SJI target of carbon steel X65 material has been designed to study the effect of corrosion with different hydrodynamics when a fluid flows across the target. Annular electrodes are placed at three different characteristic regions as shown in the schematic cross section shown in Figure 8-13.

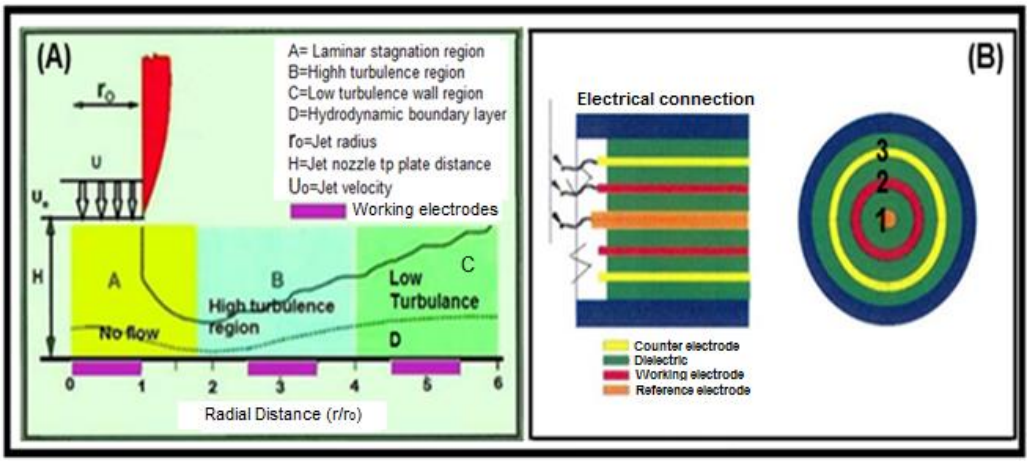

Figure 8-12 Model and design of submerged jet impingement target by Efird [24]

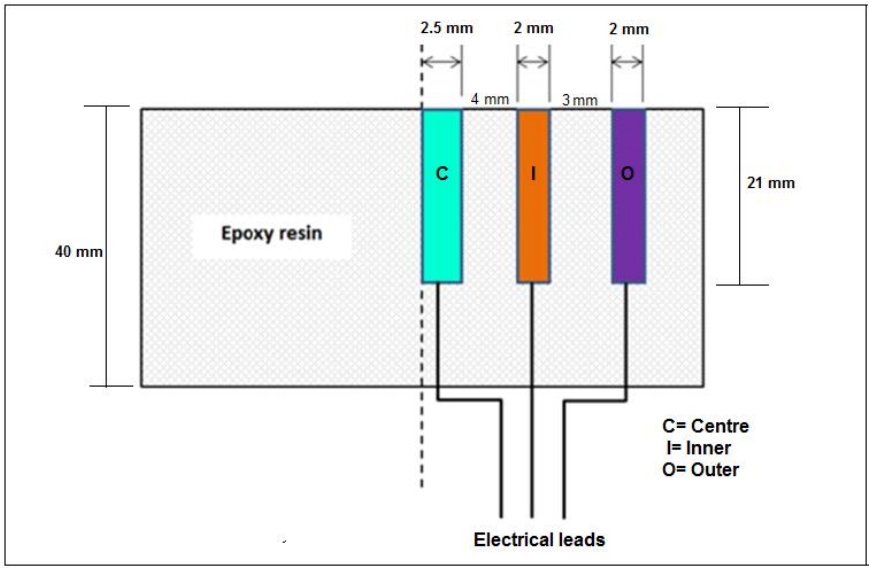

Figure 8-13 Experimental set-up of electrodes within the target surface exposed to jet impingement from the vertical nozzle

The centre electrode (C) is placed at a radius 0-2.5 mm from the centre of the target and inner electrode (I) at 6.5-8.5 mm while the outer electrode (O) is at 11.5-13.5 mm from the target centre. The nozzle is 5 mm in diameter, (nozzle radius r_o=2.5mm) and positioned at a fixed distance (H) 5 mm from the target. By placing the electrodes as those in Figure 8-12, a response of the velocity and shear stress is expected at each electrode position as predicted by Efird and as reported in Chapter 8.2.

To model the fluid flowing across the target surface, computational fluid dynamic (CFD) simulations have been conducted at different jet velocities (from 2 to 20 m/s) using commercial CFD software “3D flow”. It is expected that the turbulence model will predict the fluid flow velocity, shear stress, and shear velocity distribution across the target when impacted by a jet directed at 90 degrees to the target surface with a specific jet velocity. The CFD parameters used are recorded in Table 8-2.

Table 8-2 CFD parameters

Parameters	Values
Initial water temperature (^oC)	25
Boundary conditions	
Zmax pressure	101325 Pa
Zmin	Wall at 25^o C
Ymin	outflow
Ymax	outflow
Cell size (mm)	0.3
Mesh type	Cartesian/cubic
Pressure (Pa)	101325
Turbulence model	Renormalized group (RNG)
Slip flow	No

Figure 8-14 shows the 2D velocity and shear stress profiles for each region when a fluid at 10 m/s impinges onto the target. The different regions were identified on the surface of the target to show how the velocity distribution may influence the corrosion reactions at the electrode surfaces.

The simulation results using a jet flow rate of 10 m/s, estimates fluid velocities across the target in the range of 0-6.2 m/s, and shear stresses of a range 0-140 Pa. As shown in Figure 8-14, variations are distinguished based on the colour.

For example, the centre area (blue to light blue) is followed by a region of highest velocity (yellow-red) and finally less intense intermediate low turbulence outer region (green to blue) as predicted by Efird [23]. The shear stress has a similar pattern or trend because it is directly proportional to velocity.

Figure 8-14 shows the velocity and shear stress profiles as a function of radial distance for the range of jet velocities 10 m/s.

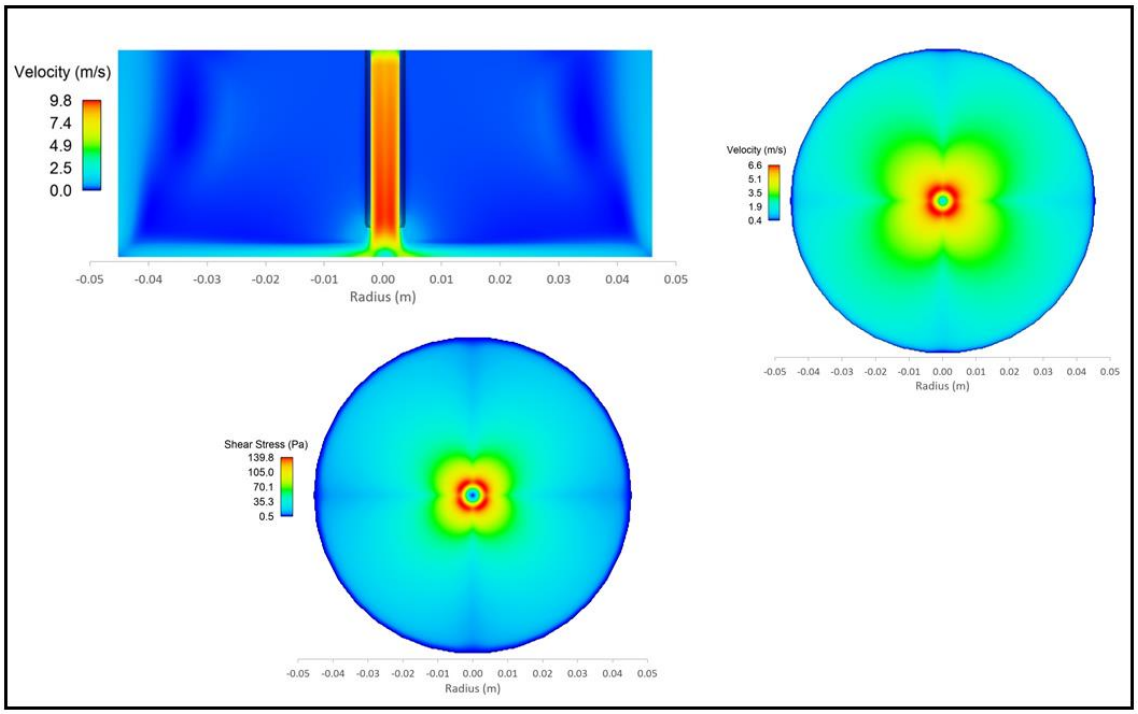

Figure 8-14 2D CFD simulation of fluid distribution at 10 m/s with (A) showing jet flow rate impinging on target at 90 degrees, (B) the velocity profile across the target in x and y and (C) the shear stress across the SJI target surface.

As seen in Figure 8-15, from the centre of the target, the velocity and shear stress profiles rise rapidly within the first few mm. Around 3.5 mm the velocity and the shear stress values are at a maximum. Beyond this distance the intensity decreases slowly.

The position of the annular electrodes (3 electrode rings) in this current study, based on the electrode positions of Efird in Figure 8-12, are plotted in Figure 8-16 for the centre (C) inner (I) and outer (O) electrodes with the predicted velocity and shear stress profiles for a jet of 10m/s.

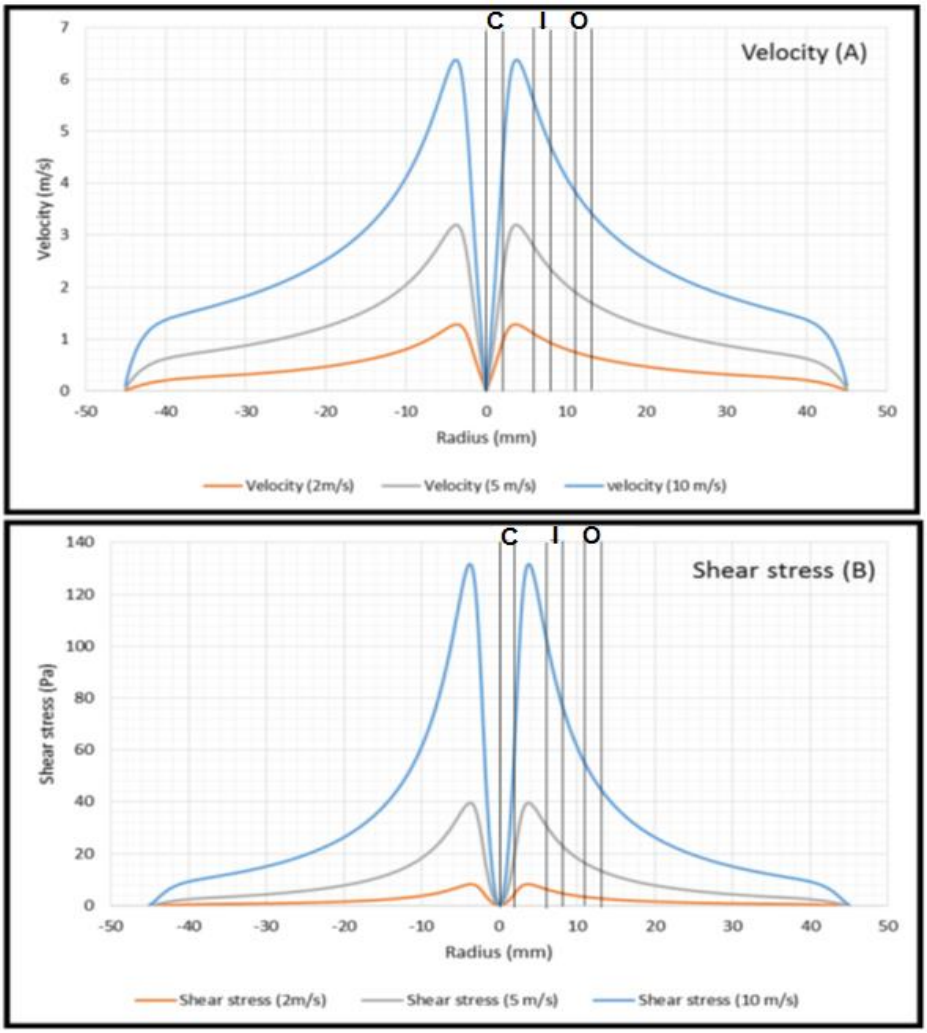

Figure 8-15 Target across diameter with velocity (A) and radial distance with shear stress (B)

It can be seen that that the inner electrode is indeed in a region with a higher turbulence as compared to the outer electrode which is at a lower velocity position. The shear stress also has a similar trend. The difference in terms of the velocities between the inner and outer electrodes will depend on the starting jet velocity. Thus for high velocities the difference is more significant, for example in Table 8-3 that shows the velocity and shear stress profile at jet velocity at 10 m/s.

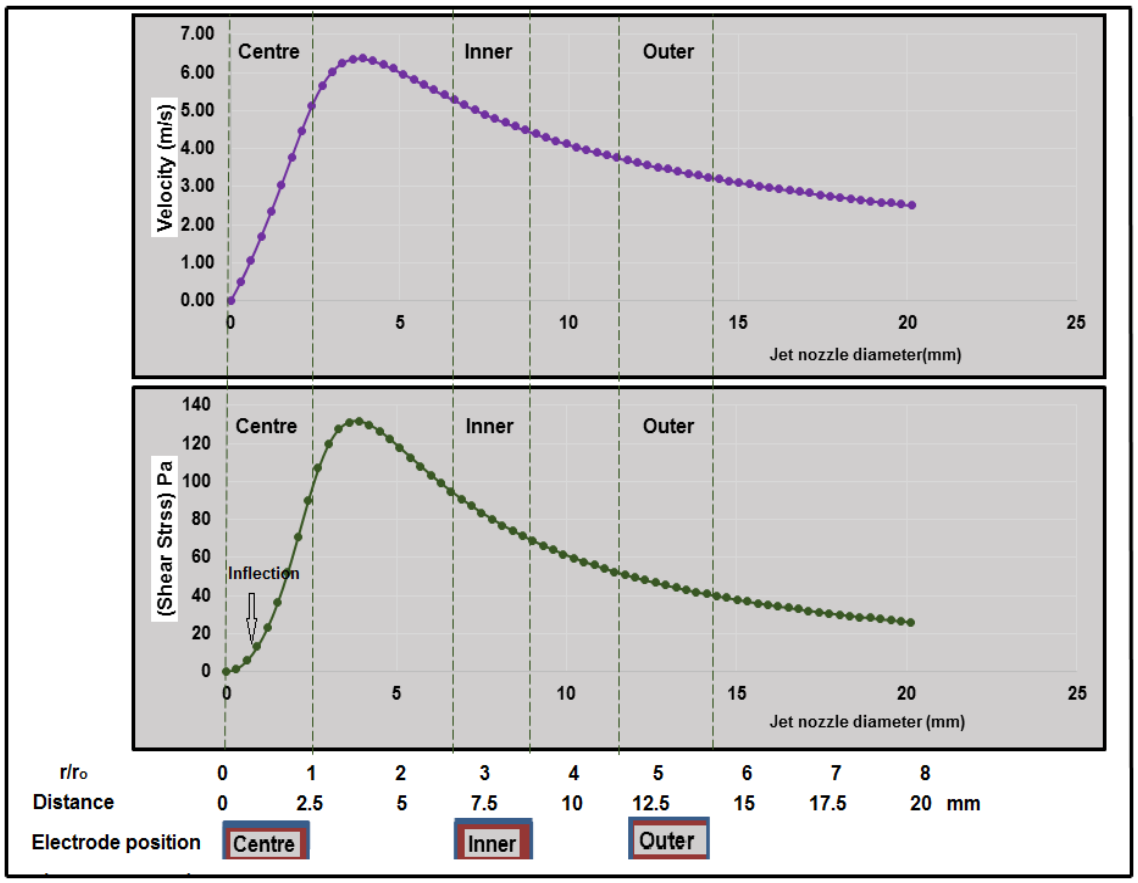

Figure 8-16 Estimated shear stress and velocity with radial position from the target centre, r=0 to outer edge

The electrode positions on the SJI target from the current study, deliberately made to be coincident with electrode positions reported by Efird, are compared in Figure 8-16. Efird [102] reports that region A, the location of the centre electrode, is referred the stagnant region due to no flow in this area. As seen in Figure 8-16, electrode C with a radius of 0-2.5 mm, is not a stagnant region, there is high activity directly after the zero position and which reaches a significant value at the edge of the centre electrode. Across the centre electrode the velocity ranges from 0 to 5 m/s just beyond this electrode, the velocity reaches a maximum of 6.4 m/s. In the centre electrode, the shear stress changes from 0 to 50 Pa, beyond this electrode, it reaches a maximum of 130 Pa. A small inflection can be seen with the shear stress, and the high intensity values are a little lower than the ratio reached for the velocity at the outer edge of the electrode. The activity at the electrode will decrease as the radius increases, and for the inner

and outer electrodes, the velocity, shear stress, and shear velocity decrease gradually. Further discussion regarding the hydrodynamic effect on the SJI target is given in the next chapter.

Table 8-3 describes the average value for velocity and shear stress from CFD analysis. Although there is a significant increase in activity of the electrode in area 1, the average value of the velocity and the shear stress in area 1 is still lower than in area 2 and area 3. Area 2 has the highest velocity and the shear stress followed by for electrode in area 3.

Table 8-3 The optimum velocity and shear stress of electrode in centre, inner and outer at flow rate 2, 5 and 10 m/s

	Centre		Inner		Outer	
	Velocity (m/s)	Shear stress (Pa)	Velocity (m/s)	Shear stress (Pa)	Velocity (m/s)	Shear stress (Pa)
2 m/s	0.5±0.4	2.4±2.3	0.9±0.05	5.2±0.5	0.7±0.24	2.9±0.21
5 m/s	1.3±0.9	10.5±10.1	2.5±0.12	25.1±2.2	1.8±0.07	14.2±1.0
10 m/s	2.5±1.8	32.7±22.9	4.9±0.24	84±7.4	3.6±0.14	47.6±3.34

Table 8-3 shows the velocity has a positive correlation with the shear stress. At jet velocities of 2, 5 and 10 m/s, the average velocity in the centre region of the SJI target is in the range 0.5-2.5 m/s, while for the inner area is between 1-5 m/s and followed by the outer region in a range 0.7-3.6 m/s. The shear stress values obtained also vary. In the centre area, the shear stress is in a range 3-33 Pa, whereas the inner zone has values from 5.2-85 Pa and followed by the outer region between 1-3.6 Pa.

The results of CFD simulations are compared with laboratory tests using the electrochemical method. Laboratory testing has been carried out using different jet velocities of 0, 2, 5, 8 and 10 m/s as explained in previous sections. Figure 8-17 shows the corrosion rate of the parent metal (PM) at 0, 2, 5 and 10 m/s. It was observed in Figure 8-17 that the rate of corrosion of the PM at certain jet velocities varied depending on the position of the electrode on the SJI target (outer, inner and centre).

It can be seen that the inner electrode i placed in an area which has the highest hydrodynamic condition (inner) as it has the highest corrosion rate experimentally determined compared with the corrosion rates obtained at electrodes in the outer and centre region.

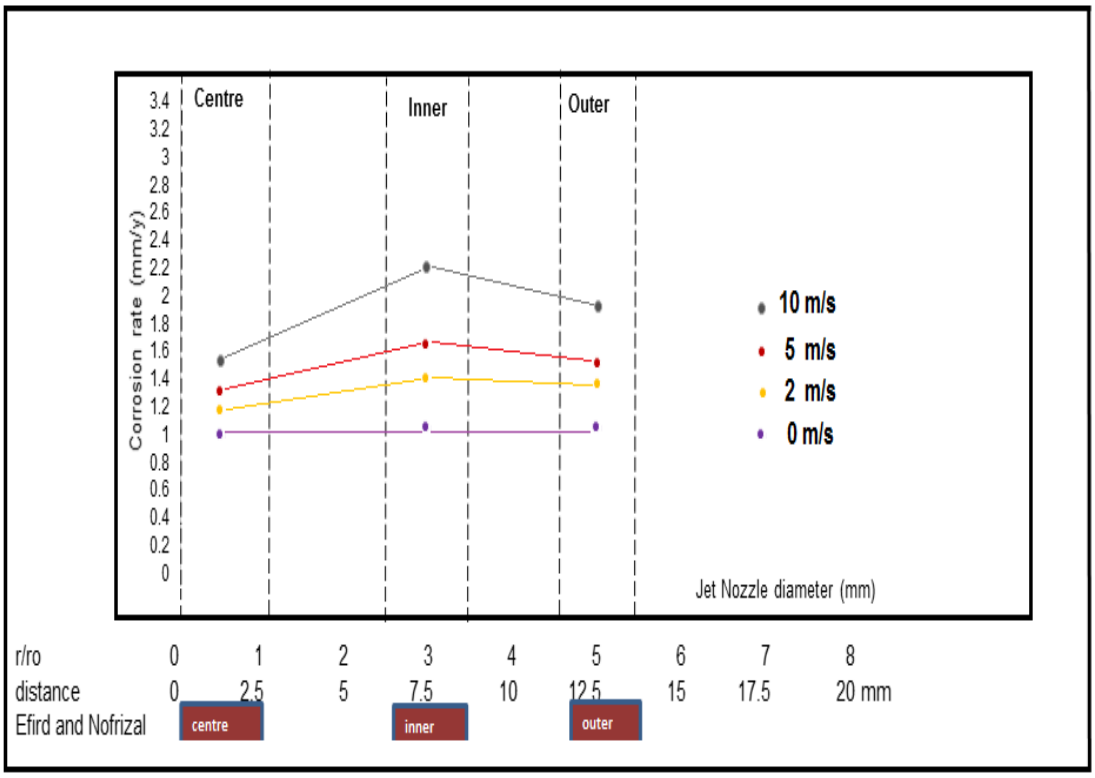

Figure 8-17 The experimentally determined corrosion rates of the PM from electrochemical analysis at flow rate 0, 2, 5, 8 and 10 m/s

In no-flow condition (0 m/s) the corrosion rate for all electrodes placed in outer, inner and centre is almost the same (~ 1 mm/y), this has been predicted because at no-flow conditions the hydrodynamic effect of the fluid was minimum.

Higher jet velocities result in higher turbulence levels and an increase in the mass transfer rates of corrosive species from bulk solution to the steel surface, therefore, the corrosion rate increases gradually when flow velocity increases. Figure 8-17 shows that for flowing conditions, there is an increase in the corrosion rate for each electrode in all regions, and it is indeed faster when the jet velocity increases. For example at a jet velocity of 10 m/s, the corrosion rate of the PM in the centre, inner and outer was 1.5, 2.2 and 1.9 mm/y, respectively. A similar

pattern was also found at jet velocities of 2 and 5 m/s. This is supported by the CFD results for electrodes in the centre, outer and inner electrodes during flowing conditions.

To increase the understanding about the target and to see the effect of self-corrosion and galvanic interactions on the target, a plot of corrosion rate with velocity across the target is provided both for self-corrosion (Figure 8-18A) and galvanic corrosion (Figure 8-19A). Equivalent plots of corrosion rate with shear stress are provided for uncoupled and coupled corrosion rates respectively in Figures 8-18B and 8-19B.

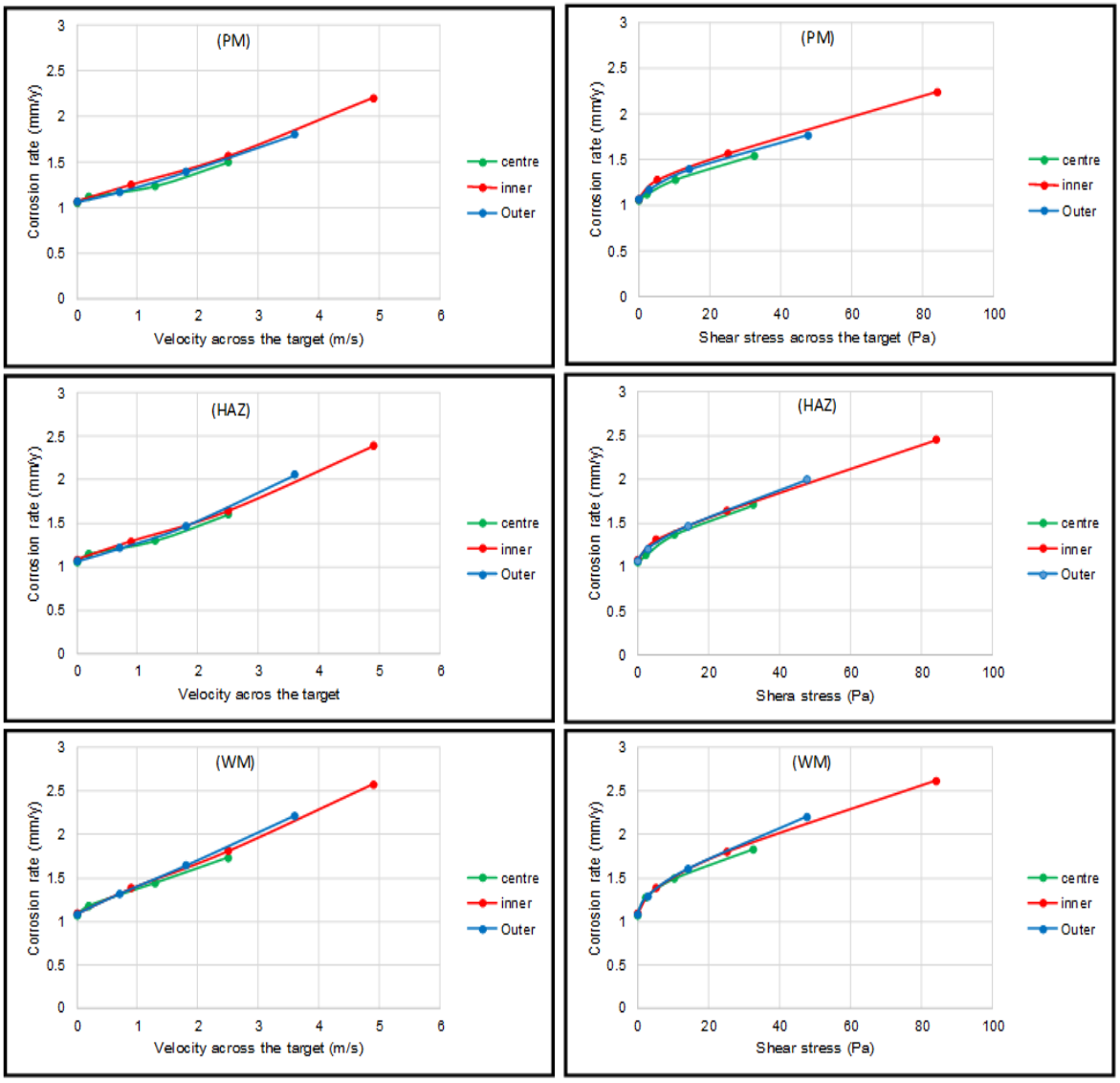

Figure 8-18 Self corrosion rate with velocity and shear stress across the target

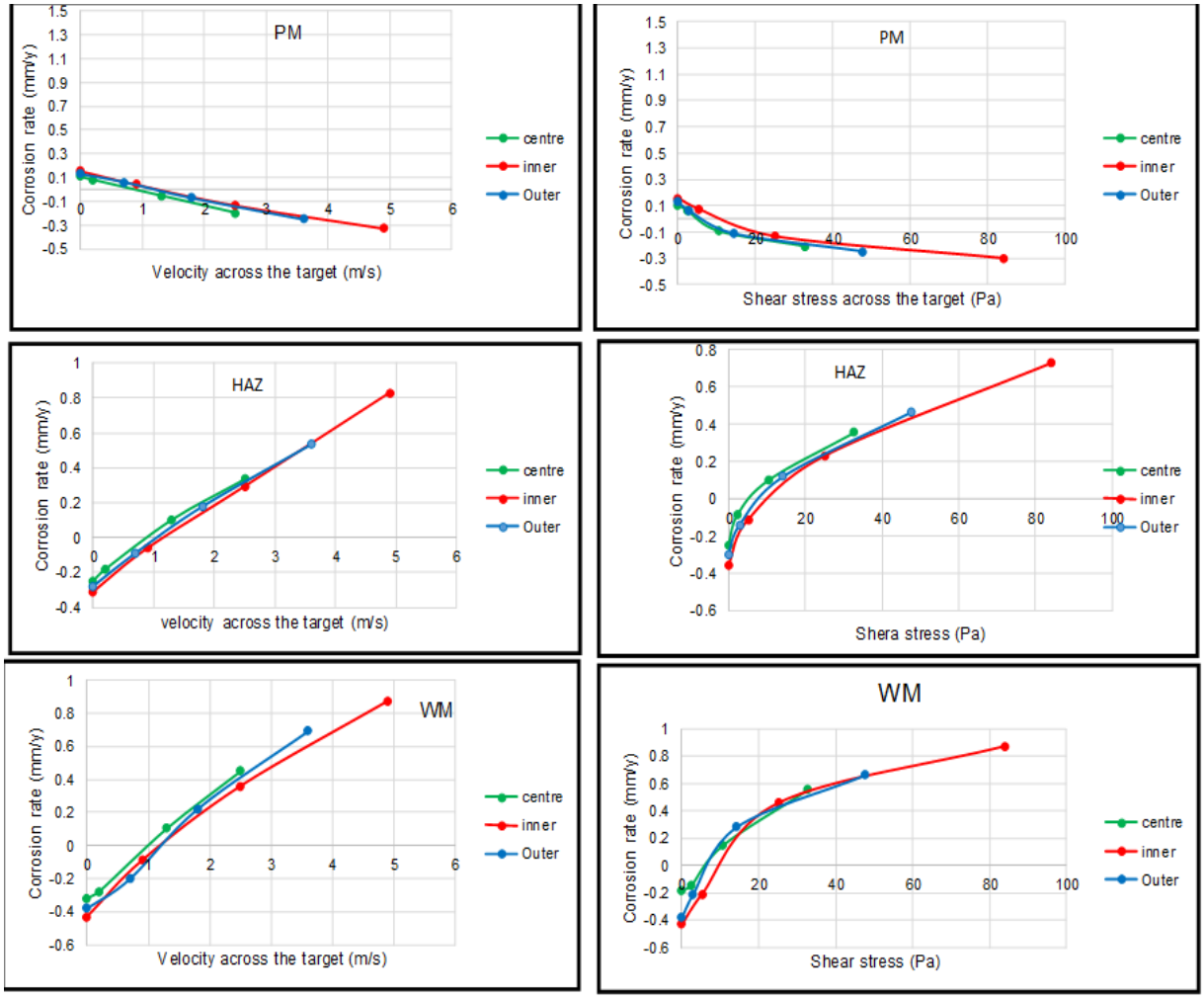

Figure 8-19 Galvanic corrosion rate with velocity and shear stress across the target

These graphs show the performance of the target from different parts of the weldment (PM, HAZ and the WM) and different locations (centre, inner and outer electrodes) on the target. A positive correlation is found for almost every situation as the velocity or the shear stress increases, the self-corrosion increases with a linear trend. This shows that the wherever the electrode is positioned a similar degree of self-corrosion is experienced. This trend is an indication to show that the target used in this study is working well.

The most interesting is the plot between the galvanic corrosion rate with velocity across the target (Figure 8-19 A) and shear stress (Figure 8-19B). From the literature the contribution of galvanic corrosion to preferential weld corrosion is under discussion. Some papers do not include galvanic corrosion rate as a

significant parameter causing the preferential weld corrosion. The galvanic measurements when available show anodic or cathodic behaviour and data from self-corrosion and galvanic corrosion rate as a parameters to describe PWC [21,22,178]. However, other papers argue that the galvanic corrosion rate is essential and play a significant contribution to PWC and calculate the total corrosion rate (self-corrosion plus galvanic corrosion rate) as an essential parameter to describe the PWC [13,15].

The plots of galvanic corrosion rate with velocity or shear stress across the target (Figure 8-19) are predominantly linear with positive correlation. However the PM is protected, so that, as the flow rate increases, the rate of corrosion decreases in a negative direction with increasing velocity. The HAZ and the WM are anodic and as seen in Figure 8-19, for HAZ and the WM, the corrosion increases when the velocity or shear stress increases. This information confirming galvanic behaviour is linked positively correlated with velocity and shear stress. Additionally the information is beneficial to the argument about the reasonable approach for calculating the total corrosion rate as an essential parameter for preferential weld corrosion.

8.4 Chapter Summary

- ✓ Flow accelerated corrosion has been studied by SJI.
- ✓ CFD analysis was performed to understand the fluid dynamic velocity and shear stress profiles. The different regions are identified on the target surface to show how fluid velocity affects the electrode surfaces after the corrosion reaction.
- ✓ The corrosion rate across the inner electrode is higher than that across the outer electrode of the target.
- ✓ It was found that the centre electrode in a flowing environment is not stagnant position, there was a high activity directly after the zero position and a wide range of velocities experience, reaching a significant value beyond that of the inner electrode.
- ✓ The measured corrosion rates across the target agree with the CFD simulation.

9 GENERAL DISCUSSION

The challenge of galvanic corrosion, especially in a high velocity environment to quantify corrosion on an X65 weldment surface is of considerable practical significance. The objective of this chapter is to discuss the significant findings from experimental work and place them in the context of reported literature.

The corrosion behaviour of an X65 carbon steel weldment, comprising a number of parts; parent metal, heat affected zone and weld metal within an SJI target, in brine saturated with CO_2 is assessed and linked to characteristics of the welded joint, type of environment and operating conditions. In the previous chapter, details about the design and construction of the SJI target, and the results of testing and interpreting data to assess the performance of the target was carried out. Further discussion regarding the suitability of the SJI target, supported by data from CFD modelling, will increase the understanding of flow accelerated corrosion, particularly at high velocity and high wall shear stresses.

9.1 Weldment corrosion

In this study, analysis of the weldment has been with a target using submerged jet impingement. A jet with velocities ranging from 0-10 m/s was used, this was initially expected to be comparable to wall shear stresses of 0-285 Pa similar to those used in the oil and gas industries [28]. From the CFD simulation undertaken in this research, much lower fluid velocities and wall shear stresses are estimated as discussed further in section 9.2.

The advantage of the SJI target is that, in this case, it has nine working electrodes. In this research three materials from the weldment, PM, HAZ, WM are located together in a circular form in three different locations. From one experiment, nine electrodes can be recorded. In addition, the hydrodynamic activity for each part of the weld region of the target can be evaluated at the same time.

In this study, the exposure time during electrochemical measurement was 20-24 hours. 20-24 hrs for a corrosion experiment does not necessarily represent the behaviour of corrosion in a year (mm/y) but is predictive. In the case of flowing conditions without oxygen and inhibitor, 1mm/year is equivalent to 2.7 µm/ day. Although 3 microns is very small amount of to measure the depth of material modification, the currents are sensitive and accurate over the 24 hours. However, in this study,while steady state has tried to be achieved, in some cases i appears a longer time period would have been an advantage. The measurements are accurate and reproducible but only cover the time period measured.

9.1.1 Uninhibited no-flow

A stagnant environment is an ideal condition to determine the performance of the target because in this state, all of electrodes on the SJI target have a similar environment condition. The electrode surfaces and the brine solution do not depend on the external agitation or mobility; thus the target is free from laminar or turbulent effect.

The results of galvanic measurements when the three materials are coupled in no-flow condition are shown in Figure 4-3. The PM in the outer electrode is in the anodic position and has the highest positive current (12.7 µA / cm^2). The PM will corrode faster giving partial protection to the WM (-33 µA / cm^2) and the HAZ (-22.4 µA / cm^2). This condition is expected due to the large area of PM and will provide more protection on the HAZ and the WM from the weldment corrosion attack [16,60,99,178].

This is an interesting result which indicates that for weldments in the petroleum industry, if the galvanic contribution is significant then the WM and the HAZ will be safe from PWC, when not inhibited, particularly during the commissioning or the shutdown conditions without any flow [184].

The trends of galvanic corrosion current found in the outer electrode are similar to the electrodes placed in the inner and centre region of the weldment in a no-flow condition. The consistent results of the galvanic characteristics are pleasing

regardless of where the electrode is located in a static environment and supports that the target is performing well.

The galvanic corrosion trend contrasts with previous research by Adegbite *et al.* [13,16], with the X65 SJI target reported (target A) in Figure 9.1. Adegbite reports the HAZ in the inner ring has positive current (anodic), while the same weldment (HAZ) in the outer and centre electrodes have negative currents (cathodic).

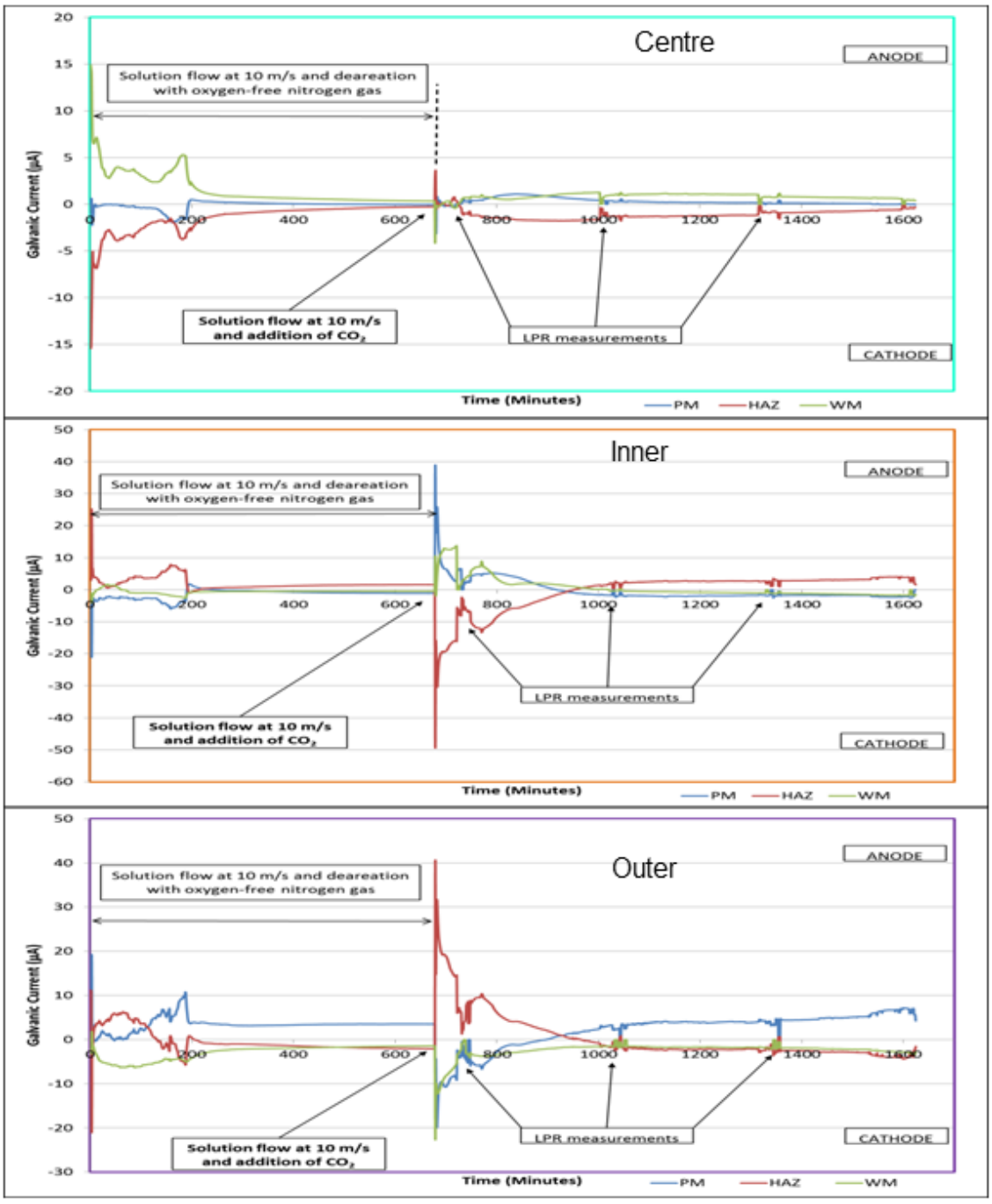

Figure 9-1 Galvanic characteristic in no-flow condition by Adegbite et al. [13]

It is seen that in Adegbite research [13], the range of electrode positions across his target are not always equivalent in stagnant conditions. This is concerning. However this difference between electrode positions with the same hydrodynamic conditions was reported to be due to the difference in local composition and/or microstructure within the electrode areas, occasioned by the variance in production or fabrication errors.

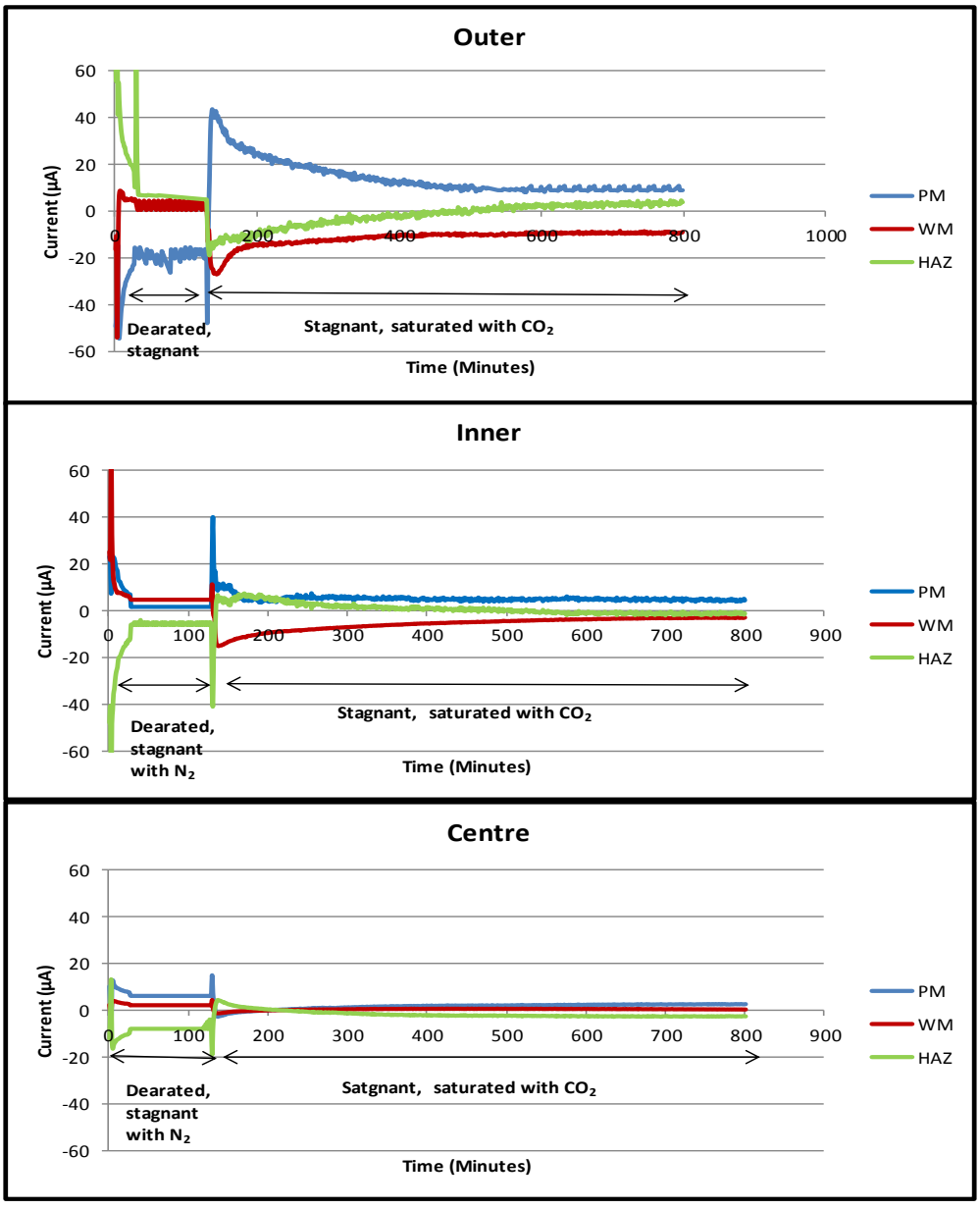

Figure 9-2 Galvanic characteristics without flow from Adegbite target measured by Nofrizal

The Target A used by Adegbite was available for evaluation in similar stagnant conditions to that used for the main target (the focus of this work). Results for galvanic corrosion show that unlike when used by Adegbite, the galvanic characteristics for all three regions are similar as seen in Figure 9.2.

The trend is similar to the current target (Nofrizal) with cathodic HAZ and WM. It is helpful to see that the target regions are all very similar, giving some repeatability. Thus the target has three working equivalent weldment regions. The difference the Target A behaviour between Adegbite's research and the new data is attributed to additional polishing carried out. Significant material is removed by the polishing action, which allow the electrodes, now with significant material thickness removed i.e. 2-5 mm, to behave equally in an uninhibited stagnant brine saturated with CO_2. Figure 8.13 shows a schematic cross section of the target where 21 mm of electrode material is available. Adegbite may have been slowly removing material from 21 mm. The target thickness now is estimated to be at over 50% thinner below 10 mm of available material.

The self-corrosion analysis was carried out directly after the galvanic measurement was completed. The self-corrosion rates in the outer ring calculated from the Tafel plots are given in Figure 4-6. In no-flow condition, the self-corrosion of each electrode in outer, inner and centre region at 25 ^oC was around 1 mm/y. This was supported from the potential from the PM, HAZ and the WM in the range -724 to -725 mV and corrosion current density in the range 90-94 $\mu A/cm^2$. This very close similarity is expected when all electrodes are placed in a similar no-flow environment.

The uncoupled corrosion rate of the X65 weldment is given in Figure 4.7, reproduced here, to compared with predicted corrosion rates from a nomogram of Millians and deWaard, seen in Figure 9-3 [88]. When the X65 steel is exposed to CO_2 at 1 bar and 25^oC, it predicts that the corrosion rate is 1 mm/y.

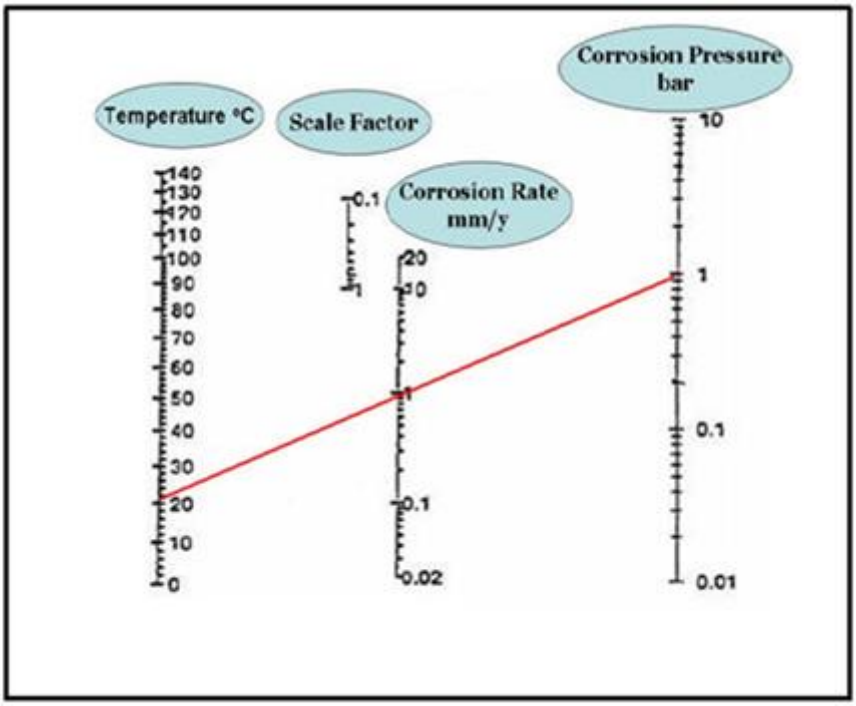

Figure 9-3 Corrosion rate prediction for X65 steel without flow at room temperature [88]

For comparison results of self-corrosion are given in Figure 9.4 comparing results in the uncoupled condition in this work (Nofrizal) with a second target A used by (a) Adegbite and (b) also by Nofrizal. Target A although a little lower in value is reasonably close to the expected value of 1mm/year.

It is not confirmed why there is a difference in corrosion rate for the two X65 materials, with similar conditions, room temperature and still brine saturated with CO_2. However it could be influenced by deaeration (as shown in Chapter 7). Fully deaerated conditions would result in lower corrosion rates (as Adegbite). Different de-aeration levels could also be responsible for the slight difference in corrosion rates for Target A. Another possible scenario is that the Target A is examined at the very end of the experimental testing period, after the vessel had been used with inhibitor. Although it was cleaned it is very difficult to remove all traces of inhibitor. It is suggested that a trace of inhibitor remained in the vessel reducing the corrosion rate a little but not significantly. However it is interesting that the WM in Target A is has a consistently lower corrosion rate, independent of operators.

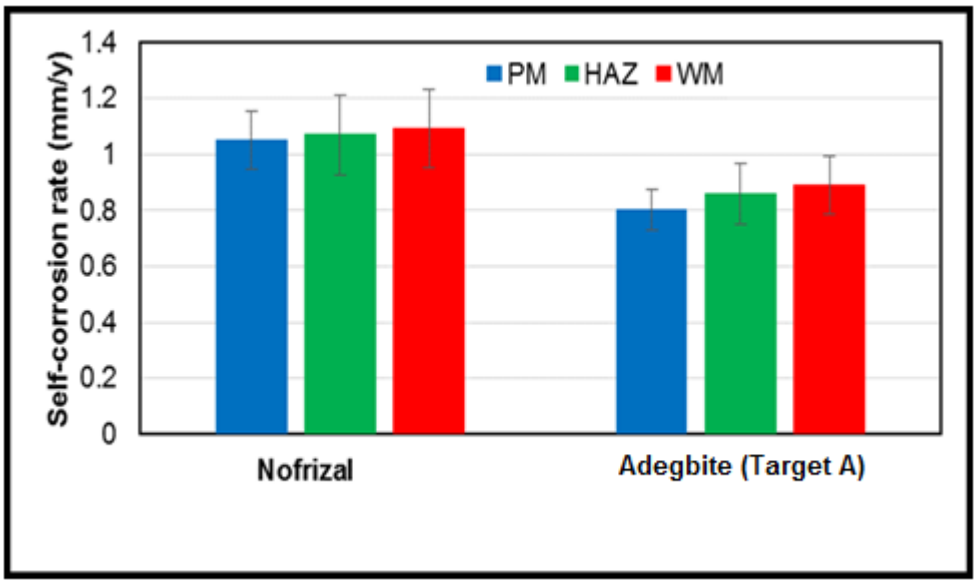

Figure 9-4 Self-corrosion of the weldment from current study (SJI) and previous weld (SJI Target A) in a stagnant uninhibited condition

9.1.2 Uninhibited flowing condition

In a flowing environment, the brine solution moves across the electrodes with a range of hydrodynamic conditions from laminar activity (centre electrode) to a range of turbulent flow (inner and outer regions). The wall shear stress and mass transfer coefficient play a significant role directly related to the loss of pressure friction from the wall and stimulates more active interaction between anions and cations in brine solutions [92].

The self-corrosion in a flowing uninhibited condition has a positive correlation with the velocity. Compared to stagnant conditions, in this research (Nofrizal) the corrosion rate has doubled (see Figure 9.4) and the PM, HAZ and the WM is 1.9; 2.1 and 2.2 mm/y, respectively.

It is suggested that when any turbulence occurs, accompanied by an increase in the wall shear stress, the immediate surface is attacked leaving the weld surface without protection [48]. Figure 9-5 is a schematic showing the effect of increasing velocity and the associated increase in current. The data shows that fluid velocity has a very significant and influential effect on corrosion behaviour. However other

factors can contribute, such as welding type and consumables, chemical composition and weld microstructure.

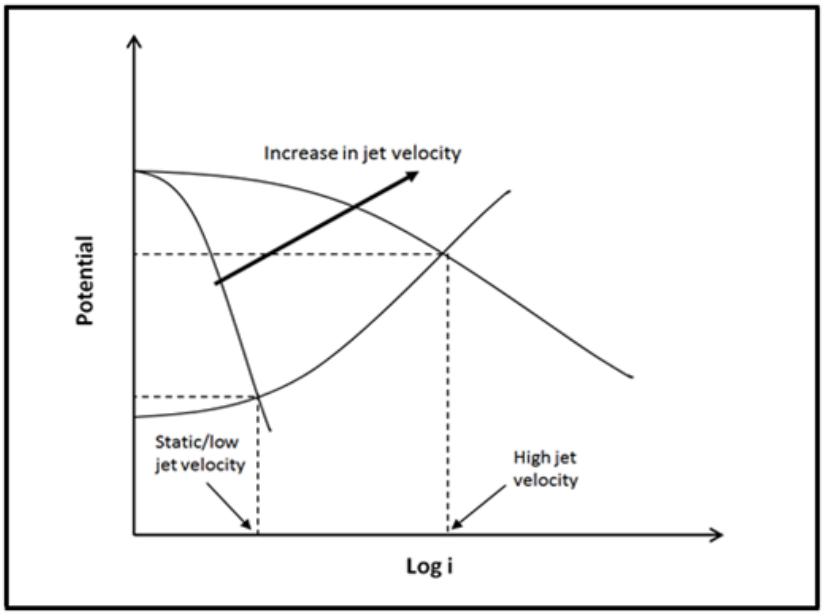

Figure 9-5 Schematic showing the effect of flow on the corrosion rate [118]

Considering fluid velocity, results from self-corrosion are reproduced in Figure 9.6 comparing this work (Nofrizal) with a second target A used by Nofrizal at a jet velocity of 10 m/s.

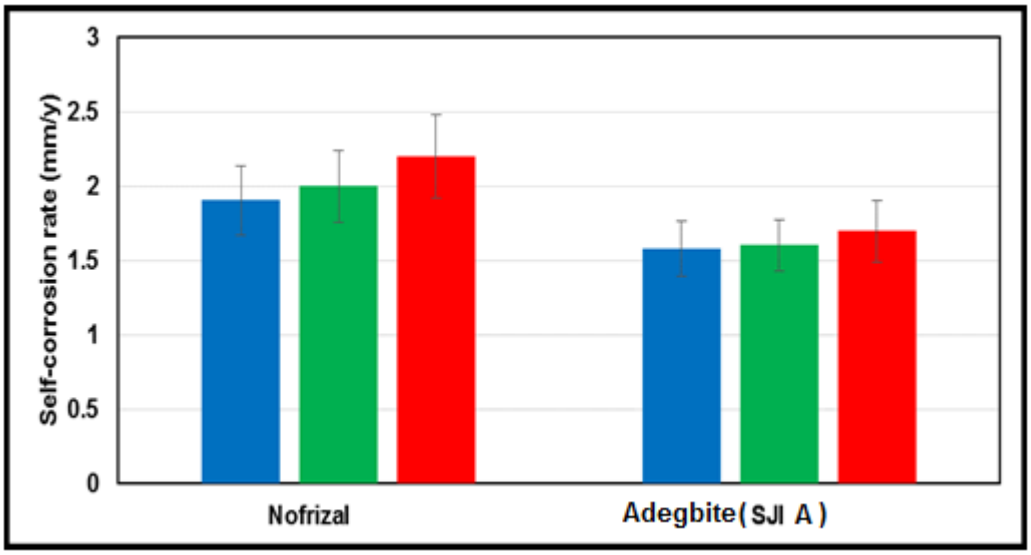

Figure 9-6 Self-corrosion of SJI (current target) and Target A in uninhibited brine at 10 m/s jet velocity

Both targets show increased corrosion rates compared to no flow (double). It is interesting that now the WM is more vulnerable in both targets. It is suggested that if, for example, there was a little more dissolved oxygen when running Target A, the corrosion rate increased further to give similar corrosion rate values and characteristics. Both indicates a PWC problem could be experienced in flowing environments.

The hydrodynamics evaluated in this study was determined by a jet in the range 0-10 m/s. At the maximum this is 10 m/s, associated with wall shear stress of 280 N/m^2. Characteristics of the weldment in the outer region in a coupled state with flow is different to a stagnant condition as described in Figure 5-2. Immediately the flow begins, the WM and HAZ switch from cathodic to anodic with current densities of 60 $\mu A/cm^2$ and 45 $\mu A/cm^2$ respectively. This provides a protection to the PM (-24 $\mu A/cm^2$). Similar trend in results are found for the weldment behaviour in the inner and centre electrodes. This condition is very unfavourable because the WM and HAZ will corrode quickly compared to the PM and this is not desirable in industrial applications. When the jet velocity decreases from 10 m/s to the lowest flow of 2 m/s, the behaviour changes such that the WM and the HAZ return to cathodic behaviour while the PM is anodic. Thus in an uninhibited flowing environment, a jet velocity of 2 m/s is a suitable for this SJI target, as the WM and HAZ behave cathodically. CFD later shows the velocity across the target at a jet velocity of 2 m/s is almost so low as to be immeasurable or to be consistent only with laminar flow. Estimates, from section 9.2 and Figure 9-16, is that the target velocity is less than 0.05 m/s at its maximum. However, when the jet velocity increases gradually from 5-10 m/s, the galvanic corrosion rate of the WM is faster than the HAZ and the PM. A similar condition was seen in the previous study by Adegbite *et al.* [16]. With jet velocities of 5 and 10 m/s, the WM and the HAZ experience preferential weld corrosion. Thus any turbulent flow appears to cause difficulties for the weldment, particularly in uninhibited conditions.

It has been shown that the velocity is a major factor influencing PWC. However other factors can contribute, such as welding type and consumables, chemical composition and weld microstructure. The latter two factors are discussed below.

9.1.2.1 Effect of chemical composition

In the literature, a compilation of weld compositions used with X65 by a number of researchers is given in Table 9.1. This shows a number of weldments were designed with different elemental weld compositions. As mentioned in Chapter 2 steel weldments are susceptible to corrosion attack.

In Table 9.1 compositions of some welds in literature are given with their corrosion behaviour coupled with X65 in a flowing brine solution (Figure 5.6). After measurement of the galvanic corrosion in coupled conditions, it was found that all show preferential weld corrosion. However, the area affected with most serious corrosion attack varies either the WM or the HAZ.

Table 9-1 Studies of PWC of X65 pipeline steel in flowing condition

Conditions		C	Si	Mn	P	S	Cr	Mo	Ni	Al	Cu	Nb	Fe	PWC	Refs
RCE, 3.5 %, 2000 rpm	PM	0.19	0.27	1.22	0.007	0.007	0.05	0.03	0.11	0.029	0.13	-	Base	HAZ	Kermani et al. 2003 [61]
	WM	0.07	0.83	1.44	0.015	0.017	0.02	0.03	0.007	-	0.28		Base		
Flow loop, 3.5 % NaCL, 1 Bar CO_2 at 60°C	PM	0.07	0.20	1.17	0.02	0.005	0.033	0.003	0.019	0.031	0.021	0.051	Base	Weld	Gulbrandsen, 2005 [105]
	WM	0.1	1.0	1.6	≤0.025	≤0.035	-	-	-	-	-	-	Base		
Re-circulating vessel, CO2 1 bar, 3.5 % NaCl	PM	0.07	0.20	1.17	0.019	0.005	0.033	0.003	0.019	0.031	0.021	0.051	Base	HAZ	Lee at all, 2005 [57]
	WM	0.08	0.70	1.17	0.019	0.005	0.50	0.60	0.70	0.03	0.02	0.051	Base		
RCE, CO2 1 bar, 3.5 %, 3000 rpm	PM	0.08	0.3	1.6	0.009	0.0005	0.02	0.01	0.04	0.04	0.02	-	Base	HAZ	Martinez, 2011
	WM	0.08	0.3	1.4	0.01	-	0.03	0.33	0.68	0.03	0.02	-	Base		[139]
RCE, CO2 1 bar, 3.5 %, 3000 rpm	PM	0.08	0.3	1.6	0.009	0.0005	0.02	0.01	0.04	0.04	0.02	-	Base	HAZ	Alawadhi, 2011
	WM	0.08	0.3	1.4	0.01	-	0.03	0.33	0.68	0.03	0.02	-	Base		[15]
SJI, 3.5 % sea water, 5 m/s	PM	0.12	0.21	0.96	0.019	0.003	0.06	0.03	0.09	0.035	-	-	Base	HAZ	Barker, 2012
	WM	0.20	0.23	1.12	0.010	0.012	0.07	0.18	0.78	0.010	-	-	Base		[22]
SJI, 3.5 % sea water, 5 m/s	PM	0.08	0.3	1.6	0.009	0.0005	0.02	0.01	0.04	0.04	0.02	-	Base	Weld	Adiqbite, 2014 [13]
	WM	0.08	0.3	1.4	0.01	-	0.03	0.33	0.68	0.03	0.02	-	Base		
Current study	PM	0.07	0.30	1.51	0.012	<0.005	0.02	0.01	0.39	0.037	0.26	0.02	Base	Weld	Current study
	WM	0.07	0.29	1.59	0.014	0.007	0.03	0.11	0.27	<0.01	0.10	<0.01	Base		

The addition of nickel at different concentrations in the weld material in uninhibited condition is highlighted. This is because a reported way to minimize attack is by alloying with the addition of 1% nickel. Further details of the corrosion attack and location (in the WM or the HAZ) are explained below:

1. A study conducted by Kermani *et al.* [61] using the RCE method at 2000 rpm where the composition of Ni was 0.11% in the PM and 0.007% in the WM. PWC occurs in HAZ.
2. PWC occurs in the HAZ shown by research conducted by Martinez [99] with the RCE method and composition of Ni 0.04% (PM) and 0.68% (HAZ).
3. Alawadhi and Robinson [15] undertook a study with RCE, a similar method a similar weld composition to Martinez. The HAZ is attacked.
4. Research carried out by Gulbrandsen [185] with a flow loop at temperature 60 ^{o} C with CO_2 using a PM composition of Ni 0.019%, and no nickel in the WM, showed corrosion took place in the WM.
5. A study with a recirculating vessel method performed by Lee [60] used a Ni composition of 0.019% (PM) and 0.7% in the WM. PWC occurs in the HAZ.
6. A study by Adegbite *et al.* [16] used a similar weld to Alawadhi & Robinson (2011) and an SJI method. PWC occurs in the WM.
7. Barker *et al.* [178] conducted a study using SJI with a composition of Ni 0.09% (PM), 0.78% (WM). PWC occurred with the HAZ.
8. The current study is conducted with the SJI method and a composition of Ni in the PM (0.39%) and 0.27 % in the WM. The WM suffered PWC.

From the above studies, it is seen that the alloying process by adding nickel with different concentrations to 0.8% does not always protect the weld from corrosion attack in flowing, uninhibited conditions. Indeed all show preferential weld corrosion. For almost all reported weldments the % Ni is higher in the WM than the parent metal. An X65 weldment is vulnerable in uninhibited flowing brine saturated with CO_2 resulting in PWC. The HAZ is always more vulnerable than the PM. The WM can be influenced by addition of Ni to reduce the rate of attack compared to the HAZ. The WM and the HAZ are more susceptible to attack than the PM. The combination of attack on both the WM and HAZ (with or without Ni) results in PWC.

Hence, the application of inhibitor to minimize the attack is suggested to create a protective film on the weld surfaces [186,187] and as discussed in section 9.1.3.

9.1.2.2 Effect of microstructure

Previous studies record that microstructure plays a significant role for corrosion of steel [136,188]. Pipeline welding is a complex process, and different microstructures are produced for different materials. The effect of temperature and holding times influence the carbon solubility in ferrite and carbon segregation to grain boundaries [189]. Carbides can precipitate at the ferrite grain boundaries during the austenite transformation, and this process is strongly related to the cooling process [190].

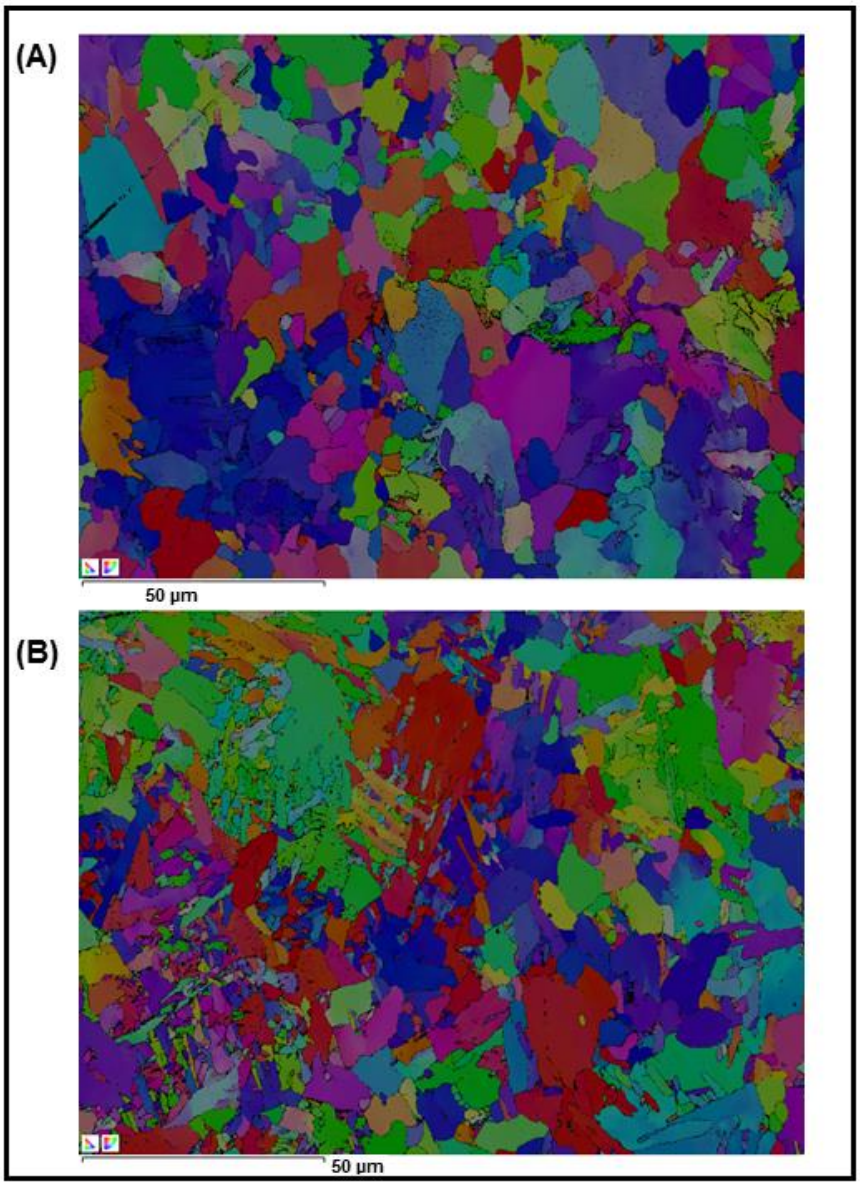

Figure 9-7 EBSD layers images for the PM (A) and the WM (B) shows a complex microstructure of the weldment

Electron backscatter diffraction (EBSD) was used to provide microstructural detail from the PM and the WM, which were predominantly ferrite (Figure 9-7). Figure 9-7, an EBSD micrograph of the parent metal (X-65) and the weld metal shows the crystalline orientation (grains) and the surface that separates individual grains from each other (grain boundaries). Other information received from the EBSD analysis is the average grain diameter as plotted in Figure 9-8.

Figure 9-8 shows the PM and WM have slightly different grain size distributions. The PM has an average grain size with a distribution function of 0.75 µm for the PM and 0.65 µm for the WM. However, the WM has 8% more grains with a size above 1 µm compared to the PM. Literature reports that the grain size of the boundary layer contributes to the corrosion reaction [60,62,191]. Grain boundaries can have weak interfaces which can be disrupted [192]. This is the reason grain boundary atoms are said to be at higher energy levels [193].

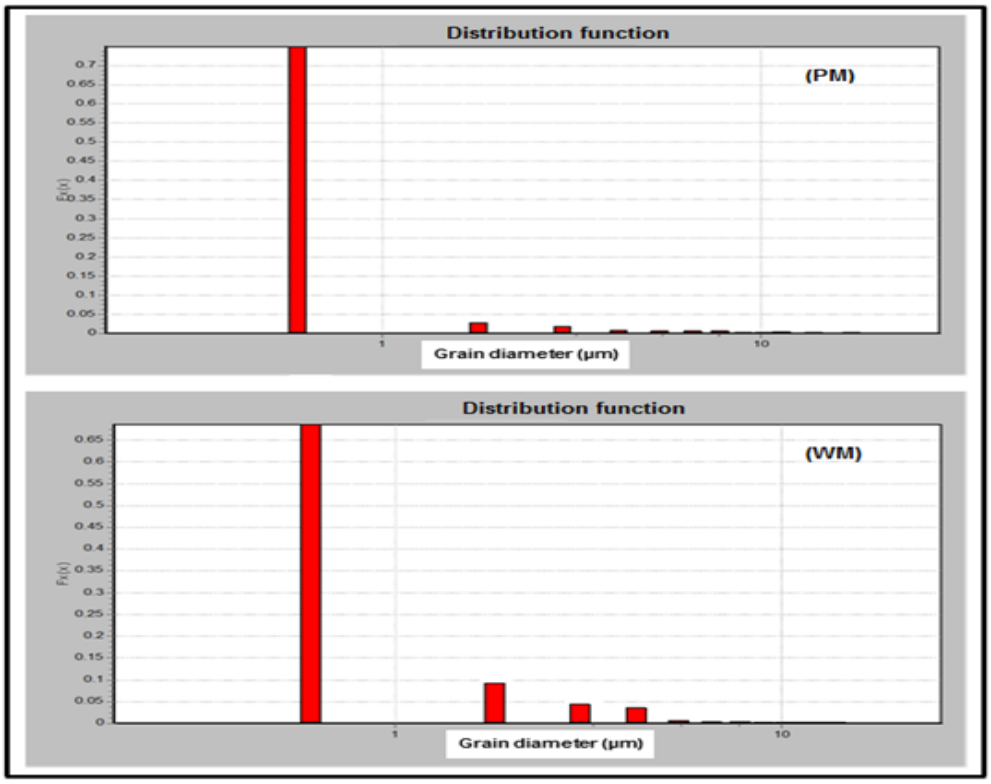

Figure 9-8 The distribution function of grains from the PM and the WM from EBSD analysis

The multi-phase weld used in this study creates an interesting WM microstructure (Figure 9-9 A). The WM has a slightly larger grain size compared to the PM and the HAZ. While this may be a reasonable explanation for slightly different corrosion rates in a flowing condition where WM corrodes faster than PM and this result is in good agreement with previous studies [21,60,97,191].

The HAZ area has an similar composition to the parent material, and thus differences in behaviour between the two regions are likely to be microstructurally related so that the rate of corrosion between the HAZ and the PM are not significantly different. However it in all cases in this work, the HAZ has a slightly higher corrosion rate.

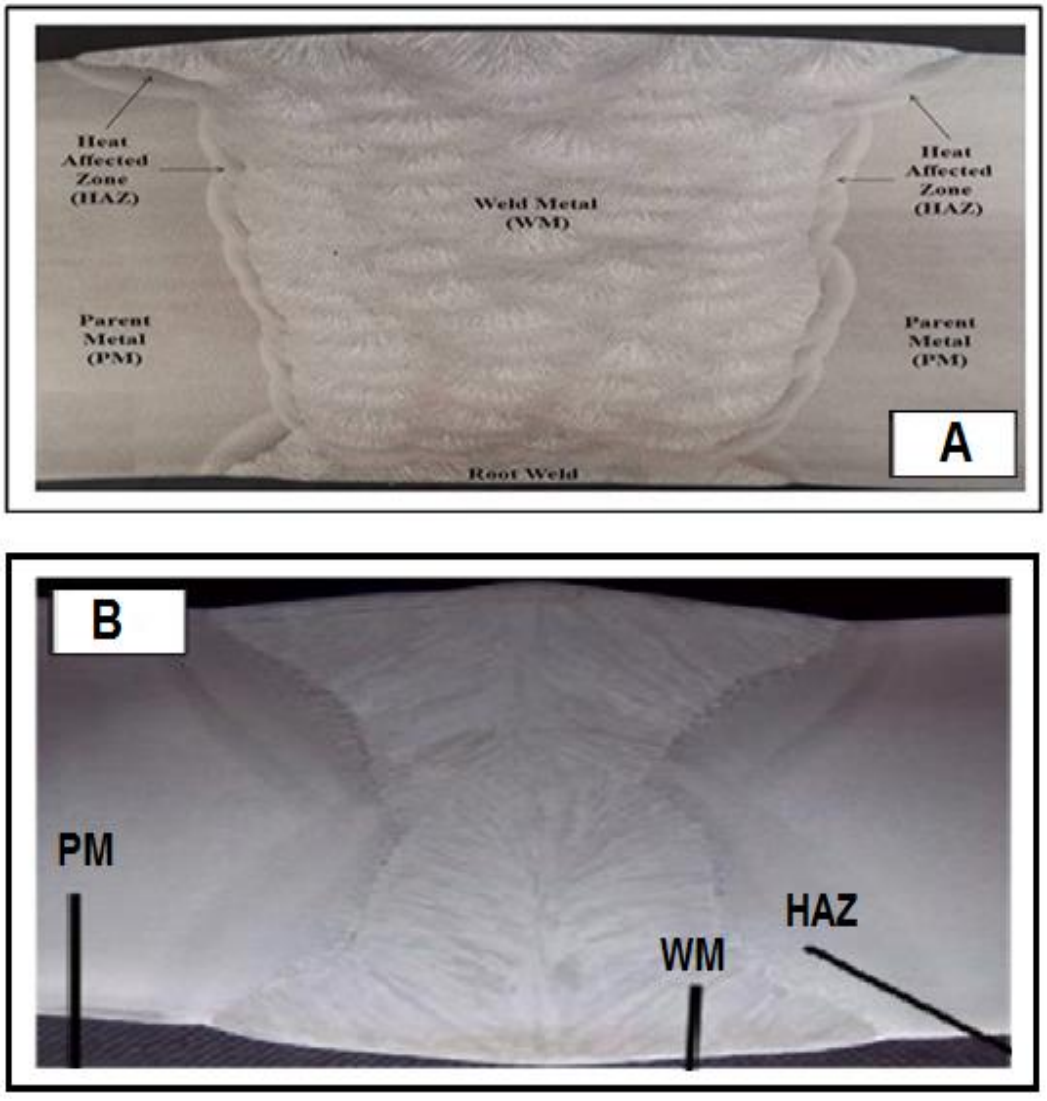

Figure 9-9 Weld microstructure of (A) current target (B) previous Target A)[118]

The previous target from Adegbite et al., [16] (Target A) has a different weld metal composition (Table 9-1) and a different type of welding process. Figure 9-9B shows this to be two single pass welds, different to the target used by Nofrizal comprising multi-pass welds (Figure 9-9A).

Galvanic measurements from Target A weldment showed similar results to current research, where the HAZ and the WM are anodic and protect the PM. The self-corrosion result for the WM, the HAZ and the PM was lower than current study. The WM for Target A has a different elemental proportion of nickel (0.8 %) to the PM 0.3 %Ni. However there is also a different microstructure from single pass welds in Target A (from Adegbite) (Figure 9-9B). The current target is from a multi-ass weld (Figure 9-9A). Although it is suspected that the weld metal has small and compact grains due to the homogeneity of the welding process (Figure 9-9B) EBSD measurements do not confirm this.

9.2 Inhibited Condition

In this study, CORRTREAT 10-569, containing glycol (poly di-ol) and amine-based poly (llysisne) is the inhibitor. The molecular structure is in Figure 9-9 [194].

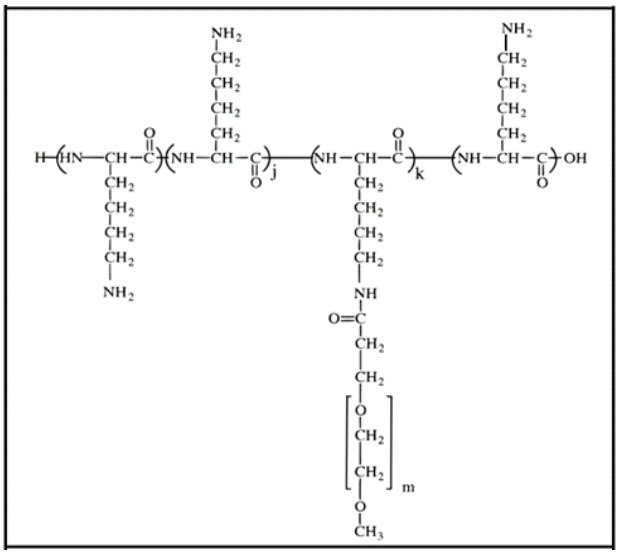

Figure 9-10 Molecular structure of poly(l-lysine)-g-poly(ethylene glycol) [194]

These chemicals are good inhibitors due to their large molecular weight, rich with electron pairs from oxygen and nitrogen molecules. More free electrons ensure the inhibitor is strongly and well adsorbed on the steel surface by transfering or

donating electrons between the solution and steel surface to form an adsorbed barrier film [195]. FTIR analysis confirms and identifies active functional groups as an inhibitor (Figure 6-2). All of the copolymers of poly(L-lysine)-g-poly(ethylene glycol) adsorb spontaneously in an electrostatically driven process onto different negatively charged metal oxide surfaces.

9.2.1 Adsorption of inhibitor on the weld surface (adsorption isotherm study)

Adsorption isotherm studies are important in understanding the mechanism of the interaction between the inhibitor and the steel surface and also the nature of the bond between the adsorbed inhibitor molecules and the metal surface.

As the polymer chains adsorb onto the surface, the amount of space left for other chains decreases, and thus, an adsorption isotherm will be observed. This is particularly important with block copolymers, because of the large volume of the adsorbing segment and because of the steric effects of the poly(ethylene glycol) segments [194].

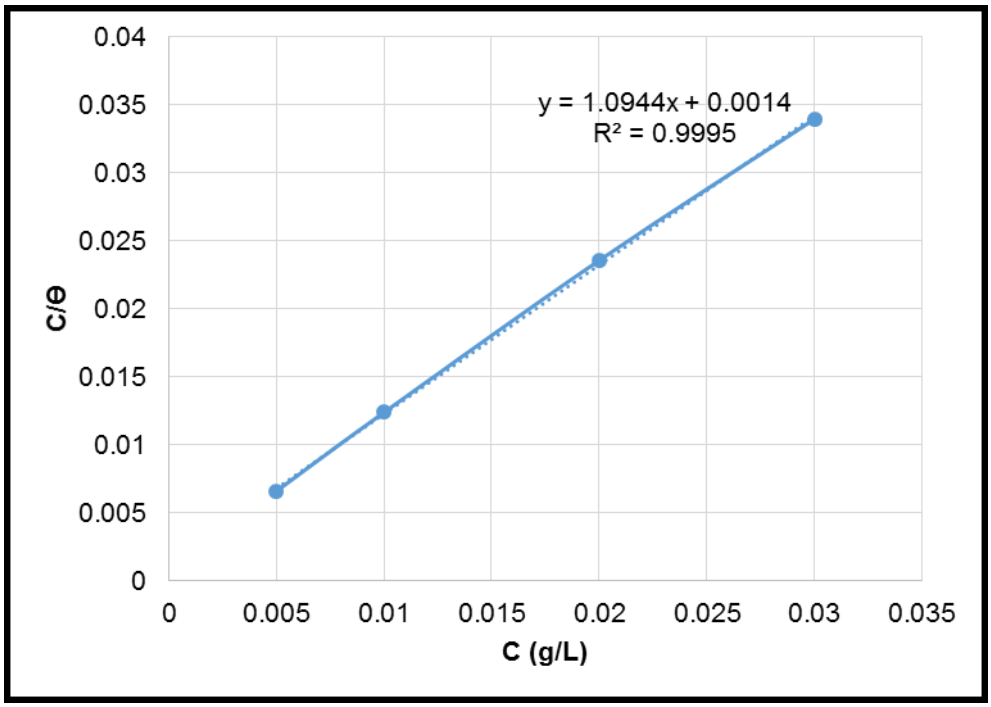

Figure 9-11 Langmuir adsorption of the CORRTREAT 10-569 on the weldment surface in the outer ring saturated with CO_2 without-flow

Figure 9-11 is a plot of C_{inh}/θ versus C_{inh} of inhibitor, a straight line with a correlation coefficient close to 1, showing that the adsorption of this inhibitor fits well to the Langmuir adsorption isotherm. The fits particularly well with experimental data from LPR measurements (outer ring) in the no-flow condition.

Table 9-2 Gibbs Free Energy of each electrode in stagnant and flowing conditions at 5 and 10 m/s

Flow rate	Weld position	Weldment	R^2	K_{ads}(mol L^{-1})	ΔG°_{ads}(kJ mol^{-1})
No-flow	Outer ring	PM	0.9993	1428.76	-35.71
		WM	0.9959	1111.11	-35.07
		HAZ	0.9989	2000	-36.55
	Inner ring	PM	0.9997	1428.57	-35.72
		WM	0.9999	714.28	-36.09
		HAZ	0.9998	1666.66	-35.07
	Centre	PM	0.9997	2000	-36.54
		WM	0.9997	1111.11	-35.07
		HAZ	0.9992	1666.67	-36.07
5 m/s	Outer ring	PM	0.9995	666.66	-33.19
		WM	0.9993	1000	-34.81
		HAZ	0.9997	625	-33.96
	Inner ring	PM	0.9997	357.14	-32.21
		WM	0.9998	588.23	-33.47
		HAZ	0.9998	555.56	-33.32
	Centre	PM	0.9997	526.32	-33.18
		WM	9989	833.33	-34.34
		HAZ	0.9987	1428.57	-35.41
10 m/s	Outer ring	PM	0.9991	625	-33.62
		WM	0.9989	714.28	-33.96
		HAZ	0.9996	500	-33.06
	Inner ring	PM	0.9997	588	-33.46
		WM	0.9994	714.28	-33.95
		HAZ	0.9998	357.14	-32.21
	Centre	PM	0.9996	1000	-34.81
		WM	0.9996	833.33	-34.34
		HAZ	0.9995	1250	-35.36

The Gibbs free energy ($-\Delta G^{\circ}_{ads}$) was calculated from Equation 2-38 and 2-39. The ΔG°_{ads} values are in the range -32 to -36 kJ mol^{-1} for the weldment in each section with and without flowing conditions, supporting typical physisorption of

the inhibitor on the weldment. The negative values of ΔG^{o}_{ads} revealed the spontaneity of the adsorption process [17]. The higher K_{ads} values obtained for weldment in the no-flow condition (-35 to -36.5 kJ mol^{-1}), mean that the CORRTREAT inhibitor is more strongly adsorbed onto the weld surface than when the artificial sea water flows with jet velocity of 5 and 10 m/s [18].

9.2.2 No-flow condition

A concentration of 30 ppm was chosen for maximum inhibitor efficiency for the PM, the WM, and the HAZ. The inhibitor efficiency (86-90%) is comparable with Alawadhi & Robinson (2009) [98] with the same inhibitor. The galvanic and self-corrosion measurements are applied to calculate the total corrosion rate and then the results were compared to results from the uninhibited state.

In the inhibited condition, the corrosion rates of coupled and uncoupled parts of the weldment in each region in stagnant and flowing brine decreased significantly due to the inhibitor adsorbed onto the weldment surfaces. The adsorption process is rapid and was ultimately limited by the packing of the inhibitor side chains at the surface. The resulting adsorbed layer drastically reduces subsequent inhibitor adsorption as in Figure 9-12.

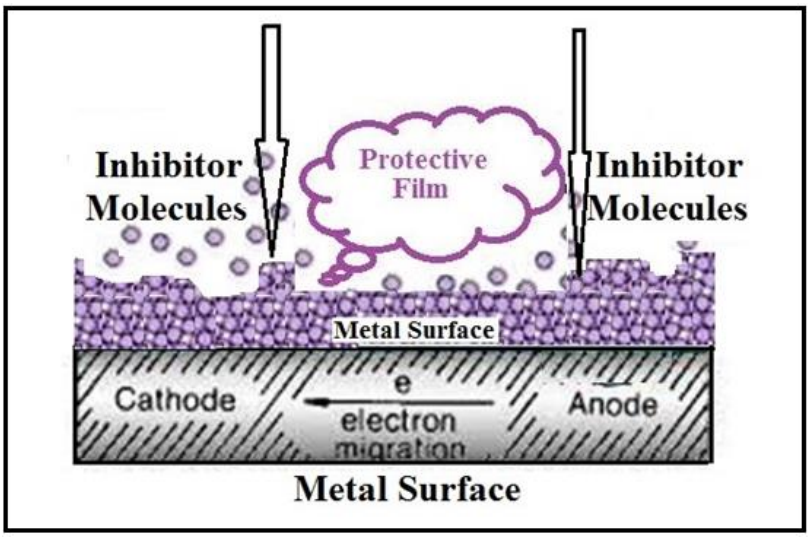

Figure 9-12 The attachment of the inhibitor molecule on the metal surfaces [46]

The galvanic characteristics of the weldment in the outer region in inhibited brine saturated with CO_2 at no-flow conditions is shown in Figure 6-3. The PM is in an

anodic position providing a very small galvanic current density of 4 μA/cm^2 compared to stagnant uninhibited brine where the current density is 20 μA/cm^2. Formation of the inhibitor film minimises access of corrosive substances to the weld surface. The inhibitor molecules either attach to the metal or react with the surface to form a thin, adherent adsorbed layer [196].

The self-corrosion of PM, HAZ and WM when inhibited decreases significantly. The inhibitor covering the weld surfaces was effective to minimise the corrosion rate significantly from about 1 mm/y to 0.1 mm/y. The decrease in self-corrosion corresponds with changes in potential becoming more positive to -640 mV from -725 mV uninhibited. Interestingly, unlike the current target many other weldments reported (Figure 6.10) in the inhibited condition, appear to have protected weld metal and the inhibitor protects the weldment irrespective of composition and PWC in a stagnant inhibited environment is less likely. Without flow there is less disruption to the adsorbed inhibitor film formation during the exposure time.

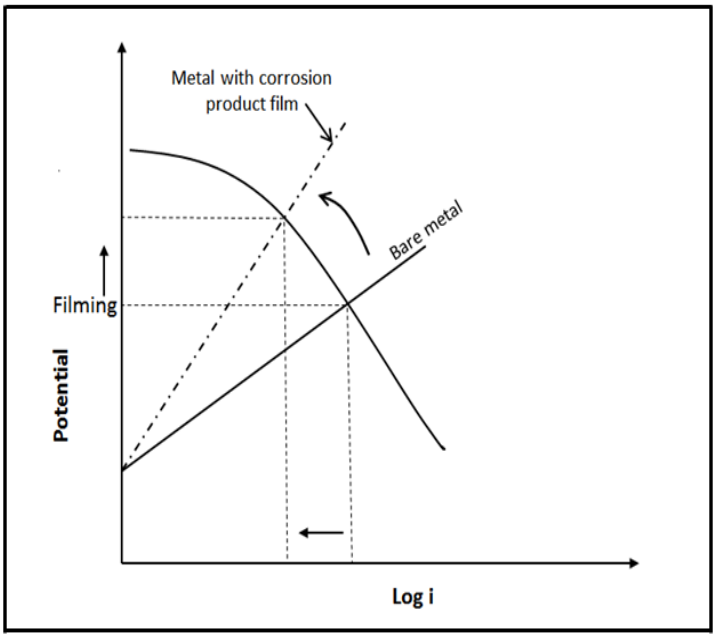

Figure 9-13 Evans diagram of anodic curve with inhibitor film formation [74]

Addition of corrosion inhibitor shows the reduction in corrosion rate of the weld. Figure 9-13 is an Evans diagram showing that the anodic current plot moves to a negative direction because of the influence of an adsorbed film on the electrode

surface. This is supported by previous research which also found the formation of an inhibited films on steel surface [5, 7, 56, 66, 131].

Figure 9-14 is a compilation the self-corrosion rate in inhibited no-flow condition. In inhibited condition, for many cases, the self-corrosion of the WM and the HAZ is lower than the PM. However in this condition the weldment is not free from PWC attack.

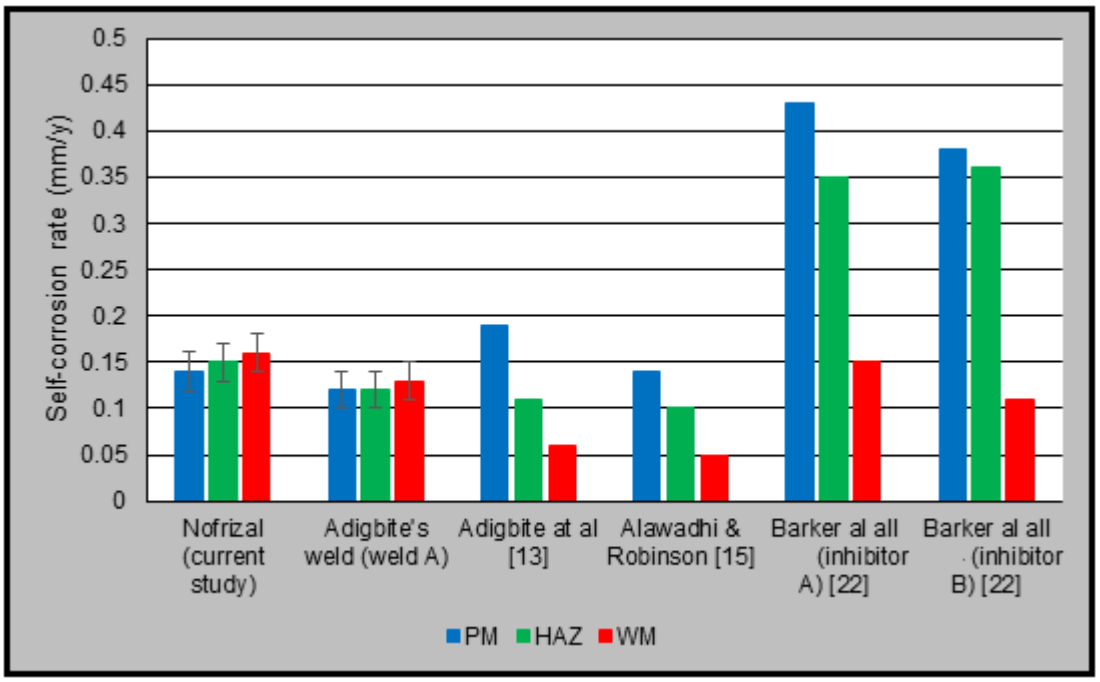

Figure 9-14 Comparison data of self-corrosion in inhibited no-flow conditio

9.2.3 Flowing condition

As with stagnant conditions, in a flowing brine, 30 ppm is the optimum inhibitor concentration for PM, WM and HAZ for efficiency in the range 82-84 % as shown in Table 6-5. The galvanic response at a jet velocity of 10 m/s in inhibited brine solution saturated with CO_2 is given in Figure 6-1.

The presence of inhibitor reduces the WM current, and it becomes less anodic. The WM current density is slightly higher (5.33 µA / cm^2) than the HAZ (1.22 µA / cm^2) and the PM (-6.56 µA / cm^2). Thus the inhibitor is effective in a flowing environment, and the corrosion rate is reduced by around 70% compared to an uninhibited flowing environment. With the higher shear stress, the inhibitor

adsorbed film might be incomplete or partially removed and it does not completely protect the weld in the flowing environment. Some part of the weld is still exposed with localised corrosion as reported in literature [178].

In this study, different jet velocities in an inhibited condition (2, 5, 8 and 10 m/s) were explored. With the weldment, a jet velocity of 2 m/s is the optimum velocity that can protect the weld with less total corrosion (the WM and the HAZ) compared to total corrosion of the PM (Figure 8-10). At all higher jet velocities PWC was experienced in an inhibited flowing environment.

The corrosion rate in inhibited conditions is compared to research reported in the literature and shown in Figure 6-11. In the present study, in an inhibited flowing condition, the corrosion rate of the WM is higher than PM and HAZ. This result is different from other studies where the HAZ has a higher corrosion rate. In the current weldment the nickel content of the weld metal is comparable to that in the parent metal (0.3-3.4%). All other weldments reported in the previous study have higher nickel contents (0.78%) compared to PM (0.2%). Thus is seems the composition of the weld metal might be important here for ensuring protection.

However, when the target that was used in previous studies by Adegbite (Target A) was evaluated using the flow loop and corrosion cell of this current research, different results were obtained and the WM shows a higher corrosion rate than the HAZ and PM. Aside from the equipment (flow loop), the preparation of the target may differ. Particularly with regard to grinding the target, the material removal can result in changes in microstructure, or/and a smeared amorphous surface layer. The previous weldment within the target, which initially had a target depth of 40 mm. This was polished many times until a target depth of only 23 mm remained, representing only 2 mm of metal remaining, very close to the electrical connections, and a total of 20 mm removed. This material removal by grinding may result in a different area or microstructure.

9.3 Surface Analysis

The weld surface appearance after exposure to brine for 20 hours is shown in Figure 9.15 in stagnant or flowing, inhibited or uninhibited conditions. The inhibitor minimises the metal loss significantly and the surface remains smooth and free from cracks or cavitation or metal attack. At high flow rates and uninhibited conditions the surface is vulnerable to corrosion attack. This supported the expected protection from the inhibitor.

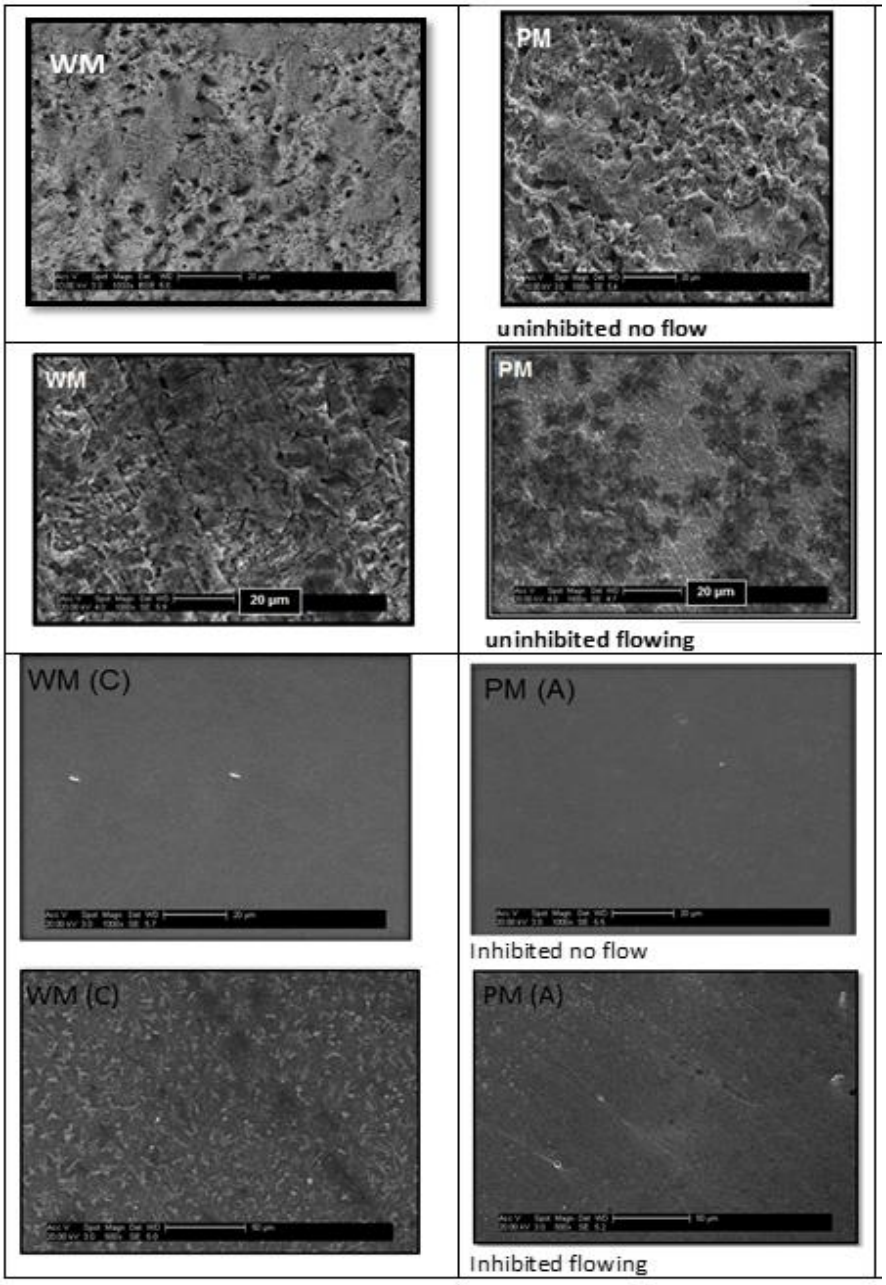

Figure 9-15 The SEM images for weld metal (WM) after immersion with brine saturated with CO_2 stagnant and flowing, inhibited and uninhibited

The XRD analysis for flowing uninhibited and saturated with CO_2 after 20 hours shows cementite peaks, Dissolution of ferrite leaving cementite (Fe_3C) remains from the corroded matrix of the metal.

As expected the intensity of cementite peaks on surfaces in a flowing uninhibited environment is greater, particularly on the weld metal, than those determined in a stagnant environment. No evidence of a $FeCO_3$ film was found in this study.

From the examples above CORRTREAT oilfield inhibitor 1059 protects the weld from corrosion attack in a still, non-flowing environment of brine saturated with CO_2.

9.4 Effect of Flow and Target Hydrodynamics

Studying the performance of the SJI target in flowing conditions is challenging due to the severe corrosion attack found compared to stagnant or still conditions. With turbulent flow, the physical interaction between the metal surface and the brine solution involves increased wall shear stress and high velocity across the target [25,27].

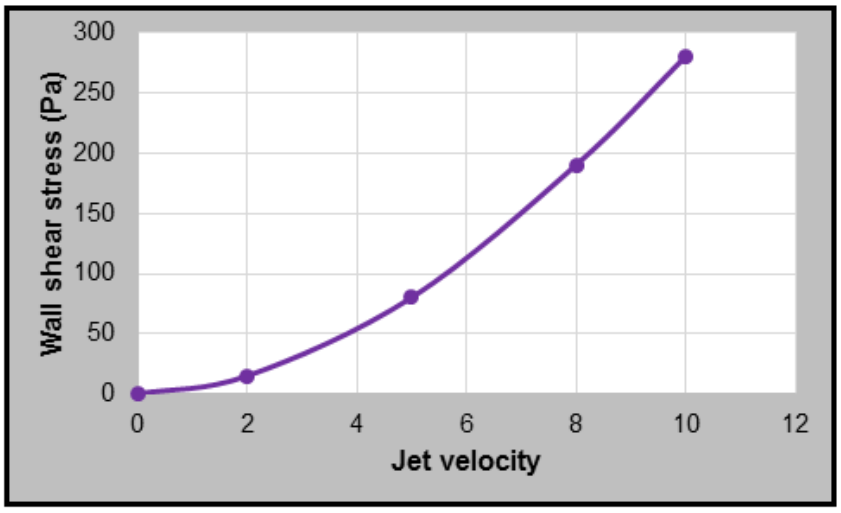

Figure 9-16 Wall shear stresses estimated from the jet velocities with the SJI

In this study, the wall shear stress, which is the isothermal loss due to fluid friction, has been determined in two different ways. Initial assumptions were that flow rate from the jet nozzle is similar to the flow rate across the target. The value of shear stress is shown in Figure 9-16 using Equation 2-23, which relates wall shear

stress with the wall jet area. A positive correlation between the velocity and the shear stress is observed. The shear stresses obtained at jet velocities of 0, 2, 5, 8 and 10 m/s are 0, 15, 81, 191 and 286 Pa, respectively.

The estimated shear stress values assume no losses across the target or to other sources and are high compared to results obtained in previous research using the SJI and RCE methods [15,16]. Further there is no differentiation of average shear stresses values to particular areas such as the centre, inner and outer regions of the SJI target.

A second method used to estimate shear stresses across the target is through CFD analysis. As shown in Figure 9-17 (also shown in Figure 8-16), a simulation using CFD analysis undertaken in this research provides detailed information of fluid velocities across the target, so that the wall shear stress at every point or region on the target is known precisely.

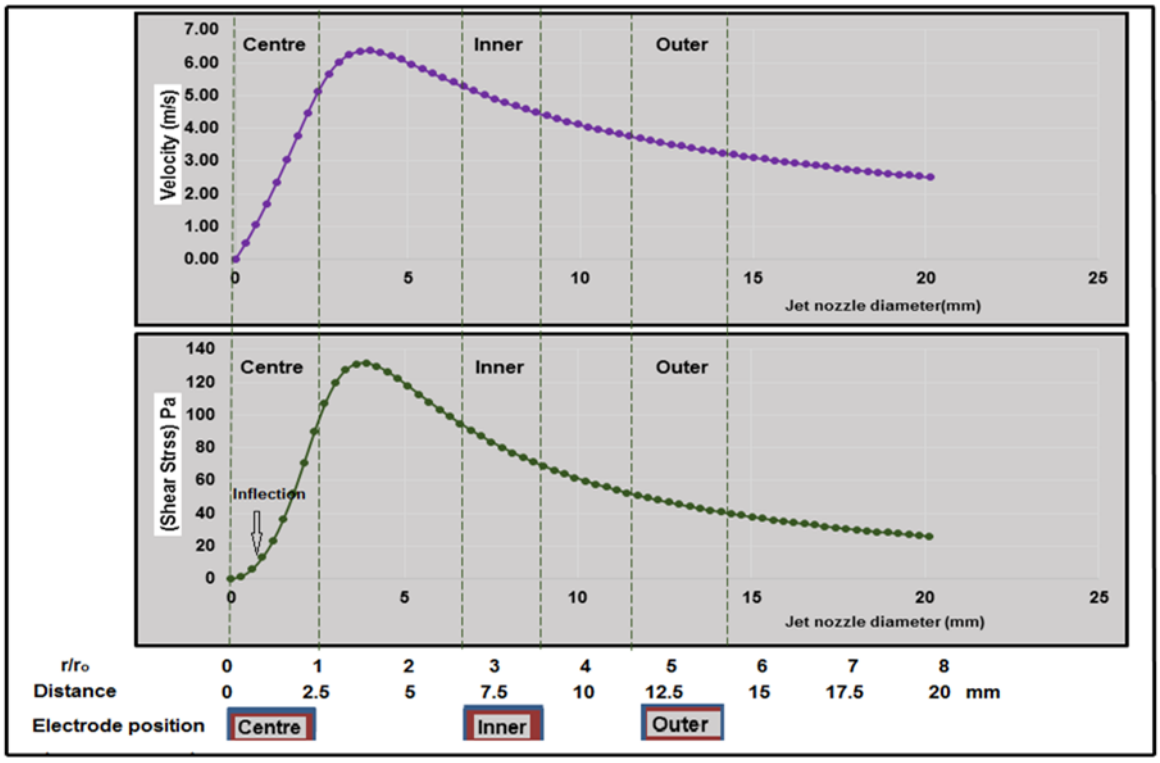

Figure 9-17 Estimated shear stress and velocity across the target with radial position from target centre r=0 to outer edge with a jet velocity of 10 m/s

Figure 9-18 shows the relationship between wall shear stress with jet velocity and velocity across the target for electrodes in the centre, inner and outer regions at jet velocities of 0, 2, 5 and 10 m/s. The wall shear stresses (red line) in the inner electrode area are greatest in the outer and the centre regions. In this inner region when the jet velocity is 10 m/s, the wall shear for the centre area, outer and inner are 66, 94 and 168 Pa respectively. CFD simulation indicates that there are quite different shear stress and fluid velocities across the target along the radial direction with normal impact of the fluid.

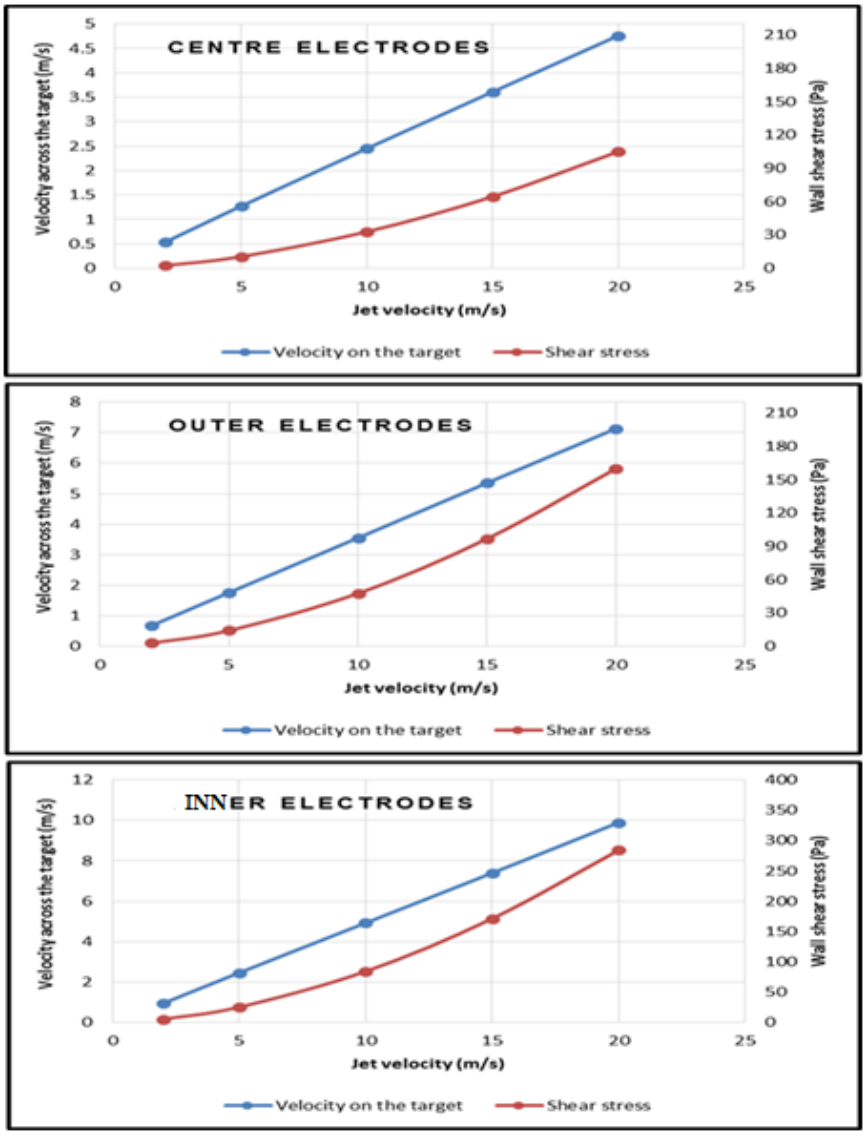

Figure 9-18 The velocity and wall shear stress values across the target from CFD data analysis from starting jet velocities of 0-10 m/s (x-axis)

9.4.1 Position of electrodes on the target

One of the advantages of using CFD analysis is that the characteristics of the flow across the target and wall shear stress at each point along the radial distance can be plotted. In the example given in Figure 9-17, the calculated change in velocity and shear stress as a function of radial distance from the target centre is plotted for a jet velocity of 10 m/s.

Chapter 8 describes the features of the change in hydrodynamics across the target and from the CFD analysis a range of turbulence is determined. From the CFD simulation a maximum is seen at around r/r_0= 1.6 or where r=4 mm (actually 3.9 mm). Efird [24] describes three regions across the target as in Figure 8-12; no flow, high turbulence and low turbulence and places each electrode in the centre of these three different zones. One observation is that with the current electrode positions on the target, the area of maximum turbulence is missed.

A second issue is that the zone nearest the target centre, referred to as the no flow zone, is actually region of rapidly changing turbulence across the electrode. The larger the central electrode and greater the radial distance from the centre the greater the turbulence, to a maximum at r/r_0= 1.6.

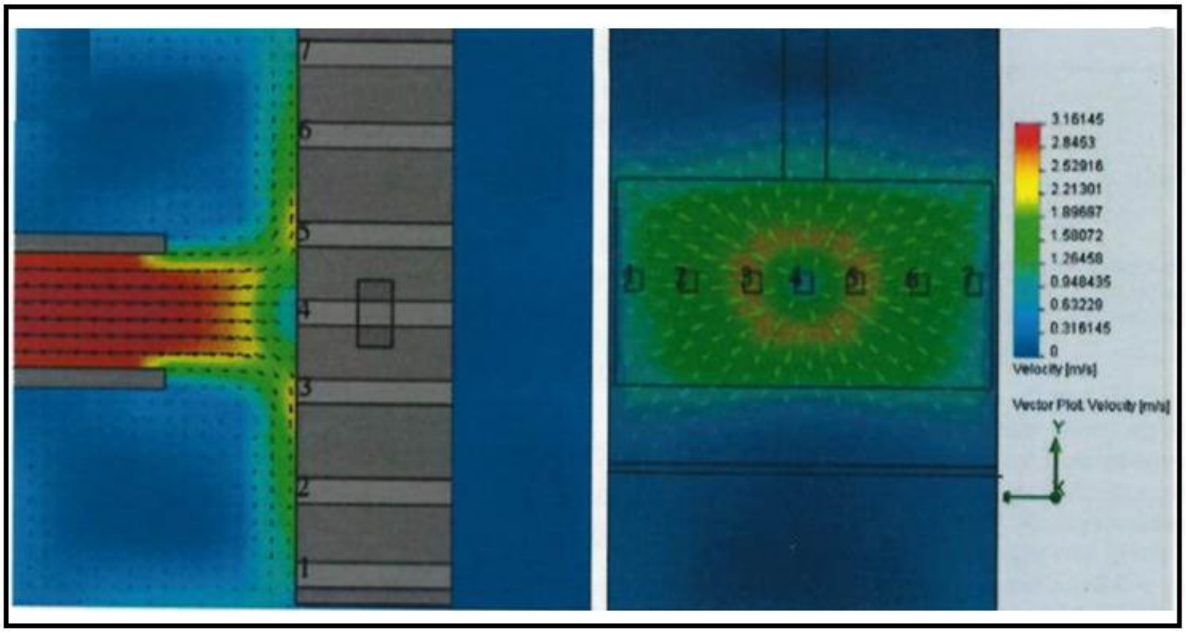

Figure 9-19 Velocity profiles at a jet velocity of 3 m/s obtained from CFD simulation of Zhang and Cheng [117]

Zhang & Cheng [117], carried out computational fluids dynamic (CFD) simulations for flow over seven electrodes mounted on to a plate. The position of the seven microelectrodes is marked with number 1-7. It is reported that the Figure 9-19 (as shown in Figure 2.31) is reproduced here illustrating that, at an increasing radial distance from the centre, areas 1,2 and 7,6, Zhang and Cheng found the velocity of fluid flow and the shear stress decrease due to low turbulence in line with increasing the thickness of the jet wall. The intensity of shear stress is directly proportional to the rate of corrosion. A decrease in mass transfer rate and shear stress results in a decrease in the rate of corrosion of the steel surface. In the boundary layer area, the resulting flow velocity and shear stress decrease further, resulting in a decrease in the corrosion rate. Figure 9-19 shows that in region 5 and 3, where maximum flow velocity occurs, the shear stress is higher than in region 4 where the jet comes into contact with the plate. Interestingly, a small area of maximum velocity of 3 m/s is achieved on the target from an impinging jet velocity of 3 m/s.

The simulation results are supported by other findings from literature that show a variation of velocity and shear stress for each electrode placed in different areas of a jet impingement target [102,104,118].

In this research, as shown in Figure 9-17, the electrode exposed to the highest turbulence is the inner region with radial distance between 6.5-8.5 mm from the target centre. Here the flow characteristics feature high turbulence, significant fluid velocities across the target and high wall shear stresses. The higher the flow across the target, the greater the mass transfer rate which enhances reactive species transport towards the electrode surface, accelerating the cathodic reaction [197]. Analysis using electrochemical methods to determine the corrosion rates, with radial distance from the target centre, support the observation that the corrosion rate in the inner region is higher than in the other areas.

With the further increase in radial distance, the turbulence decreases and the fluid velocity across the target decays (as in Figure 8-16). Generally the reduction in velocity and the resulting decreasing shear stress is seen in lower corrosion

rates of the steel. The changes in mass transfer rate and in shear stress, across the target from the centre, results in a corresponding correlation with corrosion rates of the X65.

In the current study, an electrode was placed in the centre region with a radial position range from 0-2.5 mm. In the CFD simulation of this current study (Figure 9-17) as the radial distance increases away from a target centre the centre region is an area of rapidly increasing turbulence with rising shear stress and rising velocity across the target. Simulations and experimental validation show the no-flow region as predicted by Efird [24] would need to be much smaller than 0.5mm from the target centre. It is also possible for laminar flow, as Lu [198], to be experienced below 0.5 mm or less.

9.4.2 Alternative electrode layout for target

In this study, after validation using the CFD analysis, it is seen that the region with the highest turbulence does not coincide with an electrode on the SJI target. Indeed based on the CFD simulation, the precise position of the electrodes can be re-arranged to obtain both the maximum shear stress, a less turbulent region and a region of greatly reduced flow (close to the centre) simultaneously. Two alternative arrangements of electrodes within a SJI target are proposed. These differ with the size of the electrodes and depend on manufacturability.

The current electrodes are 2 mm deep set at centre to 2.5 mm, inner electrode 7.5 +/-1 mm and outer at 12.5+/-1 mm radial distance from the target centre when the jet nozzle has a 2.5 mm radius (Figure 9-17).

With centre electrodes of 1.5-2 mm, an arrangement as outlined in Figure 9.20 is proposed (layout 1). Placing one electrode at the site of maximum turbulence 4 +/-1mm and an outer electrode at 13+/-1mm about 50-70% of the maximum (depending on velocity or wall shear stress respectively). As the wall shear stress falls faster than the velocity with radial distance, there is a comprise to be made between velocity and shear stress reduction (Figure 9-20).

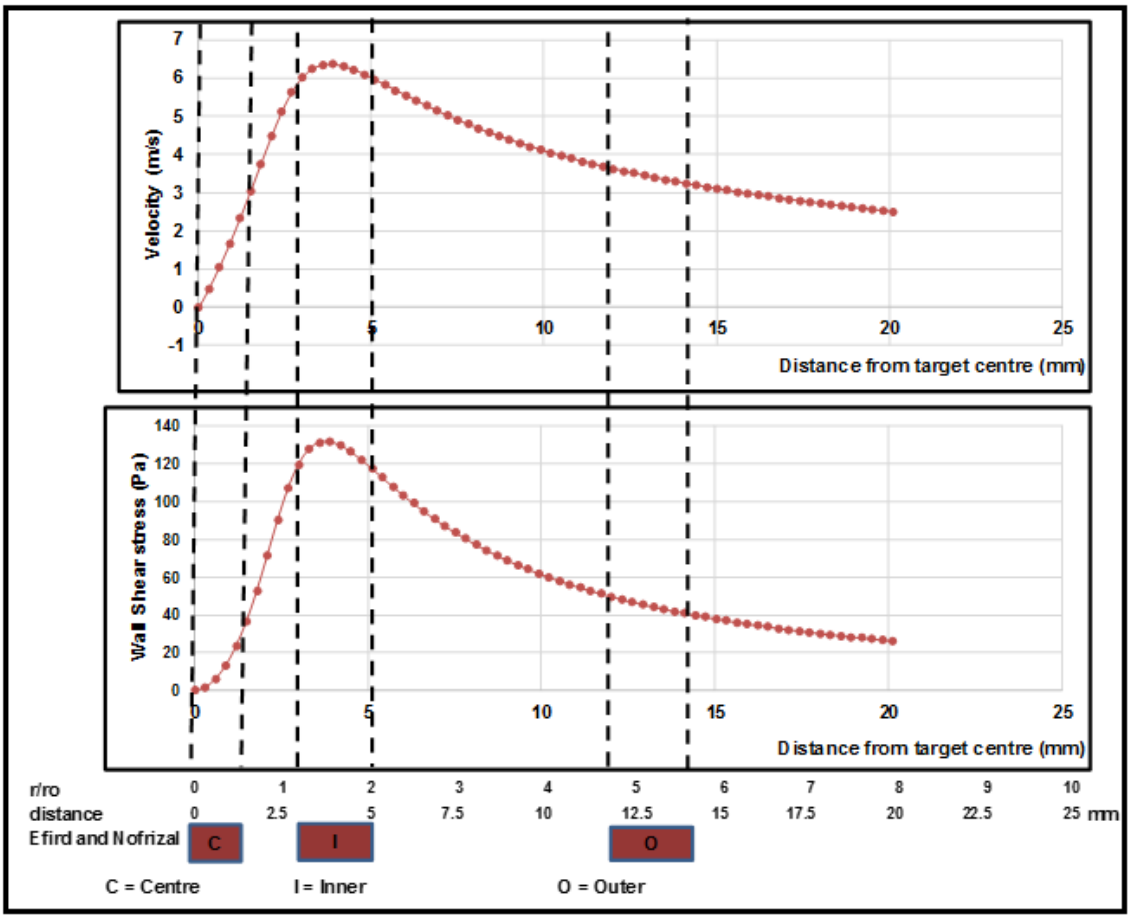

Figure 9-20 Proposed electrode position 1 based on CFD analysis result

With the new electrode arrangement, the average shear stress obtained from the electrode in the centre, outer and inner electrode at 10 m/s of jet velocity is approximately 13, 45 and 126 Pa, respectively. At the inner electrode, the wall shear stress which is currently said to be exposed to high turbulence has highest value in this position, however, this value obtained is still lower compared to the shear stress value from calculation using the equation 2-23 of 280 Pa as shown in Figure 9-16. Using calculation 2-23, the jet velocity is assuming equal to velocity across the target, so that, the shear stress value found higher than the CFD simulation.

Central electrodes, at low flow are desirable, but difficult with electrode diameters less than 2 mm, and is challenging to manufacture as a three electrode set (PM, WM and HAZ). However it is discussed in Section 9.4.3.

There is another option to place the electrode set at a long distance from the centre on a large diameter target to minimise fluid velocity and shear stress. Figure 9.21 shows this to be a radius of 30-40 mm from the centre. A large target would have the advantage of a number of electrode regions of a manageable width being placed. For example, an SJI target with two electrode regions; at maximum and low turbulence (Figure 9-21).

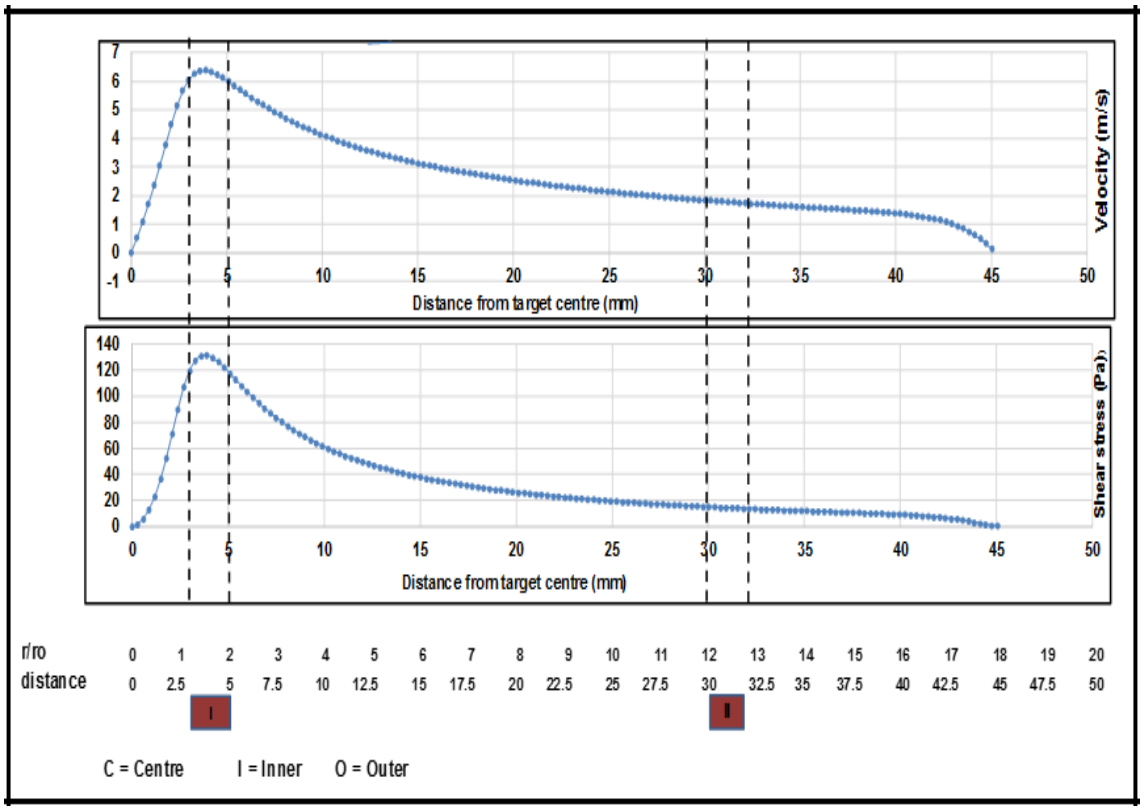

Figure 9-21 Proposed electrode position 2 based on CFD analysis result

With the new electrode arrangement, the average shear stress obtained from the electrode in the highest and lower turbulence electrode at 10 m/s of jet velocity is approximately 126 and 14 Pa, respectively.

The next proposed arrangement (Figure 9-22) places an electrode in a region close to the jet wall (position III). Another possibility is to put the electrode in the highest turbulence (I) and next in less turbulence area (II). The proposed position for location III is between 43-45 mm, and it is expected that the electrode at this position (position III) has very low turbulence velocity and can represent the electrode in the centre region.

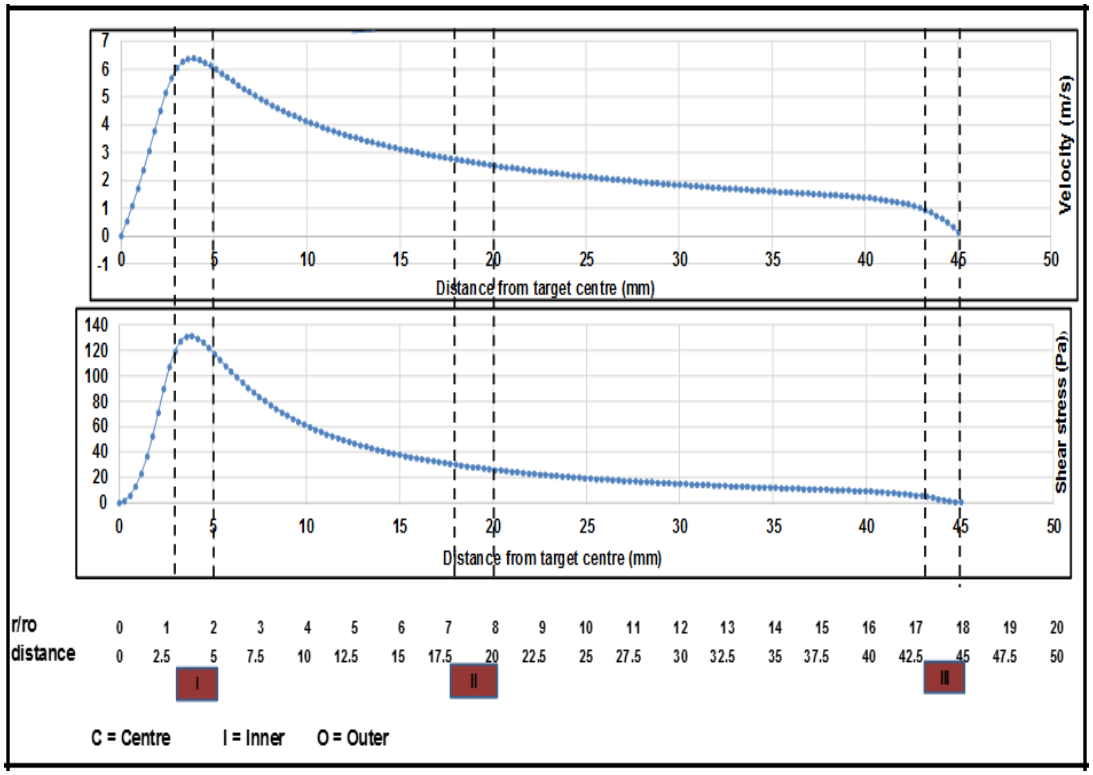

Figure 9-22 Proposed electrode position 3

With the this electrode arrangement, the average shear stress obtained from the electrode in the position 1, 2 and 3 at 10 m/s of jet velocity is approximately 126, 28 and 2.4 Pa, respectively.

The summary of all alternatives and the optimum value of velocity and shear stress is in Table 9-4.

Table 9-3 The velocity and shear stress of the electrode at different position

	Centre electrode position from zero 0-2.5 mm		Inner electrode position from zero 3-5 mm		Outer electrode position from zero 6-8 mm	
Current position	Velocity (m/s)	S. Stress (Pa)	Velocity (m/s)	S. Stress (m/s)	Velocity (m/s)	S. Stress (Pa)
	2.5±1.8	32.7±32	4.9±0.2	84±7.4	3.6±0.1	47.6±3.3
Proposed position 1	Centre electrode position from zero 0-1.5 mm		Inner position from zero 3-5 mm		Outer electrode position from zero 7.5-9.5 mm	
	Velocity (m/s)	S. Stress (Pa)	Velocity (m/s)	S. Stress (m/s)	Velocity (m/s)	S. Stress (Pa)
	1.4±1.4	13.4±14.1	6.2±0.2	126±5.3	3.4±0.1	45±3.0
Proposed position 2	Centre electrode (blank or put PM in this position)		Highest position from zero 3-5 mm		Lower turbulence position from zero 30-32 mm	
	Velocity (m/s)	S. Stress (Pa)	Velocity (m/s)	S. Stress (m/s)	Velocity (m/s)	S. Stress (Pa)
	x	x	6.2±0.2	126±5.3	1.7±0.03	14.3±0.5
Proposed position 3	Highest turbulence position 3-5 mm		Lower turbulence position 18-20 mm		Position close to jet wall 43-45 mm	
	Velocity (m/s)	S. Stress (Pa)	Velocity (m/s)	S. Stress (m/s)	Velocity (m/s)	S. Stress (Pa)
	6.2±0.2	126±5.3	2.6±0.07	28.1±1.4	0.5±0.2	2.4±1.6

9.4.3 Centre electrode

In this research, a SJI target with 3 different regions (outer, inner and centre) has been used. The electrodes in the outer and inner region are in a ring form while in the centre electrodes are circular, close to each other (Figure 9-16).The position of the electrode in the centre position gives difficulty when measuring the corrosion rate. As shown in Figure 9-23, the centre electrode is not equivalent for the PM, WM and HAZ at this central point. Thus, results of the corrosion rate for the three electrons area are higher than expected and variable. Also, the electrodes in the centre position are more sensitive and this is illustrated with a large standard deviation associated with the central electrodes, thought to be due to:

- Rapidly increasing turbulence on the central electrode over a very short distance.
- The position of the PM, HAZ and WM are not equivalent in the central zone (different hydrodynamics at different positions).
- Electrode sizes are very tiny (small surface area), especially for WM and HAZ, there is a high probability of increased contribution from crevice corrosion and significant modifications from small changes in microstructure.

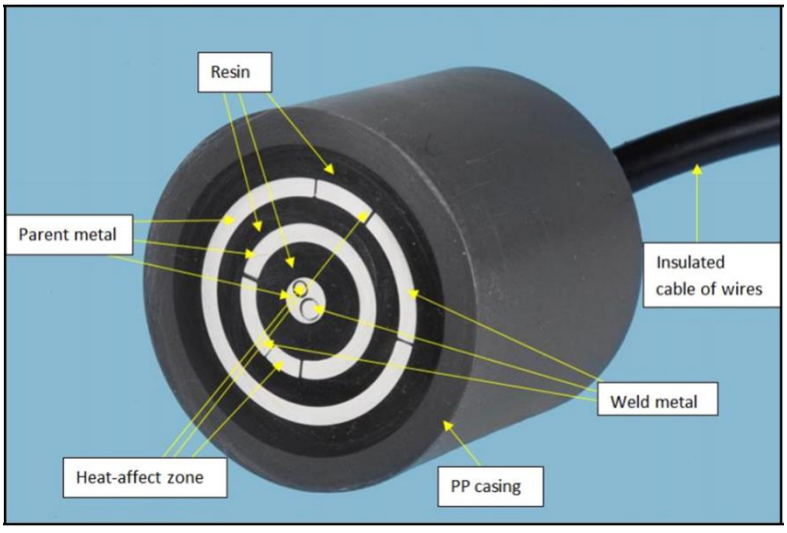

Figure 9-23 Position of the electrodes on the SJI target shows the small area of electrode in the centre

The following suggestions are to increase the accuracy of the electrode in the centre region:

1. The positions of the electrode placed at a radius of 0-2 mm, ideally 0-1 mm, can be put side by side as Figure 9-24. From this it is expected that all of the electrodes in the centre will have a similar hydrodynamic response in a flowing condition and with a reduced radius, the turbulence and subsequent corrosion rate reduces.

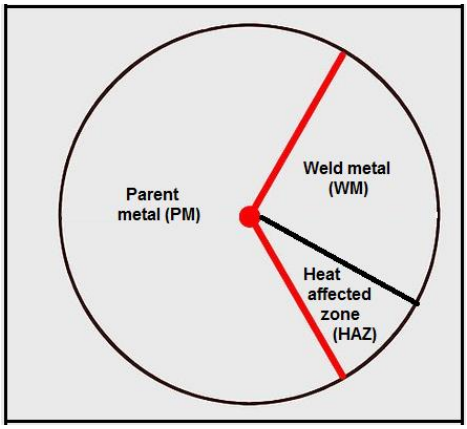

Figure 9-24 Alternative electrode position on the centre electrode

1. Place the electrode set at a greater radial distance, so that the velocity across the target is similar across a 2 mm ring. This study recommends anything greater than 30 mm. This method has disadvantages because the target diameter will be large and a large corrosion cell is also required.
2. Another alternative is to replace all electrodes in the centre position with the parent metal material (PM) as a bench mark, the study can focus on the electrodes in other positions where the velocities and shear stresses are clearly defined.

9.4.4 Jet velocities for high shear stresses

One significant advantage of SJI is the ability to use very high fluid velocities and shear stresses across a surface. At the start of this research, the aim was to use SJI to examine a range of jet velocities for a variety of application needs and a range from 0-10 m/s equivalent to approximately 0-300 Pa wall shear stress was chosen. Following the CFD simulation carried out for this research, the weldment

positions experiencing the greatest turbulence are the inner set of electrodes on the target. Thus at the maximum jet velocity of 10 m/s the inner electrode experiences half of this value (4.9±0.24) and a shear stress of 84±7 Pa. If a higher velocity is required the options are:

- To increase the jet velocity.
  Further simulations at 15 and 20m/s were conducted (9-25).

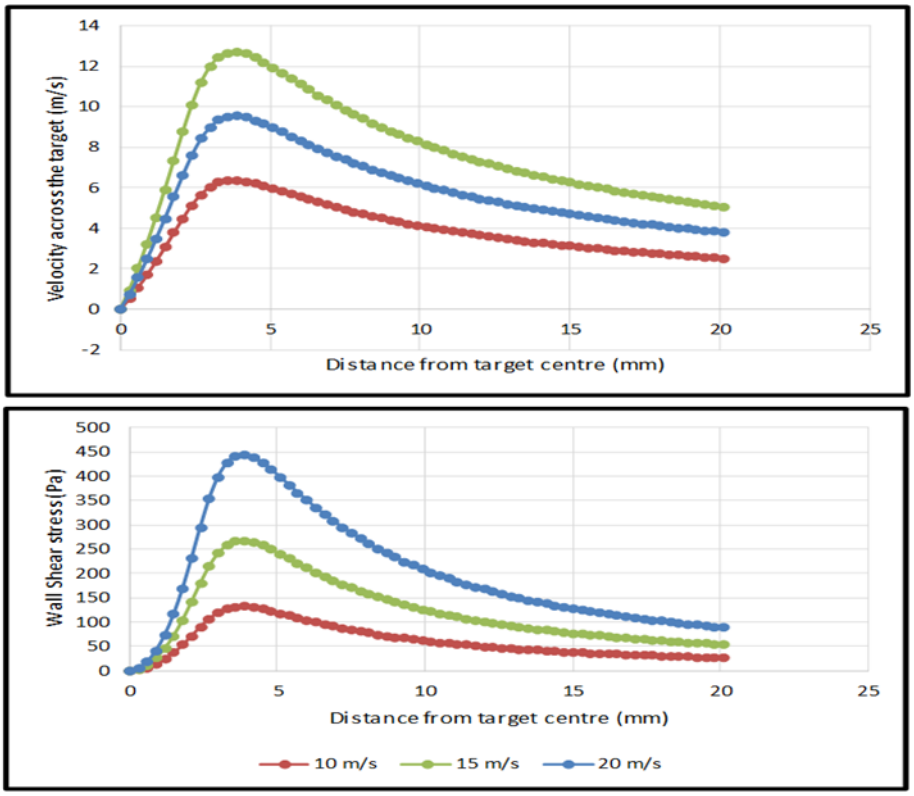

Figure 9-25 The velocity across the target and shear stresses for jet velociies of 10, 15 and 20 m/s

Thus with the target used in this research, using electrode positions recommended by Efird [24] and Adegbite [14], to achieve 10 m/s on the inner electrode set, a jet velocity of 20 m/s is required. Further examination shows that the inner electrode set on the target is 50% of the jet velocity value, the outer electrode set is about 33.3% and the centre electrodes, about 25% but a wide spread. Thus as a guide, a jet velocity, twice the value of the required velocity on the inner electrode set of the target is required.

- Re-position the inner electrode set.
  From CFD simulation maximum turbulence is achieved approximately 4mm or at r/r_o= 1.6 from the target centre. Therefore to achieve 10 m/s at the maximum position on the target, a jet velocity of just over 15 m/s is required (Figure 9.20-9-22).

A similar approach to can be taken to achieve high wall shear stresses. To achieve high wall shear stresses:

- Increase the jet velocity
  To achieve 300 Pa on the inner electrode of the current target, a jet velocity of 20 m/s is required. About 200 Pa is achieved on the inner electrode at a jet velocity of 15 m/s whereas 100 Pa is achieved at 10 m/s.
  Further examination shows that the inner electrode set on the target is 30% of the calculated wall shear stress (Equation 2-23).

- To re-position the inner electrode set.
  From CFD simulation, maximum turbulence is achieved approximately 4 mm or at r/r_o = 1.6 from the target centre.

9.5 Validation of CFD analysis

Some validation is based on

1. reproducing similar corrosion rate values to those given in the literature
2. reproducing similar corrosion rate trends across the target (qualitative information) the velocity and shear stress contours of the previous studies.
3. A further check was conducted to validate quantitatively comparing data from Zhang and Cheng [117]. The parameters used in the reference were modelled using the Nofrizal CFD model to check any correlation. Parameters were kept constant (turbulence/fluid properties/temperature) and two parameters were changed in order to replicate the model in the literature (Figure 9-26):

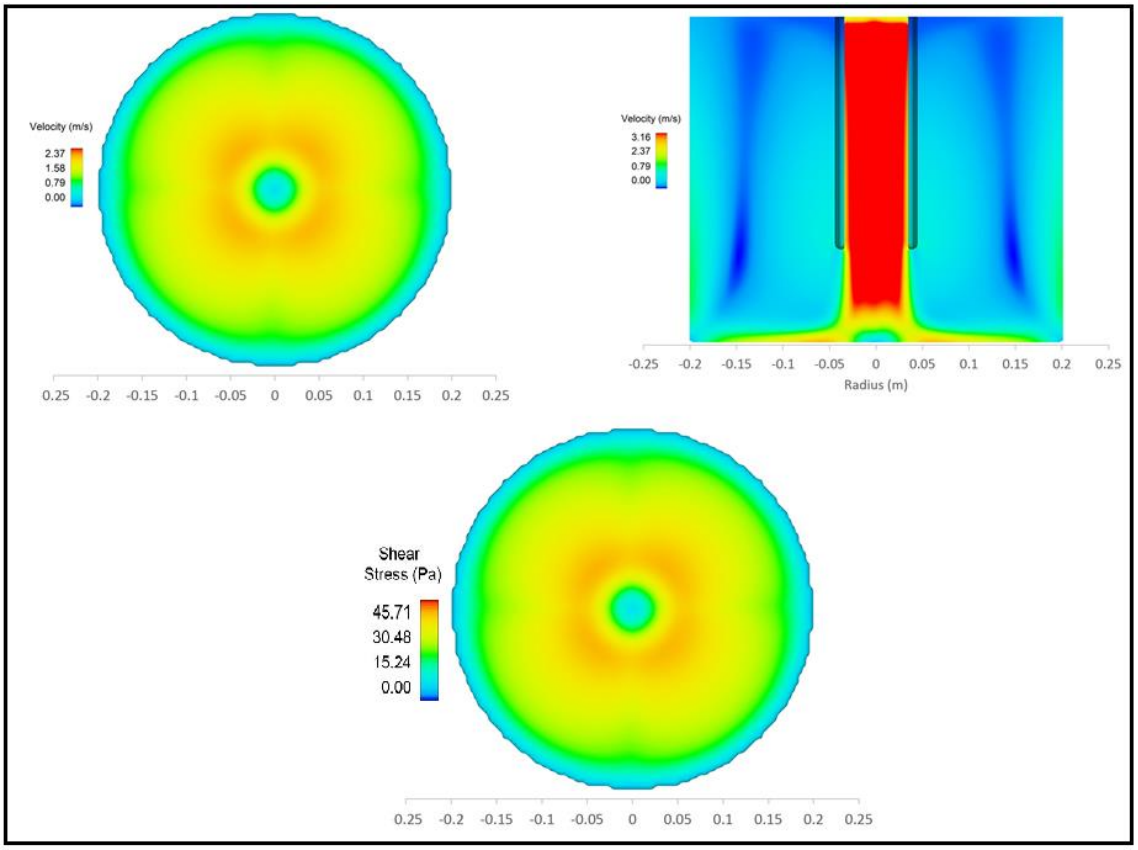

Figure 9-26 The CFD images used parameter from previous study [117] to validate the current CFD model

Figure 9-26 shows the variation of jet velocity and shear stress across the target at jet velocity of 3 m/s. The result from this simulation has a similar trend to the current study shown in Figure 8-14.

9.6 Application of Research Findings

Oil and gas environments vary by location within upstream and downstream oil and gas operations. The aqueous environment with dissolved gases (CO_2 and H_2S) is quite hostile for any metals (particularly steels) and corrosion is a significant concern.

Prevention and control of corrosion with particular attention to galvanic corrosion is an extremely important in a whole range of environments but particularly in a marine and in oil and gas production facilities which must be actively managed and regular, effective monitoring of assets carried out.

The following actions to mitigate the negative effect of galvanic corrosion in various industries are recommended:

1. In the oil and gas industry, the commissioning (no-flow) is one of the important steps before production process; however, it was demonstrated that the susceptibility to galvanic corrosion still possible. So that, the application of an inhibitor during the commissioning process is needed.
2. In a flowing environment, the addition of inhibitor is essential, and, as far as possible, inhibitor must be present if the jet velocity is above a critical velocity of 2 m/s to protect the WM and the HAZ from PWC. At higher velocities the inhibitor becomes less efficient, thus care should be taken as the velocity increases in inhibited conditions for continued protection.
3. Any dissolved oxygen is very damaging and can be a severe problem in offshore applications. Thus preventing aeration of sea-water and other production liquids will minimise the risk of galvanic attack in oil and gas facilities.
4. Adequate chemicals (inhibitor and other agents) must be maintained at optimum concentration to minimise the environmental impact particularly for the sea ecosystem.
5. The rate and severity of galvanic corrosion is affected by the ratio of the cathode area to the anode area. The larger the area of the cathode in relation to the anode (i.e., the higher the cathode to anode ratio), the greater the rate of reduction at the anode, thus the more severe the resulting galvanic corrosion. By contrast, the smaller the cathode to anode area, the less detrimental the ensuing deterioration. During the preliminary design stages, it is worthwhile to ensure that the area of the more anodic metal is made as large as possible in relation to the cathode.
6. An effective, continuous monitoring system of galvanic corrosion in oil and gas facilities should be implemented.

9.7 Chapter Summary

Addition of inhibitor on the corrosion system at no-flow and flowing inhibitor is crucial to reduced the corrosion of the weldment. In the no-flow environment,

similar to storage and shut-in environment, the vulnerability of welding X65 steel to the PWC still observed with minimum impact. However, the negative effect of weld corrosion is significant increases at a higher velocity, regardless of the presence of chemical inhibitors.

It is important to highlight that the submerged jet impingement target used in this study demonstrated an excellent ability to evaluate the PWC in the flowing environment.

10 CONCLUSIONS AND RECOMMENDATIONS

This chapter summarises the contributions to knowledge gathered from the research undertaken, particularly regarding the application of the submerged jet impingement (SJI) method, effectiveness of a SJI target constructed from three materials (coupled and uncoupled) and the hydrodynamic behaviour when applied to weldments in X65 pipelines immersed in brine saturated with CO_2.

The research discusses a number of effects and mechanisms of corrosion processes influencing PWC, based on galvanic and self-corrosion measurements and surface analysis.

From the work undertaken, it is concluded that:

- The use of an SJI impingement target supported by CFD is a highly informative tool to support predictions and validate corrosion rates of an X65 pipeline steel weldment.
- Corrosion rates of coupled and uncoupled electrodes comprising three materials PM, WM and HAZ (in three locations: centre, inner and outer rings on a constructed target are equivalent when immersed in non-flowing artificial sea water saturated with CO_2.
- In this condition, without inhibitor and with no flow, the immersed uncoupled X65 weldment corrodes at room temperature around 1 mm/y.
- In a no-flow condition, the galvanic characteristics on all weldments are similar and the WM is cathodic to HAZ and PM. This minimises the total corrosion rate of WM as it is partially protected by the sacrificial corrosion of PM and HAZ.
- The self-corrosion in a flowing uninhibited condition has a positive correlation with velocity. Compared to stagnant conditions, when the brine is directed at at 10 m/s corrosion rate doubles to 2 mm/y.
- In uninhibited artificial sea-water saturated with CO_2 and flowing conditions, with jet velocities of 2, 5, 8 and 10 m/s, the weld metal becomes anodic and preferentially corrodes in comparison with the parent metal. Thus a PWC problem is experienced in flowing environments.

- Weld metal with nickel to 0.8 wt% does not always protect the weld from corrosion attack in flowing, uninhibited conditions. Indeed all show preferential weld corrosion. The HAZ is always more vulnerable than the PM
- Dissolution of ferrite leaves porous cementite (Fe_3C) at the surface particularly in a flowing uninhibited environment. No evidence of a $FeCO_3$ film was found in this study.
- With an inhibitor the total corrosion rate, calculated from the sum of galvanic and self-corrosion rate, of each part of the weldment in the inhibited brine with 0, 5 and 10 m/s environment is significantly reduced (an order of magnitude) compared to the uninhibited condition. The highest total corrosion rate values for no-flow, 5 and 10 m/s, are in the range 0.14, 0.23 and 0.27 mm/y respectively. In comparison uninhibited values are 1.2, 2.7 and 3.9 mm/y respectively.
- Dissolved oxygen, with or without inhibitor poses a severe threat to the integrity of oil and gas infrastructure. The effect of 20 cm^3 added air (or 4 cm^3 added oxygen) doubles the corrosion rate compared to deaerated conditions. When there is no deaeration the corrosion rate is 4 times greater than the deaerated corrosion rate.
- The application of a CORRTREAT oil and gas inhibitor was effective in reducing the corrosion rate of an X65 weldment and to prevent the weldment from PWC, particularly in no-flow conditions.
- The maximum inhibitor efficiency is obtained with a CORRTREAT 10-569 inhibitor concentration 30 ppm for the weldment.
- The EIS and LPR measurement showed a good agreement to evaluate to corrosion of weld and analysis the inhibitor performances.
- A modelling approach to accurately obtain the relationship of mass transfer and shear stress on the SJI target was developed. CFD model was used to describe the hydrodynamics across the target (velocity and wall shear stress with radial distance can be plotted.
- The target centre, is a region of rapidly increasing turbulence across the electrode to a maximum approximately 4±1 mm (for a 2.5 mm radius nozzle) or r/ro = 1.6 from the target centre.

- With a jet velocity of 10 m/s the inner electrode experiences half of this value (4.9±0.24) and a shear stress of 84±7 Pa. If 10 m/s on the target is required at the inner electrode a jet velocity of 20 m/s is required.
- The inner electrode set on the target experiences 50 % of the set jet velocity, the outer electrode experiences 33.3 % and the centre electrodes, about 25 %. Thus as a guide, a jet velocity, twice the value of the required velocity on the inner electrode set of the target is required.
- The inner electrode set on the target experiences 30 % of the expected wall shear stress calculated from the jet velocity
- Alternative electrode positions are suggested to represent a wide range of shear stress and fluid velocities across the target with good precision and accuracy. With a repositioned electrode at maximum turbulence, 10 m/s is predicted on the target from a jet velocity of just over 15 m/s is required.

10.1 Recommendations and Further Work

The use of submerged jet impingement has been shown to be working well and is ideal to evaluate PWC in flowing conditions. Therefore, the opportunity to create some new ideas to complete this study are considered, especially for studies on low alloy carbon steel in offshore oil and gas production and engineering systems in general. Further focused research areas, requiring systematic studies, for better predicative capabilities include:

- Developing a high temperature capability to better explore a range of opportunities using SJI to simulate and predict behaviour. An example would be development of iron carbonate films and the application of submerged jet impingement to evaluate PWC in flowing conditions at elevated temperatures.
- Use of SJI to conduct research in erosion-corrosion which has to use different concentrations and sizes of suspended sand to simulate specific down-hole conditions that are very demanding for effective corrosion inhibition.
- Studies on the effective inhibitor concentration in different environments such as H_2S, and acetic acid environments.
- Research with dissimilar welded joint configurations produced typical of application in oilfield environments.

- Research in different characteristic service environments, during commissioning, operating and well shut down.
- The length of corrosion experiment (exposure time) is suggested to be longer than 24 hours to observe the transition of the HAZ from cathodic to anodic as shown in Figure 5-2.

Also, the importance of service conditions beyond the scope of this research is a potential areas for further study towards predicting and controlling the accelerated flow of PWC.

REFERENCES

1. Kane HE. Galvanic Corrosion Prevention Guide for Water Cooling Systems. Industries Advanced Energy; 2017.1–7.

2. Banfield TA. The Painting of Ships. Anti-Corrosion Methods and Materials. 1955; 2(10): 302–316.

3. Bhaskaran R., Palaniswamy N., Rengaswamy NS. A review of differing approaches used to estimate the cost of corrosion (and their relevance in the development of modern corrosion prevention and control strategies). Anti-Corrosion Methods and Materials. 2005; 52(1): 29–41. Available at: DOI:DOI 10.1108/00035590510574899.

4. Fontana M. Corrosion Engineering. 3rd edn. Michael BB, Stephen MC, Shank ME, Charles AW, Garth LW (eds.) New York: McGraw-Hill; 1986.

5. Ahmad Z. Principles of corrosion engineering and corrosion control. 1st edn. Oxford: Butterworth-Heinemann. 2006.

6. Uhlig HH., Revie RW. Corrosion and Corrosion Control. John Wiley & Sons, Inc.1985.

7. Winning IG., Bretherton N. Evaluation of weld corrosion behavior and the application of corrosion inhibitors and combined scale/corrosion inhibitors. Corrosion. 2004; (04538): 1–18.

8. Lahiri AK. Applied Metallurgy and Corrosion Control. In: Indian Institute of Metals (ed.) Applied Metallurgy and Corrosion Control. 2017.17–38. Available at: DOI:10.1007/978-981-10-4684-1.

9. Davis J. Corrosion of Weldments. 1st edn. Davis JR, Associates D& (eds.) Ohio. 2006.

10. Abduh M. The 50 major engineering failures in oil and gas and hydrocarbon industry (1977-2007). Integrity Engineering. Reksalindo; 2008. Available at: https://www.scribd.com/document/215642171/The-50-Major-Engineering-Failures.

11. Perez TE. Corrosion in the Oil and Gas Industry : An Increasing Challenge for Materials. Metals & Materials Society. 2013; 65(8): 1033–1042. Available at: DOI:10.1007/s11837-013-0675-3.

12. Joshua S., Yereth R. Oil leak has minimal impact on BP's Alaska output. Reuters. 2009. Available at: https://uk.reuters.com/article/us-bp-alaska-spill/oil-leak-has-minimal-impact-on-bps-alaska-output-idUKTRE5AT3FE20091201.

13. Adegbite MA., Robinson MJ., Impey SA. Flow Accelerated Preferential Weld Corrosion of X65 Steel in Brine Containing Carbon Dioxide and Oxygen. Cranfield University. 2014.

14. Adegbite MA., Robinson MJ., Impey SA. Electrochemical Evaluation of Flow Accelerated Preferential Weld Corrosion of X65 Pipeline Steel Using Jet Impingement. A Journal of the Institute of Corrosion. 2013; 10–13.

15. Alawadhi K., Robinson M. Preferential weld corrosion of X65 pipeline steel in flowing brines containing carbon dioxide. Corrosion Engineering, Science and Technology. 2011; 46: 318–329.

16. Adegbite MA., Robinson MJ., Impey SA. Evaluation of Flow Enhanced Preferential Weld Corrosion of X65 Pipeline Steel Using a Novel Submerged Impingement Jet. Society of Petroleum Engineers. 2016.1–12.

17. Gabe DR., Walsh FC. The rotating cylinder electrode : a review of development. J. Appl. Electrochem. 1983; 13: 3–22.

18. Nesic, S., Wang, S., Cai, J. and Xiao Y. Integrated CO_2 corrosion-multiphase flow model. In SPE International Symposium on Oilfield Corrosion. Society of Petroleum Engineers. 2004.

19. Vera JR., Parsi M., Kara M., Sharma P., Katy F. Appropriate rotating cage speed for testing inhibitors under field simulated flow conditions. NACE - International Corrosion Conference Series. 2017.1–15.

20. Filho JCC., Orazem ME. Application of a Submerged Impinging Jet to Investigate the Influence of Temperature, Dissolved CO_2, and Fluid Velocity on Corrosion of Pipeline-Grade Steel in Brine. Corrosion. 2001; (01058).

21. Barker R., Hu X., Neville A. The influence of high shear and sand impingement on preferential weld corrosion of carbon steel pipework in CO_2 -saturated environments. Tribiology International. Elsevier; 2013; 68: 17–25.

22. Barker R., Hu X., Neville A., Cushnaghan S. Inhibition of Flow-Induced Corrosion and Erosion-Corrosion for Carbon Steel Pipe Work from an Offshore Oil and Gas Facility. Corrosion. 2013; 69(2): 193–203.

23. Efird KD., Wright EJ., Boros JA., Hailey TG. Correlation of steel corrosion in pipe flow with jet impingement and rotating cylinder tests. NACE Journal Paper. 1993; 49(12): 992–1003. Available at: DOI:10.5006/1.3316026.

24. Efird KD. Jet Impingement Testing for Flow Accelerated Corrosion. NACE Corrosion Conference. 2000; (52).

25. Schmitt G., Mueller M. Critical Wall Shear Stresses in CO_2 Corrosion of Carbon Steel. Corrosion. 1999; (44).

26. Enilari BT., Kara F. Slug Flow and it's Mitigation Techniques in the Oil and Gas Industry. SPE Nigeria Annual International Conference and Exhibition. 2015; Available at: DOI:10.2118/178378-MS.

27. Efird KD. Flow accelerated corrosion testing basics. NACE Corrosion Conference. Texas; 2006. pp. 1–16.

28. Craddock H., Daneilsen B., Mamann A., Caird S. Preferential Weld Protection Corrosion Inhibitor for Topsides Gas Producing Facility under High Shear and Sweet Condition. NACE International. 2004; 04425.

29. Mahajanam V., Joosten MW., Production C., Technology A. Guidelines for Filler-Material Selection To Minimize Preferential Weld Corrosion in Pipeline Steels. SPE International Conference on Oilfield Corrosion, Aberdeen, UK,. 2011. 5–12.

30. Winning IG., Bretherton N., McMahon A., McNaughtan D. Evaluation of weld corrosion behavior and the application of corrosion inhibitors and combined scale/corrosion inhibitors. Corrosion. 2004; (04538): 1–18.

31. Davis J. Alloying: Understanding the Basic. ASM International; 2001. 1-11 p. Available at: https://www.asminternational.org/documents/10192/3466171/06117_Chapter 3B.pdf/a764507a-3499-4d23-b348-5536d31c0ba2.

32. Bhadeshi H., Honeycombe R. Steel-Microstructure and Properties. Third. Cambridge: Butterworth-Heinemann; 2006.

33. Tomita Y. Development of fracture toughness of ultrahigh strength low alloy steels for aircraft and aerospace applications. Materials Science and Technology. 1991; 7(6): 481–489.

34. Tomita Y., Okawa T. Effect of modified heat treatment on mechanical properties of 300M steel. Materials Science and Technology. 1995; 11(3): 245–251.

35. Tang J., Shao Y., Guo J., Zhang T., Meng G., Wang F. The effect of H2S concentration on the corrosion behavior of carbon steel at 90 °C. Corrosion Science. 2010; Available at: DOI:10.1016/j.corsci.2010.02.004.

36. Kvarekval J., Olsen S., Skjerve S. The Effect of O_2 On CO_2 Corrosion In PH Stabilised Gas/Condensate Pipelines. Corrosion 2005. 2005; (05305): 1–21.

37. Wang S., George K., Nešić S. High pressure CO_2 corrosion electrochemistry and the effect of acid acetic. Nace International. 2004; (04375): Paper No. 375.

38. Kairi NI., Kassim J. The effect of temperature on the corrosion inhibition of mild steel in 1 M HCL solution by Curcuma longa extract. Int. J. Electrochem. Sci.,. 2013; 8: 7138–7155. Available at: DOI:10.1016/j.matchemphys.2008.01.028.

39. David SA., Babu SS., Vitek JM. Welding: Solidification and Microstructure. The Mineral, Metal & Material Society. 2003.

40. Khan I. Solidification and phase transformations in wedding transformations in welding. 2003.

41. Sloderbach Z., Pajak J. Determination of ranges of components of heat affected zone including changes of structure. Archives of Metallurgy and Materials. 2015; 60(4): 2607–2612. Available at: DOI:10.1515/amm-2015-0421.

42. API. Welding of Pipelines and Related Facilities. Industry Petroleum. American Petroleum Institute. 2013.

43. Z. Śloderbach JP. Determination of ranges of components of heat affected zone including changes of structure. Archives of Metallurgy and Materials. 2015; 60(4): 2607–2612.

44. Ropital, F, Chauvin Y. Corrosion and Degradation of Mettalic Materials: Understanding the Phenomena and. Applications in Petroleum and Process Industries. 1st ed. Paris: Editions Technip. 2010.

45. Callister WD. Materials Science and Engineering, An Introduction. 7th (ed.) 2007.

46. Rahim AA. Physico-Chemical Characterisation of Mangrove Tannins as Corrosion Inhibitors. University Sains Malaysia; 2005.

47. Nofrizal N., Rahim AA., Saad B., Raja PB., Syah AM., Yahya S. Elucidation of the Corrosion Inhibition of Mild Steel in 1.0 M HCl by Catechin Monomers from Commercial Green Tea Extracts. Metallurgical and Materials Transactions A. 2012; 43(4): 1382–1393.

48. Li T., Yang Y., Gao K., Lu M. Mechanism of protective film formation during CO2 corrosion of X65 pipeline steel. Journal of University of Science and Technology Beijing, Mineral, Metallurgy, Material. 2008; 15(6): 702–706.

49. Martin RL. Corrosion Consequences of Oxygen Entry into Oilfield Brines. Corrosion. 2002; (02270).

50. Oldfield JW. Electrochemical Theory of Galvanic Corrosion", in Hack, H. P. (ed.) Galvanic Corrosion, American Society for Testing of Materials. United State; 1988. 5–22.

51. Huang L., Brown B., Nesic S. Investigation of Environmental Effects on Intrinsic and Galvanic Corrosion of mild Steel weldment in CO_2 Environment. Corrosion. 2014. 1–15.

52. Hara, T., Asahi, H., Kaneta H. Effect of flow velocity on carbon dioxide corrosion behaviour in oil and gas environme118nts. CORROSION/98, paper 118, NACE International,Houston, TX.. Corrosion. Houston: NACE International. 1998. paper no. 118.

53. Altas steels. Galvanic corrosion. Technical. Melbourne; 2010. Available at: http://www.atlassteels.com.au/site/pages/service-centre-locations.php.

54. Olvera-Martínez ME., Mendoza-Flores J., Genesca J. CO_2 corrosion control in steel pipelines. Influence of turbulent flow on the performance of corrosion inhibitors. Journal of Loss Prevention in the Process Industries.

Elsevier Ltd; 2015; 35: 19–28. Available at: DOI:10.1016/j.jlp.2015.03.006

55. Davis JR. The Effects and Economic Impact of Corrosion. Corrosion Understanding the Basics. 2000; 1–21. Available at: DOI:10.1016/S0257-8972(02)00586-8.

56. Burkle DP. Understanding the Formation of Protective $FeCO_3$ on to Carbon Steel Pipelines during CO_2 Corrosion. PhD Thesis, The University of Leeds. 2017.

57. Offshore-Technology. Natuna Gas Field – Greater Sarawak Basin. 2007. Available at: https://www.offshore-technology.com/projects/natuna/

58. Alawadhi K., Robinson M. Inhibition of weld corrosion in flowing brines containing carbon dioxide. Corrosion Management UK. 2011; 10–13.

59. Scully JC. The Fundamental of Corrosion. 2nd edn. Exeter: Pergamon Press; 1990.

60. Lee CM., Bond S., Woollin P. Preferential Weld Corrosion: Effects of Weldment Microstructure and Composition. Corrosion. 2005; (05277): 1–16.

61. Kermani B., Linne C., Dougan M., Cochrane R., Gonzales JC. Development of low carbon Cr-Mo steels with exceptional corrosion resistance for oilfield applications. Corrosion. 2001; (01065).

62. Turgoose S., Palmer JW., Dicken GE. Preferential Weld Corrosion of 1% Ni Welds: Effect of Solution Conductivity and Corrosion inhibitors. Corrosion. 2005; (05275): 1–22.

63. Gooch T. Corrosion behavior of welded stainless steel. Welding Journal. 1996; 75(5).

64. Song FM. Electrochimica Acta A comprehensive model for predicting CO_2 corrosion rate in oil and gas production and transportation systems. Electrochimica Acta. 2010; 55: 689–700. Available at: DOI:10.1016/j.electacta.2009.07.087.

65. Haeryong J., Unji K., Gyutae S., Hyundong L., Chunsik L. Effect of Dissolved Oxygen (DO) on internal corrosion of ater pipes. Environmental Engineering Research. 2009; 14(3): 195–199. Available at: DOI:10.4491/eer.2009.14.3.195.

66. Rosli NR., Choi Y., Young D. Impact of Oxygen Ingress in CO_2 Corrosion of Mild Steel Nor. Corrosion. 2014; (4299): 1–15.

67. Sun Y., Nesic S. A Parametric Study and Modelling On localized CO_2 Corrosion in Horizontal Wet Gas Flow. Corrosion. 2004; (04380): 1–24.

68. Nyborg R., Dugstad A. MESA corrosion attack in carbon steel and 0.5 % chromium steel. Corrosion NACE International. 1998.

69. Nafday OA., Nesic S. Iron Carbonate Scale Formation and CO_2 Corrosion in the Presence of Acetic Acid. Corrosion. 2005; (05295): paper No. 05295.

70. Muñoz A., Genesca J., Duran R., Mendoza J. Mechanism of $FeCO_3$ Formation on API X70 Pipeline Steel In Brine Solutions Containing CO_2. Corrosion. Houston. 2005. 1–14.

71. Burkle D., De Motte R., Taleb W., Kleppe A., Comyn T., Vargas SM., et al. In situ SR-XRD study of $FeCO_3$ precipitation kinetics onto carbon steel in CO_2-containing environments: The influence of brine pH. Electrochimica Acta. 2017; Available at: DOI:10.1016/j.electacta.2017.09.138.

72. F. Farelas BB and SN. Iron Carbide and its Influence on the Formation of Protective Iron Carbonate in CO_2 Corrosion of Mild Steel. NACE - International Corrosion Conference Series. 2013. 1–15.

73. Dugstad A. Mechanism of protective film formation during CO_2 corrosion of carbon steel. Corrosion/98. 1998; (31): 1–11.

74. Mora-Mendoza JL., Turgoose S. Fe3C influence on the corrosion rate of mild steel in aqueous CO_2 systems under turbulent flow conditions. Corrosion Science. 2002; 44(6): 1223–1246. Available at: DOI:10.1016/S0010-938X(01)00141-X.

75. Sun Y., Nesic S. A parametric study and modelling on localized CO_2 corrosion in horizontal wet gas glow. Corrosion. 2004; (04380): 1–24.

76. Crolet JL., Thevenot N., Nesic S. Role of Conductive Corrosion Products in the Protectiveness of Corrosion Layers. Corrosion. 1998; 54(3): 194–203. Available at: DOI:10.5006/1.3284844.

77. Farelas F, Galicia M, Brown B, Nesic S, Castaneda H. Evolution of dissolution processes at the interface of carbon steel corroding in a CO_2 environment studied by EIS. Corrosion Science. 2010; 52 (2), 509-517.

78. Dugstad A. Formation of Protective Corrosion Films during CO_2 Corrosion of Carbon Steel. Eurocorr. Trondheim, Norway: NACE International. 1997.

79. Kermani B. Depiction of Metallurgical Parameters as Governing CO_2 Corrosion. NACE - International Corrosion Conference Series. 2014. 7–9.

80. Kermani, M. B. and Morshed A. Carbon Dioxide Corrosion in Oil and Gas Production - A Compendium. Corrosion. 2003; 59(8).

81. Marion GM., Catling DC., Kargel JS. Modeling aqueous ferrous iron chemistry at low temperatures with application to Mars. Geochimica et cosmochimica Acta. 2003; 67(22): 4251–4266.

82. Nesic, S. Lee, J. and V. Ruzic V 2002. A mechanistic model of iron carbonate film growth and the effect on CO_2 corrosion of mildsteel. CORROSION NACE International. 2002; no. 2237.

83. Garside J., Davey RJ. From Molecules to Crystallizers—An Introduction to Crystallization. Oxford University Press. 2000.

84. Li D., Zhang L., Ma W., Lu M., Han D., Wang L. Effects of temperature on CO_2 corrosion of tubing and casing steel. Corrosion 2013. 2013; (2426).

85. Al-Sayed MSA. Effect of Flow and pH on CO_2 corrosion and inhibition. University of Manchester. 1989.

86. Abd El-Nabey BA., Khamis E., Thompson GE., Dawson JL. Effect of temperature on the inhibition of the acid corrosion of steel by benzaldehyde thiosemicarbazone: Impedance measurements. Surface and Coatings Technology. 1986; 28(1): 83–91. Available at: DOI:10.1016/0257-8972(86)90119-2.

87. Bílko K., Gulbrandsen E. Kinetic and mechanistic study of CO_2 corrosion inhibition by cetyl trimethyl ammonium bromide. Electrochimica Acta. 2008; 53: 5423–5433. Available at: DOI:10.1016/j.electacta.2008.02.096.

88. De Waard C., Williams DE. Monogram for predicting CO_2 corrosion of carbon steel is based on the deWaard- Milliams equation. NACE Corrosion. 2004.

89. Wang S., George K., Nesic S. High Pressure CO_2 Corrosion Electrochemistry and the Effect of Acetic Acid. Corrosion. 2004; (04375): 1–17.

90. J. Han Y., Yang B., Brown S., Nesic S. Roles of passivation and galvanic effects in localized CO2 corrosion of mild steel. CORROSION NACE International. 2008; No. 08332.

91. Gao M., Pang X., Gao K. The growth mechanism of CO_2 corrosion product films. Corrosion Science. Elsevier Ltd; 2011; 53(2): 557–568. Available at: DOI:10.1016/j.corsci.2010.09.060.

92. Hunnik EWJ van., Pots BFM., Hendriksen ELJA. The Formation of Protective $FeCO_3$ Corrosion Product Layers In CO_2 Corrosion. Corrosion NACE. 1996; (6).

93. Z. F. Yin, Y. R. Feng, W. Z. Zhao, Z. Q. Bai GFL. Effect of temperature on CO_2 corrosion of carbon steel. Surface and Interface Analysis. 2009; 41(6): 517–523.

94. Tanupabrungsun T., Brown B., Nesic S., Technology M. Effect of pH on CO_2 Corrosion of Mild Steel at Elevated Temperatures. Corrosion. 2013; (2348): 1–11.

95. Nesic S. Key issues related to modelling of internal corrosion of oil and gas pipelines–A review. Corrosion Science. 2007; 49(12): 4308–4338.

96. Pessu, F., Barker, R. and Neville A. The influence of pH on localized corrosion behavior of X65 carbon steel in CO_2-saturated brines. Corrosion. 2015; 71(12): 1452–1466.

97. Adegbite MA., Impey SA., Robinson MJ. The influence of hydrodynamics on the preferential weld corrosion of X65 linepipe steel in flowing brine containing carbon dioxide. Corrosion. Texas; 2014. 1–14.

98. Alawadhi K. Inhibition of Weld Corrosion in Flowing Brines Containing Carbon Dioxide. Cranfield University; 2009.

99. Martinez M., Robinson M., Macdonald A., Alawadhi K., Nelson G. Control of Prefrential Weld Corrosion of X65 Pipeline Steel in Flowing Brines Containing Carbon Dioxide. Corrosion NACE. Houston; 2011; (11268): 1–14.

100. Meng Q., Jovancicevic V., Petrolite B., Land S. Electrochemical Evaluation of CO_2 Corrosion Inhibitors in High Turbulence Multiphase Fluid Flow. NACE - International Corrosion Conference Series. 2008. 1–14.

101. Hausler RH., Guenter S. Hydrodynamic and Flow Effects on Corrosion Inhibition. Corrosion. 2004; (04402): 1–20.

102. Efird K D. Disturbed Flow and Flow-Accelerated Corrosion in Oil and Gas Production. Journal of Energy Resources Technology. 1998; 120:1, 72.

103. Praturi AK., Brodkey RS. A stereoscopic visual study of coherent structures in turbulent shear flow. Journal of Fluid Mechanics. 1978; 89(2): 251–272.

104. Fang CS., Liu B. Corrosion Induced by Change in Hydrodynamics. Corrosion. 2004; (04661): 1–11.

105. Roberge P. Corrosion Testing Made Easy: Erosion-Corrosion. NACE Press. CORROSION NACE International. 2004;

106. Silverman D. Rotating cylinder electrode – geometry relationships prediction of velocity- sensitive corrosion. Corrosion. 1988; 44(42).

107. Silverman D. Rotating cylinder electrode for velocity sensitivity testing. Corrosion. 1984; 40: 220–226.

108. Akeer ES. Effect of Carbon Steel Composition and Microstructure on CO_2 Corrosion. Ohio University. 2014.

109. Schmitt G., Bakalli M. A Critical Review of Measuring Techniques for Corrosion Rates under Flow Conditions. NACE - International Corrosion Conference Series. Houston. 2006.

110. Gabe DR., Wilcox GD. The rotating cylinder electrode : its continued development and application *. Jurnal of Applied Electrochemistry. 1998; 28(49): 759–780.

111. Ferreiraa LRM., Ponteb HA., Sanchesb., Schmidlin L., Abrantesb., Gomes ACT. CO_2 Corrosion in the Region Between the Static and Turbulent Flow Regimes. Materials Research. 2015; 18(2): 245–249.

112. Kumar A., Ling S., Pacheco JL., Desai SK., Reddy R V. Effects of rotating cage autoclave design on shear stress and flow pattern. NACE - International Corrosion Conference Series. 2013. 1–13.

113. ASTM G 184 “Standard Practice for Evaluating and Qualifying Oil Field and Refinery Corrosion Inhibitors Using Rotating Cage”. 2006.

114. ASTM G 202 “Standard Test method for Using Atmospheric Pressure Rotating Cage”. 2009.

115. Jose C. Cardoso Filho. MEO. Application of a Submerged Impinging Jet to Investigate the Influence of Temperature, Dissolved CO_2, and Fluid Velocity on Corrosion of Pipeline-Grade Steel in Brine. Corrosion. 2001; (01058).

116. Giralt F., Trass O. Mass Tranfer from Crystalline Surface in a Turbulance Impinging Jet. Part 2: Erosion and diffusional Tranfer. The Canadian Journal of Chemical Engineering. 1976; 54(3): 148–155.

117. Zhang GA., Cheng YF. Electrochemical characterization and computational fluid dynamics simulation of flow-accelerated corrosion of X65 steel in a CO_2-saturated oilfield formation water. Corrosion Science. Elsevier Ltd; 2010; 52(8): 2716–2724. Available at: DOI:10.1016/j.corsci.2010.04.029.

118. Joshua O., Callum R., Richard B., Anne N. Erosion-corrosion interaction of X-65 carbon steel in aqueous CO_2 environment. Wear. 2018; (414–415): 376–389.

119. Kosec T., Otmaˇ H. Investigation of the corrosion protection of chemically and electrochemically formed patinas on recent bronze. Electrochimica Acta. 2010; 56(2): 722–731. Available at: DOI:10.1016/j.electacta.2010.09.093.

120. Groysman A. Corrosion for everybody. Springer Science & Business Media. New York; 2010. Available at: DOI:10.1007/978-90-481-3477-9_1

121. Ramachandran S., Ward MB., Bartrip KA., Jovancicevic V., Petrolite B., Land S. Inhibition of the Effects of Particle Impingement. Corrosion. 2002; (02498): 1–12.

122. Patni N., Agarwal S., Shah P. Greener Approach towards Corrosion Inhibition. Chinese Journal of Engineering. 2013.

123. Koch G. Cost of Corrosion. In: El-Sherik AM (ed.) Trends in Oil and Gas Corrosion Research and Technologies. 2017. 3–30.

124. Papavinasam S. Evaluation and selection of corrosion inhibitors. Uhlig’s Corrosion Handbook. second edition. New York: Wiley & Sons, Inc. 2000. 1169-1178.

125. Azhar EM., Traisnel M., Mernari B., Gengembre L., Bentiss F., Langrenee M. Electrochemical and XPS studies of 2,5-bis(n-pyridyl)-1,3,4-thiadiazoles

adsorption on mild steel in perchloric acid solution. Applied Surface Science. 2002; 185: 197–205.

126. Vracar LM., Drazic DM. Adsorption and corrosion inhibitive properties of some organic molecules on iron electrode in sulfuric acid. Corrosion Science. 2002; 44: 1669–1680.

127. Leahy M., Cook S., Mok WY. Quantitative Assessment of Preferential Weld Corrosion in Operator Supplied Weight Loss Coupons Using White Light Interferometry. Society of Petroleum Engineers - Offshore Europe Oil and Gas Conference and Exhibition 2017. 2017; SPE-186311.

128. Revie RW. Uhlig's Corrosion Book. second. New York: John Wiley & Sons, Inc.; 2000.

129. Mansfield F. Corrosion mechanisms. O'Connor PDT (ed.) New York: Marcel Dekker Inc; 1987. 119-164; 202-204. Available at: https://doi.org/10.1002/qre.4680030313.

130. Dugstad A. Mechanism of Protective Film Formation During CO_2 Corrosion of Carbon Steel. Corroion NACE. 2007; (31).

131. Finšgar M., Jackson J. Application of corrosion inhibitors for steels in acidic media for the oil and gas industry : A review. Corrosion Science. 2014; 86: 17–41. Available at: DOI:10.1016/j.corsci.2014.04.044.

132. Taj S., Al-ameen A., Road H., Papavinasam S., Revie RW. Development of green inhibitors for oil and gas applications. Corrosion NACE International. 2006. 1–9.

133. Tiu Brylee DB., Advincula RC. Polymeric corrosion inhibitors for the oil and gas industry : Design principles and mechanism. Reactive and Functional Polymers. Elsevier B.V.; 2015; 95: 25–45. Available at: DOI:10.1016/j.reactfunctpolym.2015.08.006.

134. Papavinasam, S., Revie, R. W., Attard, M., Michaelian, K., Sun, H., Demoz, A. & Donini JC. Inhibitor Selection for Internal Corrosion Control of Pipelines: 1. Laboratory Methodologies. CORROSION NACE International. 1999; No. 99.

135. Lopez D., Perez T., Simison S. The Influence of Microstructure and Chemical Composition of Carbon and Low Alloy Steels in CO_2 Corrosion. A State-of-the-art Appraisal. Material and Design. 2003; 24: 561–575.

136. Wang J., Atrens A. Microstructure and grain boundary microanalysis of X70 pipeline steel. Journal of Material Science. 2003; 38: 323–330.

137. Thompos S., Colvin D., Krauss G. Continuous cooling transformations and microstructures in a low carbon, high-strength low-alloy plate steel. Metall. Trans. A. 1990; 21: 1493.

138. López DA., Simison NS., DeSánchez SR de. Effect of Temperature on Adsorption Behavior and Corrosion Inhibition Performance of Imidazoline-

Type Inhibitor. Corrosion Sciences. 2005; 47(3): 735–755.

139. Paolinelli LD., Simison SN. The Influence of Steel Microstructure, Chemical Composition and Precorrosion on CO_2 Corrosion Inhibitor Efficiency. NACE - International Corrosion Conference Series. 2007.

140. Gulbrandsen E. How Does Fluid Flow Affect Performance of CO_2 Corrosion Inhibitors? Society of Petroleum Engineers - Offshore Europe Oil and Gas Conference and Exhibition. 2005; SPE 95095: 6–7.

141. Gulbrandsen, E., Nesic, S., Hesjevik, S. M., Skjfrve, S., Sundfer, B., Burchardt, T. and Stangeland A. Effect of Pre-corrosion on the Performance of Inhibitors for CO_2 Corrosion of Carbon Steel. NACE - International Corrosion Conference Series. 1998; No. 98013.

142. Inhibitor I., Ding Y., Brown B., Young D., Nesic S., Singer M., et al. Effect of Temperature on Adsorption Behavior and Corrosion Inhibition Performance of Imidazoline-Type Inhibitor. Corrosion 2000; (9350): 1–15.

143. Mahgoub FM., AlNowaiser FM., AlSudairi AM. Effect of temperature on the inhibition of the acid corrosion of steel by benzimidazole derivatives. Protection of Metals and Physical Chemistry of Surface. 2011; 47(3): 381–394.

144. Chen HJ. High Temperature Corrosion Inhibition Performance of Imidazoline and Amide. Corrosion NACE. 2000; (00035).

145. Gulbrandsen E., Kvarekval J. High temperature and high flow velocity tests for CO_2 corrosion inhibitors. Corrosion. 2001.

146. Abd El-nabey BA., Khamis E., Thomson GE., Dawson JL. Effect of temperature on the inhibition of the acid corrosion of steel by benzaldehyde thiosemicarbazone: impedance measurements. Surface and Coatings Technology. 1986; 28(1): 83–91.

147. Mamdouh M. Salama BNB. Study of factors affecting CO_2 corrosion and inhibitor effectiveness using a multi-phase flow loop. Corrosion Conference & Expo. 2009; (09476): 17.

148. Ashassi-Sorkhabi H., Asghari E. Effect of hydrodynamic conditions on the inhibition performance of l-methionine as a “green” inhibitor. Electrochimica Acta 54 (2008) 162–167. 2008; : 162–167.

149. Nesic, S., Nordsveen, M. and Stangel A. A Mechanistic Model for CO_2 Corrosion with Protective Iron Carbonate Films. Corrosion NACE. 2001.

150. Efird KD. Jet impingement testing to investigate flow effects on corrosion. Efird Corrosion International, Inc.,Texas; April 2013.

151. Lagrenee, M., Mernari, B., Bouanis, M., Traisnel, M. & Bentiss F. Study of the mechanism and inhibiting 4H-1 , 2 , 4-triazole on mild steel corrosion in acidic media. Corrosion Science. 2002; 44: 573–588.

152. Ferreira ES., Giacomelli C., Giacomelli FC., Spinelli A. Evaluation of the inhibitor effect of l -ascorbic acid on the corrosion of mild steel. Material Chemistry and Physics. 2004; 83: 129–134. Available at: DOI:10.1016/j.matchemphys.2003.09.020.

153. El Azhar M., Traisnel M., Mernari B., Gengembre L., Bentiss F., Langrenee M. Electrochemical and XPS studies of 2,5-bis(n-pyridyl)-1,3,4-thiadiazoles adsorption on mild steel in perchloric acid solution. Applied Surface Science. 2002; 185: 197–205.

154. Popova A., Sokolova E., Raicheva S., Christov M. AC and DC study of the temperature effect on mild steel corrosion in acid media in the presence of benzimidazole derivatives. Corrosion Science. 2003; 45: 33–58.

155. Ige OO., Barker R., Hu X., Umoru LE., Neville A. Assessing the in fluence of shear stress and particle impingement on inhibitor efficiency through the application of in-situ electrochemistry in a CO_2 -saturated environment. Wear. 2013; 304: 49–59. Available at: DOI:10.1016/j.wear.2013.04.013

156. Hua Y., Barker R., Neville A. The journal of Supercritical Fluids Comparison of corrosion behaviour for X-65 carbon steel in supercritical CO_2-saturated water and water-saturated / unsaturated supercritical CO_2. The Journal of Supercritical Fluids. Elsevier B.V.; 2015; 97: 224–237. Available at: DOI:10.1016/j.supflu.2014.12.005

157. Ohtsuka T., Nishikata A., Sakairi M., Fushimi K. Electrochemical Measurement of Wet Corrosion. Electrochemistry for Corrosion Fundamental. Springer Science & Business Media.; 2018. 17–39.

158. Poorqasemi E., Abootalebi O., Peikari M., Haqdar F. Investigating accuracy of the Tafel extrapolation method in HCl solutions. Corrosion Science. Elsevier Ltd; 2009; 51(5): 1043–1054. Available at: DOI:10.1016/j.corsci.2009.03.001.

159. Mccafferty E. Validation of corrosion rates measured by the Tafel extrapolation method. 2005; 47: 3202–3215. Available at: DOI:10.1016/j.corsci.2005.05.046

160. Scully JR. Polarization Resistance Method for Determination of Instantaneous Corrison rate. Corrosion. 2000; 56(2): 199–218.

161. Baboian R. NACE Corrosion Engineer's Reference Book. National Association of Corrosion Engineers; 2002.

162. Chemistry L. Corrosion: Undesirable Redox Reactions. 2017. Available at: https://chem.libretexts.org/Bookshelves/General_Chemistry/Map%3A_A_Molecular_Approach_(Tro)/19%3A_Electrochemistry/19.9%3A_Corrosion%3A_Undesirable_Redox_Reactions (Accessed: 21 February 2018).

163. Pidcock A. Control of Magnesium Alloy Corrosion through the Use of Engineere Intermatallic. Cranfield University; 2014.

164. Walter GW. A review of impedance plot methods used for corrosion performance analysis of painted metals. Corrosion Science. 1986; 26(9): 681–703.

165. Popova A., Sokolova E., Raicheva S., Christov M. AC and DC study of the temperature effect on mild steel corrosion in acid media in the presence of benzimidazole derivatives. Corrosion Science. 2003; 45(1): 33–58. Available at: DOI:10.1016/S0010-938X(02)00072-0.

166. Hamdy A., El-Gendy NS. Thermodynamic, adsorption and electrochemical studies for corrosion inhibition of carbon steel by henna extract in acid medium. Egyptian Journal of Petroleum. Egyptian Petroleum Research Institute; 2013; 22(1): 17–25. Available at: DOI:10.1016/j.ejpe.2012.06.002

166. Yao N. Introduction to the Focused Ion Beam System. Basic and Application. 1st edition. Cambridge. Cambridge University Pres. 2007; 1-10.

168. Cullity BD., Stock SR. Elements of X-ray diffraction. Third. United States of America: Pearson; 2013.

169. Guzonas DA., Rocheford PA., Turner CW. Corrosion product characterisation by Fibre Optic Raman Spectroscopy. Ontario.

170. Huang H., Feng X., Du C., Wu S., Song W. One-step pyrolytic synthesis of small iron carbide nanoparticles/3D porous nitrogen-rich graphene for efficient electrocatalysis. Journal of materials chemistry A. 2015; (9).

171. Allison C., Robinson MJ. Assessment of Vented Flexible Liners for Corrosion Protection of Pipelines. Corrosion. 2011; (11300): 1–14.

172. Nesic S., Nordsveen M., Nyborg R., Stangeland A. A mechanistic model for CO2 corrosion with protective iron carbonate films. Corrosion 2001; (01040): 28.

173. Park E., Zhang J., Thomsom S., Ostrovski O., Howe R. Charatcerization of Phase Formed in the Iron Carbide Process by X-Ray Diffraction, Mossbauer, X-Ray Photoelectron Spectroscopy, and Raman Spectroscopy Analyses. Metallurgical and Material Transaction B. 2001; 32B: 839–845.

174. Forero AB., Núñez MMG., Bott IS. Analysis of the corrosion scales formed on API 5L X70 and X80 steel pipe in the presence of CO_2. Materials Research. 2013; 17(2): 461–471. Available at: DOI:10.1590/s1516-14392013005000182.

175. Kermani B. Depiction of Metallurgical Parameters as Governing CO_2 Corrosion. Corrosion 2014. 2014; (3813): 3813.

176. Hu X., Barker R., Neville A., Gnanavelu A. Case study on erosion-corrosion degradation of pipework located on an offshore oil and gas facility. Wear. 2011; 271(9–10): 1295–1301.

177. Hu X., Neville A. CO_2 Erosion-Corrosion of Steel (API X65) in Oil and Gas Condition-A Systematic Approach. Wear. 2009; 267: 2027-2032.

178. Barker R., Hu X., Neville A., Cushnaghan S., Limited SUK. Assessment of Preferential Weld Corrosion of Carbon Steel Pipework in CO_2-Saturated Flow- Induced Corrosion Environments. NACE Corrosion Conference. Houston; 2012.

179. Hummel DO., Scholl FK. Infrared Analysis of Polymer Resins and Additives An Atlas. I. New York: John Wiley & Sons, Inc.1971. 48-62.

180. Barker R., Hu X., Neville A., Cushnaghan S., Limited SUK. Assessment of Preferential Weld Corrosion of Carbon Steel Pipework in CO_2-Saturated Flow- Induced Corrosion Environments. NACE Corrosion Conference Series. 2012 ; (3) 2208-2229.

181. Dong S., Liu W., Zhang J., Lin X., He J., Lu M. Effect of oxygen on CO_2 corrosion and erosion-corrosion behaviour of N80 steel under high temperature and high pressure. Corrosion NACE. 2014. 1–14.

182. Zhang Y., Gao K., Schmitt G. Inhibition of Steel Corrosion Under Aqueous Supercritical CO_2 Conditions. Corrosion NACE. 2011;

183. Dayalan E., Moraes de FD., Shadley JR., Shirazi SA., Rybicki EF. CO_2 Corrosion Prediction in Pipe Flow under $FeCO_3$ Scale-Forming condition. Corrosion. 1998; (51).

184. Alink B., Outlaw B., Jovancicevic V., Ramachandran S., Campbell S. Mechanism of CO_2 Corrosion Inhibition by Phosphate Esther. Corrosion. 1999; (37).

185. Nesic, S., Postlethwaite, J. and Olsen S. An electrochemical model for prediction of CO_2 corrosion. CORROSION NACE International. (131). 1995;

186. Obanijesu EO., Gubner R., Barifcani A., Pareek V., Tade MO. Influence of corrosion inhibitors on hydrate formation temperature along the subsea natural gas pipelines. Journal of Petroleum Science and Engineering. Elsevier; 2014; 120: 239–252. Available at: DOI:10.1016/j.petrol.2014.05.025

187. Li W. Mechanical Effects of Flow on CO_2 Corrosion Inhibition of Carbon Steel Pipelines. PhD Thesis. Department of Chemical and Biomolecular Engineering and the Russ College of Engineering and Technology. 2016.

188. Nybborg R., Dugstan A. Mesa corrosion attack in carbon steel and 0.5 % chromium steel. Corrosion Conference & Expo. 2008; 08332.

189. Halvorsnand A., Sontvedt T. CO_2 Corrosion model for carbon steel including a wall shear stress model for multiphase flow and limits for production rate to avoid mesa attck. Corrosion International. 1999; 42.

190. Wang JQ., Atrens A., Cousen DR., Kinaev N. Microstructure of X52 and

X65 Pipeline Steels. Journal of Material Science. 1999; 34: 1721–1728.

191. Merlin J., Merle P., Garnier S., Bouzekri M., Soler M. Experimental determination of the carbon solubility limit in ferritic steels. Metallurgical and Materials Transactions A. 2004; 35(1655–1661).

192. Mintz B., Campbell P. Growth of grain boundary carbides in C–Mn steels. Materials Science and Technology. 1989; 5(2): 155–161.

193. Gulbrandsen E., Dugstad A. Corrosion loop studies of preferential weld corrosion and its inhibition in CO_2 environments. Corrosion. 2005; (05276).

194. Gollapudi S. Grain size distribution effects on the corrosion behaviour of materials. Corrosion Science. Elsevier Ltd; 2012; 62: 90–94. Available at: DOI:10.1016/j.corsci.2012.04.040

195. Luo W., Xu Y., Wang Q., Shi P., Yan M. Effect of grain size on corrosion of nanocrystalline copper in NaOH solution. Corrosion Science. Elsevier Ltd; 2010; 52(10): 3509–3513. Available at: DOI:10.1016/j.corsci.2010.06.029

196. Kenausis GL., Vörös J., Huang N., Elbert DL., Hubbell JA., Textor M., et al. Poly(l -lysine)- g -Poly(ethylene glycol) Layers on Metal Oxide Surfaces: Attachment Mechanism and Effects of Polymer Architecture on Resistance to Protein Adsorption. The Journal of Physical Chemistry B. 2002; 104(14): 3298–3309. Available at: DOI:10.1021/jp993359m

197. Ali Fathima AA., Subhashini S. Corrosion inhibition, adsorption andthermodynamic properties of poly(vinyl alcohol-cysteine) in molar HCl. Arabian Journal of Chemistry. 2014; 10: S3358–S3366.

198. StephenTait W. Corrosion Prevention and Control of Chemical Processing Equipment. Handbook of Environmental Degradation of Materials (Second Edition). 2012. pp. 863–886.

199. Schmitt, G. A. and Mueller M. Critical Wall Shear Stresses in CO_2 Corrosion of Carbon Steel. NACE - International Corrosion Conference Series. 1999.

200. Lu YC. A flow-impingement facility for corrosion and electrochemical studies in high–temperature aqueous solutions. NACE International. 2004; (4677): 1–13.

201. J.M. Domínguez Olivo, B. Brown, S. Nesic, Modeling of Corrosion Mechanisms in the Presence of Quaternary Ammonium Chloride and Imidazoline Corrosion Inhibitors, NACE International, 2016, paper no. 7406

202. Gaurav Ravindra Joshi, Elucidating Sweet Corrosion Scales, PhD Thesis. School of Material Corrosion and Protection Centre, faculty of Engineering and Physical Sciences, University of Manchester, 2015.

APPENDICES

Appendix A Publication and Presentation

A.1 Conference Paper

N. Nofrizal, S. A Impey, M. J Robinson, “The effect of flow rate on the preferential weld corrosion of X65 pipeline steel”, conference proceeding (EUROCORR-Montpellier France 2016)

A.2 Oral Presentations

- ✓ N. Nofrizal, S. A Impey, M. J Robinson, “The effect of flow rate on the preferential weld corrosion of X65 pipeline steel”, conference proceeding (EUROCORR- Montpellier France 2016)
- ✓ N. Nofrizal, S. A Impey, K. Georgarakis, “Preferential weld corrosion of high strength pipeline steel” (Presented in Corrosion Science Symposium 2017- Birmingham University)
- ✓ N. Nofrizal, S. A Impey, K. Georgarakis, Corrosion of High Strength Pipeline Steel Weldment Using Submerged Jet Impingement”, (Presented in Corrosion Science Symposium 2018- Leeds University)

A.3 Poster Presentation

Manufacturing Doctoral Community Cranfield University, UK, “PhD poster presentation day”. 25 April 2018 (received an award as the best poster)

Appendix B (Example EDX Analysis result)

EDX of PM after 20h exposure in uninhibited brine saturated with CO_2 without flow reported in Table 4-3

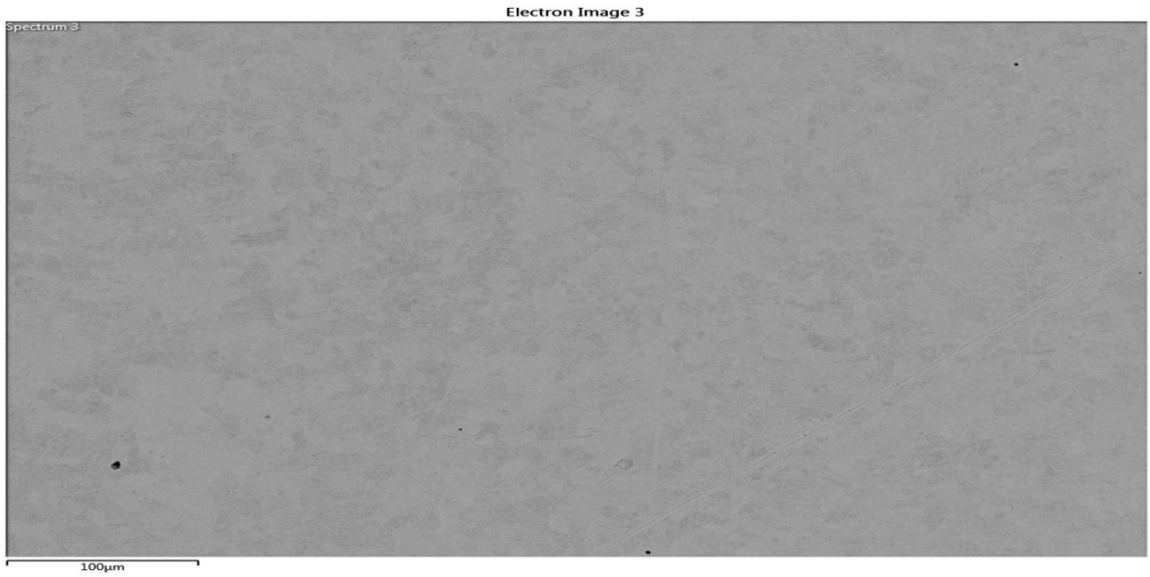

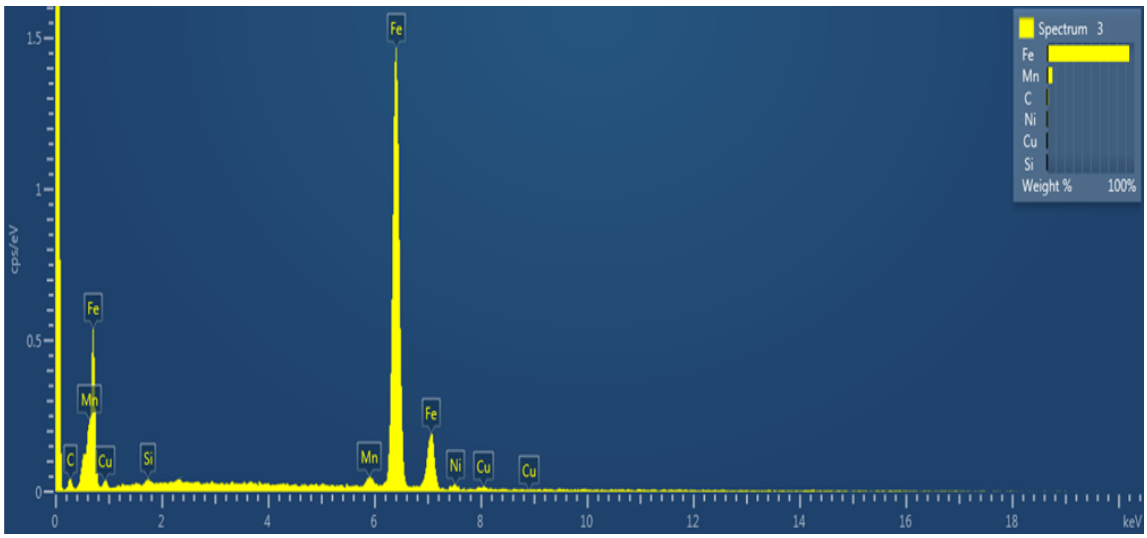

Spectrum	Line Type	Apparent	k Ratio	Wt%	Wt% Sigm	Atomic %
C	K series	0.86	0.02159	0.69	0.48	3.13
Si	K series	1.24	0.01409	0.11	0.11	0.66
Mn	K series	11.32	0.11616	1.62	0.19	1.37
Fe	K series	626.63	6.26629	97.1	0.52	94.13
Cu	K series	1.29	0.01423	0.19	0.11	0.65
Ni	K series	1.32	0.01221	0.29	0.23	0.21
Total				100		100

Appendix C (Calculation examples)

C.1 Calculation of corrosion rate (CR) from LPR measurement

The I_{corr} can be calculated using Equation C1-1

$$i_{corr} = \frac{B}{R_p} \quad \text{(C1-1)}$$

B = Stern-Geary coefficient (V decade^{-1}), can be calculated from Equation C2-2

$$B = \frac{b_a b}{2.3\,(b_a b_c)} \quad \text{(C2-2)}$$

In this study, the B value was maintained as 26 mV decade^{-1}. The choice of a value of B is open to some debate but, in this study, a value of B of 26 mV decade^{1} was used. This is in line with previous workers in the field of CO_2 corrosion [72,108,201,202].

To measure the corrosion rate (mm/y), the I_{corr} can calculated at the first step using equation 1.

For example to calculate the corrosion rate of weld metal (WM) in the outer electrode in a still, non-flowing environment.

R_p = polarisation resistance from the linear regression (slope)

R_p = 274 Ω.cm^2 (for WM)

$$i_{corr} = \frac{B}{R_p}$$

$$i_{corr} = \frac{26\text{x}10^{-3}\,V}{274\ \Omega.cm^2} = 9.48\text{x}10^{-5}\ A/cm^2$$

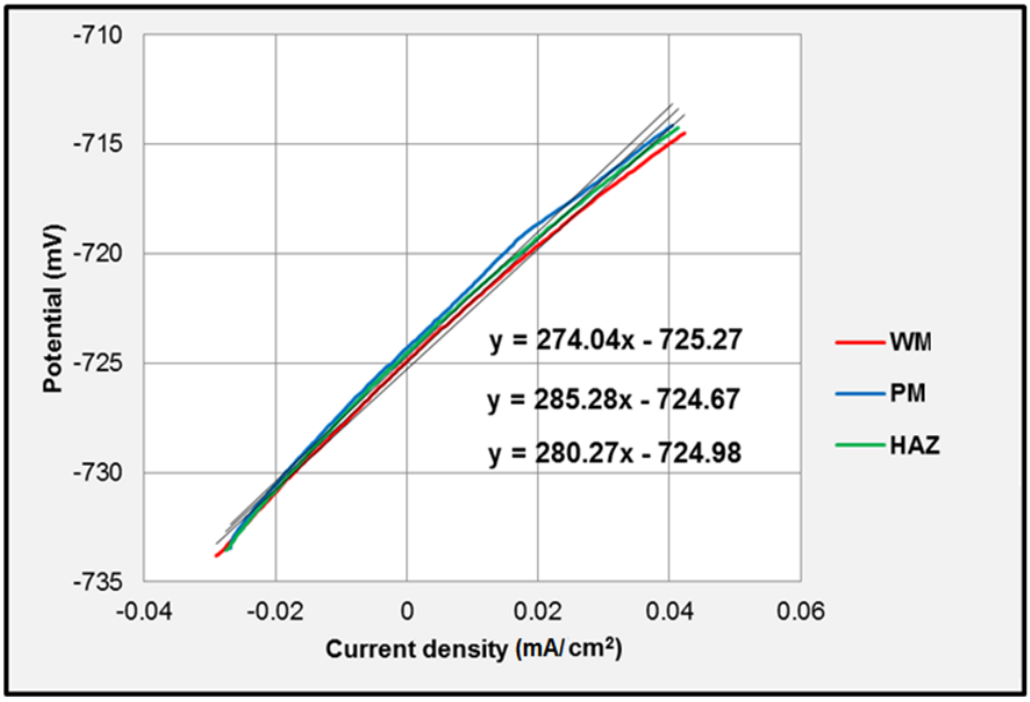

To calculate the corrosion rate (mm/y), **Faraday's law** is used

$$m = \frac{i_{corr}}{F}\frac{M}{n}$$

Where

m= metal loss (g)

F = Faraday's constant = 96485 C $mole^{-1}$

n = number of electrons transferred = 2

M = atomic weight metal (g $mole^{-1}$) = 55.85 g $mole^{-1}$

i_{corr} = Corrosion current density (A/cm^2)

A (Ampere) = Coulomb/second (Cs^{-1}), so

i_{corr} = Corrosion current density (A/cm^2)

= $94.8x10^{-6}$ A/cm^2

= $94.8x10^{-6}$ Cs^{-1}/cm^2

$$m = \frac{(9.48x10^{-5}\ Cs^{-1}\ cm^{-2})\ (55.85\ g\ mol^{-1})}{(96485\ C\ mol^{-1})\ (2)} = 2.7x10^{-8}\ g\ cm^{-2}\ s^{-1}$$

Using $\rho = 7.89\ g\ cm^{-3}$

then,

$$m = \frac{2.7 \times 10^{-8}\ g\ cm^{-2}\ s^{-1}}{7.89\ g\ cm^{-3}}$$

$m = 3.4 \times 10^{-9}\ cm\ s^{-1}$.

To get corrosion rate in mm/y from metal loss m

multiply m by 31536000 (seconds in a year)

Corrosion Rate CR (mm/y) $= (3.4 \times 10\text{-}9\ cm\ s^{-1}) \times (31536000\ s\ y^{-1})$

$= 0.11\ cm\ y^{-1}$

$= 1.1\ mm\ y^{-1}$

If I_{corr} $94.8\ \mu A/cm^2 = 1.1\ mm y^{-1}$

So, $1\ \mu A/cm^2 = 0.0116\ mm\ y^{-1}$

Therefore the corrosion rate in mm/y = **$0.0116\ mm\ y^{-1}$**

C.2 Calculation of Gibbs free energy ΔG^{o}_{ads} (adsorption isotherm)

The Langmuir adsorption isotherm is expressed according to Equation C2-1 and the free Gibbs energy equation equation C2-2

$$\frac{C}{\theta} = \frac{1}{K_{ads}} + C \qquad \text{(C2-1)}$$

$$\Delta G^{o}_{ads} = - RT \ln C_{water} K_{ads} \qquad \text{(C2-2)}$$

Where, C is the concentration of inhibitor

θ is the surface coverage determined by IE/100,

K_{ads} is the adsorption equilibrium constant and

ΔG^{o}_{ads} is the standard Gibbs free energy,

R is molar gas constant,

T is the temperature, IE is the inhibitor efficiency

C_{water} is the concentration of water in 1000 g/L.

By plotting values of C/θ versus values of C, straight line graphs were obtained (see Figure C2-1), which shows that the Langmuir adsorption isotherm is obeyed

For example to calculate PM metal in a still, non-flowing environment:

C (ppm)	C (g/L)	Efficiency (IE %)	Θ=(IE/100)	C/Θ
5	0.005	75.5	0.755	0.006623
10	0.01	80.6	0.806	0.012407
20	0.02	84.8	0.848	0.023585
30	0.03	88.3	0.883	0.033975

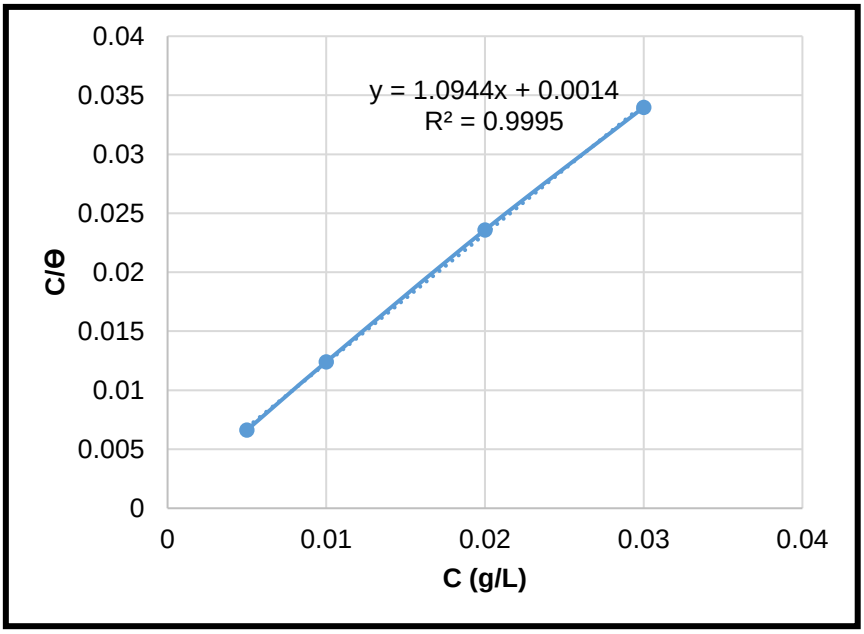

Figure C2-1. Langmuir adsorption isotherm for CORRTREAT 10-569 on parent metal

From linear regression, it is found that the intercept is 0.0014, so

$$\frac{1}{K_{ads}} = \text{intercept (from graph)}$$

$$\frac{1}{K_{ads}} = 0.0014 \text{ g L}^{-1}$$

$$K_{ads} = \frac{1}{0.0014}$$

$$K_{ads} = 714.3 \text{ L g}^{-1}$$

$$\Delta G^0_{ads} = -RT \ln C_{water} K_{ads}$$

R= 8.314462 J mole^{-1} K^{-1}

C_{water} = 1000 g L^{-1}

T = 273 + 25 =298 ^{o}K

ΔG^0_{ads}= -8.31 J/ mole^{-1}K^{-1} (298^{o}K) ln (1000×714.3)

= -32.72 kJ/mole